EVALUATE UNSATURATED SOIL BEHAVIOR USING CONSTANT WATER CONTENT TRIAXIAL TESTS

By

Lin Li

RECOMMENDED:

Dr. Gang Chen

Dr. Robert Lytton

Dr. Yuri Shur

Dr. J. Leroy Hulsey

Dr. Xiong Zhang
Advisory Committee Chair

Dr. Robert Perkins
Chair, Department of Civil and Environmental Engineering

APPROVED:

Dr. Douglas Goering
Dean, College of Engineering and Mines

Dr. John Eichelberger
Dean of the Graduate School

28 April 2015
Date

EVALUATE UNSATURATED SOIL BEHAVIOR USING CONSTANT WATER CONTENT TRIAXIAL TESTS

A

Dissertation

Presented to the Faculty

of the University of Alaska Fairbanks

in Partial Fulfillment of the Requirements

for the Degree of

DOCTOR OF PHILOSOPHY

By

Lin Li, M.S.

Fairbanks, Alaska

May 2015

ABSTRACT

The triaxial test has been extensively used to evaluate both saturated and unsaturated soil behaviors. The conventional triaxial test apparatus for saturated soils cannot be used to test unsaturated soils due to difficulties in soil volume and suction measurement. In 1961, a suction-controlled triaxial test apparatus was developed to investigate behavior of unsaturated soils. Since this development, the suction-controlled test has been widely used for unsaturated soil characterization. Most important concepts concerning unsaturated soil mechanics were developed based upon results from suction-controlled tests. However, the suction-controlled triaxial test on unsaturated soils, which is a drained test, is usually laborious, time-consuming, and costly, and may not be justifiable for routine engineering projects. The constant water content (undrained) test has been widely used to investigate saturated soil behaviors. However, for unsaturated soils, due to difficulties in direct, rapid, and reliable suction measurement, the constant water content test was rarely used for unsaturated soil behavior evaluation. In addition, accurate volume change measurement of unsaturated soils was a great challenge for researchers.

Recently, the Modified State Surface Approach (MSSA) has been developed to calibrate unsaturated soil behaviors. According to MSSA, both results from suction-controlled and constant water content triaxial tests can be used for constitutive behavior calibration on unsaturated soils. In this study, a new triaxial test system was developed to investigate unsaturated soil behaviors through constant water content triaxial tests. To measure soil suction variation during testing, a new type of high-suction tensiometer was developed based on a commercial miniature pressure transducer. A 15 bar air-entry ceramic disc was used as the filter of the high-suction tensiometer. After saturation and calibration, this new type of high-suction

tensiometer could be utilized for matric suction measurement on unsaturated soils with a maximum measurable suction up to 1100 kPa determined via a free evaporation test. To measure the volume change of unsaturated soils during triaxial testing, a photogrammetry-based method was developed by integrating photogrammetry, optical-ray tracing, and least-square estimation techniques. Through two validation tests on a stainless steel cylinder and a saturated sand specimen, the average point and total volume change measurement accuracy were determined to be approximately 0.065 mm and 0.05%, respectively. With this method, the conventional triaxial test apparatus for saturated soils can be used for triaxial testing on unsaturated soils without any modification. In addition to total volume change measurement, the newly developed photogrammetry-based method can also be used to investigate the deformation characteristics of soils during triaxial testing such as full-field deformation, volumetric strain non-uniformity, full-field strain distribution, and shear band evolution process.

To evaluate the performance of the new triaxial testing system, a series of constant water content triaxial tests were carried out on unsaturated soils. New methods were proposed to characterize shear strength of the tested unsaturated soils. Also, an example was given to calibrate the constitutive behavior of an unsaturated soil based on results from the constant water content triaxial tests. Analysis results indicated that the proposed triaxial testing system is a cost effective and time efficient alternative to the suction-controlled triaxial testing system.

In geotechnical and highway engineering, many projects involve unsaturated soils at shallow depths with low confining stresses (less than 100 kPa). To investigate the behavior of unsaturated soils at low confining stresses, the new triaxial testing system was simplified to a modified unconfined compression testing system. In this simplified system, negative air pressure (i.e., vacuum pressure) was used to provide the low confining stress for the triaxial tests. The

high-suction tensiometers were used to monitor soil matrix suction variation during testing. A photogrammetric method was utilized for deformation measurements of unsaturated soils during triaxial testing. A series of undrained triaxial tests was also carried out to demonstrate the use of the modified unconfined compression testing system for unsaturated soil behavior evaluation under different confining stresses.

ACKNOWLEDGMENTS

I would like to express my heartfelt gratitude and sincere appreciation to my advisor, Dr. Xiong Zhang for his enthusiasm and guidance. I would also like to thank Dr. Gang Chen, Dr. Yuri Shur, Dr. Robert Lytton, and Dr. Leroy Hulsey for serving as my committee members and for their continuous professional support during my Ph.D program.

I wish to acknowledge Alaska Department of Transportation and Public Facilities and Alaska University Transportation Center for their financial support throughout this study. The authors would also like to thank Eric's Machine shop for its help on the test equipment modification. Thanks also go to our laboratory manager, Gary Tyndall. Acknowledgements also go to my friends who have helped me in this research program. Finally, I must thank my wife (Jia Li) for her surprisingly deep understanding of the time to be away from her.

TABLE OF CONTENTS

LIST OF FIGURES

Page

LIST OF TABLES

CHAPTER 1. INTRODUCTION

1.1 Problem Statement

The triaxial test has been widely used to charaterize both saturated and unsaturated soils. The conventional triaxial test apparatus for saturated soils cannot be used to test unsaturated soils due to difficulties in soil volume and suction measurements. Bishop and Donald (1961) developed the first suction-controlled triaxial test apparatus for unsatuated soil behavior investigation. Since this development, the drained suction-controlled test has been extensively used. Most important concepts concerning unsaturated soil mechanics were developed based on results from suction-controlled tests (Delage 2002). However, the suction-controlled tests are too laborious, time-consuming, and costly, and cannot be justified for routine engineering projects. It can take up to two to three years to characterize the constitutive behavior of an unsaturated soil (e.g. Sivakumar 1993; Sharma 1998; Hoyos 1998). Previous studies on evaluating unsaturated soil behavior using constant water content (i.e. undrained) triaxial tests are limited due to the difficulties in direct, rapid, and reliable matric suction and volume change measurements. As a result, there is a great need of a new testing system for fast characterization of unsaturated soils. In addition, in the past, it was difficult to use the results from the constant water content tests for constitutive behavior calibration of unsaturated soils. Recently, a Modified State Surface Approach (MSSA) (Zhang and Lytton 2009a; 2009b; 2011) has been developed to calibrate unsaturated soil behaviors. According to MSSA, both results from suction-controlled and constant water content triaxial tests can be used to characterize constitutive behavior of unsaturated soils.

1.2 Research Objectives

The main objectives of this project are: (1) develop a new type of high-suction tensiometer for suction measurement on unsatuarted soils during triaxial testing under undrained condition; (2) develop a new method for unsaturated soil deformation measurements during triaixal testing; (3) develop a new triaixal test system for unsaturated soil behavior evaluation; (4) validate the concept that results from constant water content triaxial tests can be used as an alternative to the results from suction-controlled triaxial tests for unsaturated soil characterization; (5) develop a simplified system for triaixal tests on unsaturated soils under low confining stress conditions;

1.3 Research Methodology

To develop a new type of high-suction tensiometer for suction measurement on unsatuarted soils during triaxial testing, literatures on development of high-suction tensiometers were reviewed as presented in Chapter 2. A new type of high-suction tensiometer was designed, fabricated, saturated, and calibrated. The detailed development process for this new type of high-suction tensiometer is presented in Chapter 2. After saturation, the high-suction tensiometers can be used for suction measurement on unsaturated soils during triaxial testing. The performance of the developed tensiometers were evaluated through a series of unconfined compression tests on unsaturated soils under undrained condition.

To measure the total and localized volume changes of unsaturated soils in the confining chamber during triaxial testing, a photogrammetry-based method was developed. The mathmatical derivation and validation of the photogrammetry-based method are presented in the Appendix (i.e. Zhang et al. 2015). The post-processing (e.g. accuracy self-check, volume calculation, and strain calculation) of the photogrammetry-based method is presented in Chapter

3. In addition, examples on using results from the photogrammetry-based measurements for soil deformation characterization are given to demostrate the capabilities of the method.

With the newly developed high-suction tensiometers and the photogrammetry-based deformation measurement method, the conventional triaxial test apparatus for saturated soils was modified for the triaxial tests on unsaturated soils as presented in Chapter 4. Through a series of constant water content triaxial tests on unsaturated soils with different moisture contents, the capabilities of the new testing system were evaluated. In Chapter 4, New methods were also proposed to characterize shear strength and constitutive behavior of unsaturated soils using results from the constant water content triaxial tests.

With the newly developed high-suction tensiometers, a new modified unconfined compression test system, which is a simplified version of the new triaxial testing system, was developed for unsaturated soil characterization under low confining stresses (lower than 100 kPa) as presented in Chapter 5. The unsatuarted soil suction variation during testing was monitored using two newly developed high-suction tensiometers. A photogrammetric method was adopted to measure both the total and localized volume changes of unsaturated soils during triaxial testing. In this testing system, the confining load was applied through vacuum pressure. To evaluate the performance of the new system, a series of constant water content (undrained) triaxial tests was conducted on unsaturated soils with different water contents. Based on results from these undrained triaxial tests, shear strength properties of the tested unsaturated soil were characterized as presented in Chapter 5.

All conclusions from this research project are summarized in Chapter 6. Recommendations for future study are also presented.

1.4 References

Bishop, A. W., and Donald, I. B. (1961). The experimental study of partly saturated soil in the triaxial apparatus. Proceedings, 5th International Conference on Soil Mechanics, 1, pp.13–21.

Delage, P (2002). "Experimental unsaturated soil mechanics." Proc. 3rd Int. Conf. on Unsaturated Soils, UNSAT, (3) 973-996, Juca JFT, De Campos TMP, Marino FAM, Recife, Brazil, Balkema.

Hoyos, L. R., (1998) "Experimental and Computational Modeling of Unsaturated Soil Behavior under True Triaxial Stress States," Ph.D. dissertation, Georgia Institute of Technology, Atlanta.

Sharma, R. S., (1998) "Mechanical Behaviour of Unsaturated Highly Expansive Clays," Ph.D. Thesis, University of Oxford, UK.

Sivakumar, V. A., (1993) "Critical State Framework for Unsaturated Soil," Ph.D. Thesis, University of Oxford.

Zhang, X., and Lytton, R. L., 2009a, "Modified State-Surface Approach to the Study of Unsaturated Soil Behavior. Part I: Basic Concept," Can. Geotech. J., Vol. 46, No. 5, pp. 536-552.

Zhang, X., and Lytton, R. L., 2009b, "Modified State-Surface Approach to the Study of Unsaturated Soil Behavior. Part II: General Formulation," Can. Geotech. J., Vol. 46, No. 5, pp. 553-570.

Zhang, X., and Lytton, R. L., 2011, "Modified State-Surface Approach to the Study of Unsaturated Soil Behavior. Part III: Modeling of Coupled Hydromechanical Effect," Can. Geotech. J., Vol. 49, No. 1, pp. 98-120.

Zhang, X., Li, L., Chen, G., and Lytton, R. L., (2015) "A Photogrammetry-Based Method to Measure Total and Local Volume Changes of Unsaturated Soils during Triaxial Testing," Acta Geotechnica, Vol. 10, No.1, pp. 55-82.

CHAPTER 2. DEVELOPMENT OF A NEW HIGH-SUCTION TENSIOMETER[1]

2.1 Abstract

Nowadays, direct measurement of matric suction on unsaturated soils in the laboratory is still a great challenge for researchers. In this study, two new high-suction tensiometers were designed and fabricated based on commercial pressure transducers. Ceramic discs with an air-entry value of 15 bar were used as the filters for both tensiometers. The design, fabrication, saturation, and calibration processes are addressed in detail. Also, the maximum attainable suction was determined to be around 1100 kPa through free evaporation tests. Compared with existing high-suction tensiometers, both newly developed high-suction tensiometers proved to be robust and reliable for measuring matric suction of unsaturated soils.

[1]Li, L. and Zhang, X. (2014) "Development of a New High-Suction Tensiometer." Soil behavior and Geomechanics: pp. 416-425. doi: 10.1061/9780784413388.043.

2.2 Introduction

In the past few decades, a great effort has been dedicated to measuring matric suction of unsaturated soils. Reviews of conventional suction measurement methods on unsaturated soil are found in Fredlund and Rahardjo (1993), Ridley and Burland (1993), and Rahardjo and Leong (2006). High-suction tensiometer is considered to be the most suitable for measuring suction changes during triaxial testing. Basically, the theory of suction measurement using tensiometers is based on water tensile strength, which is the stress when a liquid ruptures or cavitates according to Guan and Fredlund (1997). Cavitation starts as vapor bubbles begin to form in water, which is triggered at gaseous or other hydrophobic surfaces. The vapor bubbles are commonly referred as potential cavitation nuclei. Water usually cavitates when the hydrostatic pressure is close to the vapor pressure. However, if the radii of cavitation nuclei are sufficiently reduced, water has the ability to sustain a high tension without cavitation which is the principle of highsuction tensiometer.

For conventional tensiometers, negative pressure measurement is limited to approximately -100 kPa due to the cavitation of water in the tensiometer (Fredlund and Rahardjo 1993). Thus, the application of conventional tensiometers is limited on unsaturated soils with low matric suction (0 to 100 kPa). The first attempt of direct measurement on soil with suction higher than 100 kPa was achieved by Ridley and Burland (1993) at Imperial College. It was found that during the use of a pressure plate for the suction measurement of a Kaolin sample, a water pressure ranging from -100 to - 300 kPa was detected by a reservoir transducer after an instant reduction of the air pressure in the chamber to an atmospheric level. This phenomenon was also found during the measurement of pore water pressure of a saturated soil specimen (equilibrium pore water pressure of 20 kPa) under a stress path with a confining pressure of 400

kPa by using pore water pressure sensor PDCR 81. Under undrained conditions, when the confining pressure was released relatively slowly to atmospheric pressure, a reduction in probe pressure was also detected and stabilized at -365 kPa. The high negative pressure in the probe slightly decreased and was maintained for about two hours before jumping to -100 kPa. Inspired by this phenomenon, by replacing the porous stone of PDCR 81 with a 15 bar ceramic disc, a new suction probe for measuring the matric suction of unsaturated soil was developed by Ridley and Burland (1993) as shown in Figure 2.1. A well saturated high-suction tensiometer could reach a negative pore water pressure up to -1370 kPa.

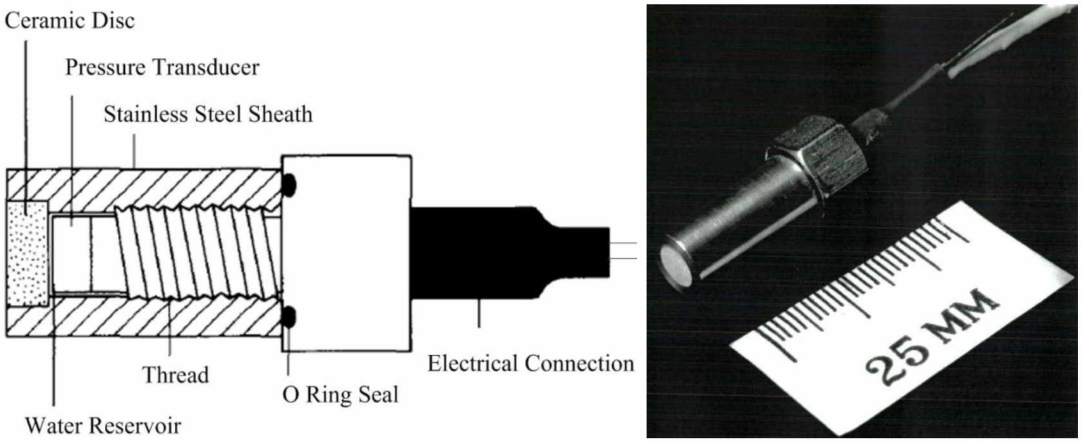

Figure 2.1 Tensiometer developed by Ridley and Burland (1993)

Since 1993, more of these high-suction tensiometers were developed and successfully used in laboratory and field experiments. At University of Saskatchewan, Guan and Fredlund (1997) reported the development of a tensiometer based on a high-range pressure transducer (150 bar, without thread) manufactured by Entran Devices, Inc., Fairfield, USA (Model: EPN-0762AI*-I50SY) instead of using a thread-type transducers. Meilani et al. (2002) presented the development of a tensiometer based on a PDCR 81 pressure transducer using 5 bar air entry ceramic disc. Similar designs are found for tensiometers developed by Tarantino and Mongiovi (2002), Take and Bolton (2003), and Lourenco et al. (2006). As described in Lourenco et al.

(2006), for all these high-suction tensiometers, a similar structure was found that comprises (1) a high air entry disc to prevent tensiometer cavitation at low suction, (2) a water reservoir to generate a negative water pressure, and (3) a transducer for pressure measurement. Differences among the tensiometers are mostly related to the dimensions, materials used, and sealing characteristics.

2.3 Tensiometer Fabrication

Based on the literature review of existing high-suction tensiometers, a new design for the tensiometer, which incorporated with the purchased EPXO pressure transducer, was presented as schematically shown in Figure 2.2. Similar to previously developed high-suction tensiometers (Ridley and Burland 1993; Meilani et al. 2002; Lourenco et al. 2006), the tensiometer developed in this study also included three parts: which are the pressure transducer, ceramic disc, and housing. However, unlike the other tensiometers, the ceramic disc was glued to a stainless steel ring instead of directly glued to the housing.

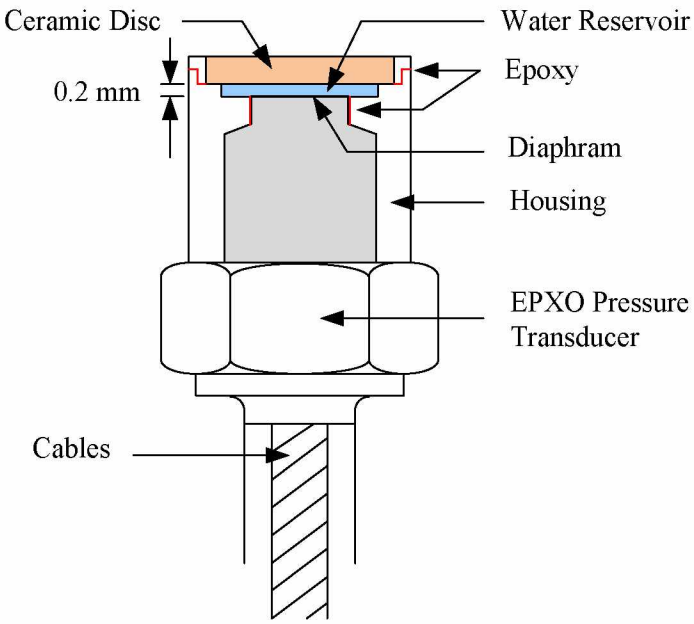

Figure 2.2 Schematic plot of the developed tensiometer (not to scale)

A pressure transducer, epoxy, housing, a ceramic disc, and a stainless steel ring were required for the tensiometer fabrication (see Figure 2.3). The housing was designed and precisely machined with thread inside to incorporate with the thread on the pressure transducer. Also, a platform inside the housing, on which the stainless steel ring will rest, was used to provide a gap between the ceramic disc and the transducer diaphragm. Due to the presence of this gap, an empty room space was generated and used as a water reservoir. Ceramic disc with air-entry value of 15 bar was used as a filter to prevent air from entering the water reservoir. The fabrication process for the tensiometer was mainly divided into three steps:

Figure 2.3 Preparation for tensiometer fabrication

1. The EPXO pressure transducer, ceramic disc, stainless steel ring, and housing were carefully cleaned to remove any possible grease contamination that could weaken the sealing due to used epoxy. A ceramic disc as shown in Figure 2.3 (2.5 mm in thickness and 10 mm in diameter) was glued to the stainless steel ring (10 mm and 13 mm in inner and outer diameters with a height of 2 mm as shown in Figure 2.4) using epoxy, with a roughly a 0.25 mm protuberance at the both sides (Figure 2.5a). During this process, more epoxy use was encouraged to ensure a good sealing. Once glued together, the ceramic disc in the ring was twisted to remove all possible air bubbles which that could probably bring leakage to the tensiometer. After curing, the epoxy on the outer side surface of the ceramic disc ring was carefully removed. Then, as shown in Figure 2.5b, the ceramic disc was ground to 2 mm by using a 600 grit abrasive disc to remove the epoxy that infiltrated in the ceramic disc and generate a fresh surface.

2. The housing (Figure 2.3) used to hold the stainless steel ring (with ceramic disc inside) in place was screwed to the pressure transducer (Figure 2.5a) with some epoxy inside (red line in

Figure 2.2). Unlike the O-ring seal at the very end of the housing used by Ridley and Burland (1993), epoxy was used only at the side of the pressure transducer diaphragm. In this way, the thread was outside of the water reservoir instead of inside, which could probably reduce the possibility of cavitation according to Guan (1996). Once cured, the epoxy that squeezed out to the surface of the diaphragm during assembly was carefully removed (as shown in Figure 2.5c).

3. The stainless steel ring with ceramic disc inside (Figure 2.5b) was glued to the stainless steel housing with a suitable amount of epoxy and twisted to remove trapped air, as described before. Pressure was then applied to the interface between the stainless steel ring and housing to ensure a good contact during curing of the epoxy. Figure 2.5d shows the tensiometer after fabrication. After curing, the strength of the epoxy was fully achieved and the tensiometer can be submerged into de-aired water for saturation. A water reservoir (0.2 mm thickness and 12.7 mm3 in volume in this case) underneath the ceramic disc was required to generate a negative pressure and provide a room for the outward deflection of the diaphragm. The volume of the water reservoir is recommended to be as small as possible to shorten the time for of the saturation process and reduce the possibility of cavitation. However, the water reservoir cannot be too small to tolerate the outward deformation of the sensor diaphragm under negative pressure.

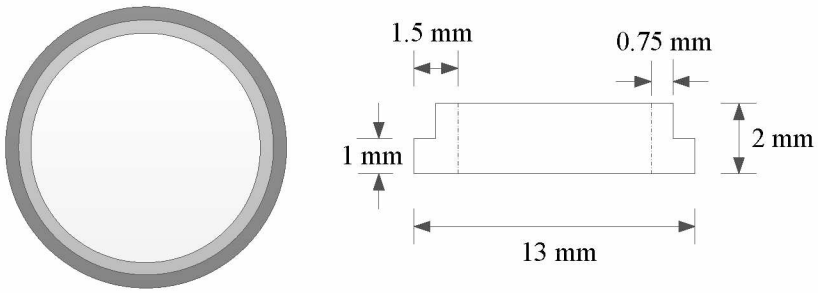

Figure 2.4 Layout of the stainless steel ring

Figure 2.5 Tensiometer fabrication

The main difference between the design in this study and previous designs (Ridley and Burland 1993; Meilani et al. 2002; Lourenco et al. 2006) is the use of the stainless steel ring. Three main benefits were introduced with the use of this ring:

1. The assembly process was divided into three steps, which limits the possibility of mistakes. Each step is easy to perform. In other words, poor sealing was unlikely to happen with this design.

2. The quality of the assembly can be well controlled. Surplus epoxy can be removed, and a fresh ceramic surface can be generated to eliminate any stains on its surface or introduced during assembly process, which could also reduce the possibility of cavitation once saturated.

3. If the tensiometer does not work well due to poor sealing, the ring (with the ceramic disc inside) can be easily detached and replaced from the pressure transducer without causing any damage to the ceramic disc or pressure transducer.

According to Marinho et al. (2008), if good contact is not established between the soil pore water and the porous filter of the tensiometer, misleading observations of matric suction will be obtained. To ensure a good contact between the tensiometer and soil specimen and hold the tensiometer in place during testing, a grommet was fabricated using silicone rubber. Detailed fabrication process is shown in Figure 2.6. First, to prevent introducing air bubbles, as shown in Figure 2.6a, silicone rubber (in white and blue) was gently mixed together. A stainless steel mold as shown in Figure 2.6b was set up. After being fully mixed, silicone rubber was then poured into the mold as shown in (Figure 2.6c). This process also required great patience to avoid producing air bubbles. Silicone rubber cured after several hours. Then, mold could be released (Figure 2.6d). Edge of the grommet was trimmed as shown in Figure 2.6e to fit the size of tensiometer. The inner diameter of the grommet was designed to be less than the outer diameter of the tensiometer housing. Therefore, the grommet can hold itself well in place. Figure 2.6f is a picture of the tensiometer with the grommet on. The grommet should be mounted on the tensiometer all the time. In case of any possible drop or collision, the silicone rubber grommet could provide absorption of the shock energy which could reduce the possibility of damage to the tensiometer.

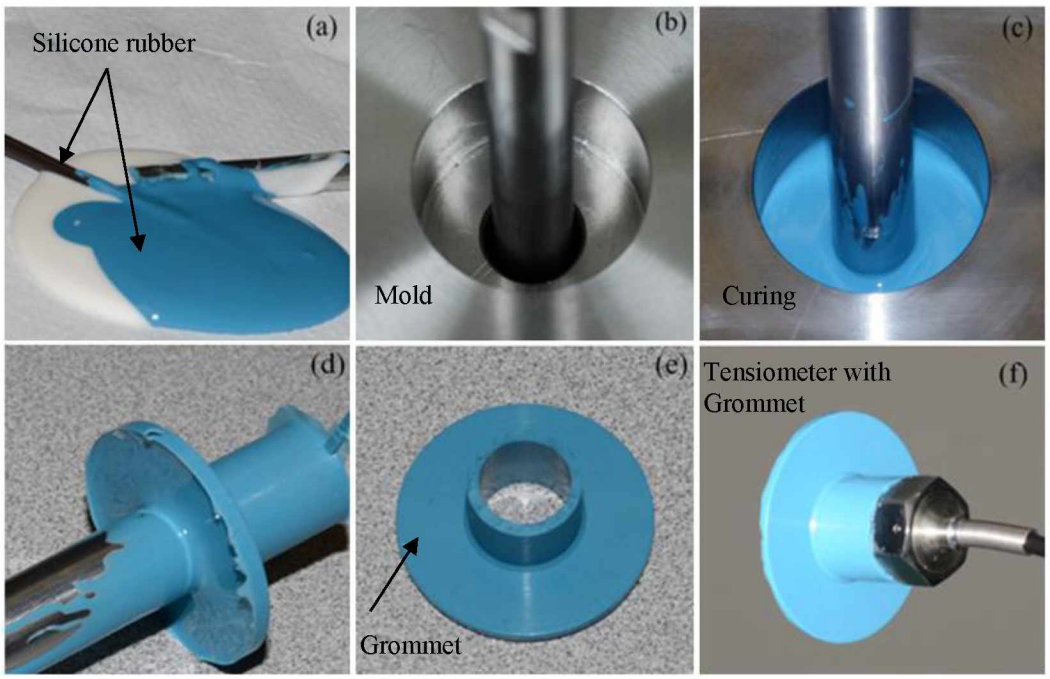

Figure 2.6 Grommet fabrication using silicone rubber

2.4 Tensiometer Saturation

For the saturation process, unlike with previous tensiometers (Ridley and Burland 1993 and Guan and Fredlund 1997), no special equipment is required. The tensiometer was installed on the triaxial test apparatus and submerged into de-aired water. After this, a significant pressure increase of the water reservoir in the tensiometer was expected due to the formation of a wetting front saturating the ceramic disc as long as the tensiometer was well sealed. As the wetting front moved towards the reservoir, the air trapped in the ceramic disc was progressively compressed, and causing the pressure increase in the reservoir.

During saturation, an water pressure of 600 kPa was applied to dissolve the air trapped in ceramic disc and underneath the ceramic disc, which is commonly referred as prepressurization. Usually, for the initial saturation, to dissolve all the trapped air, two to three pre-pressurization cycles in one week were required. When all air trapped in the water reservoir and ceramic disc

dissolved into water, the saturation was considered to be finished. The saturation can be easily identified by blowing the ceramic disc at the tensiometer tip, if the pressure quickly dropped to lower than -100 kPa, the tensiometer was considered to be saturated and usable for suction measurement. After each suction measurement, the tensiometer was kept in de-aired water all the time. Usually, after the initial saturation, several hours under a pressure of 600 kPa were sufficient to saturate the high-suction tensiometers developed in this study.

2.5 Tensiometer Calibration and Maximum Attainable Suction

Since the presence of epoxy could possibly result in some deformation of the diaphragm due to hardening, calibration of the tensiometer was performed after sensor saturation to obtain an accurate measurement, which is consistent with the real condition of use. For the calibration process, the tensiometers were calibrated in a positive pressure range. Negative pressure range calibration is based on extrapolation, which is also used by Lourenco et al. (2008). The accuracy of the calibration can be checked by the water pressure immediately after cavitation, which should be approximately -100 kPa. In other words, a tensiometer cavitation pressure reading close to -100 kPa indicates a good calibration. Three cycles of cell pressure between 0 to 600 kPa were applied to calibrate the tensiometers under pressure change. When there was a cell pressure change, water flows inwards or outwards due to the pressure increases or decreases, respectively. The pressure were was applied in steps and followed by waiting periods (2 minutes) to ensure the pressure equilibrium. Only the final readings, when equilibrium was achieved, were used for tensiometer calibration. Two of the tensiometers were fabricated. The calibration results for these tensiometers are tabulated in Table 2.1. By plotting those voltage output against applied pressure, a strong linear relationship between both can be found in Figure – 2.7a.

Table 2.1 Tensiometers calibration

Applied Pressure (kPa)	Tensiometer Reading (mV)					
	Tensiometer 1			Tensiometer 2		
	Cycle 1	Cycle 2	Cycle 3	Cycle 1	Cycle 2	Cycle 3
0	0.654	0.66	0.657	1.131	1.133	1.131
100	1.395	1.393	1.391	1.906	1.904	1.904
200	2.127	2.122	2.12	2.671	2.667	2.667
300	2.85	2.85	2.852	3.428	3.427	3.43
400	3.578	3.578	3.571	4.189	4.189	4.183
500	4.297	4.301	4.297	4.941	4.945	4.941
600	5.01	5.016	5.014	5.687	5.691	5.691

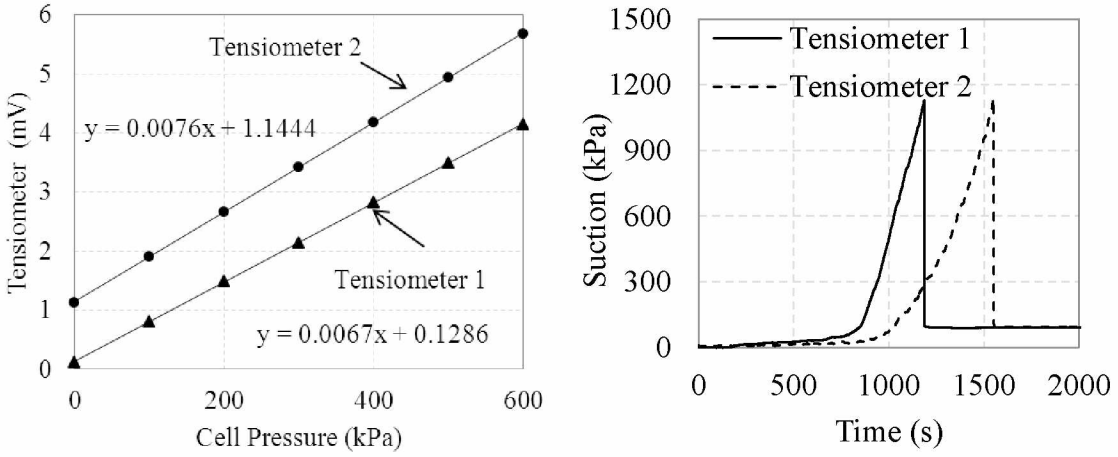

(a) **(b)**

Figure 2.7 High-suction tensiometer calibration and maximum attainable suction

Maximum attainable pressure of a high-suction tensiometer is highly dependent on the saturation process. Guan and Fredlund (1997) indicated that the maximum measurable suction could be affected by the growth of pre-existing gas bubbles, air entry value of the ceramic disc, and the nucleation of vapor bubbles. In this study, it was also found that the maximum attainable suction associated with each different saturation process and tensiometers are different. Usually, a tensiometer with a high air entry ceramic disc at a high degree of saturation could reach a higher suction measurement. After calibration, the free evaporation test reported by Guan and

Fredlund (1997) was used for the determination of the maximum attainable pressures. Due to water evaporation, the pore water pressure inside the tensiometer gradually decreased with time. The pressure right before the cavitation is the maximum attainable suction for the tensiometer. Free evaporation test results are presented in Figure 2.7b. For both tensiometers, 15 bar ceramic discs were used as the filters. The maximum attainable pressures measured were around 1100 kPa which is below 15 bar.

After saturation and calibration, tensiometers were ready to be used for matric suction measurement on unsaturated soils. Figure 2.8 shows the suction measurements using both tensiometers on a 70 × 140 mm silt specimen during undrained unconfined compression test. Tensiometers were attached to the specimen surface at the middle height and partially covered by rubber membrane for sealing purpose. To ensure a good contact between tensiometers and specimen surface, a small vacuum pressure (-5 kPa) was applied to the inside of soil specimen. With increase of applied axial load, matric suction of soil specimen slightly decreased. This undrained unconfined compression test was conducted for soil specimens with different moisture contents, as shown in Figure 2.9, repeated suction change was found which indicated that the suction measurement was reliable.

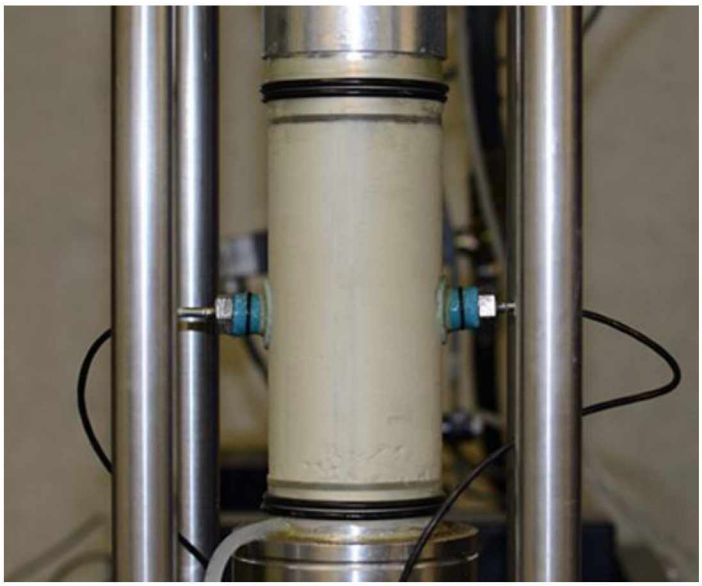

Figure 2.8 Matric suction measurements on an unsaturated soil specimen

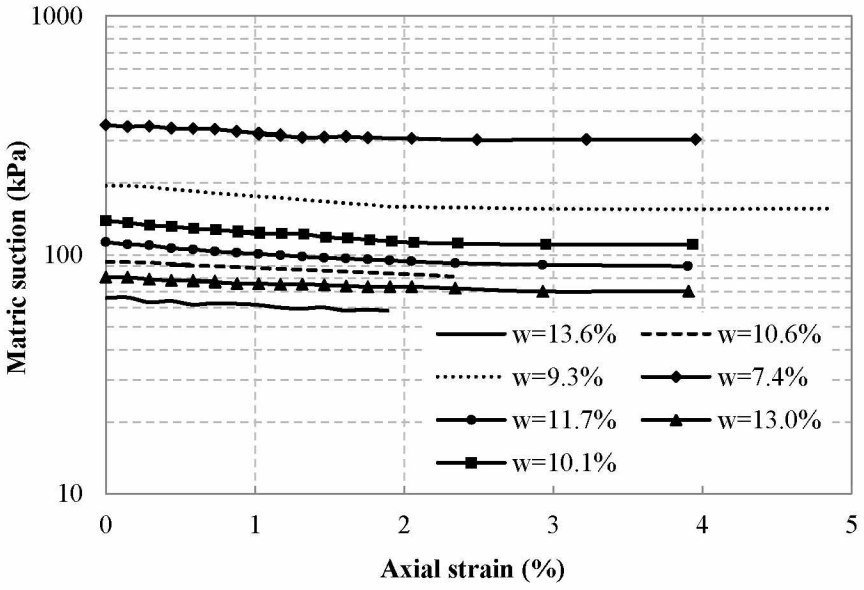

Figure 2.9 Matric suction measurements results on soil samples with different moisture contents during unconfined compression test

2.6 Conclusions

Based on a comprehensive review of existing high-suction tensiometers, a new highsuction tensiometer for matric suction measurement on unsaturated soils was developed. The

use of a stainless steel ring significantly reduced the chance of poor sealing and simplified the assembly process. Also, the tensiometer can easily be taken apart without causing any damage to the ceramic disc. In other words, the tensiometer is easy to fix if there is any malfunction. To ensure a good contact between a soil specimen and the tensiometer, grommet was fabricated using silicone rubber. After saturation and a careful calibration, the tensiometers were proved to have a maximum attainable suction at of around 1100 kPa (with 15 bar ceramic disc). Also, the undrained unconfined compression test results indicated that tensiometer is reliable and can provide repeated suction measurement results.

2.7 References

Fredlund, D. G., and Rahardjo, H. (1993). Soil Mechanics for Unsaturated Soils. New York: John Wiley and Sons.

Guan, Y. (1996). The measurement of soil suction. Ph.D. dissertation, University of Saskatchewan, Saskatoon.

Guan,Y. and Fredlund, D.G. (1997). "Use of Tensile Strength of Water for the Direct Measurement of High Soil Suction." Canadian Geotechnical Journal 36, pp. 604–614.

Lourenco, SDN, Gallipoli, D, Toll, D.G, and Evans, F.D. (2006) "Development of a commercial tensiometer for triaxial testing of unsaturated soils." Proceedings of 4th international conference on unsaturated soils, Phoenix, Geotechnical Special Publication 147, vol. 2. pp. 1875–1886.

Marinho. F. A. M., Take W. A., Tarantino A. (2008). "Measurement of Matric Suction Using Tensiometric and Axis Translation Techniques." Geotech. Geol. Eng 26: pp.615–631.

Meilani, I., Rahardjo, H., Leong, E.C., and Fredlund D.G. (2002). "Mini suction probe for matric suction measurements." Canadian Geotechnical Journal 39. pp. 1427-1432.

Rahardjo, H. and Leong, E. C. (2006). "Suction measurements." In: Proc. of the 4th International Conference on Unsaturated Soils, April 2006, Carefree, AZ, Geotechnical Special Publication No.147, pp. 81–104.

Ridley, A.M. and Burland, J.B. (1993). "A new instrument for the measurement of soil moisture suction." Géotechnique, 43(2), pp. 321 – 324.

Ridley, A.M. and Burland, W.K. (1993). ''A new instrument for the measurement of soil moisture suction.'' Géotechnique 43, No. 2, pp. 321-324.

Take, W.A. and Bolton, M.D. (2003). "Tensiometer saturation and the reliable measurement of matric suction." Géotechnique 53 (2): pp. 159–172.

Tarantino, A. and Mongiovi, L. (2002). "Design and construction of a tensiometer for direct measurement of matric suction." In: Proc. Third Int. Conf. on Unsaturated Soils, Recife 1, pp. 319–324.

CHAPTER 3. MEASURING UNSATURATED SOIL DEFORMATIONS DURING TRIAXIAL TESTING USING A PHOTOGRAMMETRY-BASED METHOD[1]

3.1 Abstract

When characterizing an unsaturated soil behavior using triaxial test apparatus, it is required to measure soil deformation during loading. Recently, a photogrammetry-based method has been developed for total and localized volume change measurements on unsaturated soils during triaxial testing. In this study, more in-depth discussions on the photogrammetry-based method are addressed such as system setup, measurement procedure, accuracy self-check, data post-processing, and difference from the conventional image-based methods. Also, an application of the photogrammetry-based method on unsaturated soil deformation measurements is presented through a series of undrained triaxial tests with different loading paths. After testing, three-dimensional (3D) models of the tested soils during testing were constructed through the 3D coordinates of measurement targets on specimen surface. Clear barreling processes for soils during deviatoric loading were observed from the constructed 3D models at different axial strain levels. Soil volume changes and volumetric strain non-uniformities during isotropic and deviatoric loadings were extracted based upon detailed analyses on different soil layers. Through a full-field strain distribution analysis, an evolution process of a shear band was captured for the soil during deviator loading under a low confining pressure. The photogrammetry-based method is proved to be very powerful for in-depth soil deformation characteristics investigation.

---

[1] Li, L., Zhang, X., Chen, G., and Lytton, R. (2015) "Measuring Unsaturated Soil Deformations during Triaxial Testing Using a Photogrammetry-Based Method" Canadian Geotechnical Journal, (accepted).

3.2 Introduction

Triaxial test is commonly used to characterize both saturated and unsaturated soils. The volume or volume change of a soil specimen is an essential parameter in understanding deformation and shear strength characteristics of the soil. For triaxial test on a saturated soil, soil volume change can be directly measured through monitoring water exchange of the soil specimen. For an unsaturated soil, due to the presence of air phase, the volume change is no longer equal to the changes in water volume. As a result, the conventional method to measure volume change of saturated soils cannot be used any more. In the past few decades, several methods has been developed to measure unsaturated soil volume changes during triaxial testing as summarized by Geiser et al. (2000), Sharma et al. (2006), Laloui et al. (2006), Hoyos et al. (2009), and Zhang et al. (2015).

Double-wall cell method, proposed by Bishop and Donald (1961) as shown in Figure –3.1a, is the most extensively used method for unsaturated soils volume change measurements. An inner cell was added to the conventional triaxial test apparatus and equal cell pressure was applied on both sides to ensure no lateral deformation of the inner cell. The volume change of the soil specimen was then deduced by measuring the variation of the mercury level in the inner cell. Several modifications were made on the double-wall cell method later by Wheeler (1988), Cui and Delage (1996), and Ng et al. (2002). However, the principle of the volume change measurement was the same. The double-wall cell method requires major equipment modifications on the conventional triaxial test apparatus for saturated soils and is therefore expensive. A typically double-wall cell triaxial testing system costs over $100,000 and is complex to operate. The volume change measurement accuracy can be influenced by water absorption of the inner cell. The water absorption is sensitive to chamber pressure, temperature,

and time which makes the system calibration extremely difficult. Steel inner cell can be an alternative to solve the water absorption problem. However, for this non-transparent inner cell, it is difficult to examine the existence of air bubbles in the cell which are difficult to be removed and can also influence the measurement accuracy. A carefully calibrated double-wall cell can measure total volume change to an accuracy of 0.25% (GDS 2009).

Some other methods have also been used to measure the volume change of unsaturated soil such as direct measurements of the air and water volumes using digital pressure volume controllers (Adams et al. 1996; Geiser 1999; and Laudahn et al. 2005), local displacement measurement using miniature LVDTs (Clayton et al. 1989), Hall Effect transducers (Clayton and Khatrush 1986), and profile determination using laser scanners (Romero et al. 1997). As pointed out by Geiser et al. (2000), Sharma et al. (2006), Hoyos et al. (2008), and Zhang et al. (2015), these methods also have their limitations and were rarely used.

With the increasing availability of inexpensive digital cameras, more and more image-based methods have been developed for deformation measurements on soils during triaxial testing. The most widely used image-based method is presented by Macari et al. (1997). A stationary camera was mounted "far away" from the triaxial system. Images were captured for the soil specimen in the triaxial cell during loading. To simplify the refraction correction process, the setup for the measurement system was idealized as presented in Figure 3.1b. A two-dimensional (2D) refraction correction model developed by Parker (1987) was adopted to correct the magnification due to refraction of the confining fluid and chamber in the line of vision between the specimen and the camera. By detecting the edges of the specimen through the captured images, volume changes of the tested specimen could be computed. The advantage of this method lies in its simplicity: a conventional triaxial cell could be used without any modification. For this image-

based method, only a 2D image of the specimen could be obtained for each measurement. As shown in Figure 3.1(b), for points at locations of P, P_1, and P_2, their positons on the captured 2D image were the same. Since the specimen deformation during testing was in 3D, soil 3D deformation could not be obtained unless two requirements were satisfied: (1) when deforming, the deformation occurred homogenously along the radial direction; and (2) soil remained to be axisymmetric after deforming. Also, to apply the 2D refraction correction model, some other requirements were needed to be satisfied: (1) the soil specimen and the confining acrylic chamber are perfectly cylindrical and installed vertically; (2) the shooting direction of the digital pinhole camera exactly passes through the center of the chamber as shown in Figure 3.1b; (3) the soil specimen is installed exactly at the center of the confining chamber which is also shown in Figure 3.1b; (4) deformation of the acrylic cell wall under water pressure is negligible; (5) the relative positions of the pinhole camera, triaxial chamber, and the soil specimen are known. With the similar system setup and refraction correction model, Lin and Penumadu (2006) presented a new image-based method to analyze soil deformations in a series of combined axial-torsional tests under undrained condition. Instead of edge detecting, some measurement points in a grid pattern with spacing of 10 mm were marked on the membrane which covered the soil specimen. The movements of these measurement points were tracked during testing through digital image analysis technique. The system setup in Macari et al. (1997) was also adopted by Gachet et al. (2007) to measure soil volume changes during triaxial testing. However, in this case, several calibrations, which included perspective correction, axial, and radial calibrations, were used as a replacement of the 2D refraction correction model to correct the magnification effect due to the confining fluid and chamber. For these image-based methods (Macari et al. 1997; Lin and Penumadu 2006; and Gachet et al. 2007), due to the difficulties in accurate determine the

locations of the camera station and the triaxial cell chamber for refraction correction, a sophisticated system calibration is required to achieve an accurate measurement. Even though, the measurement accuracy of the image-based methods is still not high. As addressed in Lin and Penumadu (2006), the obtained measurement accuracy was reported to be 0.2 mm and 0.3 mm in the vertical and circumferential directions, respectively. In Gachet et al. (2007), the volume measurement accuracy was determined to be 0.6%.

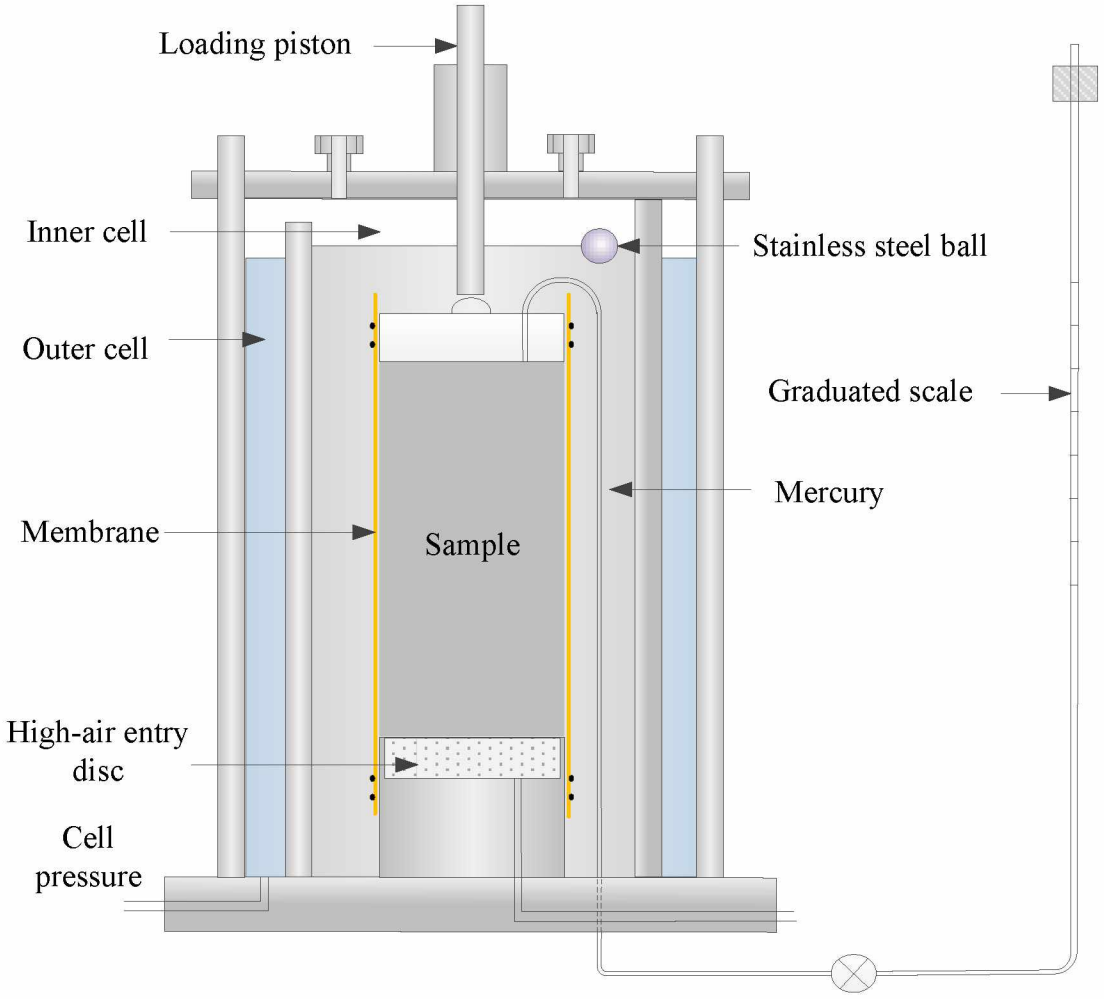

(a)

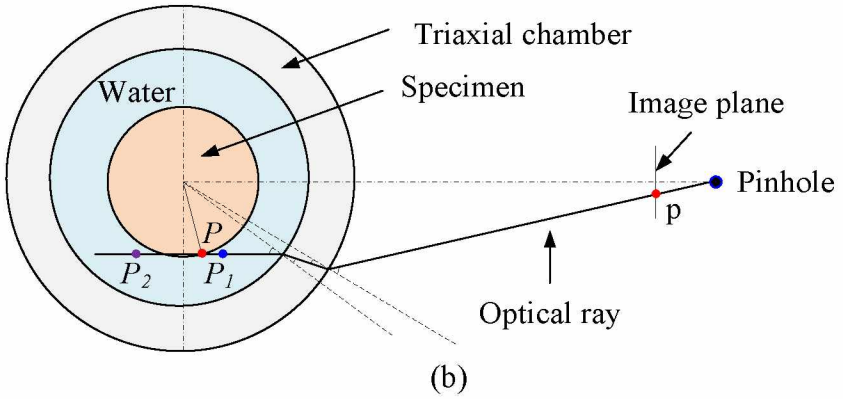

Figure 3.1 (a) Double-wall cell triaxial test apparatus (modified from Bishop and Donald 1961); (b) Image-based method (modified from Macari et al. 1997).

According to recent findings (Alshibli et al. 2000; Rechenmacher and Saab 2002; Desrues 2004; and Rechenmacher 2006), in addition to volume change, localized deformation has a significant impact on soil behavior. As addressed in Sachan and Penumadu (2007), strain localization is considered to be a major factor which controls the overall mechanical response of the specimen, at or near failure. The developments of appropriate constitutive models for these soils and the appropriate quantification of their failure states depend on accurate experimental quantification of shear band formation, growth, and evolution. Meanwhile, more and more attention was drawn on investigate of localized deformation in soil during triaxial loading (Lin and Penumadu 2006; Rechenmacher 2006; Sachan and Penumadu 2007; Rechenmacher and Medina-Cetina 2007; and Bhandari et al. 2012).

In Lin and Penumadu (2006) and Sachan and Penumadu (2007), strain localization was obtained based on the deformation of the point grid. Different from digital image analysis, digital image correlation (DIC) technique was reported to be utilized for soil deformation measurements under triaxial condition (Rechenmacher 2006; Rechenmacher and Medina-Cetina 2007; and Bhandari et al. 2012). The displacement measurement was derived by mapping, between digital

images, overlapping subsets of pixels or overlapping clusters of sand grains at many points across the specimen surface. However, in Rechenmacher (2006) and Rechenmacher and Medina-Cetina (2007), due to the difficulties in dealing with refraction, DIC cannot be directly used for deformation measurements on soils located in a triaxial chamber with or without confining fluid. Instead, the confining load was applied through vacuum pressure. Therefore, the applied confining load was limited to less than -100 kPa. Bhandari et al. (2012) reported the use of DIC technique for soil deformation measurements under triaxial condition. A 3D refraction model was developed to deal with the refractions at the interfaces of air-cell and cell-water. Three cameras around the testing system at intervals of 120^{o} were used to capture images of a deforming soil specimen at various instants. However, this DIC method suffered most of the limitations from the image-based methods (Macari et al. 1997; Lin and Penumadu 2006; and Gachet et al. 2007) due to similar system setup.

Till now, quantitative full-field deformation measurements on unsaturated soils remain to be a great challenge for researchers. Therefore, full-field 3D deformation measurement on an unsaturated soil during triaxial testing has never been investigated due to lack of a suitable measurement method with acceptable cost and accuracy. In Zhang et al. (2015), a new photogrammetry-based method was developed to measure full-field deformation of unsaturated soils during triaxial testing. The average point position and volume change measurement accuracies were determined to be 0.065 mm and 0.1% through two validation tests on a stainless steel cylinder and a saturated sand specimen, respectively. In Zhang et al. (2015), the principle and mathematical derivation of the photogrammetry-based method were presented. In this study, more in-depth discussions on this newly developed photogrammetry-based method are addressed which included system setup, measurement procedure, accuracy self-check, data post-processing,

and difference from the conventional image-based methods. Also, to better understand the capabilities of the photogrammetry-based method for deformation measurement on unsaturated soils, a series of undrained triaxial tests were conducted during which soil deformations were measured based upon the 3D coordinates of measurement targets on soil surface. The abundance of accurate surface displacement data enables a means to quantify local deformation to particulate-scale intensity. After testing, soil deformation characteristics such as total volume change, volumetric strain non-uniformity, barreling, shear band evolution, and full-field strain distribution during triaxial testing were obtained using the photogrammetry-based measurement method.

3.3 A Photogrammetry-Based Method

3.3.1 Measurement Principle

The photogrammetry-based method for deformation measurements on unsaturated soils is based on principle of photogrammetry. The general principle of photogrammetry for 3D geometry measurement can be found in Mikhail et al. (2001). However, for a triaxial test on an unsaturated soil, triaxial cell is filled with confining fluid. Due to refraction, significant distortion of the tested soil specimen can be observed when viewing from the outside of the triaxial cell. Similar to the working mechanism of a human eye, a camera also considers optical rays travel in straight lines. As a result, a distorted specimen is captured on the image using a camera outside of the triaxial cell. Under the multi-media condition (air, acrylic cell, and confining fluid), photogrammetry technique cannot be directly applied for measurement on the specimen. Due to refractions at the air-cell and cell-fluid interfaces, the shape and orientation of the cylindrical specimen can be significantly different when viewing from the outside of the triaxial chamber at different view angles. Once, it was believed that there is no theoretical method available for this

kind of refraction correction as presented in Baghereih et al. (2008). However, this is not the truth according to the findings in this study. It's well known that optical ray refraction follows the Snell's law. For a specific incident optical ray, as long as the refractive interface and the refractive indices of two media are known, the refracted ray can be accurately determined using Snell's law. As a result, Snell's law is adopted to trace the optical rays undergo refractions. Using the measurement for a specific point P as an example, Figure 3.2 illustrates the principle of the photogrammetry-based method.

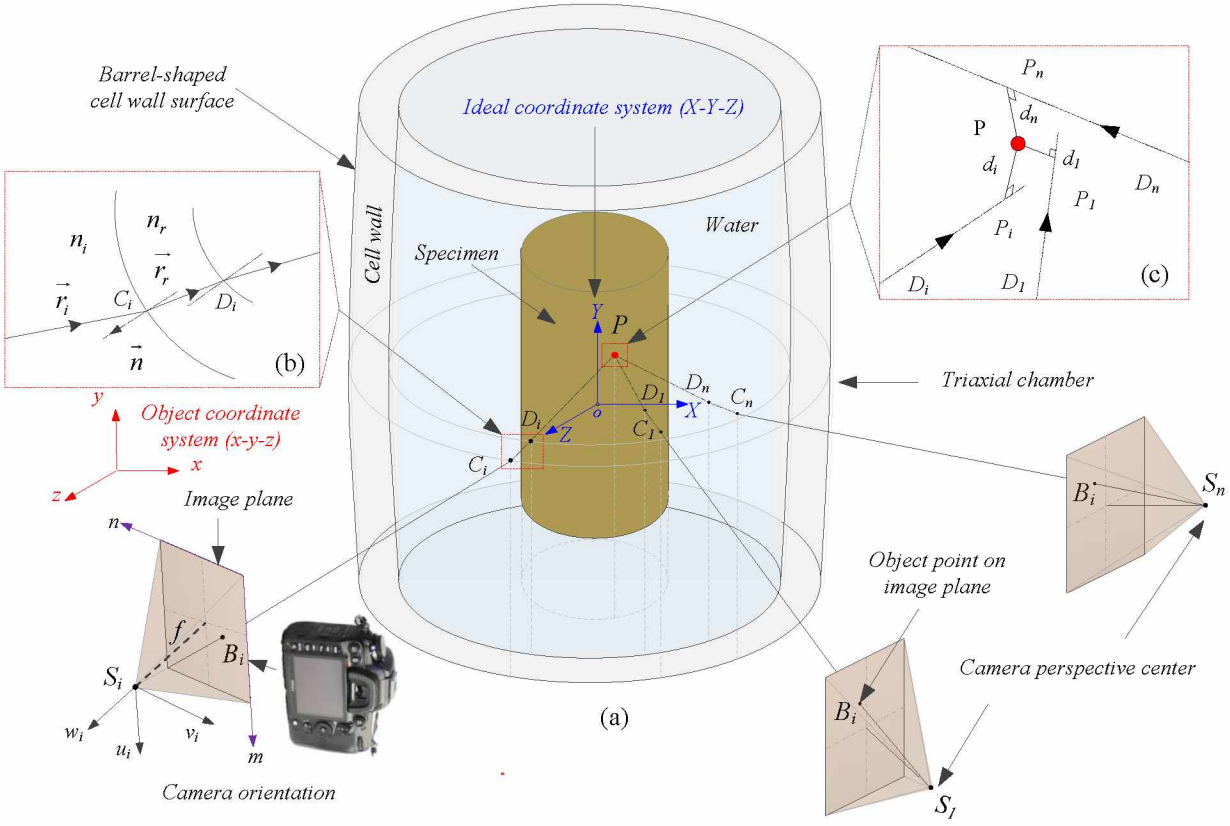

Figure 3.2 Principle of the photogrammetry-based method: (a) Schematic representation; (b) Optical ray tracing; and (c) Least-square estimation.

A cylindrical soil specimen is located inside of a triaxial chamber which is filled with water. To perform a photogrammetry-based measurement for point P at the specimen surface,

several images are captured for the specimen around the triaxial chamber. For an accurate determination of the 3D position of point P, the optical ray paths (S_iC_i to C_iD_i to D_iP_i) from the camera stations to the point as shown in Figure 3.2a must be known. The orientations of the camera stations can be accurately determined based upon principle of photogrammetry. Subsequently, the optical rays S_iC_i (same as S_iB_i) can then be constructed by connecting the corresponding camera stations S_i to their image points B_i. Due to the presence of acrylic cell, optical rays S_iC_i bends at the interface of air-acrylic cell as shown in Figure 3.2a and 3.2b. In this study, the outer surface of the acrylic cell wall is assumed to be barrel-shaped as shown in Figure 3.2a due to its better representation of the real cell surface especially under high chamber pressure. Therefore, Equation 3.1 is used to represent the outer surface of the acrylic cell wall in an ideal coordinate system (i.e. X-Y-Z in Figure 3.2a).

$$X^2 + Z^2 = AY^2 + BY + C \qquad \text{Equation 3.1}$$

where,

$X, Y, and\ Z$ = 3D coordinates of points on cell wall surface in the ideal coordinate system (X-Y-Z) and

$A, B, and\ C$ = coefficients determine the shape of the cell wall surface.

The outer surface of the triaxial cell wall can be determined based upon principle of photogrammetry. Then, according to Snell's law as shown in Equation 3.2 (Zhang et al. 2015), with given incident rays S_iC_i, refractive interface (the outer surface of the cell wall), and refractive indices of air and cell wall, the optical rays C_iD_i after refraction can be calculated.

$$\vec{r}_r = \frac{n_i}{n_r}\vec{r}_i - \left(\frac{n_i}{n_r}\ \vec{r}_i \cdot \vec{n}\ + \sqrt{1 - \left(\frac{n_i}{n_r}\right)^2\ 1 - \vec{r}_i \cdot \vec{n}^{\ 2}} \right) \vec{n} \qquad \text{Equation 3.2}$$

where,

n_i, n_r = media refraction indices before and after refraction,

$\vec{r_i}$ = unit vector of the optical ray before refraction (incident ray),

$\vec{r_r}$ = unit vector of the refracted optical ray, and

$\vec{n}$ = normal vector at the refraction interface.

Assuming a uniform cell wall thickness, the inner surface of the cell wall can be easily determined. As shown in Figure 3.2a and 3.2b, with new incident rays C_iD_i, which are the optical rays after refraction at the air-cell interface, refractive interface (the inner surface of the cell wall), and refractive indices of cell wall and water, Equation 3.2 is utilized again to determine the optical rays D_iP_i after the refraction at the cell-water interface. To facilitate the optical ray tracing, a coordinate system transformation is required between the object coordinate system and the ideal coordinate system. Also, a 3D reconstruction of the triaxial cell surface is required to determinate coefficients *A, B,* and *C*. Detailed cell wall reconstruction and optical ray tracing processes is referred to Zhang et al. (2015). After optical ray tracing, for a single point *P* at the specimen surface, optical rays D_iP_i are determined as shown in Figure 3.2b. Due to measurement error, these optical rays do not necessarily intercept at point *P*. To accurately estimate the position of the point *P* in the object coordinate system (x_p, y_p, z_p) as shown in Figure 3.2c, a least-square method is adopted as shown in Equation 3.3.

$$d_{total} = \sum_{i=1}^{n} d_i,\ d_i = \sqrt{\left(x_p - x_{di}\right)^2 + \left(y_p - y_{di}\right)^2 + \left(z_p - z_{di}\right)^2 - \left(x_p - x_{di}\ \alpha_{dpi} + y_p - y_{di}\ \beta_{dpi} + z_p - z_{di}\ \gamma_{dpi}\right)^2} \quad \text{Equation 3.3}$$

where,

d_i = distance between the estimated point position *P* and the corresponding optical ray,

x_p, y_p, z_p = 3D coordinates of the estimated point position P in the object coordinate system,

x_{di}, y_{di}, z_{di} = 3D coordinates of the intercept point D_i of the corresponding optical ray at the inner surface of the acrylic cell wall in the object coordinate system, and

$\alpha_{dpi}, \beta_{dpi}, and\ \gamma_{dpi}$ = direction cosine of the corresponding optical ray D_iP_i in the object coordinate system.

By minimizing d_{total}, a combination of $x_p, y_p, and\ z_p$ is obtained which is the best estimation of the 3D coordinates of point P in the object coordinate system. The same optical ray tracing and least-square estimation processes could be performed on any point of interest at the specimen surface to estimate its 3D position. With the 3D positions of these points on the specimen surface, full-field deformation during triaxial testing can be achieved.

3.3.2 Measurement System Setup

With the photogrammetry-based method, conventional triaxial test apparatus can be used for the triaxial tests on unsaturated soils without any modification. To perform a deformation measurement using the photogrammetry-based method, a digital single lens reflex camera (in this case, Nikon D7000 with 50 mm fixed focal length lens as shown in Figure 3.3a is required for image capturing. Besides these, some setups as shown in Figure 3.3b on the triaxial testing system are required before a soil deformation measurement using the photogrammetry-based method.

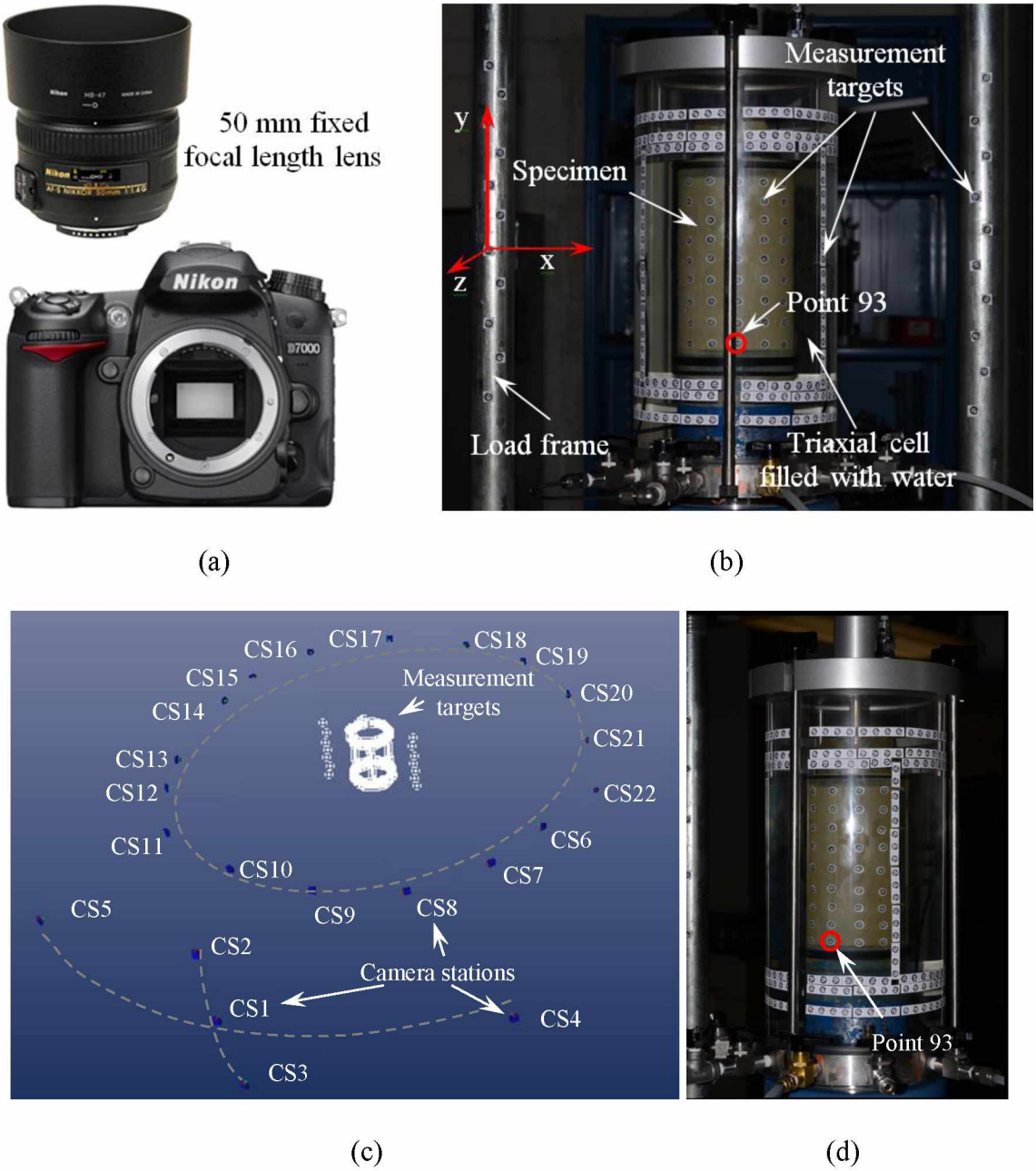

Figure 3.3 (a) Camera and lens; (b) System setup; (c) Image capturing; and (d) Image at camera station 9.

To facilitate the photogrammetry analysis, some measurement targets are required in the testing system. As shown in Figure 3.3b, some measurement targets are attached to the outer surface of the acrylic cell wall to determine its shape and orientation. Theoretically, with more

measurement targets on the cell wall, the shape and orientation can be more accurately determined. However, too many measurement targets could block the view to the soil specimen which is located inside the triaxial chamber. So, as long as the view to the specimen surface is clear, more measurement targets are encouraged to be posted to the both ends of the cell. A typical layout for those measurement targets is shown in Figure 3.3b. Some other measurement targets are fixed to the load frame to build the object coordinate system. For each deformation measurement, the same object coordinate system can be built by assigning the same 3D coordinates to those measurement targets on the load frame. In this way, movements of the measurement targets on soil surface can be easily tracked by variations of their 3D positions in the object coordinate system. To measure the full-field deformation of the tested soil, many measurement targets are posted all around the soil surface. With more measurement targets, more detailed soil surface deformation can be detected. For the newly developed photogrammetry-based method, the deformation measurements are achieved through measurement targets on specimen surface. That is to say, this newly developed method can be used for deformation measurements on both saturated and unsaturated soils during triaxial testing with the same system setup.

3.3.3 Measurement Procedure

The procedure of the photogrammetry-based method for deformation measurement on a saturated or unsaturated soil sample during triaxial testing is presented as follows:

- Camera Calibration: The principle of photogrammetry is based on pinhole camera model. To be treated as a pinhole camera, the used camera is required to be calibrated first to determine its internal characteristics such as lens focal length, image sensor resolution, and some distortion parameters. A typical calibration result for the used camera is presented in Table 3.1.

Table 3.1 Camera calibration results.

Parameter	Before Idealization	After Idealization
f (mm)	53.3964	53.3964
M (pixel)	4928	4928
N (pixel)	3264	3264
F_x (mm)	23.9966	24.6565
F_y (mm)	15.8961	16.3292
P_x (mm)	12.0691	12.3283
P_y (mm)	8.0741	8.1646
K_1 (10^{-5})	5.495	0
K_2 (10^{-9})	-4.673	0
P_1 (10^{-6})	-3.492	0
P_2 (10^{-6})	1.501	0

- System Setup: Measurement targets, which are high contrast dots with special design and can be automatically identified by software, are attached to the test specimen, acrylic cell wall, and the load frame.

- Photographing: After system setup, images around the testing system are captured following a pattern as shown in Figure 3.3c. During image capturing, the aperture is set to a small opening (at F-number of 10) to increase the depth of field which allows the whole specimen to appear in focus. In case of low light conditions, to ensure a proper exposure, the build-in flash of the camera is set on. To reconstruct a 3D model of a cylindrical specimen during triaxial testing with the system setup shown in Figure 3.3b, a typical number of 22 images with overlaps are sufficient as shown in Figure 3.3c. Five camera stations (CS1 to CS5 in the form of a cross, a typical image is shown in Figure 3.3b) appeared to be far away from the testing system to capture the whole testing system with load frame. The other 17 images (CS6 to CS22 in

Figure 3.3c from different view angles, a typical image is shown in Figure 3.3d are closer to the triaxial testing system to have a better view to the specimen surface.

- Photogrammetric Analysis: Before photogrammetric analysis, all captured images are idealized first using Equation 3.4.

$$x_c = x + x\left[K_1(x^2+y^2) + K_2(x^2+y^2)^2\right] + P_1\left[(x^2+y^2) + 2x^2\right] + 2P_2xy$$
$$y_c = y + y\left[K_1(x^2+y^2) + K_2(x^2+y^2)^2\right] + P_2\left[(x^2+y^2) + 2y^2\right] + 2P_1xy \qquad \text{Equation 3.4}$$

where,

x, y = point coordinates in x and y directions in the original images,

x_c, y_c = coordinates in x and y directions for the same point after idealization,

K_1, K_2 = radial lens distortion parameters presented in Table 3.1, and

P_1, P_2 = decentering lens distortion parameters presented in Table 3.1.

Distortions due to the used lens are eliminated for the idealized images which are considered as captured by a pinhole camera. Then, a photogrammetric analysis is performed to determine the orientations of the camera stations and the 3D positions of the measurement targets on the load frame and acrylic cell wall as shown in Figure 3.3c. During orientation process, measurement targets on specimen surface must not be involved due to refraction which is very critical for the accurate determinations of the camera orientations and 3D positions of the measurement targets on the load frame and acrylic cell wall. 3D of those measurement targets on the load frame are then assigned afterwards to build the object coordinate system.

- Acrylic Cell Reconstruction: Since the triaxial cell is assumed to be barrel-shaped in the ideal coordinate system, it is required to reconstruct the cell wall based on the 3D coordinates of measurement targets on cell wall surface using Equation 3.1. The 3D coordinates of the

measurement targets on the cell wall surface in the object coordinate system (*x-y-z*) are transformed to the ideal coordinate system (*X-Y-Z*). A least-square method is then used to determine the coefficients for cell wall reconstruction. With the thickness of the acrylic cell wall, the inner surface of the cell wall is also determined.

- Optical Ray Tracing: To determine the 3D position of a measurement target on the specimen surface, optical rays from the corresponding camera stations are constructed and traced from each corresponding camera station to the specimen surface with help of the Snell's law as shown in Figure 3.2. After ray tracing process, optical rays as well as their start points at the inner surface of the acrylic cell are determined.
- 3D Coordinates Estimation: Least-square estimation is then performed using Equation 3.3 to accurately determine the 3D coordinates of all measurement targets on the specimen surface.

3.4 Post-Processing

3.4.1 Accuracy Self-check

For the conventional image-based methods (Bhandari et al. 2012; Gachet et al. 2007; Lin and Penumadu 2006; White et al. 2005; Desrues 2004; and Macari et al. 1997), a sophisticated system calibration process is required due to difficulties in dealing with refractions at the air-cell and cell-water interfaces. As previously discussed, this system calibration can be unreliable when there are variations in ambient temperature and chamber pressure. However, for the newly developed photogrammetry-based method, the system calibration is not necessary and the measurement accuracy can be self-checked. For a specific photogrammetry-based measurement, using the setup in Figure 3.3b as an example, after a photogrammetry analysis on the captured 22

images, all the 3D positions of measurement targets on cell wall surface are determined as shown in Figure 3.4a.

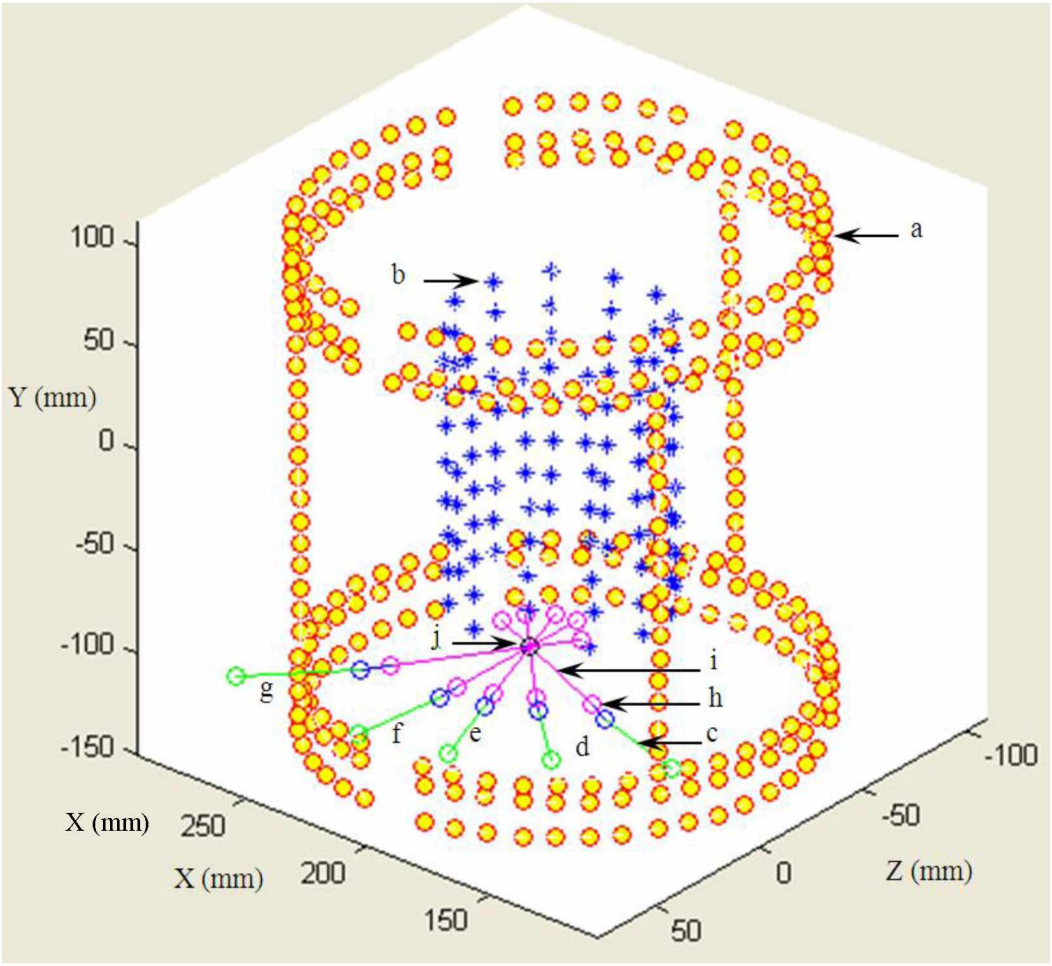

(a) Measurement targets on cell wall; (b) Measurement targets on specimen surface; (c) Optical ray from CS 8; (d) Optical ray from CS 9; (e) Optical ray from CS 11; (f) Optical ray from CS 12; (g) Optical ray from CS 13; (h) Optical ray in the triaxial cell wall; (i) Optical ray in the triaxial chamber; and (j) Point 93.

(a)

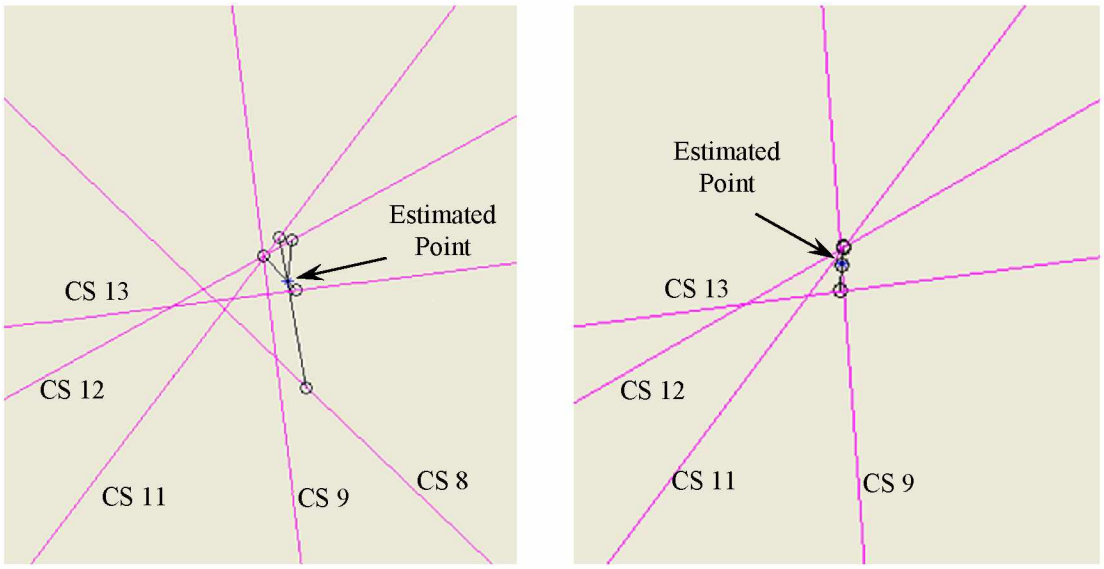

(b) (c)

Figure 3.4 (a) Optical ray tracing for point 93; (b) Estimation with the ray from CS8; and (c) Estimation without the ray from CS8.

Using point 93 at specimen surface as shown in Figure 3.3b and 3.3d as an example, an optical ray tracing process was then performed as typically shown in Figure 3.4a. Since point 93 was found on images captured at camera stations of 8, 9, 11, 12, and 13, five corresponding optical rays were constructed from their camera stations to the triaxial cell surface. At the outer surface of the triaxial chamber, optical rays bent at different intercept points and then intercepted with the inner surface of the triaxial cell wall. Directions of five optical rays changed again at the inner surface of the triaxial cell wall and then reached point 93 as shown in Figure 3.4a. Figure 3.4b shows an enlargement of five optical rays near point 93. These optical rays are lines in the 3D space without an intercept point. As shown in Figure 3.4b, the least-square method is then used to estimate the 3D position of point 93 as summarized in Table 3.2. It is found that the distances between these optical rays and the estimated point 93 varied from 0.012 to 0.226 mm with an average of 0.07 mm. The same procedure was applied to all the other points and a 3D

model of the specimen surface inside the triaxial chamber is constructed as shown in Figure 3.4a. Theoretically, with two of optical rays after the refraction at the cell-water interface, the 3D position of a measurement point on specimen surface can be determined. The distance d_i between the estimated point and any other corresponding optical ray was a self-check of the measurement accuracy. The average of the distances d_i could be considered as a proper indicator of the measurement accuracy. In this study, if the average d_i was below 0.1 mm, the measurement was considered to be accurate. Subsequently, for d_i values greater than 0.15 mm, the corresponding optical rays were deleted due to "poor" accuracy. Least-square estimation was performed again without the deleted rays to further improve the measurement accuracy. For example, at point 93, the d_i (0.226 mm) between the estimated point and optical ray from camera station 8 was deleted which reduced the total number of optical rays from five to four as shown in Figure 3.4c. Subsequently, the least-square estimation was reprocessed. As summarized in Table 3.2, it is found that the d_i between the estimated point of 93 and four optical rays vary from 0 to 0.034 mm which further reduced the average d_i to 0.023 mm. For the photogrammetry-based method, the accuracy self-check characteristic is quite unique when compared to the conventional image-based methods.

Table 3.2 Lease-square estimation results for point 93.

Image ID	d_i (mm)	x (mm)	y (mm)	z (mm)	d_i (mm)	x (mm)	y (mm)	z (mm)
8	0.226	170.032	-79.605	4.338	-	170.012	-79.631	4.341
10	0.031				0.000			
11	0.012				0.024			
12	0.013				0.034			
13	0.068				0.034			
Average	0.070				0.023			

3.4.2 Volume Calculation

With the coordinates of the measurement targets on the specimen surface, a typical point cloud was plotted in a 3D space as shown in Figure 3.5a for the specimen before any deformation. To facilitate further deformation analysis, a triangular surface mesh was then generated as shown in Figure 3.5b. An arbitrary point P_o located inside of the specimen was required to calculate the total volume of the soil specimen. By connecting this point with each point on the enclosed 3D surface, a series of tetrahedrons $P_oP_{1i}P_{2i}P_{3i}$ were formed as shown in Figure 3.5c. The volume for each one of these tetrahedrons can be easily calculated based on the 3D coordinates of points P_o, P_{1i}, P_{2i}, and P_{3i} using Equation 3.5.

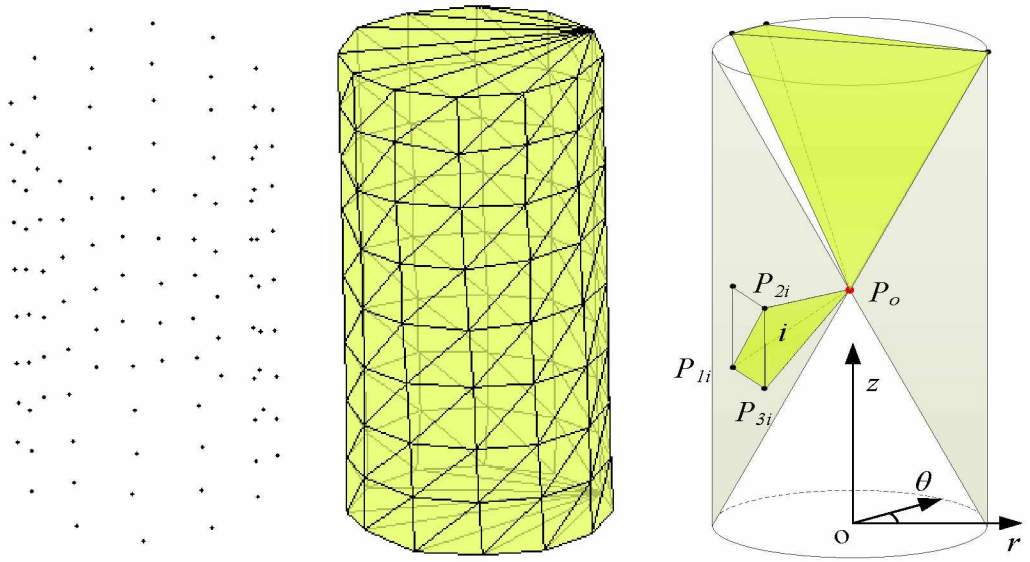

(a) (b) (c)

Figure 3.5 (a) Point cloud; (b) Enclosed 3D surface; and (c) Tetrahedrons generation.

$$V = \sum_{i=1}^{n} v_i = \frac{1}{6} \sum_{i=1}^{n} \left| \overrightarrow{P_o P_{1i}} \bullet \overrightarrow{P_o P_{2i}} \times \overrightarrow{P_o P_{3i}} \right| \qquad \text{Equation 3.5}$$

where P_o, P_{1i}, P_{2i}, and P_{3i} are four vertices of the i^{th} tetrahedron as shown in Figure 3.5c.

The total volume of the space that the triangular mesh covered is the summation of the volumes for all the tetrahedrons. This volume calculation method takes advantage of all the measurement targets on specimen surface without any assumption on specimen shape. For the same specimen, slightly different total volumes could be obtained when using different triangular meshes. So, for the same specimen, it is suggested to use the same triangular mesh for all volume calculations at different stress conditions.

3.4.3 Strain Calculation

The specimen surface deformation data can be used to evaluate the local displacement mechanisms leading to the triggering of the formation of persistent shear bands, the timing of shear band formation with regard to the achievement of peak stress, and the character of

displacements within fully formed shear bands. Previously published data only covered part of the whole soil surface (Desrues and Viggiani 2004; Lin and Penumadu 2006; Rechenmacher 2006; and Bhandari et al. 2012). Due to lack of a suitable measurement method, full-field strain distribution of soils during triaxial testing has never been reported. The method proposed in this paper for the first time makes it possible to observe full-field deformation soil behavior at smaller scales.

With the 3D positions of the measurement targets on specimen surface at different loading steps, full-field displacement and strain distributions can be extracted. Contour plots are commonly used for the visualization of displacement and strain of the specimen during triaxial testing. However, similar to the other studies (Desrues and Viggiani 2004; Rechenmacher 2006; Lin and Penumadu 2006; Chupin et al. 2012; and Bhandari et al. 2012), only discrete displacement points on the specimen's surface can be obtained from the photogrammetry-based method. Interpolation is often used by most researchers to obtain the full-field contour plots of a specimen from discrete displacement points. To facilitate strain analysis, 3D coordinates of those measurement targets in the object coordinate system (x-y-z) were transformed to a cylindrical z-r-θ coordinate system as shown in Figure 3.5c. The z-axis is set to be the center line of the sand cylinder and the origin of the cylindrical coordinate system was set to be at the bottom surface. The strain calculations were performed in this cylindrical coordinate system. In this paper, strain calculation and interpolation techniques similar to that presented in Lin and Penumadu (2006) are adopted to generate a continuous deformation field. Detailed strain calculation process is presented in Appendix A.

3.5 Triaxial Tests on an Unsaturated Soil

To evaluate the capabilities of the newly developed photogrammetry-based method, a series of undrained (constant water content) triaxial tests were performed for deformation characteristics investigation on unsaturated soils during triaxial testing. The tested material is a mixture of Fairbanks silt and Kaolin at a ratio of 85:15. Basic properties of the used soil are presented in Table 3.3.

Table 3.3 Properties of the used soil.

Properties	Value
Maximum dry density	1.836 g/cm^3
Optimum moisture content	15%
Specific gravity	2.7
Plastic limit	18.2
Liquid limit	19.7
Plastic index	1.5

3.5.1 Specimen Preparation

The soil was oven-dried and mixed with water to the desired moisture content (16% in this case). The soil was then passed through a No. 16 sieve with opening size of 1.19 mm. The reason for sieving was that the mixture prepared before sieving was extremely heterogeneous and the size of each lump varied greatly from tiny packets to lumps more than 5 mm in diameter. The material remaining on the sieve was broken up and sieved once more with the whole process repeated until all material passed the sieve. The sieved mixture was placed in a plastic bag and sealed with tape. The sealed plastic bag was kept in an air-tight container for at least 12 hours to allow the water content to equalize throughout the material. In order to achieve a uniform density throughout the specimen, soil was statically compacted in 10 layers of 14.2 mm thickness in a split mold, which hosted a latex membrane, to 142 mm in height and 71 mm in diameter

cylinders according to the method presented in Ladd (1978). The specimens were compressed at a constant rate of 1.5 mm/min which is also used by Sivakumar (1993). Before adding soil for the next layer, the compacted soil surface was lightly scratched to ensure good contact between adjacent soil layers. This process was repeated until a full specimen of 142 mm in height was achieved. After compaction, the split mold was detached and the membrane used to cover the soil cylinder was carefully removed. Then, the soil specimens were sealed in containers and conditioned to different moisture contents by controlling the number of exposures to atmosphere for about 15 minutes/day. After that, the soil specimens were sealed in plastic bags and stored in a humidity- and temperature-controlled environment for at least one month to ensure moisture equilibrium in the whole soil specimen.

3.5.2 Experimental Program

A series of undrained triaxial tests, which included an isotropic loading-unloading-reloading and a deviatoric loading-unloading-reloading process under different confining stresses, were conducted on specimens with different moisture contents. According to Fredlund and Rahardjo (1993), it is difficult to maintain an undrained condition for the pore-air due to its ability to diffuse through the pore-water. So, for the undrained triaxial conducted in this study, the vent valve was open for air exchange during testing. The system setup for the triaxial tests is typically shown in Figure 3.3b. A total number of 108 measurement targets (5 mm in diameter) in 9 rows and 12 columns with a spacing of approximately 17 mm were posted to the membrane which covered the soil surface.

The loading process for each specimen was different from each other. For specimen A with water content of 13.49%, deviatoric load was applied to the specimen under 5 kPa confining pressure to failure and then to axial displacement of 10 mm. For specimens B with water content

of 15.91%, an isotropic loading process was performed first to maximum pressures of 200 kPa and followed by a deviator stage to a maximum axial displacement of 20 mm. For specimens C with water content of 13.20% and D with water content of 15.57%, an isotropic loading process was performed first to 300 kPa and unloaded to 150 kPa and then reloaded to 400 and 600 kPa, respectively and followed by a deviator stage to a maximum axial displacement of 20 mm. Both isotropic and deviatoric loads were applied in steps during triaxial testing. After each load step, images around the testing system were captured for deformation measurement. During deviator stages, the applied deviatoric loads were recorded and presented in Figure 3.6a.

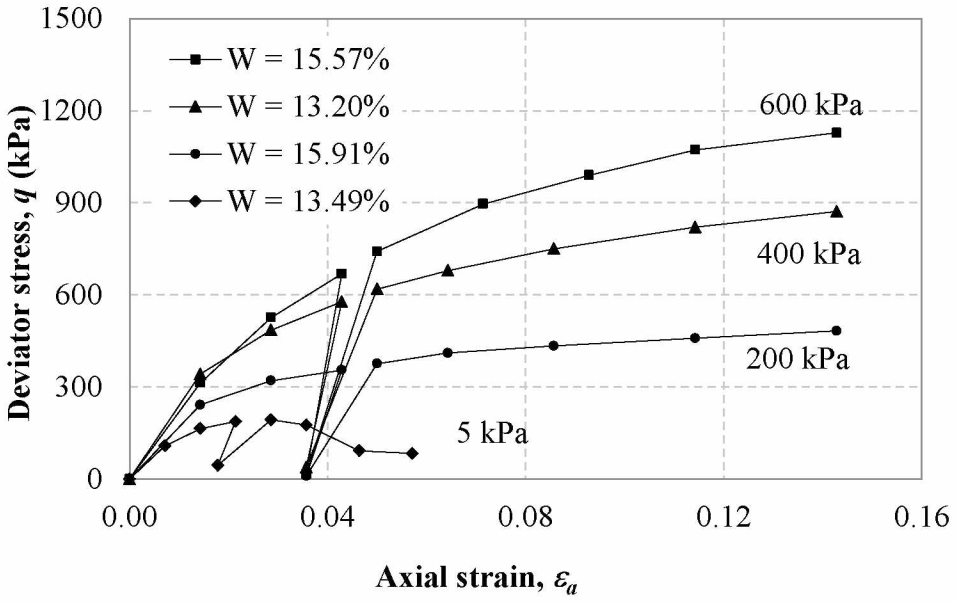

(a)

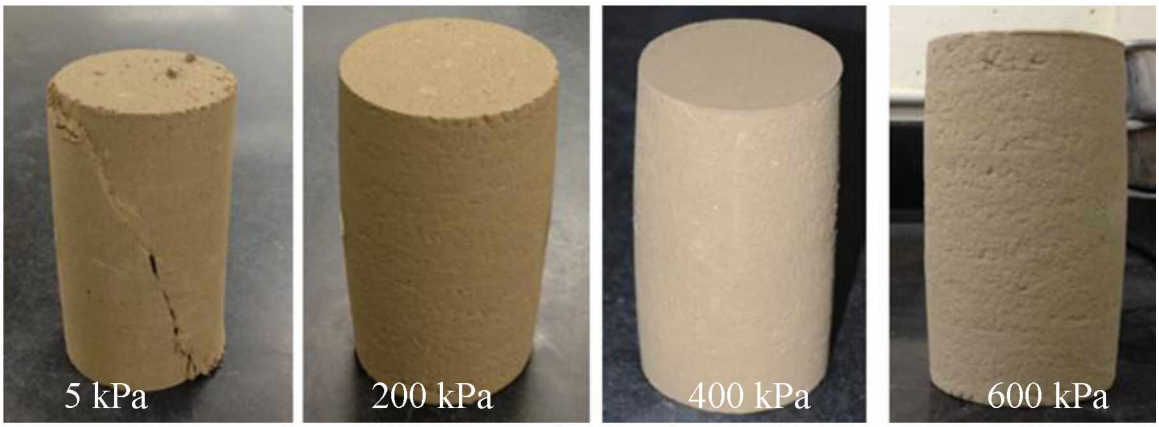

(b)

Figure 3.6 (a) Stress strain curves under different confining stresses; (b) Specimens after tests.

For specimen A under 5 kPa net confining pressure, during deviator stage, soil failed and a deviatoric stress peak was observed at an axial strain of 3%. However, for specimens B, C, and D under confining pressures of 200 kPa and higher, the applied deviatoric stress continuously increased with increasing axial strain till an axial displacement level of 20 mm. Figure 3.6b presented the pictures of four specimens after the undrained triaxial testing. A clear shear band can be identified on specimen A which was sheared under a net confining pressure of 5 kPa. However, specimens B, C, and D turned into barrel-shaped after deviatoric loading under high confining pressures.

3.6 Experimental Results

3.6.1 Volume Change

In this study, with the 108 measurement targets on specimen surface, a triangular mesh was generated which included 192 tetrahedrons from the side surface and 20 tetrahedrons from the top and bottom surfaces as shown in Figure 3.5b. Figures 3.7a and 3.7b present the triangular meshes for specimens A and C during deviatoric loading at different axial displacement levels. Since the applied axial displacement of was limited to 10 mm, deformation of specimen A was

not significant till the end of the test. However, specimen C gradually turned into barrel-shaped which is consistent with Figure 3.6b.

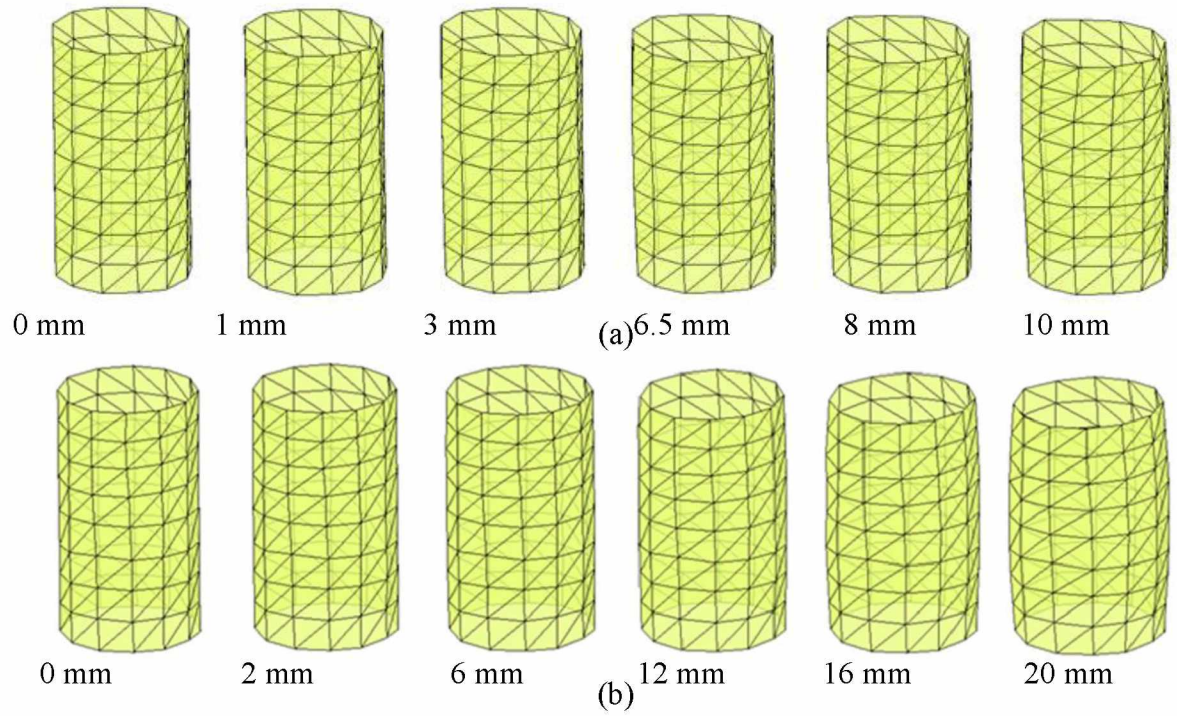

Figure 3.7 Soil deformations during deviatoric stage: (a) Specimen A (b) Specimen C.

Using the volume calculation method discussed above, soil specific volume changes during isotropic and deviatoric loadings were computed and presented in Figures 3.8a and 3.8b, respectively. Under isotropic load, for specimens with different moisture contents, as shown in Figure 3.8a, soil volumes decreased with increasing confining stress which is reasonable since the applied confining load compressed the tested unsaturated soil specimens. Similar volume change results during isotropic loading can also be found for triaxial tests on unsaturated soils under drained condition in previous studies (Wheeler and Sivakumar 1995; Rampino et al. 1999) in which the double-wall cell method was used for volume change measurements. The experimental data reported in Figure 3.8a also shows the loading collapse behavior of the tested unsaturated soil when the applied isotropic load is greater than 150 kPa. When there was an

isotropic unloading (decrease in net confining pressure), the volume of the tested specimens not fully rebounded due to the elasto-plasticity of unsaturated soils which is consistent with the findings (e.g. Rampino et al. 1999; Thu 2006). During deviatoric loading under different net confining stresses, as presented in Figure 3.8b, tests results indicate that unsaturated soil specimen undergo dilation throughout the deviator stage under 5 kPa net confining pressure. However, under high confining pressures (>=200 kPa), indicated by the slopes of the volumetric strain curves, the soil demonstrated contraction at the early age of deviator stage and then gradually stabilized (i.e. specimen B) or contraction till the end (i.e. specimens C and D) through a closer scrutiny of the volumetric verses axial strain curve. Similar volume change results during deviatoric loading at different confining stresses are also found for loose sand as presented in Desrues and Viggiani (2004).

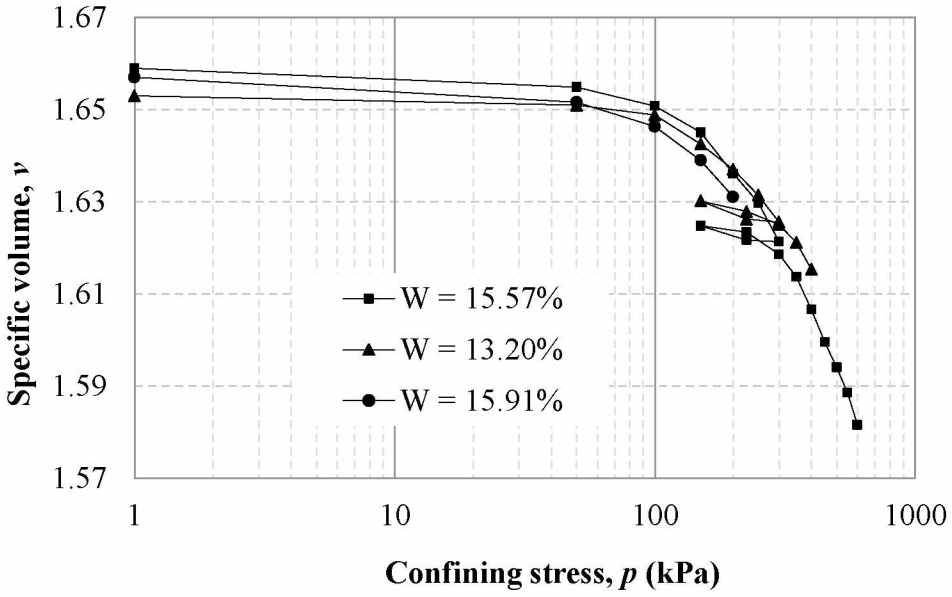

(a)

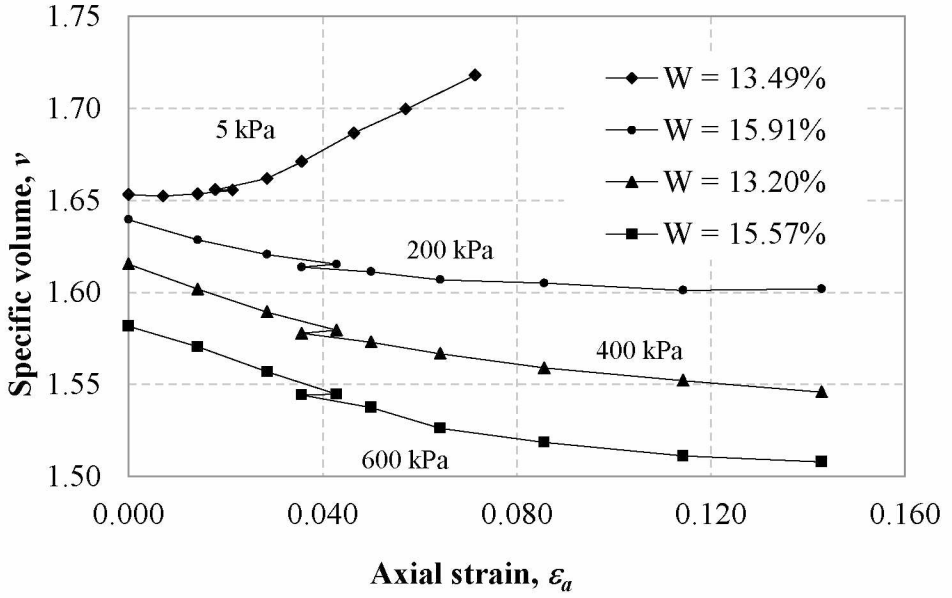

(b)

Figure 3.8 (a) Soil volume variations during isotropic loading; (b) Soil volume variations during deviatoric loading under constant confining stresses.

3.6.2 Volumetric Strain Non-uniformity

In the past, for triaxial tests on both saturated and unsaturated soils, volumetric strain for a soil specimen during testing under isotropic or deviatoric load is usually assumed to be uniform. The assumption of uniform volumetric strain might be the truth for a soil behavior under isotropic load. However, during triaxial testing under deviatoric load, soil volumetric strain throughout the whole specimen might not be uniform due to the end effect. Till now, no research effort has been published on unsaturated soil volumetric non-uniformity investigation. The major reason for this is lack of a proper method for full-field deformation measurements on soils during triaxial testing. However, with the newly developed photogrammetry-based method, the difficulties in full-field deformation measurement on unsaturated soils no longer exist.

Since there were 9 rows of measurement targets on each specimen surface, to facilitate the volumetric strain non-uniformity analysis, soil specimens were divided into 8 layers (layer one to layer eight from the top to bottom as shown in Figure 3.5b). For specimens B, C, and D, during isotropic loading, the overall volumetric strain variations and volumetric strain variations for each soil layer are plotted against applied net confining stresses as shown in Figure 3.9. Similar results can be found in Figures 3.9a, 3.9b, and 3.9c for three specimens isotropically loaded 200, 400, and 600 kPa, respectively. Variations of the volumetric strain did exist under the same isotropic load level. The major reason for this variation is believed to be neither were materials truly homogeneous at the scale of a laboratory specimen, nor were boundary conditions perfect. For specimens B, C, and D, the minimum volumetric strains are found at layers 1, 1, and 8 which were at the both ends of the specimen. This is reasonable since the end friction could constrain the adjacent soil layers from deforming. In general, the trend of the volumetric strain variation different soil layers is consistent with the corresponding overall volumetric strain.

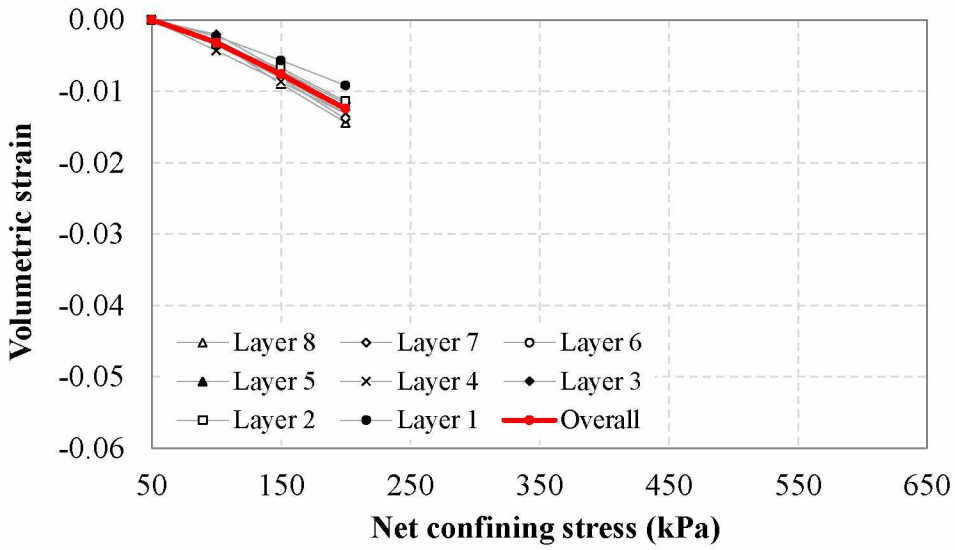
0.00
-0.01
-0.02
-0.03
-0.04
-0.05
-0.06
Volumetric strain
Layer 8
Layer 7
Layer 6
Layer 5
Layer 4
Layer 3
Layer 2
Layer 1
Overall
50
150
250
350
450
550
650
Net confining stress (kPa)

(a)

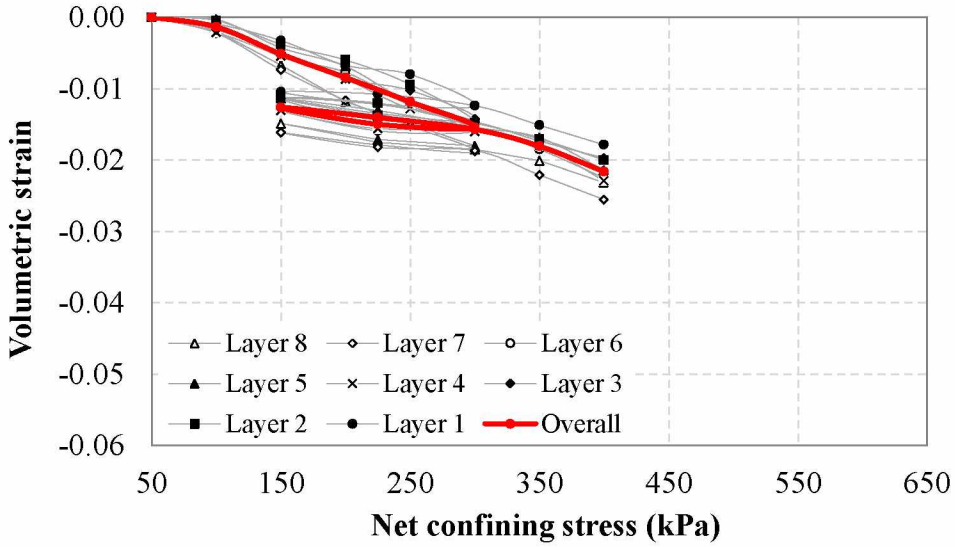
0.00
-0.01
-0.02
-0.03
-0.04
-0.05
-0.06
Volumetric strain
Layer 8
Layer 7
Layer 6
Layer 5
Layer 4
Layer 3
Layer 2
Layer 1
Overall
50
150
250
350
450
550
650
Net confining stress (kPa)

(b)

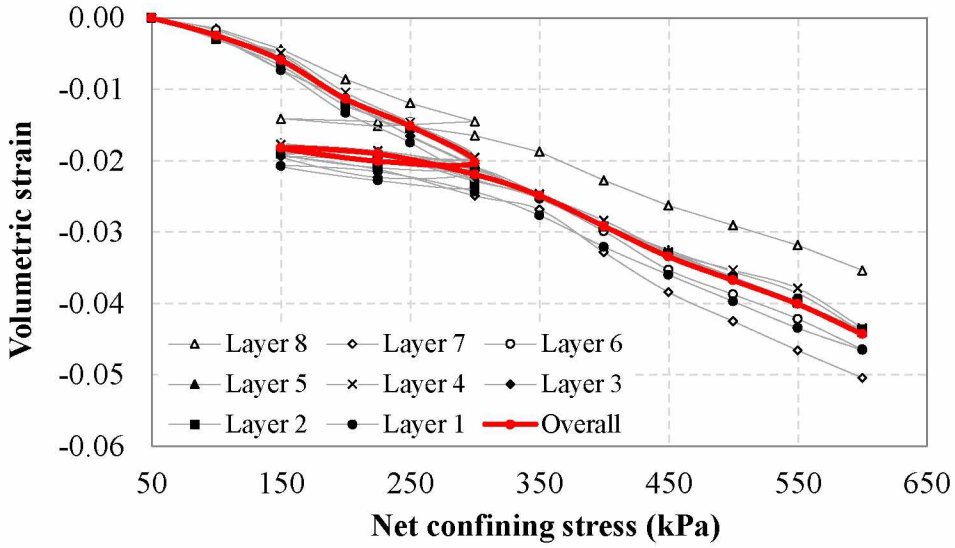

(c)

Figure 3.9 Volumetric variations during isotropic loading: (a) Specimen B; (b) Specimen C; and (c) Specimen D.

Under deviatoric load, the volumetric strain variations in each layer for four specimens are plotted against axial strain as shown in Figure 3.10. Soil volumetric strains at different layers significantly varied throughout the deviator stage. The volumetric strain variation in different layers was getting higher and higher with an increasing axial strain. At the same axial strain level, the highest volumetric strain (dilation) is found on specimen A during deviatoric loading at 5 kPa confining pressure as shown in Figure 3.10a. The overall volumetric strain for specimen A increased with increasing confining stress. However, for layer 8, soil volume decreased due to end effect during deviatoric loading which was in contrast to the overall volume change. The highest dilations are found at soil layers 4 and 5 since these two layers are at the middle of the specimen. For specimen B as show in Figure 3.10b, the overall soil volume experienced contraction and then gradually stabilized at the end of the deviatoric loading. However, soil at layers 4 and 5 at the middle of the specimen experienced shear contraction at the early age of

deviatoric loading to dilation afterwards. The lowest volumetric strains were found at layers 1 and 8 due to end effect. This result is consistent with the observation on the soil specimen after testing as shown in Figure 3.6b. The volumetric strain variations of specimens C, and D during deviatoric loading were very similar to that of specimen B as shown in Figures 3.10c and 3.10d. However, for soil layers 4 and 5, the transitions from contraction to dilation were "delayed" when compared with that for specimen B. This delay was attributed to the decreasing of the effective stress ratio.

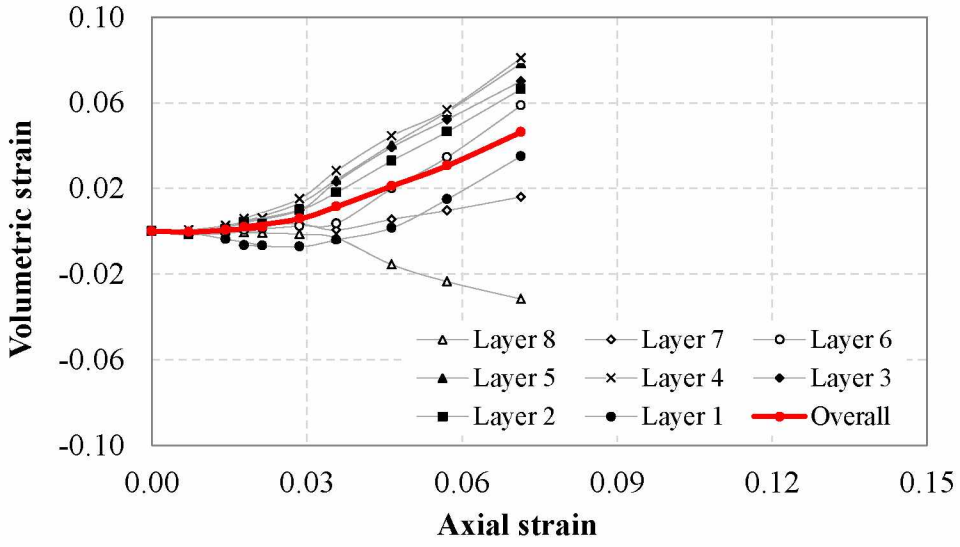

(a)

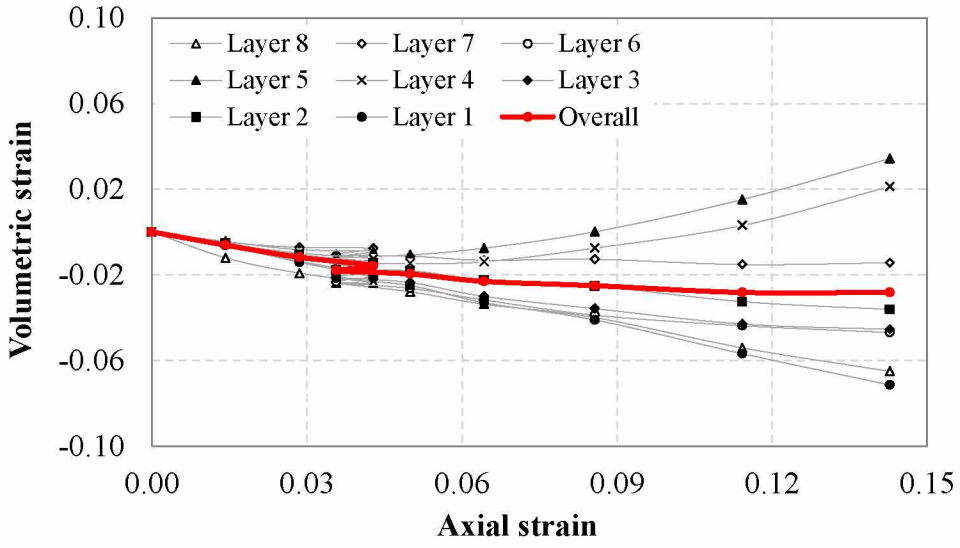
Layer 8
Layer 7
Layer 6
Layer 5
Layer 4
Layer 3
Layer 2
Layer 1
Overall
Volumetric strain
Axial strain
0.10
0.06
0.02
-0.02
-0.06
-0.10
0.00
0.03
0.06
0.09
0.12
0.15

(b)

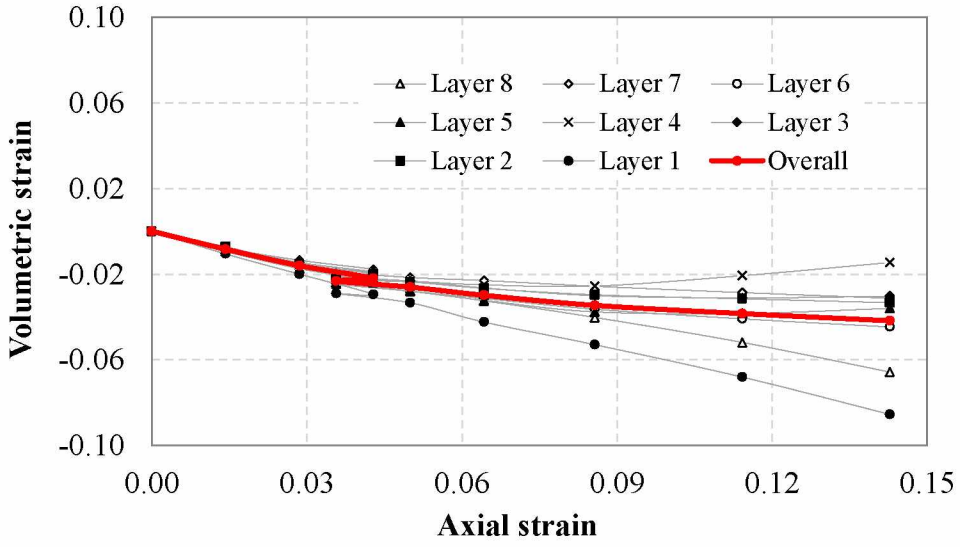
Layer 8
Layer 7
Layer 6
Layer 5
Layer 4
Layer 3
Layer 2
Layer 1
Overall
Volumetric strain
Axial strain
0.10
0.06
0.02
-0.02
-0.06
-0.10
0.00
0.03
0.06
0.09
0.12
0.15

(c)

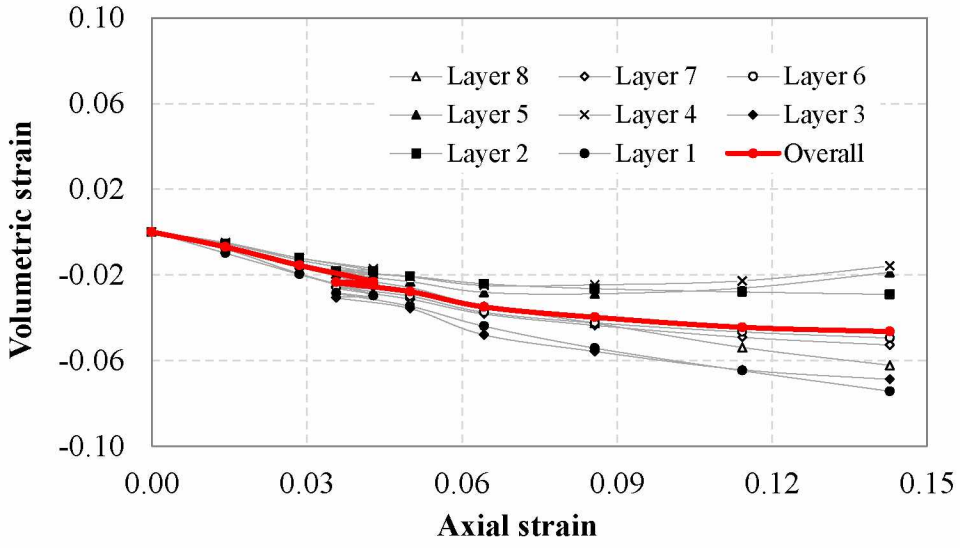

(d)

Figure 3.10 Volumetric variations during deviatoric loading under different confining pressures: (a) Specimen A; (b) Specimen B; (c) Specimen C; and (d) Specimen D.

Table 3.4 summarized the volumetric strain information for four specimens at axial strain levels of 3.6%, 8.6%, and 14.3% during deviatoric loading. At the same axial strain level, soil volumetric strains increased with increasing confining stress. The standard deviations of the volumetric strains in different layers for four specimens were getting less with increasing net confining pressure which indicated that the soil volumetric strain was getting more uniform. Also, for four specimens, the maximum difference between volumetric strain of each layer and the corresponding overall volumetric strain generally decreased with increasing net confining pressure during deviatoric loading.

Table 3.4 Volumetric strains during deviatoric loading at different axial strain levels.

Water content	Confining stress	Volumetric strain (%)								
		3.6% axial strain			8.6% axial strain			14.3% axial strain		
		Ave.	Std.	Max.	Ave.	Std.	Max.	Ave.	Std.	Max.
13.49%	5 kPa	1.14	1.34	1.68	-	-	-	-	-	-
15.91%	200 kPa	-1.81	0.52	0.74	-2.51	1.64	2.52	-2.83	3.87	6.25
13.20%	400 kPa	-2.32	0.31	0.59	-3.46	0.92	1.84	-4.18	2.26	4.38
15.57%	600 kPa	-2.36	0.49	0.71	-3.99	1.21	1.6	-4.66	2.26	3.06

Ave.: represent the average volumetric strain.
Std.: represent the standard deviation of the volumetric strain.
Max.: represent the maximum difference between volumetric strain of each layer and the corresponding overall volumetric strain.

3.6.3 Full-field Strain Distribution

With the strain calculation method presented in Appendix A, full-field strain distributions of four specimens during isotropic and deviatoric loading were obtained. Using the specimen A as an example, Figure 3.11 shows the full-field axial displacement, axial strain, and radial strain distributions during isotropic loading. Since the applied load was isotropic, theoretically, no strain localization was expected. However, as shown in Figure 3.11, localized deformation were still found in radial and axial strain distributions which is consistent with the volumetric strain results. Since the lower end of the soil specimen rested on the triaxial pedestal, no displacement was detected as shown in Figure 3.11a. The top surface of the specimen is in direct contact with the loading cell which is movable. So, the maximum displacement was found to be at the top end of the specimen. At both ends of the specimen, soil axial strains were higher than the middle part as shown in Figure 3.11b which is consistent with that the soil volumetric strains in layers 1 and 7 are higher than the other layers as presented in Figure 3.8c. It is interested to note that, under the same isotropic load, radial strain was much greater than the axial strain when a comparison was made between Figures 3.11b and 3.11c. Also, the radial strain as shown Figure 3.11c was

not evenly distributed which indicated that soil deformation was not axisymmetric during isotropic loading. Besides the detailed axial and radial strain analyses, the overall axial and radial strains at different isotropic load levels for specimens B, C, and D were also computed and summarized in Table 3.5.

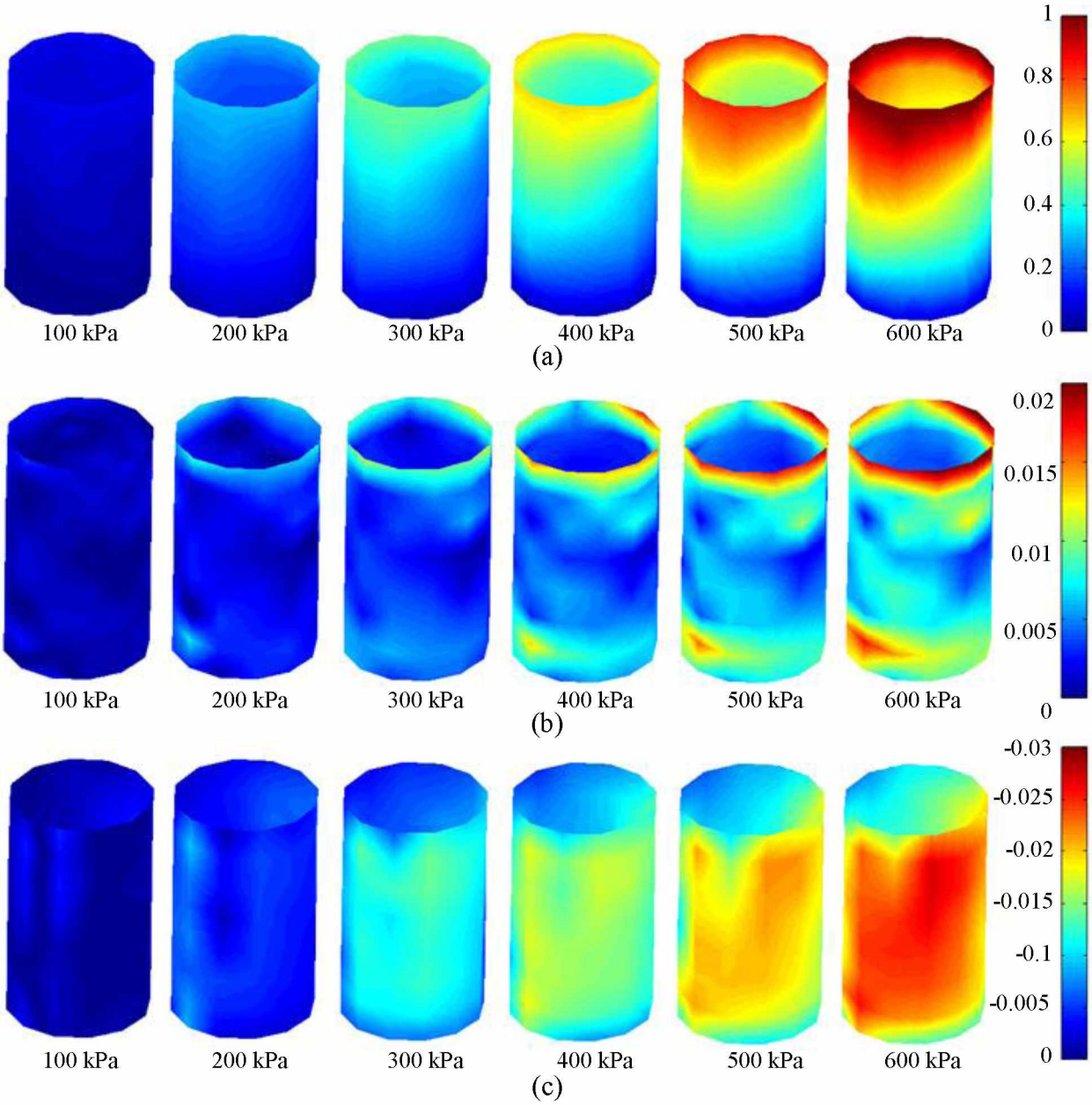

Figure 3.11 Full-field deformations of specimen D during isotropic loading: (a) Axial displacement (mm); (b) Axial strain; and (c) Radial strain.

Table 3.5 Summarized axial and radial strains during isotropic loading.

Water content	Axial and Radial Strain								
	Net confining pressure								
	200 kPa			400 kPa			600 kPa		
	ε_a	ε_r	$\varepsilon_a/\varepsilon_r$	ε_a	ε_r	$\varepsilon_a/\varepsilon_r$	ε_a	ε_r	$\varepsilon_a/\varepsilon_r$
15.91%	0.29	0.48	0.61	-	-	-	-	-	-
13.20%	0.22	0.32	0.69	0.51	0.83	0.61	-	-	-
15.57%	0.26	0.44	0.59	0.56	1.18	0.47	0.87	1.78	0.49

In Table 3.5, the overall radial strains for soil specimens were much higher than the associated axial strains under the same isotropic loading conditions which are consistent with the findings from Figure 3.11. Also, the axial to radial strain ratios slightly varied for the tested specimens at low confining pressure (200 kPa, in Table 3.5). These axial to radial strain ratios generally decreased with the increase of the isotropic load at the early stage of the isotropic loading and then stabilized. The major reason for this phenomenon was believed to be attributed to the used static compaction method (Ladd 1978) for specimen preparation. In other words, the specimen prepared using this compaction method is anisotropic. As a result, soil behavior was anisotropic under isotropic load.

Figure 3.12 presented the full-field axial displacement, axial and radial strain distributions of specimen A at different axial strain levels under 5 kPa net confining pressure. According to Figure 3.6a, specimen A failed at an axial strain level of 3% (4 mm axial displacement) during deviator stage. Failure of many engineering materials is characterized by the formation and propagation of zones of localized shear deformation. The most typical localized deformation observed in soils is linear shear banding. As shown in Figure 3.12a, at 6.5 mm displacement, which was after soil failure, no shear band is observed at the displacement

distribution plot. At 10 mm displacement, a nearly undeformed portion of the specimen sliding over the lower portion created a clear shear band which is consistent with that observed from the picture of the specimen (i.e. Figure 3.6b) after testing. As shown in Figure 3.12b, at 3 mm axial displacement, no shear band was observed. As the axial displacement became larger, concentration of strain in a local zone occurred because of actual non-uniformity of the mass and stiffness of the material. Figure 3.12b more clearly illustrated the formation of the shear band. Localized strains were found on the axial strain contours at 6.5 mm axial displacement. With increase of axial displacement, localized radial strain was getting more and more concentrated when reaching 10 mm axial displacement. Also, concentrated radial strain was found at the right side of the specimen as shown in Figure 3.12c. This is because of the presence of the failure plane which divided the soil specimen into two portions. The upper right portion was slide over the lower portion and resulted in the concentrated radial strain.

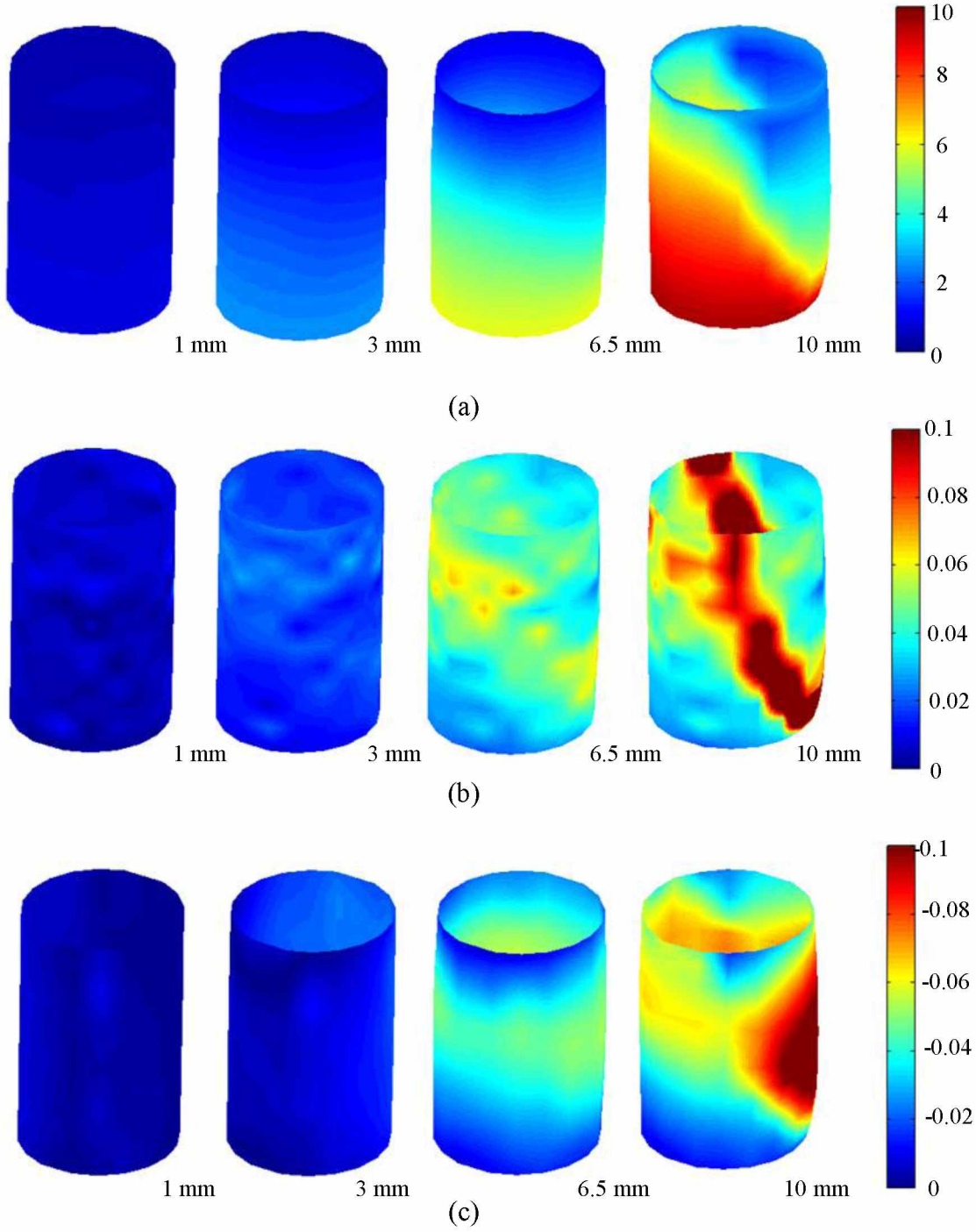

Figure 3.12 Full-field deformations of specimen A during deviatoric loading: (a) Axial displacement (mm); (b) Axial strain; (c) Radial strain.

According to Figure 3.6b, specimens B, C, and D turned into barrel-shaped after deviatoric loading to an axial displacement of 20 mm. Using specimen C as an example, Figure 3.13

presented the typical full-field axial displacement, axial and radial strain distributions at different axial strain levels during deviatoric loading. In Figure 3.13a, at the same height, the axial displacement was quite uniform. No shear band was observed on the axial displacement and axial contours which was consistent with the soil picture after testing as shown in Figure 3.6b. However, it was noted that some localized strain can still be found on the radial and axial strain contours (see Figures 3.13b and 3.13c). The reason for this distortion was believed to be attributed to the applied deviatoric load was eccentric and the non-uniformity of the specimen.

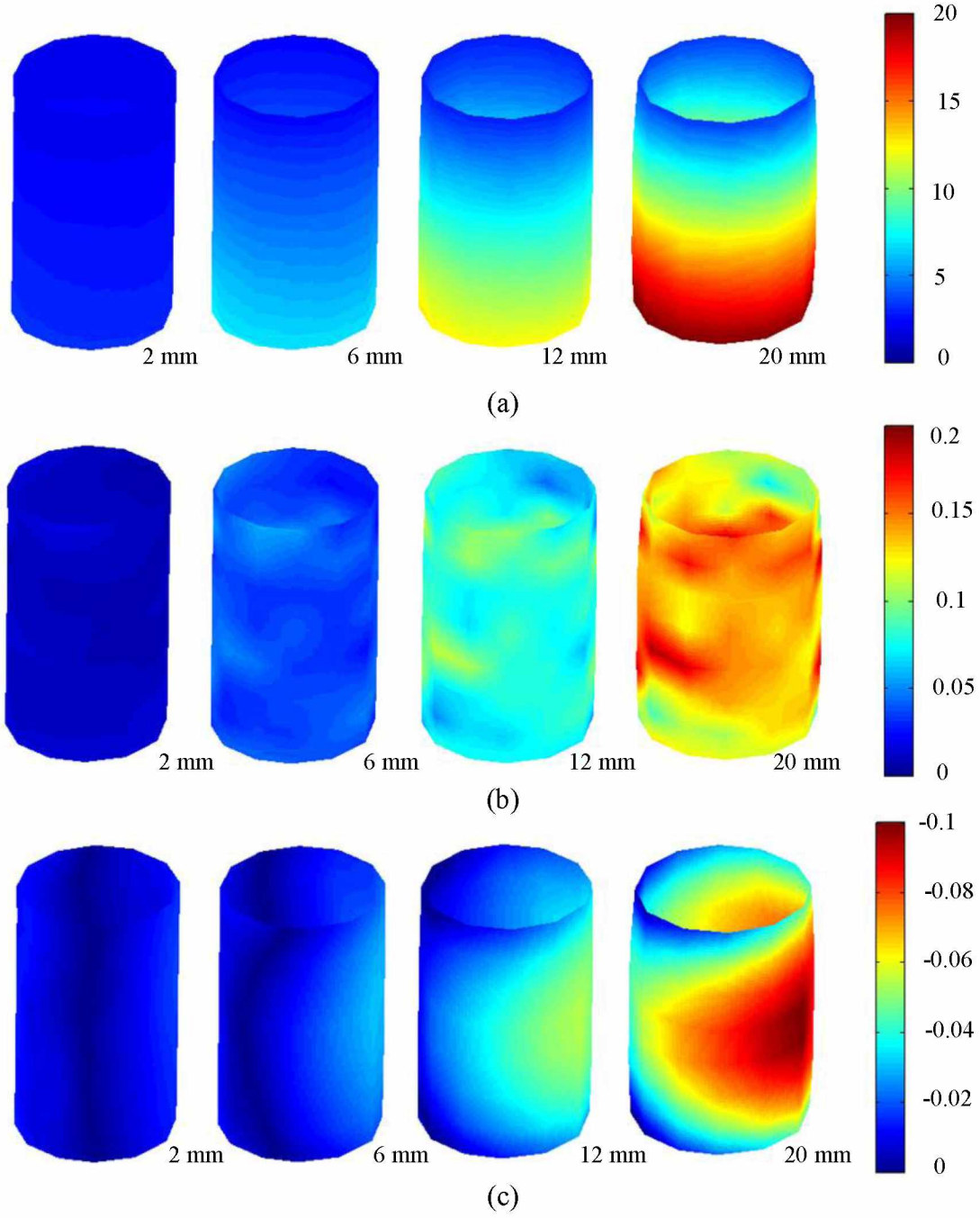

Figure 3.13 Full-field deformations of specimen C during deviatoric loading: (a) Axial displacement (mm); (b) Axial strain; (c) Radial strain

3.7 Time and Cost Efficiency

Only a digital camera with a fixed focal length lens (total cost is $1100 in this study) is required for the photogrammetry-based deformation measurement method. Before triaxial testing, the measurement targets were manually posted to the load frame, outer surface of the acrylic cell, and specimen surface which took approximately an hour. However, the setup for those targets on the load frame and cell wall surface was only required to be performed once and would be kept for future testing. Measurement targets can be directly printed on latex membranes which could significantly reduce the time required for test preparation. During triaxial testing, for a single measurement (i.e. construct the 3D model of the specimen at a specific loading condition), only two minutes were required to capture the images around the testing system for the deformation measurement. The total time for processing the captured images (included image point idealization, orientation, cell wall reconstruction, optical ray tracing, and least-square estimation) for the photogrammetry-based measurement was dependent on numbers of the images and measurement targets on specimen surface. Image point idealization and orientation processes were performed using existing photogrammetry software which typically took approximately three minutes. In this study, a MatLab-based program was developed and utilized for the cell wall reconstruction, optical ray tracing, least-square estimation, and post-processing (volume and strain calculations) which typically took approximately five minutes. In other words, a single measurement using the proposed photogrammetry-based method (from image capturing to data post-processing) could be completed in approximately 10 minutes.

3.8 Discussions

The newly developed photogrammetry-based method is also an image-based method. However, it is significantly different from the conventional image-based methods due to the following reasons: (1) the used camera for the photogrammetry-based method is calibrated in order to be treated as a pinhole camera and eliminate lens distortion. A calibrated camera is very critical and beneficial for measurement accuracy improvement; (2) for system setup, the proposed method only requires attaching some measurement targets on the load frame, triaxial cell wall, and specimen surface; (3) during image capturing, the used camera is hand hold instead of mounted on a tripod in the conventional image-based methods. With this flexibility, images can be captured at any arbitrary distances and view angles to achieve the best measurement accuracy. During image capturing, no external lighting is required as long as the build-in flash of the camera is functional which is also different from the conventional image-based methods; (4) principle of photogrammetry is adopted to accurately determine camera orientations where images are captured and shape and orientation of the triaxial chamber at different loading conditions. However, in the conventional image-based methods, the positions and orientations of the camera and cell wall are manually controlled. In the other words, the relative positions of the camera and cell wall might not be accurate; (5) triaxial cell is assumed to be barrel-shaped which is consistent with the real shape of the triaxial chamber especially under high chamber pressure. Also, the deformation of the cell wall under different chamber pressures can be detected by photogrammetry instead of neglected in the conventional image-based methods; (6) Snell's law is adopted to correct refractions at the interfaces of the air-cell and cell-water in an arbitrary 3D coordinate system instead of in an idealized 2D coordinate system which offers great flexibility for refraction correction. In other words, optical rays can be traced from different random camera

stations to the soil surface in the triaxial cell. All assumptions in the conventional image-based methods are no longer required; (7) in this study, approximately five images, instead of one for the conventional image-based methods, were utilized to determine the 3D position of a single measurement target on specimen surface. With no doubt, using more images is quite beneficial to improve measurement accuracy; (8) for the photogrammetry-based method, no system calibration is required before any measurement. However, a sophisticated system calibration is required for the conventional image-based methods. Most importantly, the accuracy of the photogrammetry-based method can be self-checked by the d_i values; and (9) with images captured all around the triaxial chamber, full-field deformation of the soil specimen can be detected during triaxial testing. With this deformation, full-field strain distributions could be extracted for in-depth soil behavior analysis. However, in the conventional image-based methods, only part of the specimen deformation could be captured.

3.9 Conclusions

A non-contact photogrammetry-based method, which is significantly different from the conventional image-based methods, is presented to measure unsaturated soil deformations during triaxial testing. With this method, the conventional triaxial test apparatus for saturated soils can be used for triaxial testing on unsaturated soils without any modification. The proposed photogrammetry-based method is accurate, time- and cost-effective, requires only a digital camera to capture images of the soil specimen during triaxial testing from which accurate full-field 3D models of the soil specimen at different loading steps are reconstructed. Most importantly, the accuracy of the photogrammetry-based method can be self-checked by the d_i values. Another advantage of the photogrammetry-based method is that it can be utilized for

deformation measurements on both saturated and unsaturated soils during triaxial testing with the same system setup.

A series of undrained triaxial tests on unsaturated soils was performed during which soil deformations were measured using the photogrammetry-based method. It was found that the photogrammetry-based method was capable of capturing soil deformation characteristics such as volume change, volumetric strain non-uniformity, barreling, full-field strain distribution, and shear band evolution. Based upon the measurement results, soil deformation was not uniformly distributed during isotropic loading. The radial strain was found to be nearly twice of the axial strain. Also, volumetric strains in different soil layers were not uniformly distributed during isotropic loading. During deviatoric loading, soil volumetric strains at different layers exhibited significant variation. Due to end effect, soil specimens gradually turned into barrel-shaped during deviatoric loading under confining pressures greater 200 kPa. Maximum volumetric strains were always found to be at the middle of the specimens. In addition, during deviatoric loading at 5 kPa net confining pressure, a clear shear band evolution process was captured based upon the deformation analysis results. Through the undrained triaxial tests on unsaturated soils, it could be concluded that the photogrammetry-based method is a powerful tool for in-depth soil deformation measurements.

3.10 References

Adams, B.A., Wulfsohn, D., and Fredlund, D.G. 1996. Air volume change measurement in unsaturated soil testing using a digital pressure-volume controller. ASTM Geotechnical Testing Journal, 19(1): 12-21.

Alshibli, K.A., Sture, S., Costes, N.C., Frank, M.L., Lankton, M.R., Batiste, S.N., and Swanson, R.A. 2000. Assessment of local deformation in sand using X-ray computed tomography. ASTM Geotechnical Testing Journal, 23(3): 274-299.

Bagherieh, A.R., Habibagahi, G. and Ghahramani, A. 2008. A novel approach to measure the volume change of triaxial soil samples based on image processing. Journal of Applied Sciences, 8(13): 2387-2395.

Bhandari, A.R., Powrie, W., and Harkness, R.M. 2012. A digital image-based deformation measurement system for triaxial tests, ASTM Geotechnical Testing Journal, 35(2): 209-226.

Bishop, A. and Donald, I. 1961. The experimental study of partly saturated soil in the triaxial apparatus. In Proceedings of the 5th international conference on soil mechanics and foundation engineering, Paris, Vol. 1, pp. 13-21.

Chupin, O.A., Rechenmacher, L., and Abedi, S. 2012. Finite strain analysis of nonuniform deformation inside shear bands in sands. International Journal for Numerical and Analytical Methods in Geomechanics, 36(14): 1651-1666.

Clayton CRI, Khatrush SA (1986) A New Device for Measuring Local Axial Strains on Triaxial Specimens. Géotechnique 36, No.4: 593–597.

Clayton CRI, Khatrush SA, Bica AVD, Siddique A (1989) The use of Hall effect semiconductors in geotechnical instrumentation. Geotech Testing J 12(1):69–76.

Cui, Y. and Delage, P. 1996. Yielding and plastic behavior of an unsaturated compacted silt, Geotechnique, 46(2): 291-311.

Desrues, J. 2004. Tracking strain localization in geomaterials using computerized tomography. X-ray CT for Geomaterials: 15-41.

Desrues, J., and Viggiani, G. 2004. Strain localization in sand: an overview of the experimental results obtained in Grenoble using stereophotogrammetry. International Journal for Numerical and Analytical Methods in Geomechanics, 28(4): 279-321.

Fredlund, D. G., and Rahardjo, H. (1993). Soil Mechanics for Unsaturated Soils. New York: John Wiley and Sons.

Gachet, P., Geiser, F., Laloui, L., and Vulliet, L. 2007. Automated digital image processing for volume change measurement in triaxial cells. ASTM Geotechnical Testing Journal, 30(2), 98-103.

GDS (2009): http://www.epccn.com/gds/datasheets/UNSAT_Datasheet.pdf.

Geiser F (1999) Comportément mécanique d'um limon non saturé: étude expérimentale et modélisation constitutive. Ph.D. thesis, Swiss Federal Institute of Technology, Lausanne, Switzerland.

Geiser, F., Laloui, L., Vulliet, L., Rahardjo, H., Toll, D., and Leong, E. 2000. On the volume measurement in unsaturated triaxial test. In Unsaturated soils for Asia. Proceedings of the Asian Conference on Unsaturated Soils, UNSAT-Asia 2000, Singapore, 18-19 May, pp. 669-674.

Hoyos, L. R., Laloui, L., and Vassallo, R. 2009. Mechanical testing in unsaturated soils. In Laboratory and Field Testing of Unsaturated Soils pp. 63-77. Springer Netherlands.

Ladd, R. S. 1978. Preparing Test Specimens Using Under compaction. ASTM Geotechnical Testing Journal, 1(1): 16-23.

Laloui L, Pe´ron H, Geiser F, Rifa'i A, and Vulliet L 2006. Advances in volume measurement in unsaturated triaxial tests. Soils and Foundations, 46(3): 341-349.

Laudahn, A., Sosna, K., and Bohdp, J. 2005. A simple method for air volume change measurement in triaxial tests, ASTM Geotechnical Testing Journal, 28(3): 313-318.

Lin, H. and Penumadu, D. 2006. Strain localization in combined axial-torsional testing on kaolin clay, Journal of Engineering Mechanics, 132(5): 555-564.

Macari, E.J., Parken, J., and Costes, N.C. 1997. Measurement of volume changes in triaxial tests using digital imaging techniques, ASTM Geotechnical Testing Journal, 20(1): 103-109.

Mikhail, E.M., Bethel, J.S., and McGlone, J.C. 2001. Introduction to modern photogrammetry Vol.). John Wiley & Sons Inc.

Ng, C.W., Zhan, L., and Cui, Y. 2002. A new simple system for measuring volume changes in unsaturated soils, Canadian Geotechnical Journal, 39(3): 757-764.

Parker, J. K. 1987. Image processing and analysis for the mechanics of granular materials experiment. In ASME Proceedings of the 19th SE Symposium on System Theory, Nashville.

Rampino C, Mancuso C, Vinale F (1999) Laboratory testing on an unsaturated soil: equipment, procedures, and first experimental results. Can Geotech J 36(1):1–12.

Rechenmacher, A. L. 2006. Grain-scale processes governing shear band initiation and evolution in sands. Journal of the Mechanics and Physics of Solids, 54(1): 22-45.

Rechenmacher, A. L., and Medina-Cetina, Z. 2007. Calibration of soil constitutive models with spatially varying parameters. Journal of Geotechnical and Geoenvironmental Engineering, 133(12): 1567-1576.

Rechenmacher, A., and Saab, N. 2002. Digital image correlation (DIC) to evaluate progression and uniformity of shear bands in dilative sands. In 15th ASCE Engineering Mechanics Division Conference.

Romero, E., Facio, J., Lloret, A., Gens, A., and Alonso, E. 1997. A new suction and temperature controlled triaxial apparatus. In Proceedings of the International Conference on Soil Mechanics and Foundation Engineering, Vol. 1, pp. 185-188.

Sachan, A., and Penumadu, D. 2007. Strain localization in solid cylindrical clay specimens using digital image analysis (DIA) technique. Soils and Foundations, 47(1): 67-78.

Sharma, R. S., Hong, L., and Singhal, S. 2006. Developments in measurement of volume change in triaxial testing of unsaturated soils. In Advances in Unsaturated Soil, Seepage, and Environmental Geotechnics, ASCE, pp. 93-101.

Sivakumar, V. 1993. A critical state framework for unsaturated soil. Ph.D thesis, University of Sheffield.

Thu, M.T. 2006, Shear strength and volume change relationship for an unsaturated soil, Ph.D thesis, Nanyang Technological University.

Wang, Qiong, and Poul V. Lade. 2001. Shear banding in true triaxial tests and its effect on failure in sand. Journal of Engineering Mechanics 127(8): 754-761.

Wheeler, S. 1988. The undrained shear strength of soils containing large gas bubbles, Geotechnique, 38(3): 399-413.

Wheeler, S. J., and Sivakumar, V. (1995). An elasto-plastic critical state framework for unsaturated soil. Géotechnique, 45(1), 35-53.

White, D., Randolph, M. F., and Thompson, B. 2005. An image-based deformation measurement system for the geotechnical centrifuge. International Journal of Physical Modelling in Geotechnics, 5(3): 1-12.

Zhang, X., Li, L., Chen, G., and Lytton, R.L. 2015. A photogrammetry-based method to measure total and local volume changes of unsaturated soils during triaxial testing. Acta Geotechnica, 10(1): 55-82.

3.11 Appendix. Strain Calculation

A small tetrahedron $P_oP_{1i}P_{2i}P_{3i}$ was separated from the specimen, as shown in Figure 3.6c, with three nodes (P_{1i}, P_{2i}, and P_{3i}) on the specimen surface and the fourth node P_o located on z axis. Any point within the element would have three displacement components: vertical displacement, u_1, radial displacement, u_2, and circumferential displacement, u_3. It was assumed that the displacement of any point within the element was a linear function of the coordinates z, r and θ as shown in Equation. 3.A.1.

$$u_{ij} = \alpha_{i1} + \alpha_{i2} z + \alpha_{i3} r + \alpha_{i4} \theta \qquad \text{Equation 3.A.1}$$

where α_{ij} are constants to be determined. Equation 3.A.1 should be satisfied at all four nodes of the element. Therefore, Equation 3.A.2 can be obtained which is in matrix format:

$$\begin{Bmatrix} u_{i1} \\ u_{i2} \\ u_{i3} \\ u_{i4} \end{Bmatrix} = \begin{bmatrix} 1 & z_1 & r_1 & \theta_1 \\ 1 & z_2 & r_2 & \theta_2 \\ 1 & z_3 & r_3 & \theta_3 \\ 1 & z_4 & r_4 & \theta_4 \end{bmatrix} \cdot \begin{Bmatrix} \alpha_{i1} \\ \alpha_{i2} \\ \alpha_{i3} \\ \alpha_{i4} \end{Bmatrix} \qquad \text{Equation 3.A.2}$$

where z_i and r_i are coordinates at the nodes, while u_{ij} (i=1 to 3, j=1 to 4) are displacements at the j^{th} node in an element. The constants α_{ij} can be obtained using Equation 3.A.2 with given nodal displacements, u_{ij}. In order to determine constants α_{ij}, the coordinates at the four nodes must be known. However, only the displacement components of those nodes on the outer surface of the specimen are known. It is reasonable to assume:

$$\begin{cases} r_4 = 0 \\ z_4 = (z_1 + z_2 + z_3)/3 \\ \theta_4 = (\theta_1 + \theta_2 + \theta_3)/3 \end{cases} \qquad \text{Equation 3.A.3}$$

After determination of the constants α_{ij}, the continuous deformation field was known and the strain components can be calculated by using the following Equation 3.A.4. The strain calculation is similar to that presented in Lin and Penumadu (2006).

$$\begin{Bmatrix} \varepsilon_z \\ \varepsilon_r \\ \varepsilon_\theta \\ \varepsilon_{r\theta} \\ \varepsilon_{rz} \\ \varepsilon_{\theta z} \end{Bmatrix} = \begin{Bmatrix} \dfrac{\partial u_1}{\partial z} \\ \dfrac{\partial u_2}{\partial r} \\ \dfrac{u_2}{r} \\ \dfrac{1}{2}\left(\dfrac{\partial u_3}{\partial r} + \dfrac{\partial u_3}{r\partial \theta} - \dfrac{u_3}{r} \right) \\ \dfrac{1}{2}\left(\dfrac{\partial u_1}{\partial r} + \dfrac{\partial u_2}{\partial z} \right) \\ \dfrac{1}{2}\left(\dfrac{\partial u_2}{r\partial \theta} + \dfrac{\partial u_3}{\partial z} \right) \end{Bmatrix} = \begin{Bmatrix} \alpha_{12} \\ \alpha_{23} \\ \dfrac{1}{r}\left(\alpha_{21} + \alpha_{22} z + \alpha_{23} r + \alpha_{24}\theta \right) + \dfrac{\alpha_{34}}{r} \\ \dfrac{1}{2r}\left(\alpha_{24} - \alpha_{31} - \alpha_{32} z - \alpha_{34}\theta \right) \\ \dfrac{1}{2}\left(\alpha_{13} + \alpha_{22} \right) \\ \dfrac{1}{2}\left(\dfrac{\alpha_{14}}{r} + \alpha_{22} \right) \end{Bmatrix}$$

Equation 3.A.4

CHAPTER 4. A NEW TRIAXIAL TESTING SYSTEM FOR UNSATURATED SOIL CHARACTERIZATION[1]

4.1 Abstract

Suction-controlled triaxial tests have been widely used to characterize unsaturated soils. However, this type of test requires sophisticated equipment and therefore is expensive and very time-consuming due to the low permeability of unsaturated soils. Only few research universities can afford the equipment, which limits the advancement and implementation of unsaturated soil mechanics.

This paper proposes a new triaxial testing system for unsaturated soils based upon the conventional triaxial test apparatus for saturated soils. Instead of controlling suction, high-suction tensiometers are adopted to monitor matric suction variations during constant water content triaxial testing. Also, a photogrammetry-based method is used to measure volume changes of unsaturated soil specimens during triaxial testing. To evaluate the capabilities of the proposed testing system, a series of constant water content triaxial tests were performed on unsaturated soils with different moisture contents. Both matric suction and volume variations during testing were monitored by the high-suction tensiometers and the photogrammetry-based method, respectively. New methods were also proposed to analyze the test results. Analysis results indicated that the proposed system is efficient and can be potentially utilized for unsaturated soil characterization.

---

[1]Li, L. and Zhang, X. (2015) "A New Triaxial Testing System for Unsaturated Soil Characterization", ASTM Geotechnical Testing Journal, (accepted).

4.2 Introduction

Triaxial tests have been widely used to characterize both saturated and unsaturated soils. For a saturated soil, its volume change is equal to the change in the water volume and can be relatively easy to measure with a volume gauge. However, for an unsaturated soil, due to the presence of air in the voids, soil volume change is no longer equal to the water exchange. Thus, a conventional triaxial test apparatus designed to test saturated soils cannot be directly utilized for testing unsaturated soils. Bishop and Donald (1961) developed a suction-controlled double-wall cell triaxial test apparatus to characterize unsaturated soils as shown in Figure 4.1. A high air-entry disc was mounted to the pedestal of the triaxial cell to control the matric suction based upon axis-translation technique proposed by (Hilf 1956). An inner cell filling with mercury was added in the conventional triaxial cell that wasFigure 4. filled with water. As the two cells were connected, changes in the confining pressure do not result in any deformation of inner cell. The soil volume change was then deduced from the change of the mercury level in the inner cell. Since this development, the suction-controlled triaxial test has been extensively used to characterize unsaturated soils (Fredlund et al. 1978; Josa et al. 1987; Wheeler 1988; Sivakumar 1993; Romero et al. 1997; Rampino et al. 1999; Ng et al. 2002; Sun et al. 2004; Thu et al. 2006). In a suction-controlled triaxial test, soil suction is maintained constant which significantly simplifies the test result analyses. However, there are several limitations associated with the double-wall cell volume change measurement method such as the need for sophisticated system calibration, sensitivity of the measurements to temperature fluctuations, water absorption (water is commonly used as the confining fluid) of the inner acrylic cell wall. With careful calibration, a volume change measurement accuracy of 0.25% can be reached (GDS 2009). In addition, suction-controlled triaxial test is a consolidated-drained test. Due to the low permeability of

unsaturated soils, suction-controlled triaxial test is very laborious, time-consuming, and costly. As a result, this test cannot be justified for routine engineering projects. Usually, it took years to characterize the stress-strain behavior of one unsaturated soil (e.g. Sivakumar 1993; Sharma 1998; Hoyos 1998).

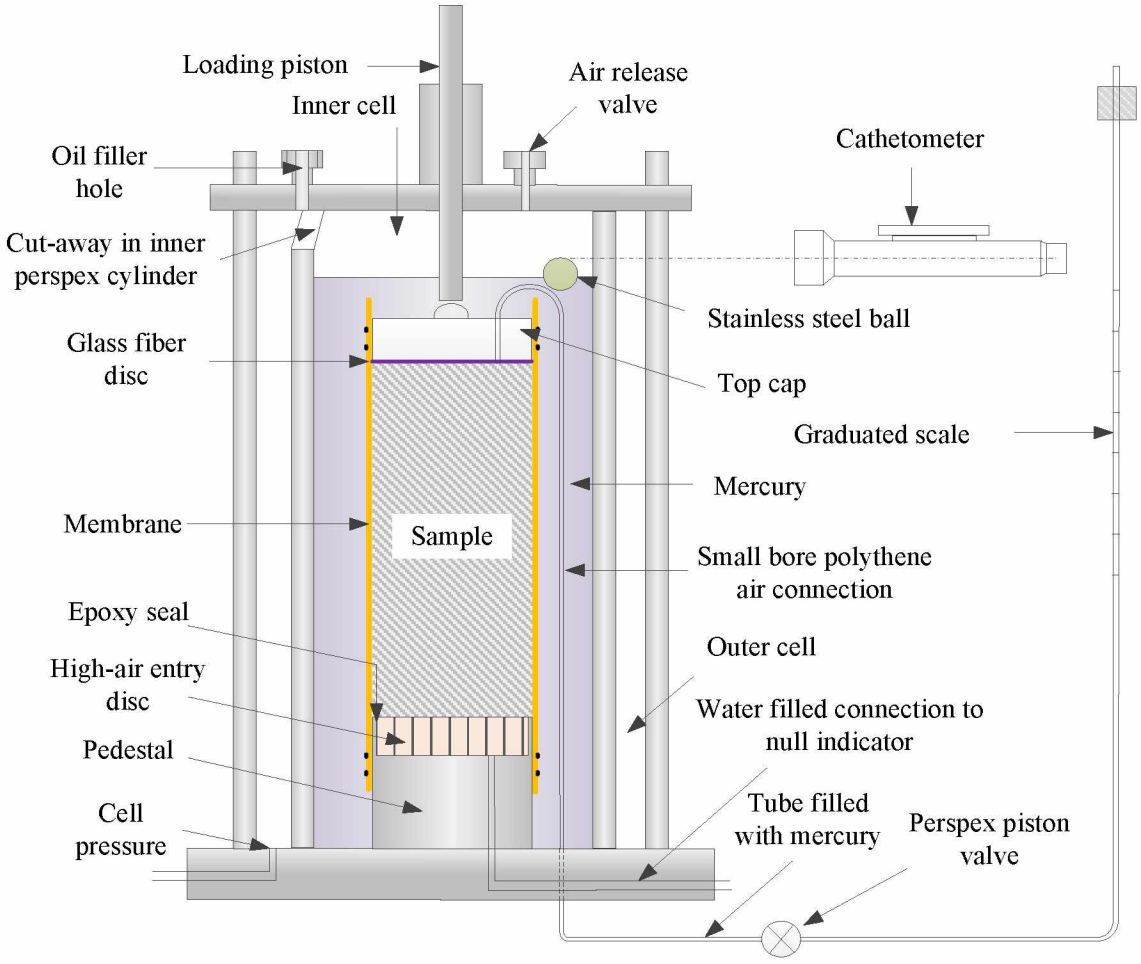

Figure 4.1 Schematic plot of the suction-controlled triaxial test apparatus for unsaturated soils (Modified from Bishop and Donald 1961).

Besides double-cell method, some other methods have been developed in the past few decades to measure unsaturated soil deformations during triaxial testing such as digital pressure volume controllers (Laudahn et al. 2005; Cabarkapa and Cuccovilo 2006); local displacement transducers (Hird et al. 1987; Clayton et al. 1989; Cuccovillo and Coop 1997), and laser scanners

(Romero et al. 1997). Previous literature reviews (Geiser et al. 2000; Sharma et al. 2006; Hoyos et al. 2009; Zhang et al. 2015) indicated that these methods have their limitations and are not extensively used.

With increasing availability of inexpensive digital cameras, image-based method is becoming more and more attractive. Several image-based methods were developed and reported to be used for soil volume change measurements during triaxial testing (Macari et al. 1997; Alshibli and Al-Hamdan 2001; Gachet et al. 2007). Macari et al. (1997) presented the use of digital image analysis technique for volumetric deformation measurements on cylindrical soil specimens during triaxial testing with help of a two-dimensional (2D) refraction correction model (Parker 1987). By detecting the edges of the specimen through the captured images, volume changes of the tested specimen were computed. Gachet et al. (2007) used a similar edge-detecting method to measure soil volume changes during triaxial testing. For the image-based methods used by Macari et al. (1997) and Gachet et al. (2007), careful system calibration is required before implementation. The refraction correction models presented in Macari et al. (1997) can only be used in an idealized system. Error due to the imperfection of the testing system was unknown. In Alshibli and Al-Hamdan (2001), part of the conventional cylindrical triaxial cell was modified to be flat to minimize the distortion due to refraction. Digital images were used to reconstruct the three-dimensional (3D) model of a soil specimen marked with grid note during triaxial testing at different axial strain levels. The cross-sections of the deformed specimen were determined using grid lines along the height of the specimen.

In terms of testing methods, consolidated undrained triaxial test is a standard test (ASTM D4767 2004) which has been widely used to investigate saturated soil behavior. However, few researchers used undrained tests to characterize unsaturated soils in the past for two reasons: (1)

reliable, rapid, and direct matric suction measurement on unsaturated soils was a challenging problem for geotechnical engineers, and (2) for unsaturated soils, the undrained test results are more complicated and there is no method available to analyze the data for constitutive modeling purposes.

A great effort has been dedicated to direct matric suction measurement on unsaturated soils using high-suction tensiometers in the past 20 years. Tensiometer has been used in the soil science to measure soil suction for a long time. However, conventional tensiometers can only be used to measure soil suction lower than 100 kPa, mainly due to water cavitation (Fredlund and Rahardjo 1993). The first attempt of direct suction measurement on an unsaturated soil with suction higher than 100 kPa was made by Ridley and Burland (1993) at the Imperial College using a high-suction tensiometer. Since then, many high-suction tensiometers (Guan and Fredlund 1997; Meilani et al. 2002; Tarantino and Mongiovi 2002; Take and Bolton 2003; Lourenco et al. 2006; Li and Zhang 2014) have been developed and successfully used in both laboratory and field experiments. A literature review on existing high-suction tensiometers and their applications can be found in Toll et al. (2013). With the recent development of high-suction tensiometers, direct and reliable suction measurements became possible. Colmenares and Ridley (2002) added a high-suction tensiometer to the top loading cap of an unconfined compression test system and successfully recorded the matric suction variation of an unsaturated soil during loading. Volume changes of soil specimens during the tests were not reported. In Thu et al. (2006), a series of constant water content triaxial tests were conducted on both saturated and unsaturated soil specimens in which soil suction and volume variations were measured using high-suction tensiometers and the double-wall cell method, respectively. However, as addressed before, there are several limitations with the double-wall cell method for volume change

measurement. In addition, constant water content test results were not analyzed due to lack of a proper method.

4.3 A New Triaxial Testing System for Unsaturated Soil Characterization

This paper proposes a new triaxial testing system for unsaturated soils based upon the conventional triaxial test apparatus for saturated soils. As shown in Figure 4.2a, a major modification to the conventional triaxial test apparatus is to post some measurement targets on the acrylic cell, load frame, and surface of the membrane (with soil specimen inside). These targets are high contrast dots with special design which can be identified automatically by software. Figure 4.2b shows the schematic plot of the proposed system. A non-contact photogrammetry-based method developed by Zhang et al. (2015) is used to accurately reconstruct the 3D models of unsaturated soil specimens from images taken during triaxial testing and calculate the soil volume change. Another major modification is that, instead of controlling suction, high-suction tensiometers developed by Li and Zhang (2014) are adopted to monitor matric suction variations during constant water content triaxial tests. Methods are also developed to analyze the constant water content test results for constitutive modeling purposes.

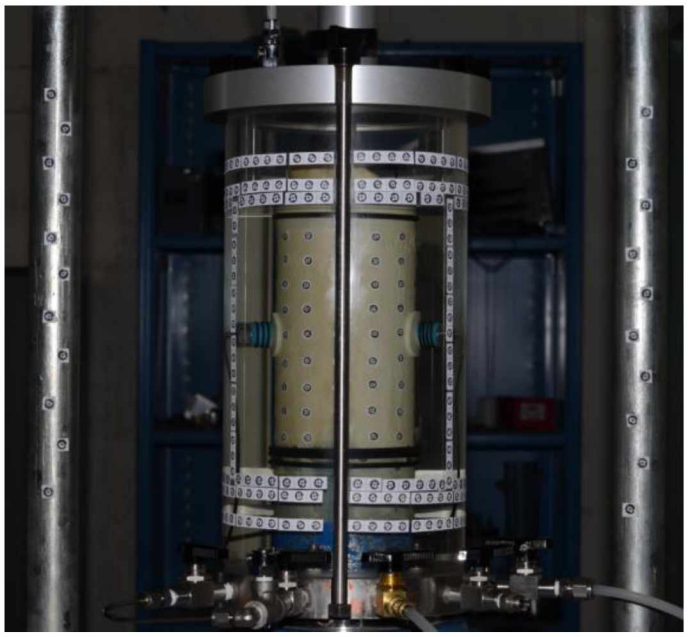

(a)

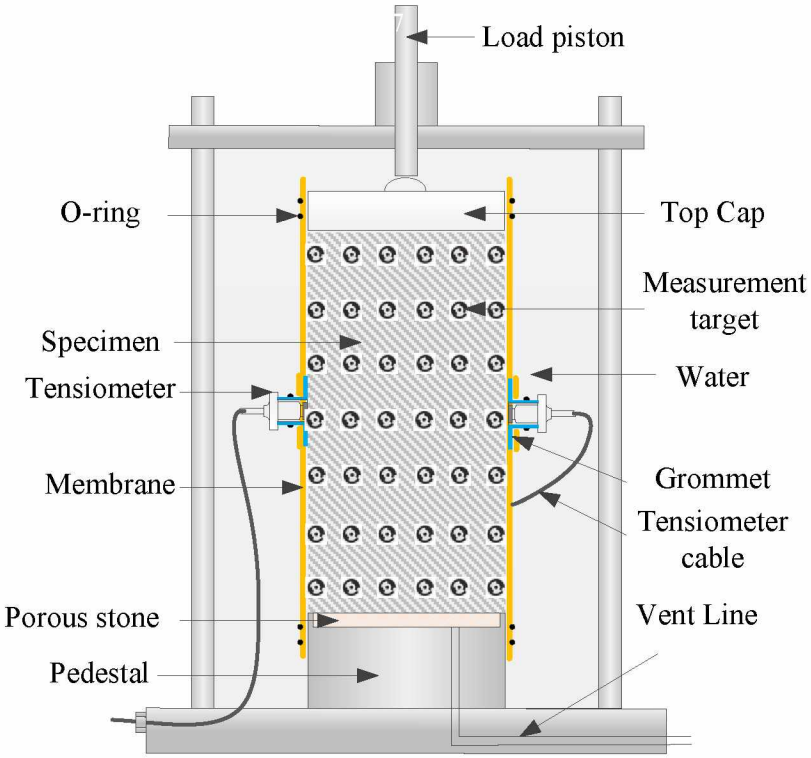
Load piston
O-ring
Top Cap
Measurement target
Specimen
Water
Tensiometer
Membrane
Grommet
Tensiometer cable
Porous stone
Vent Line
Pedestal

(b)

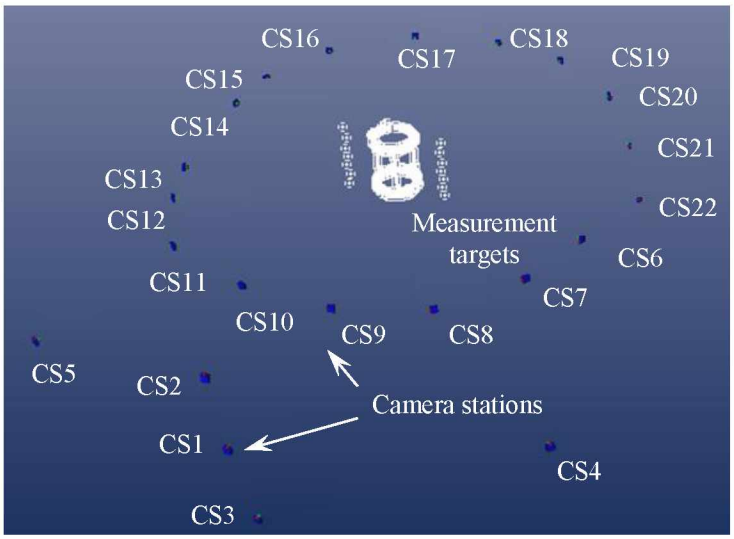

(c)

Figure 4.2 The proposed triaxial testing system: (a) Picture of the Proposed Triaxial Testing System; (b) Schematic plot; (c) Back-calculated camera positions.

The following sections first introduce the principle of the photogrammetry-based method and use of high-suction tensiometers to measure suction changes of unsaturated soil specimens. To evaluate the capabilities of the proposed testing system, a series of constant water content triaxial tests were performed on unsaturated soil specimens with different moisture contents. Both matric suction and volume variations during testing were monitored by the high-suction tensiometers and the photogrammetry-based method, respectively. In addition, examples are given to demonstrate how the test results are used for shear strength characterization and constitutive modeling purposes.

4.3.1 Volume Measurement Using the Photogrammetry-Based Method

For measuring volume changes of unsaturated soils during triaxial testing, most existing imaged-based methods suffer two limitations. First, the relative position of the camera to the triaxial testing system is essential to the reconstruction of 3D models from 2D images. In reality,

it is difficult to accurately control the location and orientation of the camera. Second, effect of refraction is difficult to take into account. Snell's law is a well-established theoretical equation. In order to apply the Snell's law, the shape and location of the acrylic cell relative to the camera position where an image is taken must be accurately determined. However, the acrylic cell often has creep deformations during triaxial testing. As a result, its shape and location may change even if the camera is at a fixed position as proposed in the image-based method (e.g. Macari et al. 1997).

Zhang et al. (2015) proposed a photogrammetry-based method to overcome the limitations in the existing image-based methods. The principle of the proposed method is shown in Figures 4.2 and 4.3. Images are captured around the triaxial system as shown in Figure 4.2a with overlaps using a digital camera. Using the measurement targets posted on the load frame and the surface of triaxial cell (or all points in the air), the orientation of each camera station where the image is taken (for example, the 3D coordinates of the perspective center S_1 and three angles for camera orientation in Figure 4.3) is back-calculated based on principle of photogrammetry as shown in Figure 4.2c. With known camera orientations and the corresponding images, the 3D coordinates of any measurement target on cell wall can be determined. Subsequently, the shape and orientation of the outer surface of the triaxial chamber are also accurately determined from 3D coordinates of measurement targets on cell wall. During this process, the measurement targets on the specimen surface were not used since refraction can cause bending of light ray and the principle of photogrammetry cannot be applied any more.

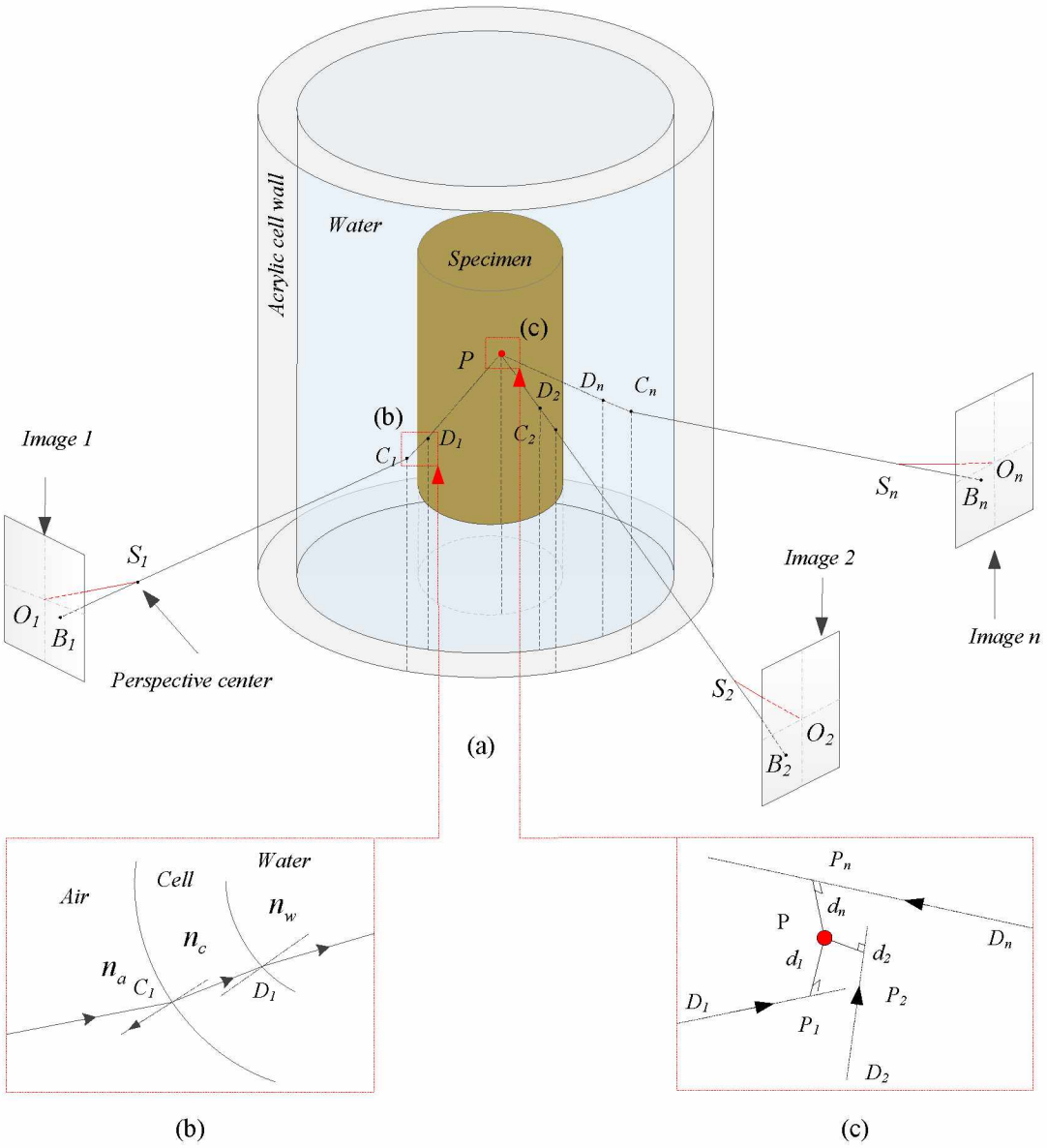

Figure 4.3 Principle of the photogrammetry-based method.

In order to reconstruct the 3D model of the unsaturated soil specimen in the triaxial cell and subsequently calculate the soil volume change, a multiple ray-tracing process is needed. Figure 4.3 schematically shows the multiple ray-tracing processes to reconstruct the 3D coordinates of a point P on the unsaturated soil specimen. In Figure 4.3, S_1, S_2, and S_n are camera positions (perspective center of the camera lens) where images 1, 2 and n are taken. B_1, B_2, and B_n are the

image points of point P on the corresponding images. O_1S_1, O_2S_2, and O_nS_n represent the shooting directions of camera station, while their magnitudes are focal length of the lens. Take image 1 as an example, since its orientation is known from the photogrammetric analysis (Figure 4.2c), the 3D coordinates of any point on the image such as point B_1 can be calculated using its position on image 1. Consequently, the light ray B_1S_1 can be determined from their 3D coordinates. Since the shape and position of the triaxial cell are also known from the photogrammetric analysis in the previous step, the intercept point between the light ray B_1S_1 and the outer surface of the triaxial cell can be calculated, which is C_1 in Figure 4.3a. With known refractive indices of air (n_a) and cell wall (n_c), shape and location of the traixial cell outer surface, direction of the incident ray B_1S_1, and the intercept point C_1 on the outer cell surface, the Snell's law can be applied to find the direction of the refractive ray C_1D_1 as shown in Figure 4.3b. Since the wall thickness of the triaxial cell is small, the inner surface of the triaxial cell wall can also be determined by assuming a uniform triaxial cell wall thickness. Subsequently, the intercept point between the light ray C_1D_1 and the inner surface of the triaxial cell can be calculated, which is D_1 in Figure 4.3b. With known refractive indices of water (n_w) and cell wall (n_c), shape and location of the triaxial cell inner surface, direction of the incident ray C_1D_1, and the intercept point D_1 on the inner cell surface, the Snell's law can be applied a second time to find the direction of the refractive ray D_1P as shown in Figure 4.3a.

Similar ray-tracing processes can be applied to images points B_2 and B_n for the same object point P on the specimen surface in images 2 and n, respectively. If there is no error, all the tracing lines D_1P, D_2P, and D_nP will converge to the same point P as shown in Figure 4.3a. However, errors unavoidably exist in the measurement and computational process and it is very likely for tracing rays not to intersect in the 3D space as D_1P_1, D_2P_2, and D_nP_n shown in Figure

4.3c. Zhang et al. (2015) proposed a least-square optimization technique to overcome this limitation. It is considered that although the tracing rays D_1P_1, D_2P_2, and D_nP_n might not intersect with each other, each tracing line represents an estimate of the light source of the object point P. As a result, the "true" location of point P should be close to those tracing rays and has the shortest distances to those tracing rays. It is therefore postulated that if the sum of square of a point's distances to all the re-tracing rays is the minimal, the point is the light source where all the rays are generated. In this way, the 3D coordinates of point P can be determined.

The above sections discuss how to obtain the 3D coordinates of a single point P on the specimen surface. The same approach is applied to numerous points on the surface of the specimen as shown in Figure 4.2a and a 3D model of the specimen can then be constructed. With the 3D model of the soil specimen, the total volume changes for the whole soil specimen can be calculated. More detailed information regarding the photogrammetry-based method can be found in Zhang et al. (2015).

Several tests were also performed to validate the photogrammetry-based method in Zhang et al. (2015). The average point and volume change measurement accuracies were determined to be 0.07 mm and 0.1% on a stainless steel cylinder and a saturated sand specimen, respectively. Zhang et al. (2015) focuses on presenting the mathematical derivation and validating the accuracy of the photogrammetry-based method using rigid steel cylinder and a saturated sand. No effort was made to measure volume change for unsaturated soil specimens. In this study, the newly developed photogrammetry-based method is used for the first time to measure volume changes of unsaturated soils during triaxial testing.

4.3.2 High-Suction Tensiometers

Adoption of axis-translation technique to a triaxial testing system to control suction is relatively simple and straightforward. However, as discussed previously, suction-controlled tests are extremely time-consuming. In order to overcome this limitation, it is suggested to use constant water content tests with suction measurements as an alternative to the suction-controlled tests to characterize unsaturated soils. Theoretically speaking, constant water content tests with suction measurements for unsaturated soils are more or less corresponding to the consolidated-undrained tests with pore water pressure measurements for saturated soils for constitutive modeling purposes. The major differences between them are: (1) it is more difficult to measure the suction (negative pore water pressure) higher than 100 kPa and (2) the test results are difficult to analyze since Terzaghi's effective stress principle does not hold true for unsaturated soils anymore.

Two high-suction tensiometers developed at the University of Alaska Fairbanks (Li and Zhang 2014) are used for suction measurements in this study. Each high-suction tensiometer includes three parts: an EPXO miniature pressure transducer, a 15 bar air-entry porous ceramic disk (10 mm in diameter and 2 mm in thickness), and a water reservoir with a clearance between transducer and ceramic disk of 0.2 mm as schematically shown in Figure 4.4a. Detailed fabrication process is presented in Li and Zhang (2014). Figure 4.4b shows a picture of the high-suction tensiometer used in this study.

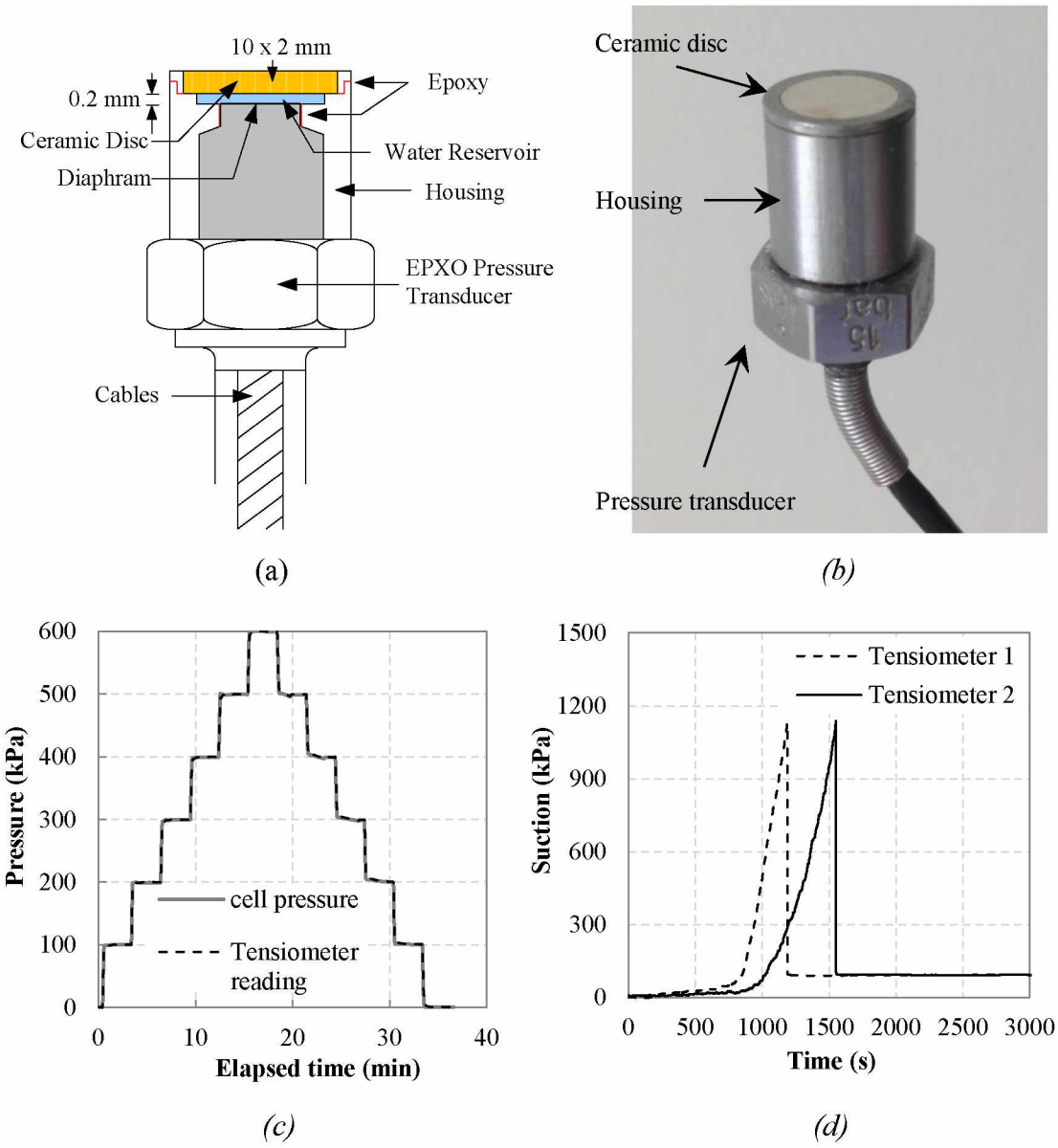

Figure 4.4 High-suction tensiometer for matric suction measurement: (a) schematic plot (not to scale), (b) picture of high-suction tensiometer, (c) response time, and (d) Free evaporation test results.

The tensiometers used in this study were saturated in a triaxial chamber. A water pressure of 600 kPa was repeatedly applied to saturate the high suction tensiometer. After that, high-suction tensiometers were calibrated in a positive pressure range. Negative pressure range

calibration was based on extrapolation, which was also used by Lourenco et al. (2008). The accuracy of the calibration could be examined by the water pressure immediately after cavitation, which should be approximately -100 kPa. After calibration, to evaluate tensiometer response time under a pressure change, a loading-unloading process was performed for the saturated tensiometers in the triaxial cell filled with water. The scanning interval for the used data logger was set to be 2 seconds during data acquisition. Figure 4.4c shows the responses of the high suction tensiometer. It can be seen that the pressure measured by the high-suction tensiometer was consistent with cell pressure variation with no delay which means tensiometer response was less than 2 seconds or nearly instantaneous. Free evaporation tests as suggested by Guan and Fredlund (1997) were also performed to evaluate the maximum attainable suction of the high suction tensiometers. Figure 4.4d shows the typical response of the fabricated high suction tensiometer during a free evaporation test. It was found that the maximum attainable suction of the used tensiometers was approximately 1100 kPa.

4.4 Validation of the New Triaxial Testing System

A series of constant water content (undrained) triaxial tests were performed on unsaturated soil specimens with different initial moisture contents.

4.4.1 Specimen Preparation

Locally available Fairbanks silt mixed with Kaolin at a ratio of 85:15 was used to fabricate the unsaturated soil specimens for the system validation. The optimal moisture content and maximum dry density are 15% and 1.836 g/cm^3, respectively. The plastic and liquid limits of the soil are 18.2% and 19.7%, respectively. The specific gravity of the soil is 2.7. Before compaction, oven-dried soil was mixed with water to a moisture content of 16%. In order to make sure the water is uniformly distributed, the mixed soil was stored in a sealed container for

two weeks. After that, the soil was taken out, thoroughly mixed again, and then compacted in 10 layers to 71 mm in diameter and 142 mm in height soil cylinders using the under-compaction procedure (Ladd 1978). The soil specimens were then conditioned to different moisture contents by controlling the number of exposures to atmosphere for about 15 minutes/day. Finally, the soil specimens were sealed in plastic bags and stored in a moisture room for at least one month to ensure suction equilibrium in the whole soil specimen. Column 2-4 in Table 4.1 summarizes the initial conditions of seventeen soil specimens used in this study. Note that the suctions for groups 1, 2, and 3 were measured under net confining pressures of 5, 50, and 50 kPa, respectively.

Table 4.1 Soil specimens used in the testing program.

Soil	Initial condition			At failure during shearing loading		
	W_c	e	s (kPa)	s_f(kPa)	σ_{1f}-u_a (kPa)	σ_{3f}-u_a (kPa)
Group 1	15.90%	0.656	28.1	36.8	96.7	5
	14.57%	0.656	57.3	64.4	128.4	5
	13.49%	0.653	171.1	128.6	197.9	5
	13.06%	0.655	241.5	165.3	249.5	5
	12.17%	0.653	387.4	257.0	290.8	5
	11.77%	0.648	501.8	323.2	336.4	5
Group 2	15.91%	0.657	73.2	-	-	200
	13.42%	0.655	145.7	-	-	200
	12.93%	0.653	254.0	121.9	749.4	200
	11.99%	0.651	374.9	172.7	787.7	200
	11.85%	0.648	418.3	197.8	831.7	200
Group 3	15.57%	0.659	34.1	-	-	600
	14.23%	0.656	76.8	-	-	600
	13.62%	0.654	130.4	-	-	600
	12.58%	0.651	265.9	-	-	600
	12.05%	0.650	364.7	-	-	600
	11.84%	0.649	430.4	-	-	600

4.4.2 Equipment

The conventional ELE triaxial test apparatus for saturated soils as shown in Figure 4.2a is used to validate the proposed triaxial testing system for unsaturated soils. The confining acrylic chamber used in this group of tests is 304 mm in height, 165 mm in outer diameter, and 9.6 mm in thickness with a refractive index of 1.491. A total number of 324 measurement targets were posted on the outside surface of the acrylic chamber, including six circles (45 targets/circle) and 3 vertical stripes (18 targets/strip). In addition, a total number of 108 measurement targets were posted on the load frame to facilitate the establishment of global coordinate system for the photogrammetry-based analyses.

A commercially available digital single-lens reflex camera (Nikon D7000) with a 50 mm fixed focal length lens (AF-S Nikkor 50 mm f/1.4G) is used to take the images needed for the validation tests. The image sensor of the camera has a resolution of 16.2 million pixels (4928H: 3264V). Photogrammetry assumes the camera lens is a pinhole. A commercial camera often uses multiple lenses to focus light and its aperture is not a point. Instead of rendering straight lines for light rays, these lenses often slightly bend them either outwards or inwards. Consequently, an image taken for squares with a commercial camera subjects to either barrel or pincushion distortions. In addition, principal distance, principal point, and format size of the image sensor varies even for the same type of camera. The focal length of the lens is also likely to be different from the specifications in the user's manual. Thus, a camera must be calibrated before being used for extraction of precise and reliable 3D metric information from images. The calibration is done by taking 12 images of a calibration sheet. The intrinsic (focal length, principal point, distortion parameters) and extrinsic (translation vector and rotation matrix) parameters are then calculated by analyzing the 12 images. The well-known self-calibrating bundle adjustment

approach is used to perform the needed calibration (Triggs et al. 2000). Table 4.2 shows the calibration results for the camera used in this study.

Table 4.2 Camera calibration results.

Parameter	Before Idealization	After Idealization
f (mm)	53.3964	53.3864
M (pixel)	4928	4928
N (pixel)	3264	3264
F_x (mm)	23.9966	24.6565
F_y (mm)	15.8961	16.3293
P_x (mm)	12.0691	12.3283
P_y (mm)	8.0741	8.1646
K_1 (10^{-5})	5.495	0
K_2 (10^{-9})	-4.673	0
P_1 (10^{-6})	-3.492	0
P_2 (10^{-6})	1.501	0

4.4.3 System Assembly and Specimen Installation

In order to accommodate the tensiometers to the testing system, two horizontal holes with threads inside were made in the base of the conventional ELE triaxial test apparatus. The end of the each hole is tapered and connected to the inside of the cell with another inclined small channel as shown in Figure 4.5. The connection wire of the high suction tensiometers was then passed through the channel, a small O-ring, and the horizontal hole to the outside. A center-hollowed bolt as shown in Figure 4.5, with the connection wire of the high suction tensiometer inside, was then screwed into the horizontal hole to compress the O-ring so that no water can be leaked out during triaxial testing.

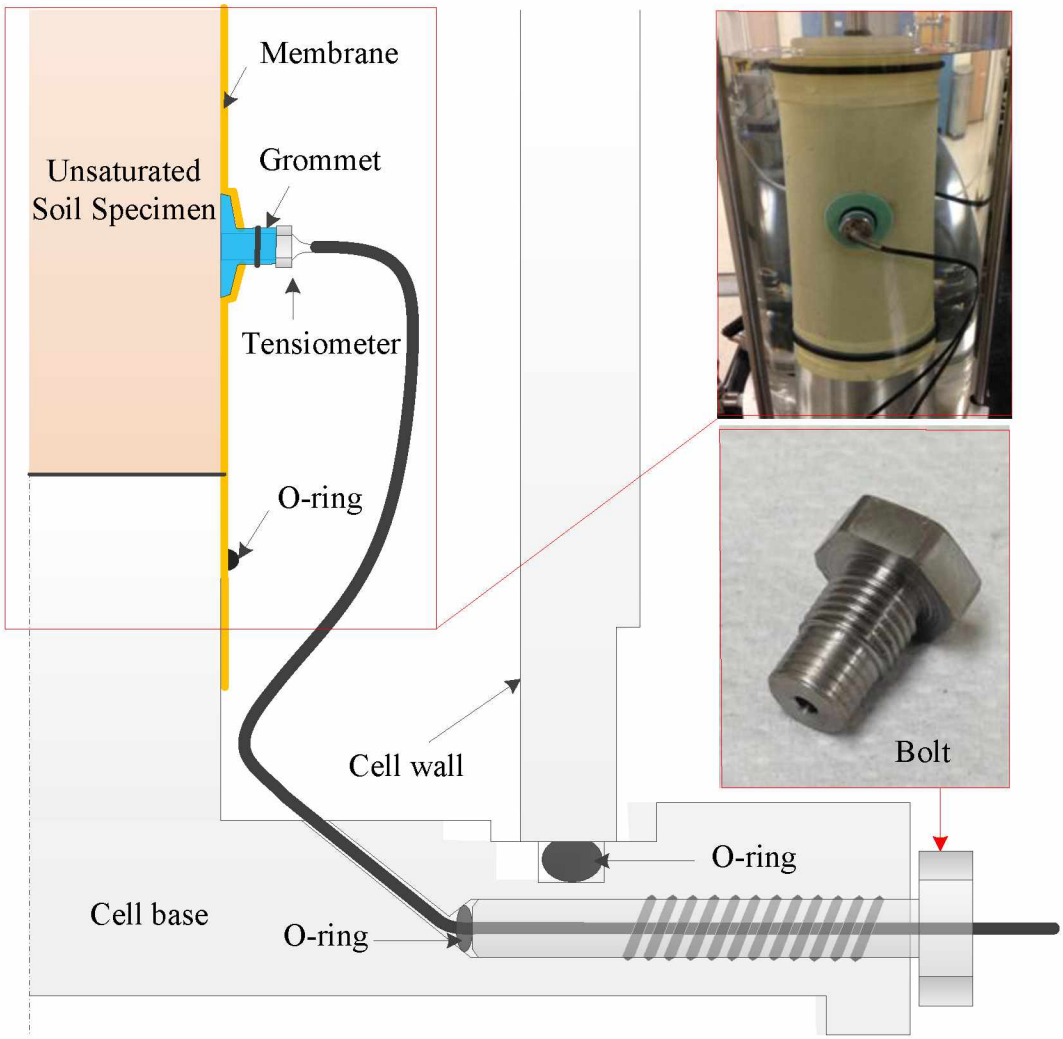

Figure 4.5 Assembly of the high-suction tensiometers to the proposed system (not to scale).

In this study, suction measurements were made at the middle instead of either bottom or top of the soil specimen to eliminate the possible ending effects as shown in Figure 4.2a. To ensure a good contact between the tensiometer and soil specimen and hold the tensiometer in place during testing, a grommet (shown in Figure 4.5) was fabricated using silicone rubber (detailed fabrication process for the grommet can be found in Li and Zhang 2014). Also, to prevent tensiometer cavitation during installation and ensure a good contact between the

specimen surface and the tensiometer, a thin layer of saturated kaolin was smeared on the surface of the ceramic disk (e.g. Colmenares and Ridley 2002; Thu et al. 2006; Le et al. 2011).

Installation of the high suction tensiometers is similar to that of the GDS mid-plane pore pressure transducer. First, the conditioned specimen is installed according the normal procedures of triaxial testing for saturated soils. The only difference was that there were two pre-cut small holes on the sample membranes for tensiometer installations. Subsequently, membrane at the pre-cut hole was carefully stretched to let the tensiometers with grommet to pass through. After the tensiometer was put on the soil specimen surface, the membrane was released to hold the tensiometer in place. Vacuum grease was pre-smeared on the back of the grommet to prevent possible leakage from the holes. A small vacuum (-5 kPa) pressure was then applied to the inside of the soil specimen to ensure good contacts between tensiometers and specimen surface. A more detailed installation process for the high-suction tensiometer can be found at: https://www.youtube.com/watch?v=g9-fqSMbIBU.

After this, a total number of 108 measurement targets (9 rows by 12 columns) were posted to the membrane surface as shown in Figure 4.2a. The measurement targets should cover the entire soil specimen for accurate volume change measurement. The acrylic cell with measurement targets on the outer surface was installed. After the whole system was filled with water, the vacuum pressure was released. Instead, a small net confining pressure (5 kPa) was applied to the soil specimen to ensure the contacts between tensiometers and specimen surface and the system is ready for soil testing.

4.4.4 Experimental Design

Three groups of constant water content tests were performed to validate the proposed triaxial testing system as shown in Table 4.1. The constant water content tests were performed

under drained conditions for the pore-air phase and undrained conditions for the pore-water phase.

Group 1 involves shearing the soil under a constant confining pressure of 5 kPa till failure is reached. Group 2 involves first isotopically loading the soil to 200 kPa and then shearing the soil to failure under constant confining pressure of 200 kPa or stop at a maximum axial displacement of 20 mm, whichever reaches first. Group 3 involves first isotopically loading the soil to 600 kPa and the shear the soil to a maximum axial displacement of 20 mm. Some tests also included unloading-reloading processes in isotropic and shearing stages. In the isotropic loading stage for groups 2 and 3, the all-around pressure was applied with an interval of 50 kPa. In the triaxial shearing stage, the soils were sheared at a loading rate of 1 mm/min. After an increase of 50 kPa in the isotropic loading stage or every 2 or 3 mm of axial displacement in the shearing stage, load was pause and maintained constant. The pore-water pressure, uw, changed with the volume change of the soil specimen caused by the loading and this pore-water pressure was measured using high suction tensiometers. Tensiometers readings generally reached equilibrium in approximately 20 minutes which is consistent with the findings in Oliveira and Marinho (2008). The suctions at equilibrium were used as the representative suction for the corresponding loading conditions. Then, the images are captured for the photogrammetry-based analyses. Photographs can be taken at any orientation (position and direction) to obtain best quality and accuracy. The following strategy was followed to achieve better measurement accuracy as suggested in Zhang et al. (2015): (1) taking at least five photographs from different orientations for each area/point of interest, (2) ensuring sufficient overlap between adjacent pictures, and (3) capturing photographs from different view angles. For each loading step mentioned above, about 22 pictures were captured, which took 2-3 minutes. It usually took 5-7

hours to complete each constant water content triaxial test. After each test, the soil specimen was taken out to measure the total weight and moisture content for further analysis.

4.5 Test Results and Data Analysis

4.5.1 Volume Change

The images taken at different loading levels were used to determine the 3D coordinates of 108 measurement targets (9 rows by 12 columns) pasted on the membrane surface as shown in Figure 4.2a using the photogrammetry-based method as described in the previous sections. By connecting each point with the adjacent points, triangular meshes were generated which reflect the soil shapes at different loading levels. Using soils at water contents of 15.90% (test 1 in group 1) and 15.91% (test 4 in group 2) as examples, Figures 4.6a and 4.6b show the deformations of two specimens during shearing under 5 and 200 kPa net confining pressures and different axial displacements, respectively. As can be seen in Figure 4.6a, when shearing to 3 mm of axial displacement under a net confining pressure of 5 kPa, the specimen remained approximately cylindrical. With an increase in the axial displacement, a shear band gradually formed in the soil specimen and finally the soil specimen failed due to the applied deviatoric load. Figure 4.6a also shows the picture of the soils specimen after failure with a clear shear band.

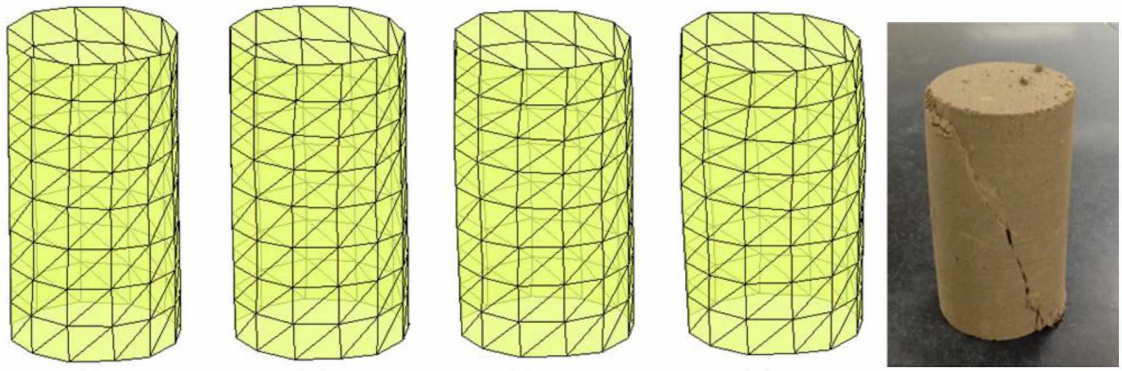

(1) 0 mm (2) 3 mm (3) 6.5 mm (4) 10 mm

(a)

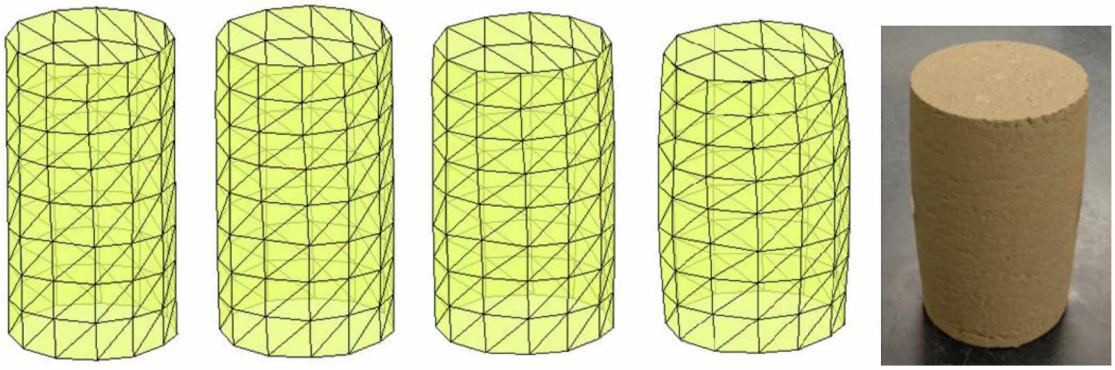

(1) 0 mm (2) 6.5 mm (3) 12 mm (4) 20 mm

(b)

Figure 4.6 Specimen deformations during shearing under different axial displacement: (a) group 1, net confining pressure of 5 kPa, and (b) group 2, net confining pressure of 200 kPa.

By contrast, when the soil specimen with nearly the same moisture content was sheared under a net confining pressure of 200 kPa, with an increase in the axial displacement, the soil specimen gradually deformed into a barrel-shape with no obvious failure plane observed as shown in Figure 4.6b. The diameter of the specimen at the center was the largest and narrows towards the two ends. The shapes were reasonable since the friction between the soil and the loading platens restrained soil from deforming at both ends. The relative high confining pressure

prevented the shear band from occurring. The results were reasonable and consistent with previous studies (Gachet et al. 2007; Qiao et al. 2008; and Uchaipichat et al. 2011).

Volumes of the specimens at different loading steps were obtained based on the triangular meshes as shown in Figures 4.6a and 4.6b using the method proposed in Zhang et al. (2015). The specific volumes of the soil specimen were then calculated based upon the measured total weight, moisture content, and specific gravity of the soil. Figures 4.7a and 4.7b show the specific volumes of soils in group 2 and 3 during isotropic loadings. Generally the specific volumes of soils decreased with an increase in the all-around pressure. A general trend can be found in both Figures 4.7a and 4.7b is that the higher the moisture content, the larger the initial specific volume. This is reasonable since suction has a confining effect on the soil and decreases in the moisture content can cause soil shrinkage. It was noted that soil specimens with high water contents experienced the highest volumetric reduction with the same loading history. This is because the moisture lubricated the soil particles and leads to smaller modulus during the isotropic loading. Both Figures 4.7a and 4.7b indicate that all v-logp curves are relatively flat when the all-around pressure is less than 50 kPa and becomes steep for all-around pressure greater than 100 kPa. This is a clear indication of soil plastic deformation, which can also be seen in Figure 4.7b when there is an unloading process. Yield stresses for each test were determined using the Casagrande's methods for further analysis as presented in the later sections.

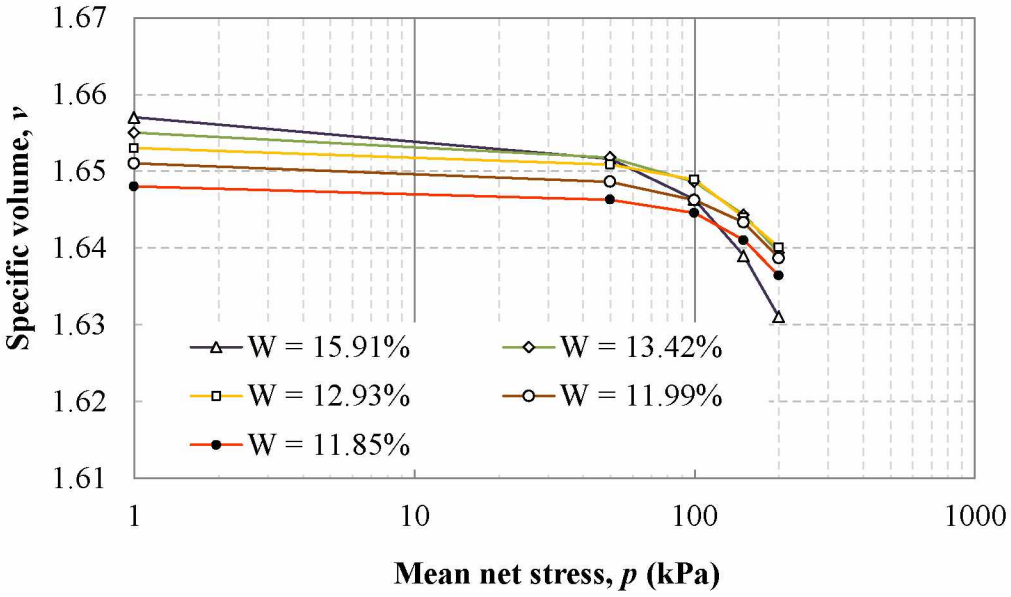

(a)

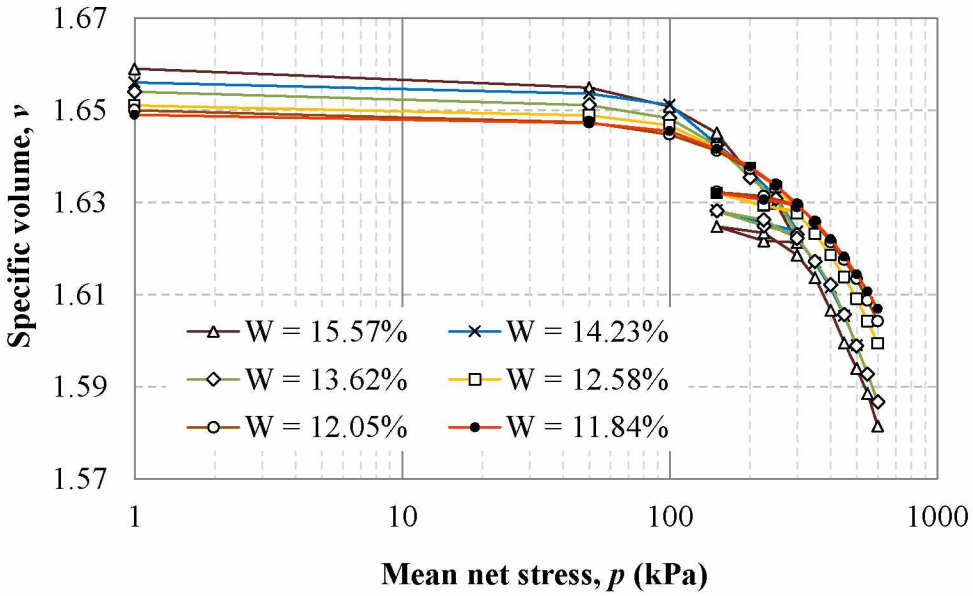

(b)

Figure 4.7 Soil volume changes during isotropic loading stage: (a) group 2, loaded to 200 kPa, and (b) group 3, loaded to 600 kPa.

Figures 4.8a and 4.8b show the specific volume changes of soils in groups 1 and 2 during shearing under net confining pressures of 5 and 200 kPa, respectively. When shearing under a net confining pressure of 5 kPa as shown in Figure 4.8a, all soils experienced volume decreases (shear compression) at the early stage (approximately 1% axial strain) and then volume increases (shear dilations) afterwards. By contrast, when soil specimens with similar moisture contents were sheared under a net confining pressure of 200 kPa as shown in Figure 4.8b, soil specimens with initial moisture contents higher than 13.42% experienced volume decreases only with increase in the axial strain or deviatoric stress, while soil specimens with initial moisture contents lower than 13.42% firstly experienced shear compression, followed by shear dilation.

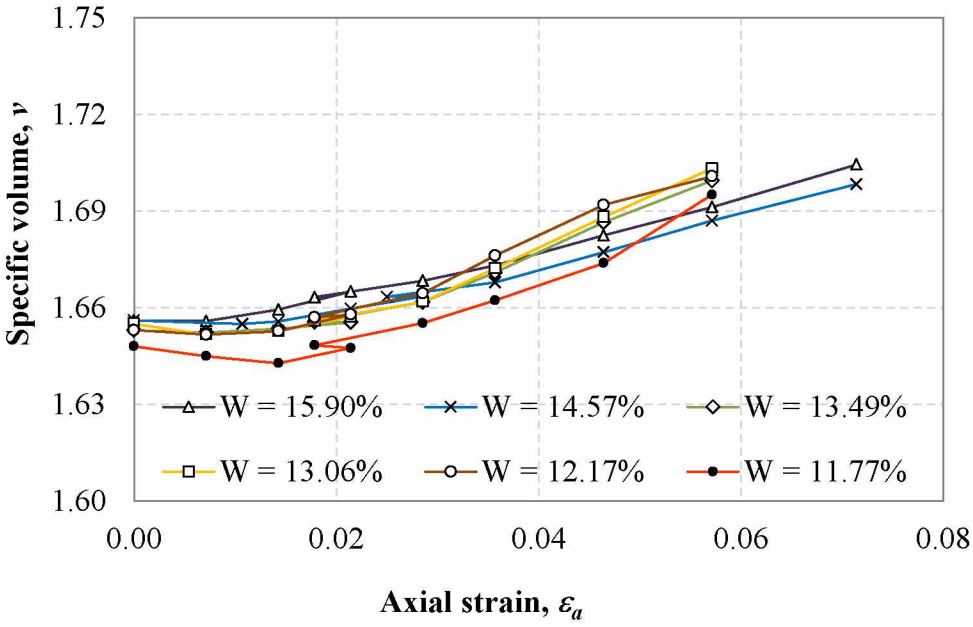

(a)

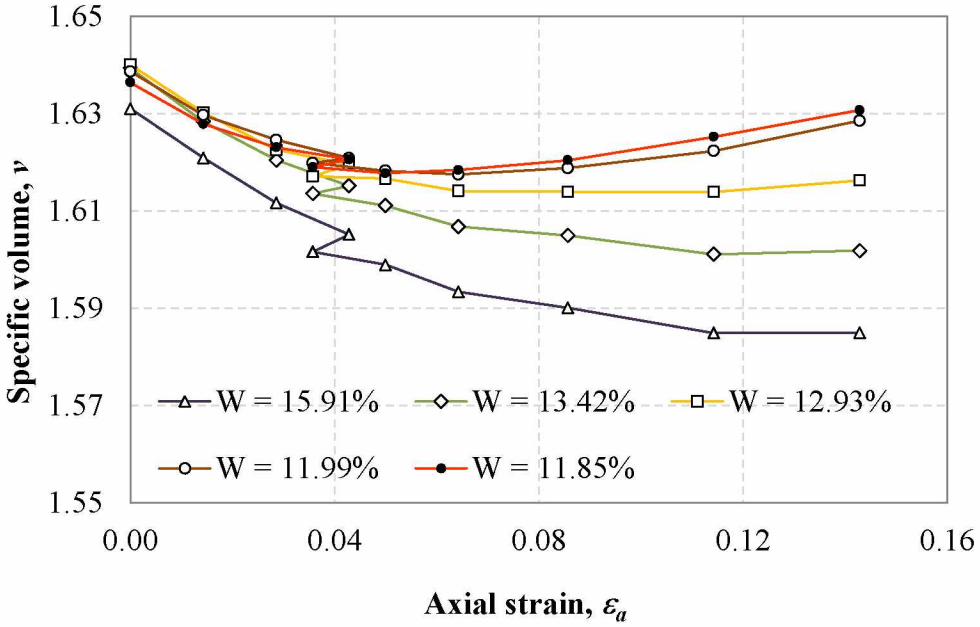

(b)

Figure 4.8 Soil volume changes during triaxial shearing stage : (a) group 1, sheared under a net confining pressure of 5 kPa, and (b) group 2, sheared under a net confining pressure of 200 kPa.

Figures 4.9a and 4.9b plotted the stress-strain curves for groups 1 and 2 sheared under net confining pressures of 5 and 200 kPa, respectively. As can be seen in Figure 4.9a, when the soils were sheared under a net confining pressure of 5 kPa, the deviatoric stresses initially increase with an increase in the axial displacement, reach a peak at an axial strain of approximately 3%, and then decrease with increases in the axial displacement. When the soils were sheared under a net confining pressure of 200 kPa as shown in Figure 4.9b, soil specimens with initial moisture contents lower than 13.42% shows similar trend, that is, deviatoric stresses initially increase with an increase in the axial displacement, and then slightly decrease with increases in the axial displacement. While for soil specimens with initial moisture contents higher than 13.42%, the deviatoric stresses always increase with an increase in the axial displacement. For all soil

specimens, it is noted that the shear strengths increased with a decrease of water content. This is reasonable since lower water content corresponds to higher suction, and suction adds a confinement to the soil specimen which leads to higher shear strength.

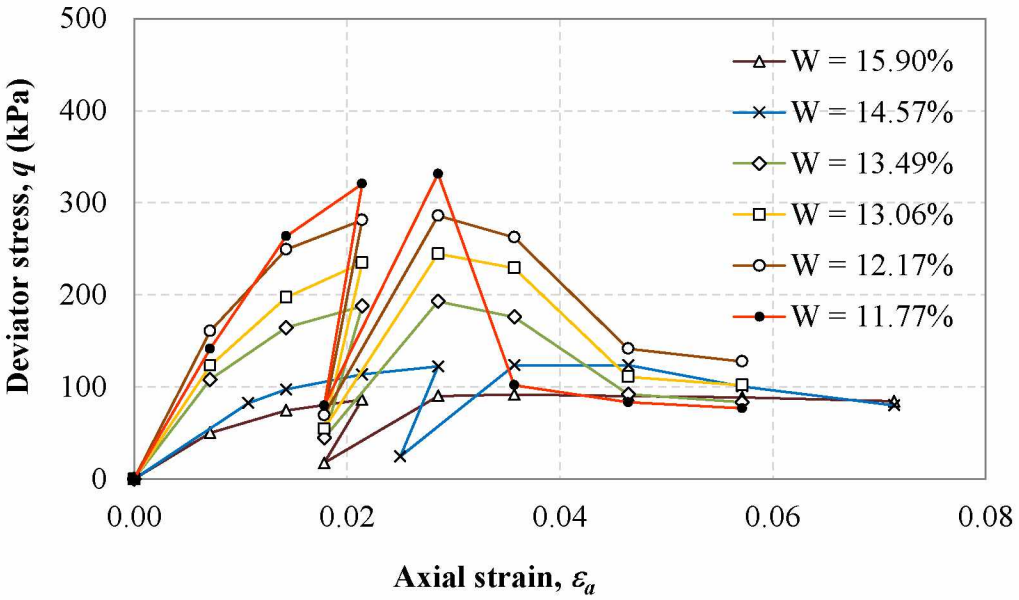

(a)

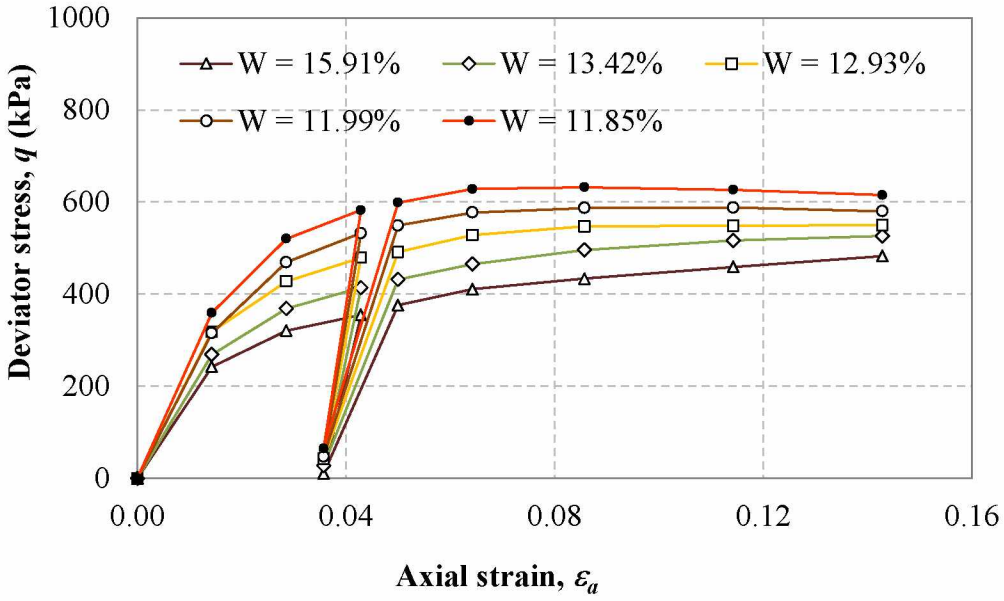

(b)

Figure 4.9 Stress-strain curves during triaxial shearing stage: (a) group 1, sheared under a net confining pressure of 5 kPa, and (b) group 2, sheared under a net confining pressure of 5 kPa.

4.5.2 Suction Variations with Time

Soil matric suction variations during constant water content triaxial testing were recorded using two high-suction tensiometers. Figure 4.10 presented a typical tensiometer response for an unsaturated soil specimen during isotropic and shear loading. The soil specimen had a water content of 11.99% and initial suction of 374.9 kPa at a confining pressure of 50 kPa. The applied confining pressure during triaxial shearing was 200 kPa. During isotropic loading, there was an immediate drop of suction associated with the increase of isotropic load, followed by a small increase in suction with time and finally reached equilibrium. These results are consistent with the test results in previous studies (Delage et al. 2008 and Le et al. 2011). By contrast, during triaxial shearing, there was typically an immediate drop in suction due to the applied deviator stress. Then, the soil suction continued decreasing slightly under constant loading, and finally

reached equilibrium with time gradually. Figure 4.10 also indicated that during unloading process, there was an immediate increase in soil suction. The soil suction then decreased with time and gradually reached equilibrium. It normally took about 5-20 minutes for the soil suction to reach equilibrium after either loading or unloading, depending upon the initial soil suction. The higher the soil suction, the more time is required for suction to reach equilibrium.

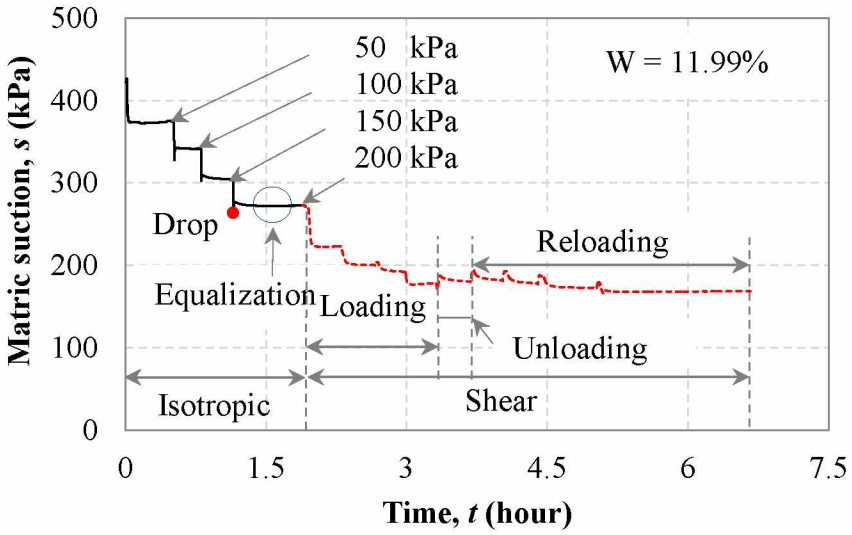

Figure 4.10 Tensiometer responses during constant water content test for a specimen in group 2.

4.5.3 Suction Variations with Loading

The suctions at equilibrium were used as the representative suctions for each load levels to plot the suction variations versus loading curves. Figures 4.11a and 4.11b show the suction variations of all soil specimens in groups 2 and 3 during isotropic loading, respectively. Generally, soil suction decreased with increasing isotropic load. Also, soils with low water contents had higher initial suction and experienced the larger reduction in suctions after the same loading history. When there is an unloading at the mean net stress of 300 kPa as shown in Figure 4.11b, there were irrecoverable suction changes, which are consistent with the irrecoverable volume changes as shown in Figure 4.7b. As shown in Figure 4.11b, the irrecoverable suction

changes decreases with increasing moisture contents. It becomes nearly invisible when the soil moisture content reaches 15.57%. It is also noted that for soils with nearly the same water content (e.g. soils with water contents of 11.85% and 11.84% in groups 2 and 3), it is noted that the measured suctions at the same isotropic load were slightly different (e.g. at 50 kPa, the measured suction were 418.3 kPa and 430.4 kPa for soils with water contents of 11.85% and 11.84%, respectively). This difference is attributed to the fact that the soil specimens might have slightly different stress histories, which will be discussed in a later section.

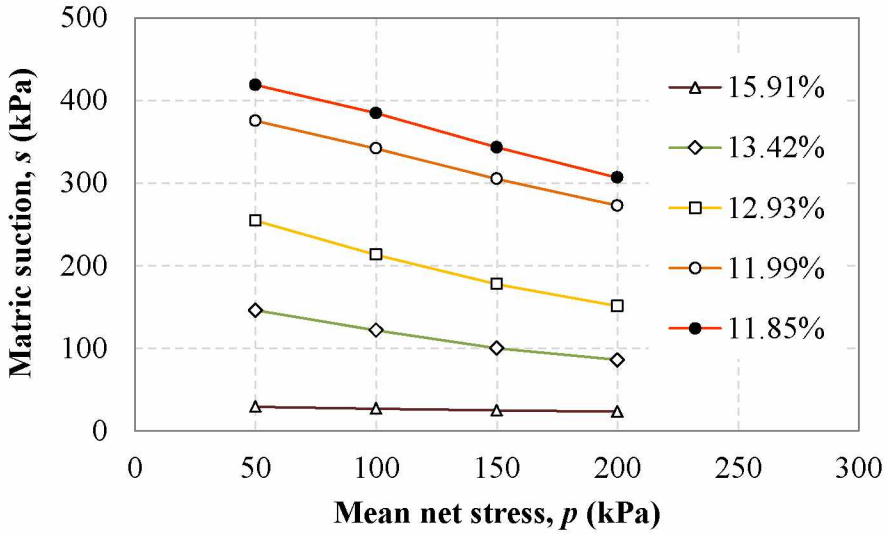

(a)

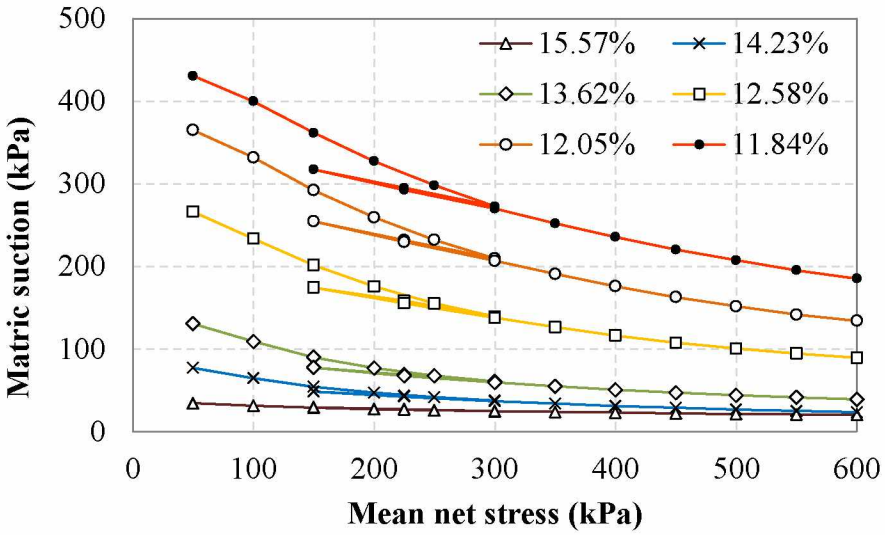

(a)

Figure 4.11 Suction variations during isotropic loading: (a) group 2, loaded to 200 kPa, and (b) group 3, loaded to 600 kPa.

Figures 4.12a and 4.12b show the suction variations of soils in groups 1 and 2 during triaxial shearing under net confining pressure of 5 and 200 kPa, respectively. The applied maximum axial strains for soils in group 1 were limited to 8% since soil normally failed before 8% strain is reached as shown in Figure 4.9a. Suction variation results, as shown in Figures 4.12a and 4.12b, indicated that matric suction variation due to applied deviatoric stress was dependent on the water content and the applied net confining pressure. At high water contents (greater than 13.42%), soil matric suctions sheared under different net confining pressures did not vary very much as shown in Figure 4.12a. For soil specimens with low water contents (less than 13.42%), soil suctions decreased throughout the tests or decreased at the early stage and then experienced a slight suction increase afterward as shown in Figure 4.12b.

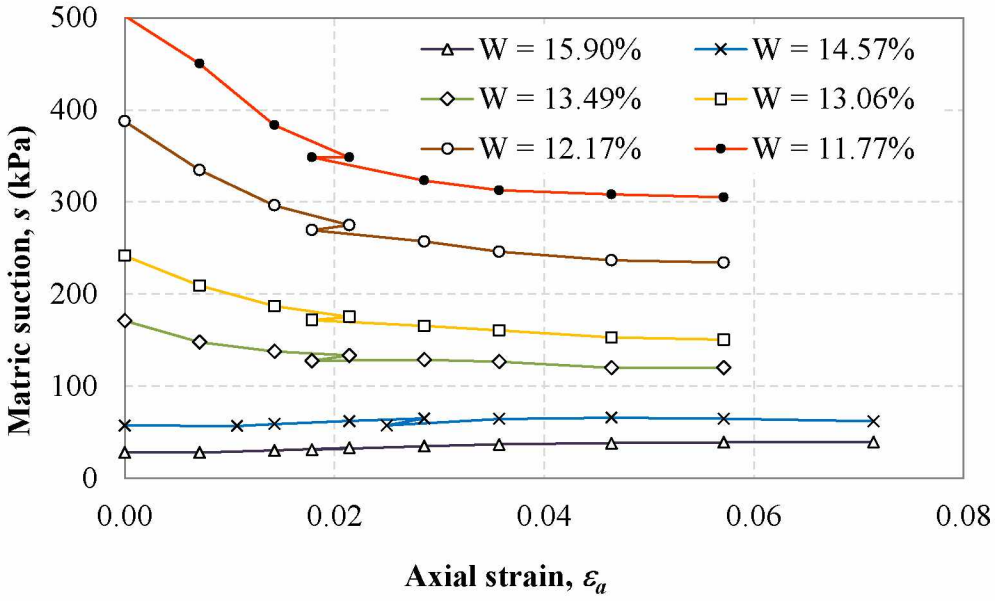

(a)

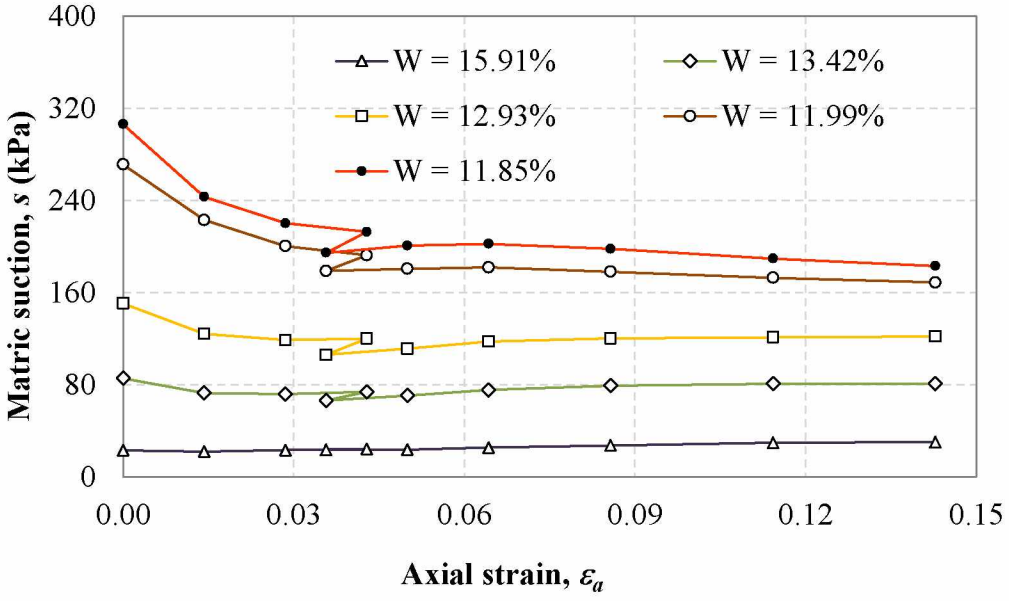

(b)

Figure 4.12 Suction variations during shearing: (a) group 1, sheared under a net confining pressure of 5 kPa, and (b) group 2, sheared under a net confining pressure of 200 kPa.

4.5.4 Shear Strength Characterization

One challenge associated with constant water content triaxial tests is how to analyze the test results. Many researchers have proposed shear strength models for unsaturated soils. Among these models, the equation proposed by Fredlund et al. (1978) is used extensively as follows:

$$\tau = c' + (\sigma - u_a)\tan\phi' + (u_a - u_w)\tan\phi^b \qquad \text{Equation 4.1}$$

where,

τ = shear stress on the failure plane,

c' = cohesion in saturated condition,

σ = normal stress on the failure surface,

u_a = pore air pressure in soil,

ϕ' = angle of friction in saturated condition,

u_w = pore water pressure in soil, and

ϕ^b = angle indicating the rate of change in shear strength relative to changes in matric suction.

Existing approaches for shear strength characterization of an unsaturated soil require use of suction-controlled triaxial tests to determine the parameters of c', ϕ', and ϕ^b in Equation 4.1 (e.g. Fredlund and Rahardjo 1993 and Thu et al. 2006). Both approaches cannot be used to analyze results from constant water content triaxial tests for the determination of c', ϕ', and ϕ^b.

This paper proposes a new method to characterize shear strength for unsaturated soils using the results from constant water content triaxial tests as follows. Figure 4.13 shows the evolution of the Mohr circle in constant water content triaxial shearing tests. A constant water content triaxial tests test is performed with a starting point of A, with an all-around (isotropic) pressure.

As the deviatoric stress increases, the diameters of the Mohr circles increase from A to B to C until D where the soil reaches failure as shown in Figure 4.13a. During this process, the suction in the soil decreases continuously to a level of s_1. The corresponding failure point on the Mohr-Coulumb failure plane is represented by F_1. Similar constant water content shearing tests with different confining pressures can be carried out to obtain Mohr circles at failure, such as the ones represented by failure points F_2 and F_3 in Figure 4.13a. These points can be used to define the failure envelope for unsaturated soils as long as they are known to be on the failure envelope. In other words, it is not necessary to perform suction controlled tests so that points F_1, F_2, and F_3 have the same suction level in order to determine the parameters in Equation 4.1. The difficulties associated with the constant water content test result analysis are two-fold: (1) all soil specimens fail at different suction levels, and (2) the stress components on the failure plane as needed by Equation 4.1 are unknown. A new method is proposed in this paper to characterize the shear strength of unsaturated soils using results from constant water content triaxial tests.

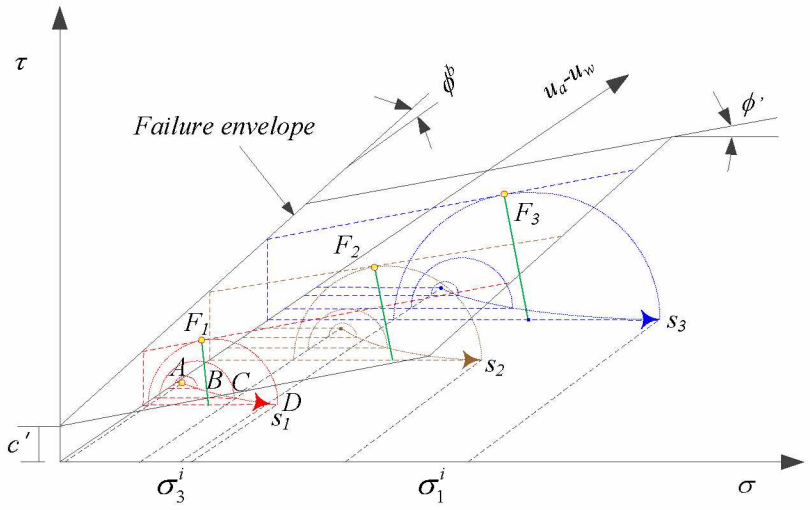

(a)

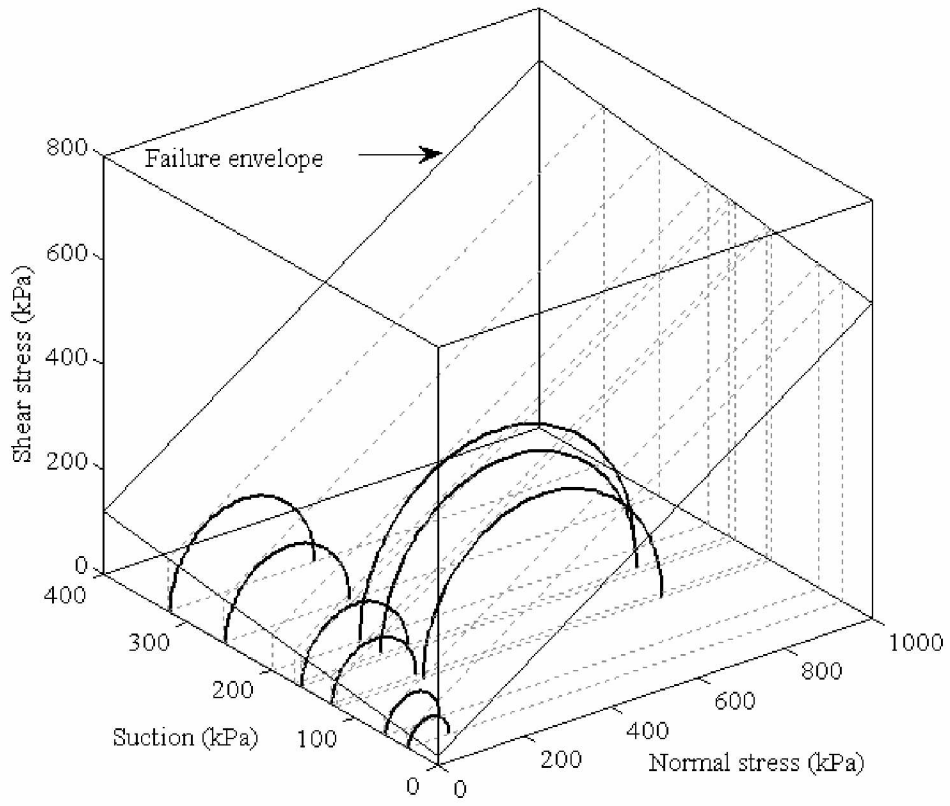

(b)

Figure 4.13 Shear strength determination: (a) evolution of Mohr-Coulomb circles during undrained shearing, and (b) Mohr-Coulomb circles at failure and the failure envelope.

By definition, the extended Mohr-Coulumb failure envelope as expressed by Equation 4.1 is a surface tangent to all Mohr circles at failure as shown in Figure 4.13a (Fredlund and Rahardjo 1993). In other words, the distances (d_i) between the centers of the all Mohr circles at failure to the failure points are the radii of the corresponding Mohr circles at failure, that is,

$$d_i - \left(\sigma_{1f}^i - \sigma_{3f}^i\right)/2 = 0 \qquad \text{Equation 4.2}$$

However, unsaturated soil behavior is highly nonlinear and there might be some experimental errors. Consequently, the extended Mohr-Coulomb failure envelope as expressed by Equation 4.1 might not be able to perfectly predict soils behavior. Error always exists as follows:

$$R = d_i - \left| \sigma_{1f}^i - \sigma_{3f}^i \right| / 2 \qquad \text{Equation 4.3}$$

Consequently, the determination of the shear strength parameters becomes an optimization problem as follows: to find a combination of the model parameters of c', ϕ', and ϕ^b, which can overall best predict all the experimental results. Specifically, it is to find a combination of the model parameters of c', ϕ', and ϕ^b to minimize the overall error between the theoretical $\left| \sigma_{1f}^i - \sigma_{3f}^i \right| / 2$ and the experimental results (d_i). When the least-square method is used the problem become as follows: to find a combination of c', ϕ', and ϕ^b to minimize the objective function F(X) as follows:

$$\begin{aligned} F(X) &= \sum_{i=1}^{n} \left(d_i - \left| \sigma_{1f}^i - \sigma_{3f}^i \right| / 2 \right)^2 \\ &= \sum_{i=1}^{n} \left\{ \frac{\left| c' + \left| \sigma_{1f}^i + \sigma_{3f}^i \right| / 2 - u_a \tan\phi' + s_{if} \tan\phi^b \right|}{\sqrt{\tan\phi'^2 + \tan\phi^{b\,2} + (-1)^2}} - \left| \sigma_{1f}^i - \sigma_{3f}^i \right| / 2 \right\}^2 \end{aligned} \qquad \text{Equation 4.4}$$

The stresses states for 9 soil specimens at failure (σ_{1f}-u_a, σ_{3f}-u_a, s_f) as shown in Table 4.2 columns 5-7 were used for the analysis as defined by Equation 4.4. The popular Broydon–Fletcher–Goldfarb–Shanno (BFGS) method (Rao 1996), which is a quasi-Newton method, was used to solve the optimization problem. It was found that best fit is reached when c', ϕ', and ϕ^b were 19.73 kPa, 30.24°, and 14.12°, respectively. The coefficient of determination (i.e. R^2) was 0.99 and the standard deviation was 3.6 kPa, which indicated a strong relationship between the independent variables (i.e. c', ϕ', and ϕ^b) and the dependent variable (i.e. σ_{1f}-u_a, σ_{3f}-u_a, s_f) by this regression equation. Figure – 4.10 shows the Mohr circles at failure and the Mohr-Coulomb failure envelope based upon the calibrated model parameters in the τ– (σ-u_a) – (u_a-u_w) space.

Inspection of Figure 4.13(b) indicates that all the predictions are very good over the entire experimental stress ranges.

4.5.5 Constitutive Modeling

Besides shear strength properties characterization, results of constant water content triaxial tests can potentially be utilized to characterize the constitutive behavior of unsaturated soils since the stress state (p-q-s) and volume of the tested soil were recorded during testing. As discussed previously, the results from the constant water content triaxial tests are much more complicated than those obtained from suction-controlled triaxial tests. Consequently, conventional methods developed for analyzing suction-controlled triaxial tests (e.g. Gallipoli at al. 2010) cannot be used for constant water content triaxial tests. Zhang and Lytton (2009a; 2009b; and 2011) developed a Modified State Surface Approach (MSSA) to explain the elasto-plastic behavior for unsaturated soils. The MSSA can be used to analyze the results from constant water content triaxial tests for constitutive modeling purpose. Due to the limited space, the exact model calibration process is not presented in this paper. Interested readers can find detailed discussions in Zhang (2010) and Zhang and Xiao (2013).

Typical examples of using the constant water content triaxial test results to calibrate the parameters in the Barcelona Basic Model (BBM) (Alonso et al. 1990) can be found in Zhang et al. (2012). In this study, based on test results from group 3, the parameters in the BBM are calibrated and shown in Table 4.3. Figure 4.14a shows the comparisons in the e-p-s space between the experimental and predicted test results based upon the model parameters in Table 4.3. Examination of Figure 4.14a indicates that the predicted results match the experimental test results very well. Figure 4.14b shows the predicted loading-collapse yield curves for the tested soils. The dotted lines are the stress paths for the constant water content triaxial tests as shown in

Figure 4.11b. Solid points represent the yield stresses for each soil specimens. Examination of Figure 4.14b indicates that those yield points belong to different yield curves, representing that those soil specimens have slightly different stress histories. These yield curves are typical for compacted silty soils (e.g. Wheeler and Sivakumar 1995), indicating the proposed testing system reasonably characterized the unsaturated soils in this study. It is worth noting that the BBM is the first one and one of the most frequently used constitutive model for unsaturated soils (Gallipoli at al. 2010). Normally, the model parameter values κ, κ_s, β, $\lambda(0)$, r, p^c, and N(0) are calibrated using suction-controlled tests which require expensive laboratory equipment and are time-consuming (each test lasts 2-3 months). By using the results form constant water content triaxial tests, the time and efforts needed to calibrate the same model parameters are significantly reduced (5-7 hours/test). In addition, the proposed triaxial testing system is much simpler than the suction-controlled triaxial testing system.

Table 4.3 Calibrated model parameters for the BBM.

Parameter	Unit	Best Fit
κ		0.0076
κ_s		0.0115
$N(0)$	—	0.666
$\lambda(0)$	—	0.053
r	—	0.376
β	MPa^{-1}	7.990
p^c	MPa	0.120

κ = slope of the unloading-reloading line associated with the mean net stress;
κ_s = slope of the unloading-reloading line associated with soil suction;
$N(0)$ = specific volume for $p = p^c$ and $s = 0$;
$\lambda(0)$ = slope of the virgin compression line associated with the mean net stress for $s = 0$;
r = parameter controlling the slope of the virgin compression line;
β = parameter that controls the slope of the virgin compression line for $s \neq 0$; and
p^c = reference stress.

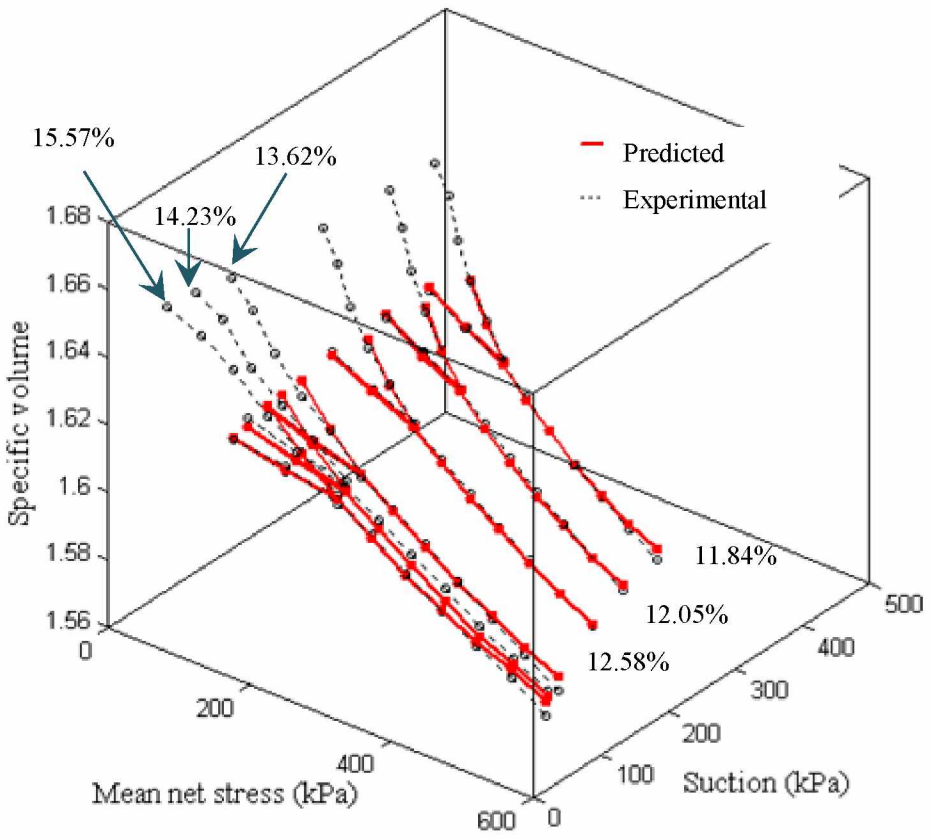
15.57%
13.62%
14.23%
Predicted
Experimental
11.84%
12.05%
12.58%
Specific volume
1.68
1.66
1.64
1.62
1.6
1.58
1.56
0
200
400
600
Mean net stress (kPa)
0
100
200
300
400
500
Suction (kPa)

(a)

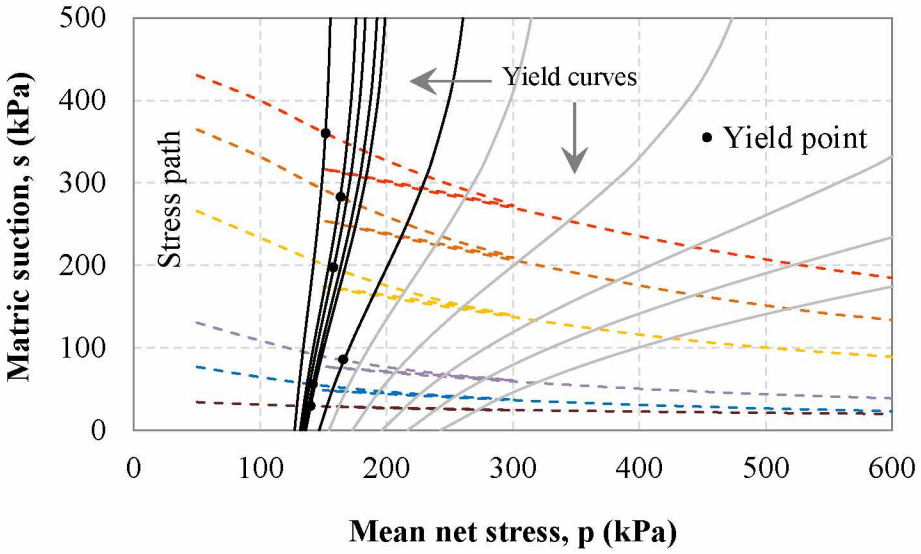

(b)

Figure 4.14 Constitutive modeling under isotropic loading conditions: (a) Comparison between experimental and predicted test results, and (b) yield curves in the p-s plane.

4.6 Conclusions

This paper proposed a new triaxial testing system for unsaturated soils based upon minor modifications on the conventional triaxial testing apparatus for saturated soils. A newly developed photogrammetry-based method was used to reconstruct 3D model for unsaturated soil specimens during triaxial testing from which the volume changes were accurately calculated. High-suction tensiometers were adopted to monitor soil matric suction during constant water content triaxial tests. Through a series of constant water content triaxial tests on unsaturated soil specimens, the capabilities of the new testing system are evaluated. New methods were also proposed to characterize shear strength and elasto-plastic model parameters using results from constant water content triaxial tests. Analyses indicated that the proposed triaxial testing system is a cost effective and time efficient alternative to the suction-controlled triaxial testing system.

4.7 References

Alonso, E. E., Gens, A., and Josa, A., 1990, "A Constitutive Model for Partially Saturated Soils," Geotechnique, Vol. 40, No. 3, pp. 405-430.

Alshibli, K. A., and Al-Hamdan, M. Z., 2001, "Estimating Volume Change of Triaxial Soil Specimens from Planar Images," Computer-Aided Civil and Infrastructure Engineering, Vol. 16, No. 6, pp. 415-421.

ASTM D 4767, 2004, "Standard Test Method for Consolidated Undrained Triaxial Compression Test for Cohesive Soils," ASTM International, West Conshohocken, PA.

Bishop, A. W., and Donald, I. B., 1961, "The Experimental Study of Partly Saturated Soil in the Triaxial Apparatus," In: Proc., 5th Int. Conf. Soil Mech., 1, pp.13-21.

Cabarkapa, Z., and Cuccovillo, T., 2006, "Automated Triaxial Apparatus for Testing Unsaturated Soils," Geotech. Test. J., Vol. 29, No. 1, pp. 21-29.

Clayton, C. R., Khatrush, S. A., Bica, A. V. D., and Siddique, A., 1989, "Hall Effect Sensors in Geotechnical Instrumentation," Geotech. Test. J., Vol. 12, No. 1, pp. 69-76.

Colmenares, J. E., and Ridley, A. M., 2002, "Stress-Strain and Strength Relationships for a Reconstituted Clayey Silt," In Proceedings of the Third International Conference on Unsaturated Soils. Unsat 2002, Vol. 2, pp. 481-484.

Cuccovillo, T., and Coop, M. R., 1997, "The Measurement of Local Axial Strains in Triaxial Tests Using LVDTs," Geotechnique, Vol. 47, No. 1, pp. 167-171.

Delage, P., Romero, E., and Tarantino, A., 2008, "Recent Developments in the Techniques of Controlling and Measuring Suction in Unsaturated Soils," In Keynote Lecture, Proc. 1st Eur. Conf. on Unsaturated Soils, pp. 33-52.

Fredlund, D. G., and Rahardjo, H., 1993, Soil Mechanics for Unsaturated Soils. New York: John Wiley and Sons.

Fredlund, D. G., Morgenstern, N. R., and Widger, R. A., 1978, "The Shear Strength of Unsaturated Soils," Can. Geotech. J., Vol. 15, No. 3, pp. 313-321.

Gachet, P., Geiser, F., Laloui, L., and Vulliet, L., 2007, "Automated Digital Image Processing for Volume Change Measurement in Triaxial Cells," Geotech. Test. J., Vol. 30, No. 2, pp. 98-103.

Gallipoli, D., D'Onza, F., and Wheeler, S. J., 2010, "A Sequential Method for Selecting Parameter Values in the Barcelona Basic Model," Can. Geotech. J., Vol. 47, No. 11, pp. 1175-1186.

GDS Instruments (2009): http://www.epccn.com/gds/datasheets/UNSAT_Datasheet.pdf.

Geiser, F., Laloui, L., Vulliet, L., Rahardjo, H., Toll, D., and Leong, E., 2000, "On the Volume Measurement in Unsaturated Triaxial Test," In Unsaturated soils for Asia. Proceedings of the Asian Conference on Unsaturated Soils, UNSAT-Asia, Singapore, pp. 669-674.

Guan, Y., and Fredlund, D. G., 1997, "Use of Tensile Strength of Water for the Direct Measurement of High Soil Suction," Can. Geotech. J., Vol. 34, No.4, pp. 604-614.

Hilf, J. W., 1956, "An Investigation of Pore Water Pressure in Compacted Cohesive Soils," Tech. Memo. No. 654, US. Dep. of the Interior, Bureau of Reclamation, Design and Construction Div., Denver.

Hird, C. C., Yung, M. P., Ackerly, S., Hellings, J., and Jardine, R., 1987, "A New Device for Measuring Local Axial Strains on Triaxial Specimens," Geotechnique, Vol. 37, No. 3, pp. 413-417.

Hoyos, L. R., 1998, "Experimental and Computational Modeling of Unsaturated Soil Behavior under True Triaxial Stress States," Ph.D. dissertation, Georgia Institute of Technology, Atlanta.

Hoyos, L. R., Laloui, L., and Vassallo, R., 2009, "Mechanical Testing in Unsaturated Soils," In Laboratory and Field Testing of Unsaturated Soils," Springer Netherlands, pp. 63-77.

Josa, A., Alonso, E. E., Lloret, A., and Gens, A., 1987, "Stress-Strain Behaviour of Partially Saturated Soils," Proc. 9th European Conz Soil Mech. Fdn Engng, Dublin, 2, pp. 561-564.

Ladd, R. S., 1978, "Preparing Test Specimens Using Under compaction," Geotech. Test. J., Vol. 1, No. 1, pp. 16-23.

Laudahn, A., Sosna, K., and Bohdp, J., 2005, "A Simple Method for Air Volume Change Measurement in Triaxial Tests," Geotech. Test. J., Vol. 28, No. 3, pp. 313-318.

Le, T. T., Cui, Y. J., Muñoz, J. J., Delage, P., Tang, A. M., and Li, X. L., 2011, "Studying the Stress-suction Coupling in Soils Using an Oedometer Equipped with a High Capacity Tensiometer," Frontiers of Architecture and Civil Engineering in China, Vol. 5, No. 2, pp. 160-170.

Li, L., and Zhang, X., 2014, "Development of a New High-Suction Tensiometer," Soil Behavior and Geomechanics, pp. 416-425.

Lourenco, S. D. N., Gallipoli, D., Toll, D. G., and Evans, F. D., 2006, "Development of a Commercial Tensiometer for Triaxial Testing of Unsaturated Soils," Proceedings of 4th international conference on unsaturated soils, Phoenix, Geotechnical Special Publication, Vol. 147. pp. 1875-1886.

Lourenço, S. D. N., Gallipoli, D., Toll, D. G., Augarde, C. E., Evans, F. D., and Medero, G. M., 2008, "Calibrations of a High Suction Tensiometer," Geotechnique, Vol. 58, No. 8, pp. 659-668.

Macari, E. J., Parken, J., and Costes, N. C., 1997, "Measurement of Volume Changes in Triaxial Tests Using Digital Imaging Techniques," Geotech. Test. J., Vol. 20, No. 1, pp. 103-109.

Meilani, I., Rahardjo, H., Leong, E. C., and Fredlund, D. G., 2002, "Mini Suction Probe for Matric Suction Measurements," Can. Geotech. J., Vol. 39, No.6, pp. 1427-1432.

Ng, C. W., Zhan, L. T., and Cui, Y. J., 2002, "A New Simple System for Measuring Volume Changes in Unsaturated Soils," Can. Geotech. J., Vol. 39, No.3, pp. 757-764.

Oliveira, O. M., and Marinho, F. A. M., 2008, ".Suction Equilibration Time for a High Capacity Tensiometer," Geotech. Test. J., Vol. 31, No. 1, pp. 1-5.

Parker, J. K., 1987, "Image Processing and Analysis for the Mechanics of Granular Materials Experiment," ASME Proceedings of the 19th SE Symposium on System Theory, Nashville, TN, March 2, 1987.

Qiao, H., Nakata, Y., and Hyodo, M., 2008, "Triaxial Compression Test for Unsaturated Sandy Soil Using Image Processing Technique," Deformational Characteristics of Geomaterials, Vol. 2, pp. 529-534.

Rampino, C., Mancuso, C., and Vinale, F., 1999, "Laboratory Testing on an Unsaturated Soil: Equipment, Procedures, and First Experimental Results," Can. Geotech. J., Vol. 36, No.1, pp. 1-12.

Rao, S. S., 1996, Engineering Optimization, Theory and Practice, Third Edition, John Wiley & Sons, Inc.

Ridley, A. M., and Burland, J. B., 1993, "A New Instrument for the Measurement of Soil Moisture Suction," Geotechnique, Vol. 43, No. 2, pp. 321-324.

Romero, E., Facio, J. A., Lloret, A., Gens, A., and Alonso, E. E., 1997, "A New Suction and Temperature Controlled Triaxial Apparatus," Proceedings of the 14th International Conference on Soil Mechanics and Foundation Engineering, Hamburg, Vol. 1, pp. 185-188.

Sharma, R. S., 1998, "Mechanical Behaviour of Unsaturated Highly Expansive Clays," Ph.D. Thesis, University of Oxford, UK.

Sharma, R. S., Hong, L., and Singhal, S., 2006, "Developments in Measurement of Volume Change in Triaxial Testing of Unsaturated Soils," In Advances in Unsaturated Soil, Seepage, and Environmental Geotechnic, ASCE, pp. 93-101.

Sivakumar, V. A., 1993, "Critical State Framework for Unsaturated Soil," Ph.D. Thesis, University of Oxford.

Sun, D. A., Matsuoka, H., and Xu, Y. F., 2004, "Collapse Behavior of Compacted Clays in Suction-Controlled Triaxial Tests," Geotech. Test. J., Vol. 27, No. 4, pp. 362-370.

Take, W. A., and Bolton, M. D., 2003, "Tensiometer Saturation and the Reliable Measurement of Matric Suction," Geotechnique, Vol. 53, No.2, pp. 159-172.

Tarantino, A., and Mongiovi, L., 2002, "Design and Construction of a Tensiometer for Direct Measurement of Matric Suction," In: Proc. Third Int. Conf. on Unsaturated Soils, Recife 1, pp. 319-324.

Thu, T. M., Rahardjo, H., and Leong, E. C., 2006, "Shear Strength and Pore-Water Pressure Characteristics during Constant Moisture content Triaxial Tests," Journal of Geotechnical and Geoenvironmental Engineering, Vol.132, No.3, pp. 411-419.

Toll, D. G., Lourenço, S. D. N and Mendes, J., 2013, "Advances in Suction Measurements Using High Suction Tensiometers." Engineering Geology, Vol. 165, pp. 29-37.

Triggs, B., McLauchlan, P. F., Hartley, R. I., and Fitzgibbon, A. W., 2000, "Buddle Adjustment – A Modern Synthesis," In: Triggs, B., Zisserman, A., and Szeliski, R. (eds.) ICCV-WS 1999. LNCS, Vol.1983, pp. 298-375.

Uchaipichat, A., Khalili, N., and Zargarbashi, S., 2011, "A Temperature Controlled Triaxial Apparatus for Testing Unsaturated Soils," Geotech. Test. J., Vol. 34, No. 5, pp. 424-432.

Wheeler, S. J., and Sivakumar, V., 1995, "An Elasto-Plastic Critical State Framework for Unsaturated Soil," Geotechnique, Vol. 45, No. 1, pp. 35-53.

Wheeler, S.J., 1988, "The Undrained Shear Strength of Soils Containing Large Gas Bubbles," Geotechnique, Vol. 38, No. 3, pp. 399-413.

Zhang, X., 2010, "Use of Results from Undrained Tests for the Constitutive Modeling of Unsaturated Soils," 5th International Conference on Unsaturated Soils, September 6-8, 2010, Barcelona, Spain.

Zhang, X., and Lytton, R. L., 2009a, "Modified State-Surface Approach to the Study of Unsaturated Soil Behavior. Part I: Basic Concept," Can. Geotech. J., Vol. 46, No. 5, pp. 536-552.

Zhang, X., and Lytton, R. L., 2009b, "Modified State-Surface Approach to the Study of Unsaturated Soil Behavior. Part II: General Formulation," Can. Geotech. J., Vol. 46, No. 5, pp. 553-570.

Zhang, X., and Lytton, R. L., 2011, "Modified State-Surface Approach to the Study of Unsaturated Soil Behavior. Part III: Modeling of Coupled Hydromechanical Effect," Can. Geotech. J., Vol. 49, No. 1, pp. 98-120.

Zhang, X., and Xiao, M., 2013, "Using Modified State Surface Approach to Select Parameter Values in The Barcelona Basic Model," International Journal for Numerical and Analytical Methods in Geomechanics, Vol. 37, No.12, pp. 1847-1866.

Zhang, X., Li, L., and Lytton, R. L., 2012, "Fast Determination of Soil Behavior in the Capillary Zone Using Simple Laboratory Tests," Technical report, No. INE/AUTC 13.14, University of Alaska Fairbanks, Fairbanks, Alaska.

Zhang, X., Li, L., Chen, G., and Lytton, R. L., 2015, "A Photogrammetry-Based Method to Measure Total and Local Volume Changes of Unsaturated Soils during Triaxial Testing," Acta Geotechnica, Vol. 10, No.1, pp. 55-82.

CHAPTER 5. A MODIFIED UNCONFINED COMPRESSION TESTING SYSTEM TO CHARACTERIZE THE STRESS-STRAIN BEHAVIOR OF UNSATURATED SOILS AT LOW CONFINING STRESSES[1]

5.1 Abstract

In geotechnical and pavement engineering, many projects involve soils at shallow depths that are unsaturated with low confining stresses. Suction-controlled triaxial tests are usually used to investigate the stress-strain (deformation and strength) behavior of these soils. However, such tests require significant equipment modifications to the conventional testing apparatus that is used for saturated soils and are time-consuming to perform. As a result, these tests cannot be justified for time-sensitive engineering projects.

This paper presents a modified unconfined compression testing system to investigate the stress-strain behavior of unsaturated soils at low confining stresses. Negative air pressure (i.e., vacuum pressure) is used to provide the low confining pressure needed for the tests. High-suction tensiometers are used to monitor soil matric suction variation during testing. A photogrammetric method is used to reconstruct the three-dimensional model of unsaturated soil specimens from which both total and localized volume changes are calculated. Methods are also proposed for unsaturated shear strength analysis. A series of tests were carried out to demonstrate the use of the modified unconfined compression testing system to evaluate the stress-strain behavior of unsaturated soil under different confining stresses. Results from this study indicate that the newly developed modified unconfined compression testing system is cost-effective in the rapid evaluation of stress-strain behavior of unsaturated soils under low confining stresses.

[1]Li, L., and Zhang, X. (2015). "A Modified Unconfined Compression Testing System to Characterize the Stress-Strain Behavior of Unsaturated Soils at Low Confining Stresses" Transportation Research Board, Washington, D. C. (accepted).

5.2 Introduction

In geotechnical and pavement engineering, many projects involve soils at shallow depths that are unsaturated and subject to low confining stresses. For example, numerous studies indicate that most unsaturated expansive slope failure occurs at a shallow depth of 2–3 m (Bao et al. 1998; Zhan 2007; Ng. et al. 2002; and Godt et al. 2008). Deformation and strength characteristics are among the most important factors that influence road pavement design. For pavement design, the depth of influence is related to the magnitude and distribution of the traffic loads imposed on the pavement structure. Considering a dual wheel of 1 m (3 ft) in width, typically 80–90% of the applied stress is dissipated within 1 m (3 ft) below the asphalt section. This is the reason why current AASHTO 1993 specifies the depth of influence as 1.5 m (5 ft) below the proposed subgrade elevation for site investigation purposes (FHWA 2006). Good drainage is also required to assure that soils are unsaturated to achieve the desired performance. Consequently, it is important to investigate the stress-strain behavior of unsaturated soils at low confining stress.

At present, suction-controlled triaxial tests are used to characterize the stress-strain (deformation and shear strength) characteristics of unsaturated soils. Figure 5.1 schematically shows a suction-controlled triaxial testing apparatus. This testing apparatus requires significant modifications to the triaxial testing apparatus used for saturated soils and is difficult to operate. A typical suction-controlled double-cell triaxial test system costs about $150,000. In addition, suction-controlled tests, which are consolidated-drained tests, are time-consuming due to the low permeability of unsaturated soils. It is not uncommon to spend two to three years fully characterizing one unsaturated soil (Sivakumar 1993; Sharma 1998; and Hoyos 1998). As a result, suction-controlled tests cannot be justified for time-sensitive engineering projects. The

development of cost-effective methods to rapidly characterize the stress-strain behavior of unsaturated soils at low confining stresses is greatly needed.

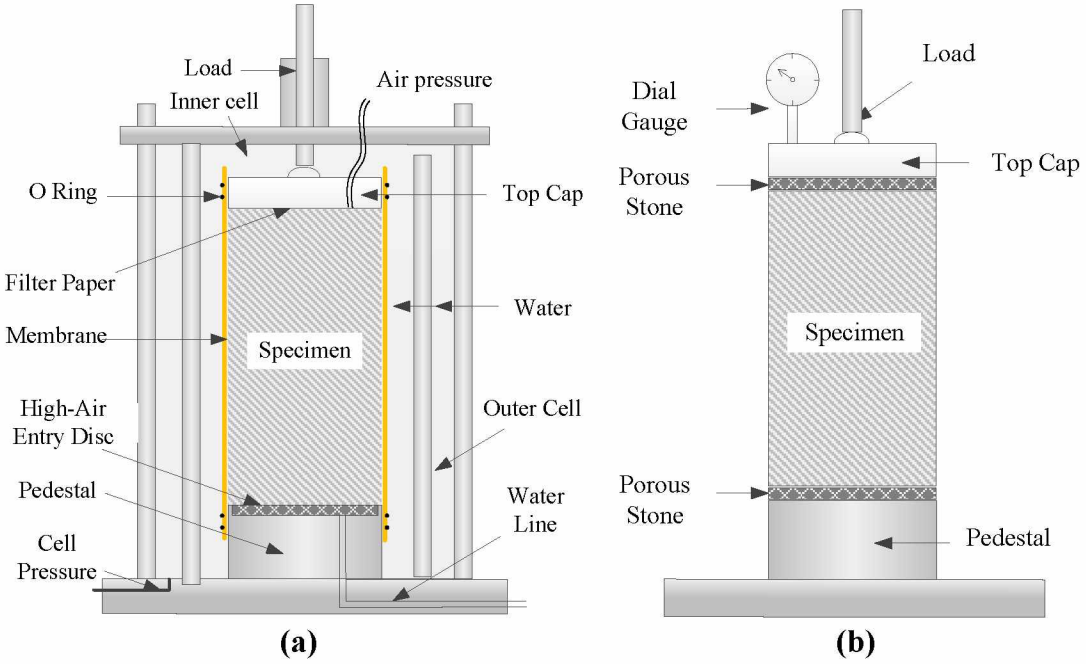

Figure 5.1 (a) Suction-controlled triaxial test apparatus; (b) conventional unconfined compression testing system.

An unconfined compression test is a triaxial compression test with zero confining pressure; it is one of the simplest and most widely performed soil tests in geotechnical engineering. Figure 5.1b shows a schematic plot of the unconfined compression test setup. Traditionally, the soil specimens used in the test are considered saturated, and have no volume change during undrained loadings (ASTM D2116 2000), although specimens are often unsaturated and experience volume changes. Normally, total stress analyses are done for the tests, since no measurement for pore water pressure is made. In its original design, an unconfined compression test cannot be used to characterize the stress-strain behavior of unsaturated soils.

A few attempts have been made to characterize the stress-strain behavior of unsaturated soils by modifying the unconfined compression tests. Colmenares and Ridley (2002) added a high-suction tensiometer to the top loading cap to measure the change in matric suction during unconfined compression tests. Soil volume change during the tests was not measured, however. Since unsaturated soils experience volume change during undrained compression, the obtained shear strength of soils from this test could be problematic. Chae et al. (2010) used a conventional triaxial testing apparatus for saturated soils to conduct unconfined compression tests on statically and dynamically compacted silty soils. A ceramic disk with an air entry value of 500 kPa was installed in the pedestal with a drainage channel connected to a water pressure transducer to measure the pore water pressure in the soil sample. An air line was connected to the top of the soil specimen to release the pore air pressure to the atmosphere. During the tests, the triaxial chamber was filled with water, but no cell pressure was applied. As a result, although a triaxial test apparatus was used, the tests were essentially unconfined. The volume change was measured by monitoring the amount of water flow in or out of the triaxial cell. The mechanism of the suction measurement is similar to the high-suction tensiometer, but the reaction time is expected to be much longer due to the larger size of the ceramic disc and associated larger volume of water in the drainage path. Although possible, applying cell pressure can cause the triaxial chamber to expand and make the volume change measurement inaccurate. As a result, this system cannot be used to characterize the stress-strain behavior of unsaturated soils at non-zero confining stresses.

This paper presents a modified unconfined compression testing system to investigate the stress-strain behavior of unsaturated soils at low confining stresses. Negative (vacuum) air pressure is used to provide the low confining pressure needed for the tests. High-suction

tensiometers are used to monitor soil matric suction variation during testing. A photogrammetric method is used to reconstruct the three-dimensional (3D) model of unsaturated soil specimens from which both total and localized volume changes are calculated. Methods are proposed for the unsaturated shear strength analysis. A series of tests were performed to demonstrate the use of the modified unconfined compression testing system in evaluating the stress-strain behavior of unsaturated soil under different confining stresses. Results from this study indicated that the newly developed modified unconfined compression test system is cost-effective in the evaluation of stress-strain behavior of unsaturated soils at low confining stresses.

5.3 Characterizing Unsaturated Soil Behavior Using Undrained Triaxial Shearing Tests

It is well known that suction has significant influences on the deformation and shear strength of unsaturated soils. Since Bishop and Donald (1961) developed the first suction-controlled triaxial (SCTX) testing apparatus, the SCTX testing method has become established as a standard method for characterizing unsaturated soils (Delage 2002). In suction-controlled tests, suction is often kept as a constant while load is applied to the soil from which the stress-strain behavior is obtained. Normally, tests are conducted at several different constant suction levels, and the results are synthesized to a constitutive model that can be used to predict soil responses under any arbitrary combination of suction and stress. Based on this approach, many models have been developed for unsaturated soils (Fredlund and Rahardjo 1993; Alonso et al. 1990; and Cui and Delage 1996). One of the examples was the shear strength equation for unsaturated soils using two independent stress state variables (net normal stress and matric suction) proposed by Fredlund et al. (1978):

$$\tau_f = c' + (\sigma - u_a)_f \tan\phi' + (u_a - u_w)_f \tan\phi^b \qquad \text{Equation 5.1}$$

where, τ_f = shear stress on the failure plane, c' = cohesion in saturated condition, σ = normal stress, u_a = atmosphere pressure, u_w = pore water pressure, $\sigma - u_{a\ f}$ = net normal stress at the failure plane, $u_a - u_{w\ f}$ = matric suction when the soil is at failure, ϕ' = angle of friction in saturated condition, and ϕ^b = angle indicating the rate of change in shear strength relative to changes in matric suction.

Figure 5.2a shows the evolution of the Mohr circle during a triaxial compression test and the process to obtain shear strength parameters in Equation 5.1. Point A represents a soil specimen with zero all-around stress and suction of s_1 at the beginning of a triaxial compression test. In a typical suction-controlled constant confining pressure shearing test, deviator stress increases, which causes the Mohr circle to increase diameters from A to B to C until D where the soil reaches failure. The failure plane is represented by point F_1, which is tangential to the failure envelope F_1F_2 at a suction of s_1. In order to obtain the failure envelope F_1F_2 at a suction of s_1, at least one additional suction-controlled test is needed with different confining pressure at the same suction of s_1. The corresponding failure plane is represented by F_2. The slope of F_1F_2 gives the $\tan\phi'$ in Equation 5.1. In order to obtain all the parameters in Equation 5.1, suction controlled tests at another constant suction level of s_2 are needed to define the failure envelope of F_3F_4. Once the failure surface envelope of F_1F_2 F_3F_4 is defined, c', ϕ', and ϕ^b can be determined and shear strength of the soil at any combination of stress and suction can be determined using Equation 5.1. The process just mentioned is straightforward. However, suction-controlled triaxial tests are drained tests. As discussed previously, due to the extremely low permeability of unsaturated soils, suction-controlled tests are very time-consuming. It is not uncommon to spend two to three months finishing one single test. To fully characterize one unsaturated soil, two to

three years are needed (Sivakumar 1993; Sharma 1998; and Hoyos 1998). As a result, suction-controlled tests cannot be justified for time-sensitive engineering projects.

It is argued in this study that undrained triaxial compression tests can be used to achieve the same objective in a much faster way with much simpler equipment. Figure 5.2b shows the evolution of the Mohr circle in undrained triaxial shearing tests. An unconfined compression test is performed with a starting point of A, with zero all-around pressure. As the deviatoric stress increases, the diameters of the Mohr circles increase from A to B to C until D where the soil reaches failure as shown in Figure 5.2b. During this process, the suction in the soil decreases continuously to a level of s_1. The corresponding failure plane is represented by F_1. Similar undrained triaxial shearing tests with non-zero confining pressure can be carried out to obtain Mohr circles at failure, such as the ones represented by points F_2 and F_3 in Figure 5.2b. These points can be used to define the failure envelope for unsaturated soils as long as they are known to be on the failure envelope. In other words, it is not necessary for points F_1 and F_2 (or F_3 and F_4) in Figure 5.4a to have the same suction level to determine the parameters in Equation 5.1. During the undrained triaxial shearing test, the suction in the soil specimen changes instantaneously with applied load. If the soil response and associated stress path, as shown in Figure 5.2b (especially soil suction), can be measured directly and quickly, the shear strength of unsaturated soil can be obtained much faster. This objective can be achieved through a modified unconfined compression testing system, discussed in the following sections.

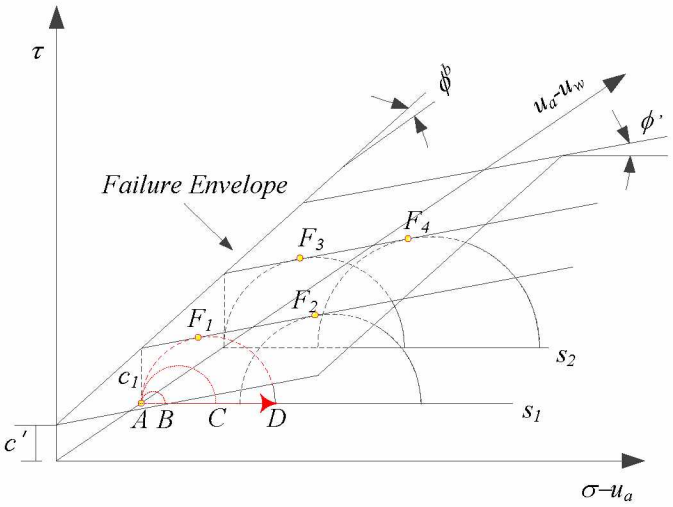

(a) Suction-controlled triaxial shearing test

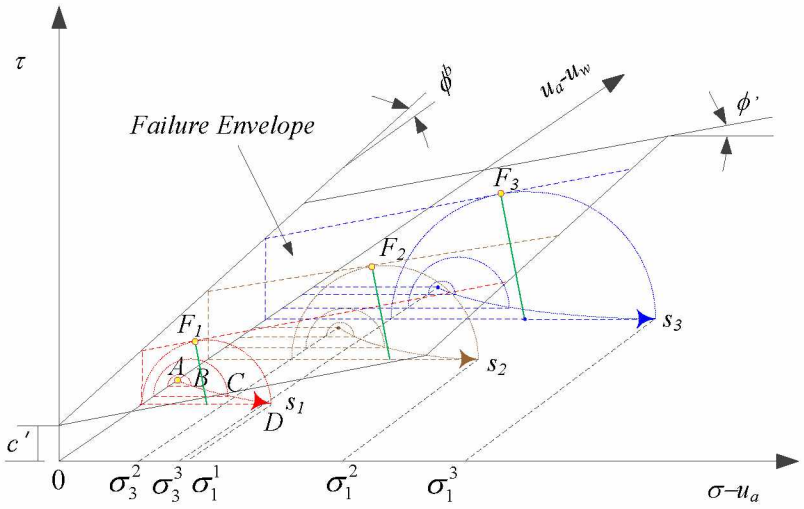

(b) Undrained triaxial shearing test

Figure 5.2 Mohr–Coulomb failure envelope for unsaturated soils.

5.4 A Modified Unconfined Compression Testing System

Figure 5.3a shows a schematic plot of the proposed modified unconfined compression testing system. The following modifications are made to a conventional unconfined compression testing system: (1) An air channel is added to the base pedestal, which is connected to a controlled vacuum pressure. The maximum confining pressure provided by the vacuum is about -

100 kPa, which should be sufficient for most problems as discussed previously. (2) Two high-suction tensiometers are installed at the middle height of the soil specimens to measure the suction changes during triaxial compression tests under undrained conditions. The reaction time of the high-suction tensiometers varies from instantaneous to a few minutes (Caruso and Tarantino 2004;Tarantino and Tombolato 2005; Chiu et al. 2005; Jotisankasa 2005; Teixeira and Marinho 2006; Cui et al. 2008; Mendes et al. 2008; Tang et al. 2009; Mendes 2011; Le at al. 2011; and Toll et al. 2011). The suction change in the soil specimens during undrained loading is instantaneous. Instead of controlling suction changes, the high-suction tensiometers directly measure the suction responses under undrained conditions, which can significantly reduce the testing time. (3) Some measurement targets are posted on the membrane covering the soil specimen, and a noncontact photogrammetric method is used to reconstruct accurate 3D model of the soil specimen from some images taken during triaxial testing. The images can be taken from any arbitrary orientation using a commercial digital camera. The reconstructed 3D model can be used to calculate both total and localized volume changes of the soils. The following sections discuss the working mechanisms of the proposed modifications.

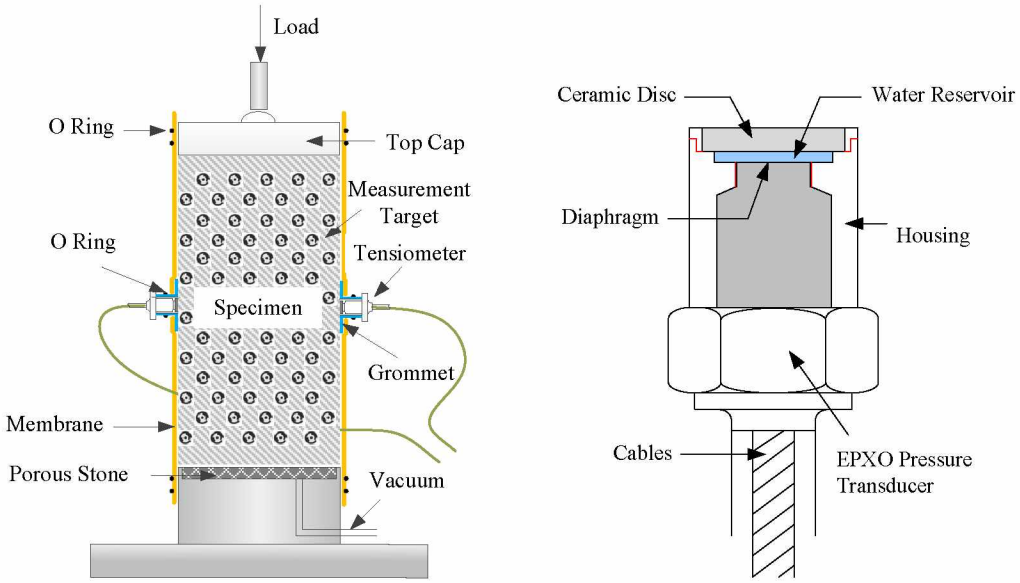

(a) New compression testing apparatus; (b) Newly developed high-suction tensiometer

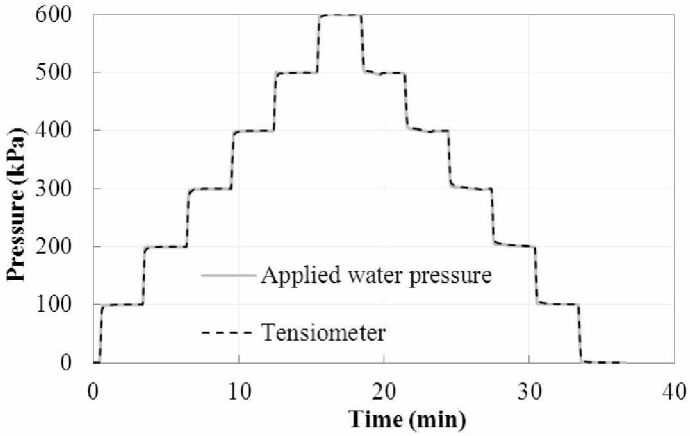

(c) Stepwise calibration curve

Figure 5.3 Modified unconfined compression testing systems and high-suction tensiometer.

5.4.1 Direct-Suction Measurement Using High-Suction Tensiometer

To characterize the stress-strain behavior of unsaturated soils using undrained triaxial compression tests, a proper suction sensor is needed to measure suction variations during undrained loading. Two factors influence the time duration of the suction measurements and, subsequently, the duration of the whole test: (1) the time needed for the soil specimen to reach

suction equilibrium, and (2) the reaction time for the suction sensor to measure suction. In a triaxial compression test, the soil specimen is considered as a representative element volume. Consequently, suction changes instantaneously with applied load throughout the whole soil specimen. Theoretically speaking, the suction equilibrium time during undrained loading is instantaneous. The time duration of the suction measurements solely depends upon the reaction time of the suction sensor.

In the past several decades, different methods have been developed to measure soil suction: the filter paper method, tensiometers, psychrometers, and the thermal conductivity suction sensor. Filter paper is not practical for triaxial compression tests. Traditional tensiometers cannot be used to measure soil suction higher than 100 kPa. Psychrometers and thermal conductivity suction sensors require a relatively long time (hours) for suction measurements. Also, the resultant suction measurement is not highly accurate and is easily affected by ambient temperature variations. In the past 20 years, there has been considerable interest in high-suction tensiometers due to their fast response time and easy maneuverability, as well as the reduction in measurement errors, because they involve a direct measurement of suction, rather than relying on indirect calibrations (Caruso and Tarantino 2004;Tarantino and Tombolato 2005; Chiu et al. 2005; Jotisankasa 2005; Teixeira and Marinho 2006; Cui et al. 2008; Mendes et al. 2008; Tang et al. 2009; Mendes 2011; Le at al. 2011; and Toll et al. 2011).

In this study, two high-suction tensiometers, built in-house and shown schematically in Figure 5.3b, were used to measure soil suction during undrained triaxial compression tests. These high-suction tensiometers were developed based on the principle first proposed by Ridley and Burland (1993), which comprised (1) a miniature EPXO transducer for vacuum pressure measurement, (2) a 15 bar high air entry disc to prevent the tensiometer from cavitation at high

suction, and (3) a water reservoir to generate negative water pressure, which can be detected by the pressure transducer. Figure 5.3c indicates the stepwise calibration results for well-saturated tensiometers. It can be seen that the high-suction tensiometer response is instantaneous. The maximum attainable suction of two high-suction tensiometers was found to be approximately 1100 kPa using the free evaporation test reported by Guan and Fredlund (1997). More details regarding the high-suction tensiometers built in-house can be found in Li and Zhang (2014).

5.4.2 Volume Change Measurement Using Photogrammetry

Soil volume change is also an indispensable part in the characterization of stress-strain behavior of unsaturated soils. A photogrammetric method was used to measure soil volume change during triaxial compression testing. The principle of photogrammetry, using an ideal pinhole camera model, is shown in Figure 5.4. In this model (Figure 5.4a), the small pinhole and the image plane correspond to the perspective center of the lens and the image sensor of a commercial digital camera. When a photograph is taken of a 3D object, a 2D image is obtained and the depth of the object is lost. Images taken from different positions are different for the same object (Figure 5.4b). The pixel position differences for the same points on different images can be used to calculate the orientation of the camera from where the images are taken. These camera orientations, together with the images, can be used to reconstruct the 3D shape of the object. If a perspective center (center of an ideal pinhole camera lens) of the left camera S_1 is taken as the origin of an arbitrary coordinate system, then there are six unknowns for the right camera orientation in Figure 5.4c: three coordinates of the perspective center S_2 (X_s, Y_s, Z_s) and three directional angles (κ, ω, ϕ). Six equations can be established by identifying six pairs of corresponding points on the two images, and the second camera orientation can be solved. Usually the distance of any two points is given as a scale (Figure 5.4b), which reduces pairs of

the corresponding points to five. Since millions of pairs of corresponding points on the two images are possible, the redundancy in information can be used to perform an optimization analysis to accurately determine the camera orientation so that the errors in measurement are minimal. In addition, multiple images can be taken from different orientations with sufficient overlap, which can provide additional redundant equations to improve the accuracy of the result. Once the camera orientations are determined, a line of sight (or ray) can be constructed from the photograph through the perspective center of the camera to the corresponding point on the object, as shown in Figure 5.4b (collinearity). The intersection of these rays (triangulation) determines the 3D coordinates of a point. Detailed mathematical derivations for the photogrammetry can be found in Mikhail et al. (2001) and Zhang et al. (2015). As a noncontact 3D measurement technique, photogrammetry has been used in different fields for more than 160 years and proven able to provide highly accurate measurements (Hampel and Maas 2003; Maas et al. 2003; and Albert et al. 2002). Many software packages are available for free downloading. In this study, photogrammetry was used to reconstruct accurate 3D models of the soil specimen from images taken during triaxial compression tests. After the 3D model was built, the total and localized volume changes of the soil specimen were calculated.

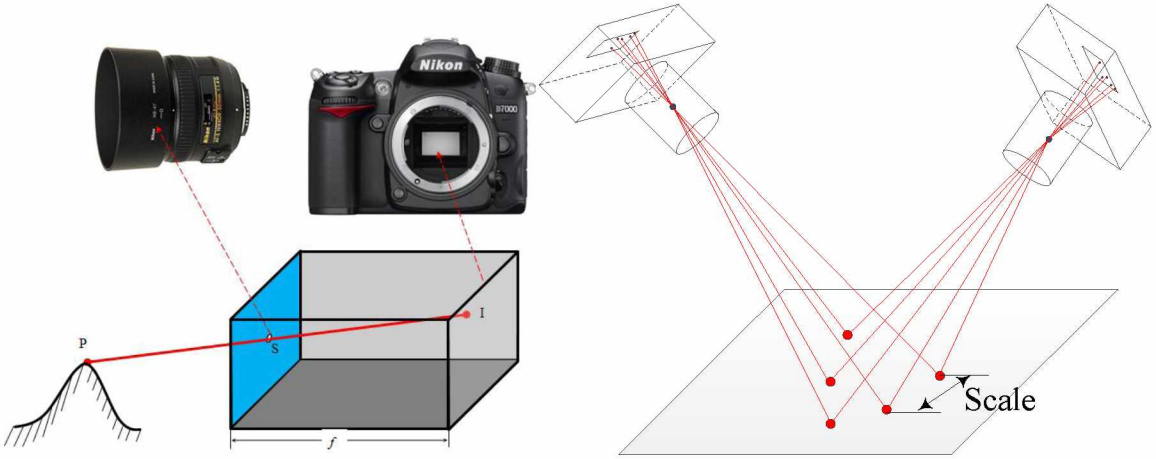

(a) Ideal pinhole camera model; (b) Image-taking process

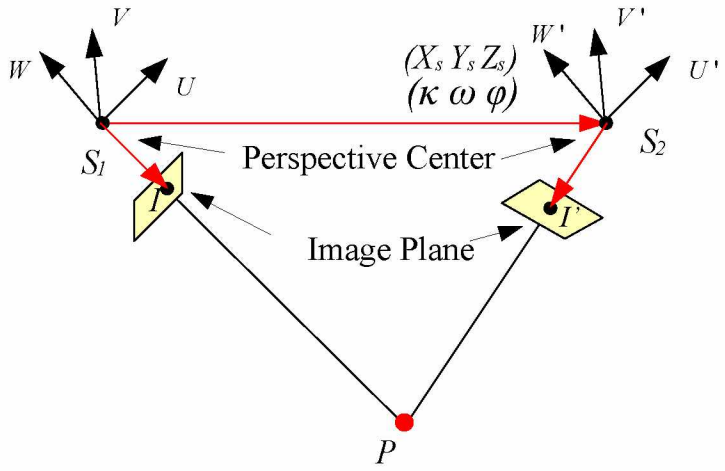

(c) Coordinate system in photogrammetry

Figure 5.4 Principle of photogrammetry.

5.5 Experimental Details

5.5.1 Camera Calibration and Image Idealization

A commercially available digital single-lens reflex camera (Nikon D7000) with a 50 mm fixed focal length lens (AF-S Nikkor 50 mm f/1.4G, shown in Figure 5.4a) was used to take the photographs needed for the validation tests. The image sensor of the camera (see Figure 5.4a) has a resolution of 16.2 million pixels (4928H: 3264V). As discussed earlier, photogrammetry assumes that the camera lens is a pinhole. A commercial camera often uses multiple lenses to

focus light, and its aperture is not a point. Instead of rendering straight lines for light rays, these lenses often bend them slightly either outwards or inwards. Consequently, an image taken with a commercial digital camera is subject to barrel or pincushion distortions, so a camera must be calibrated before being used for extraction of precise and reliable 3D metric information from images.

Since the 1950s, numerous techniques have been developed for camera calibration. The algorithms are generally based on an ideal pinhole camera model, with the most popular approach being the well-known self-calibrating bundle adjustment, which has made high-level performance commonplace (Triggs et al. 2000). Both commercial and free software have been developed for camera calibrations and are readily available (e.g., http://www.vision.caltech.edu/bouguetj/calib_doc/htmls/links.html).

A software package called PhotoModeler Scanner from Eos Systems, Inc. was used to calibrate the camera. Calibration is done by taking 12 images of a calibration sheet. The intrinsic (focal length, principal point, distortion parameters) and extrinsic (translation vector and rotation matrix) parameters are then calculated by analyzing the 12 images. Details regarding camera calibration are not elaborated here, since it is a well-established technique. Table 5.1 shows the calibration results for the camera that was used. As shown in Table 5.1, the 50 mm fixed focal length lens has an actual focal length of 53.3864 mm when the camera is treated as an ideal pinhole camera model. The principal point is not exactly at the center of the image sensor before the camera calibration, either. The parameters in Table 5.1 were used to correct the distorted images to their "true" versions. After image idealization, the images are ready to be used for the proposed photogrammetry-based method.

Table 5.1 Camera calibration results

Parameters	Symbol	Before Idealization	After Idealization
Focal Length	f *(mm)*	53.3864	53.3864
Pixel Number	M *(pixel)*	4928	4928
	N *(pixel)*	3264	3264
Image Sensor Size	F_x *(mm)*	23.9982	24.7439
	F_y *(mm)*	15.8961	16.3871
Principal Point Coordinate	P_x *(mm)*	12.0865	12.3720
	P_y *(mm)*	8.1022	8.1963
Radial Lens Distortion	K_1 *(10^{-5})*	5.443	0
	K_2 *(10^{-9})*	-2.266	0
Decentering Lens Distortion	P_1 *(10^{-6})*	-3.094	0
	P_2 *(10^{-6})*	2.023	0

5.5.2 Materials

Compacted Fairbanks silt was used to demonstrate the implementation of the proposed modified unconfined compression testing system. The optimal moisture content, maximum dry density, specific gravity, plastic limit, and liquid limit of the soils were 15.7%, 1.732 g/cm3, 2.71, 21.6%, and 24.7%, respectively.

5.5.3 Specimen Preparation

Oven-dried (105 °C) Fairbanks silt was mixed with distilled water up to 2% above the modified Proctor optimum value (15.7%). To equalize the water content in the whole mass, wet soil was sealed in an impervious container and stored for several days in a humidity- and temperature-controlled environment. Subsequently, it was compacted in soil cylinders 101.6 mm in diameter and 203.2 mm in height. To prevent compaction of the uppermost layers, causing excessive densification of the lowest ones, the under-compaction procedure (Ladd 1978) was adopted. Twenty soil specimens were compacted in identical fashion to ensure that all soil specimens had approximately the same stress history. The soil specimens were then conditioned

to different moisture contents by controlling the number of exposures to the atmosphere for about 15 minutes/day. After that, the soil specimens were sealed in plastic bags and stored in a humidity- and temperature-controlled environment for at least one month to ensure suction equilibrium in the whole soil specimen. Table 5.2 summarizes the initial conditions of the eleven soil specimens used in this study.

Table 5.2 Soil specimens used in the testing program

Test No.	Initial Condition				At Failure		
	Water Content (%)	Void Ratio	Degree of Saturation (%)	Matric Suction (kPa)	Matric Suction (kPa)	$(\sigma_3-u_a)_f$ (kPa)	$(\sigma_1-u_a)_f$ (kPa)
1	6	0.724	22.5	604.9	600.0	40	336.4
2	7.8	0.739	28.6	363.2	299.8	40	349.7
3	8.3	0.732	30.7	240.0	212.2	40	271.9
4	10.7	0.711	40.8	145.8	129.9	40	236.1
5	7.4	0.717	28.0	349.0	310.5	5	236.6
6	9.3	0.718	35.1	194.8	164.4	5	220.9
7	10.1	0.714	38.3	138.9	115.4	5	190.8
8	10.6	0.72	39.9	93.5	83.0	5	182.5
9	11.7	0.72	44.0	112.8	95.5	5	182.7
10	13	0.72	48.9	80.8	73.5	5	154.1
11	13.6	0.721	51.1	65.9	58.5	5	129.9

5.5.4 Modified Unconfined Compression Tests

The loading frame of the GCTS SSH-100 Simple Shear System was used to demonstrate the application of the proposed modified unconfined compression testing system. Figure 5.5a shows the system setup. The specimen installation process was mostly the same as that for a conventional unconfined compression test. To prevent uncontrolled losses or absorption of water from the soil specimen, the specimen was positioned without using filter paper. The major difference between the modified and the conventional unconfined compression tests was

application of vacuum confining pressure using a latex membrane and installation of two pre-saturated high-suction tensiometers at the middle height of the soil specimen. The installation of two high-suction tensiometers was identical to the installation process of the GDS Mid-Plane Pore Pressure Transducer (GDS 2010). Great care was taken to assure the least soil disturbance and prevent possible water loss due to evaporation. After installation of the soil specimen and high-suction tensiometers, low vacuum pressure (5 kPa) was applied to the inside of the soil specimen to hold the system in place. Measurement targets were posted on the latex membrane surface, as shown in Figure 5.5a. These measurement targets were used to define shape changes of the soil specimen during the triaxial tests.

Vacuum pressure was applied from a port in the base pedestal (Figure 5.5a). Two different vacuum (or confining) pressure levels (5 kPa and 40 kPa) were applied during the triaxial shearing tests. After the suction in the soil specimen reached equilibrium, indicated by stabilized tensiometer readings, pictures were taken around the testing system for future photogrammetric analysis of the initial soil volume. Images can be taken at arbitrary positions from any shooting direction. This is advantageous since images can be taken at very short distances with the best effect to improve the accuracy of the measurements. Shearing was then conducted at a constant displacement rate of 0.3 mm/min, and the applied vertical load was automatically recorded using a force transducer. The loading process was divided into multiple steps according to vertical displacement. After each desired vertical displacement was reached, shearing was paused for 15-30 minutes for soil deformation and suction to stabilize. Pictures were taken again around the testing system for future analysis of the soil volume. The corresponding soil suction and vertical load were also measured to establish the stress-strain characteristics of the soil. The shearing process was stopped after the soil specimen clearly

reached failure stage, and the soil specimen was taken out for moisture content measurement. A series of modified unconfined compression tests were conducted on soil specimens with different initial moisture contents. The final moisture contents for the tested soil specimens are shown in Table 5.2.

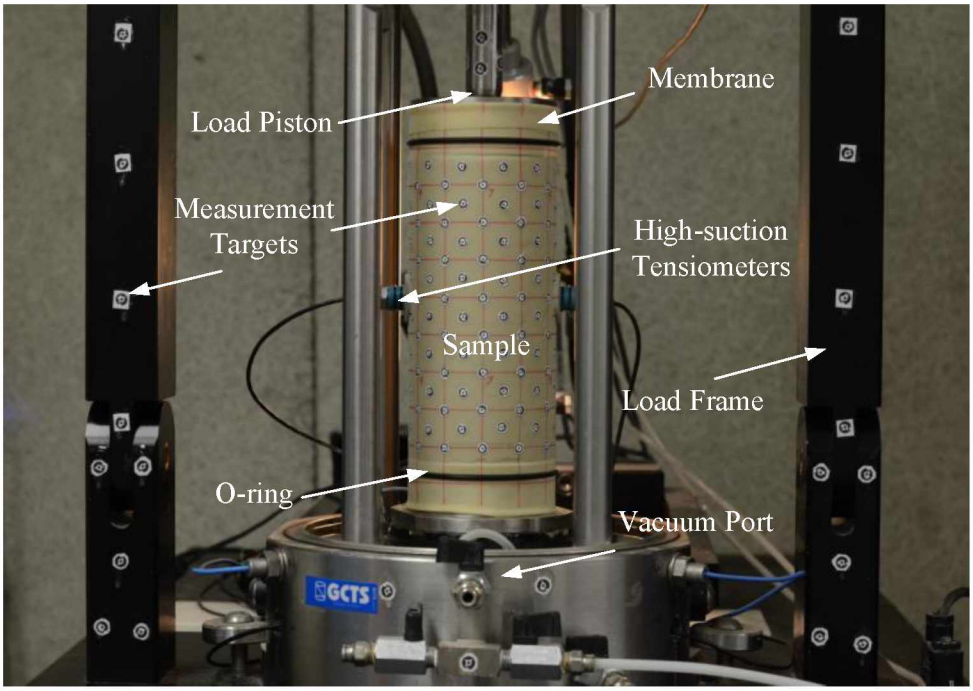

(a) System setup

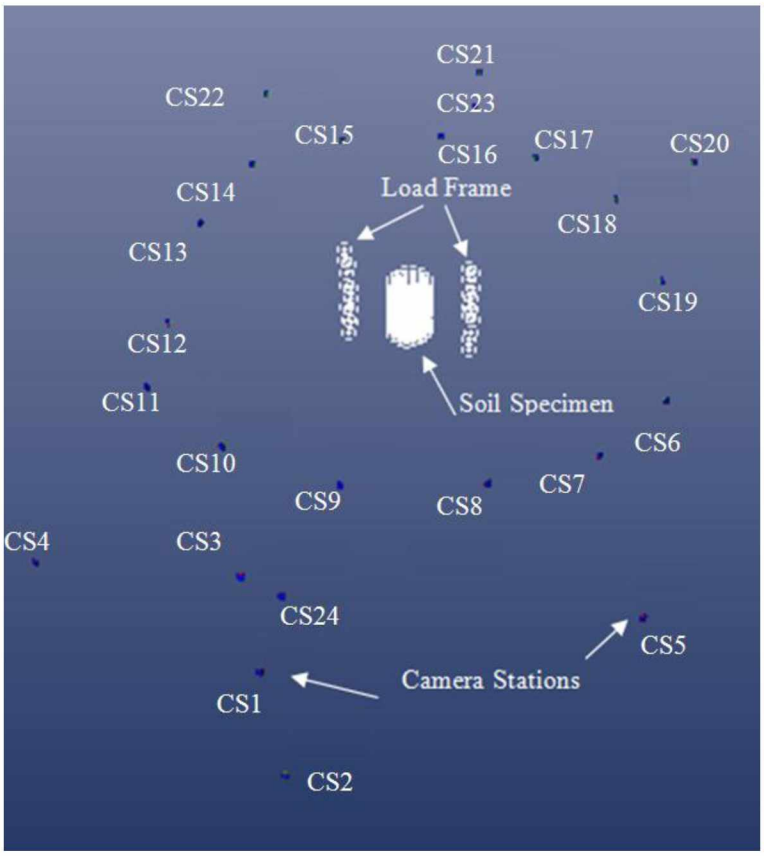

(b) Camera position and reconstructed 3D soil specimen

Figure 5.5 System setup and analysis results from photogrammetry.

5.6 Test Results

5.6.1 Results from the Photogrammetric Analysis

Figure 5.5b presents typical results from photogrammetry by analyzing the pictures, similar to Figure 5.5a. The camera positions were typical for reconstructing the full 3D model of the soil specimen. Some pictures were taken from a relatively long distance to set up a global coordinate system for photogrammetric analysis (camera positions CS1 to CS5 and CS20 to CS24). Other pictures were taken at very close positions to get a better view and obtain more accurate measurements (camera positions CS6 to CS19). These positions formed a circular shape around the testing system. Every picture taken represented a simultaneous evaluation of many

measurement targets, and multiple pictures were used to calculate the 3D coordinates of one measurement point. Typically, 20–25 pictures were sufficient for reconstructing the full 3D model of the soil specimen. The accuracy of a point measurement was less than 10 microns according to Zhang et al. (2015).

5.6.2 Mesh Generation and Strain Localization

After 3D coordinates of points on the specimen surface were obtained (see Figure 5.5b), triangular surface mesh was generated using Delaunay triangulation in MatLab®. Figure 5.6 shows the deformation process of soil 5. As shown in in Table 5.2, soil 5 had a moisture content of 9.3% and was sheared under a confining pressure of 5 kPa. Figure 5.6a shows the mesh shapes of the soil at vertical displacements of 1.8 mm, 5.8 mm, and 10 mm. A numerical interpolation technique similar to that in Lin and Penumadu (2006) was used to generate a continuous deformation field from obtained discrete points on the specimen surface. To visualize the distribution of displacement and strains in the specimen during triaxial testing, contour plots, which connect the points that share the same value of displacement (or strain), were used. Since relative, sparse measurement points were used in this preliminary study, it is more meaningful to read the pattern of a whole contour plot than to focus on the value of a single point. Figure 5.6b presents the contour plots of axial strain at vertical displacements of 1.8 mm, 5.8 mm, and 10 mm. During the triaxial shearing test, displacement was applied through the top cap. Thus, maximum axial strain was found at the top of the soil specimen. As can be seen in Figure 5.6b, when the applied vertical displacement was 1.8 mm, soil deformation was uniform. When the applied vertical displacement was 5.8 mm, a Y-shaped strain localization occurred at the upper center of the soil specimen, while axial strain at the other areas was relatively uniform. The Y-shaped axial strain localization was even severe when the applied vertical displacement was 10

mm. Axial strain localization was not visible to the human eye during the test, since the soil was covered by a latex membrane. Figure 5.6c is a photo of soil 5 after the undrained shearing test was complete. It was found that calculated strain localizations matched well with the photo of soil 5, indicating that the photogrammetric technique can provide reliable 3D full-field information about localized volume change during a triaxial shearing test. This information is what cannot be learned from most existing volume-change measurement methods.

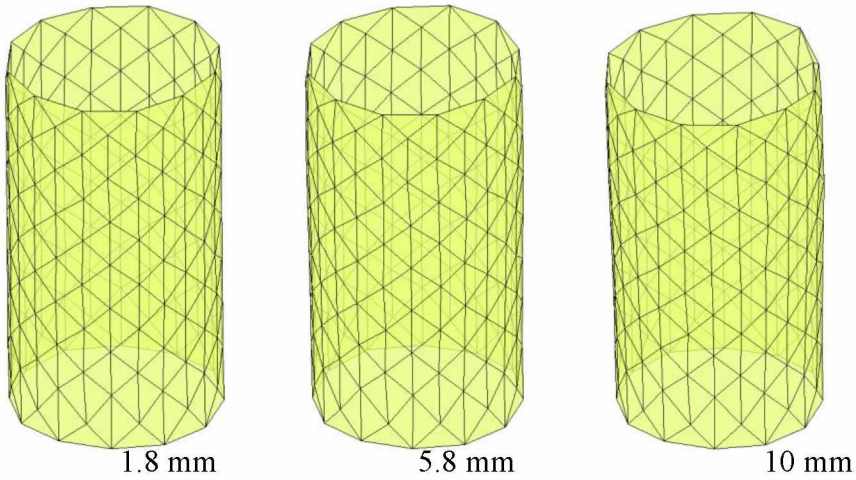

(a) Mesh generation from triangulation

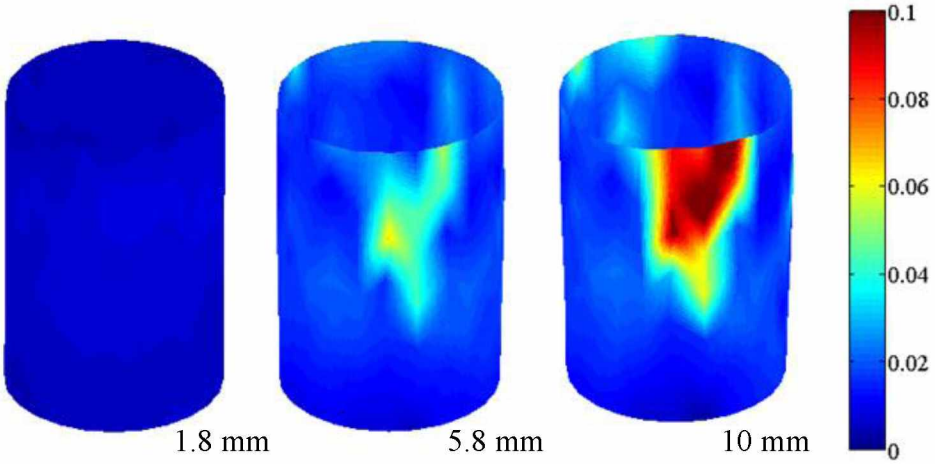

(b) Axial strain

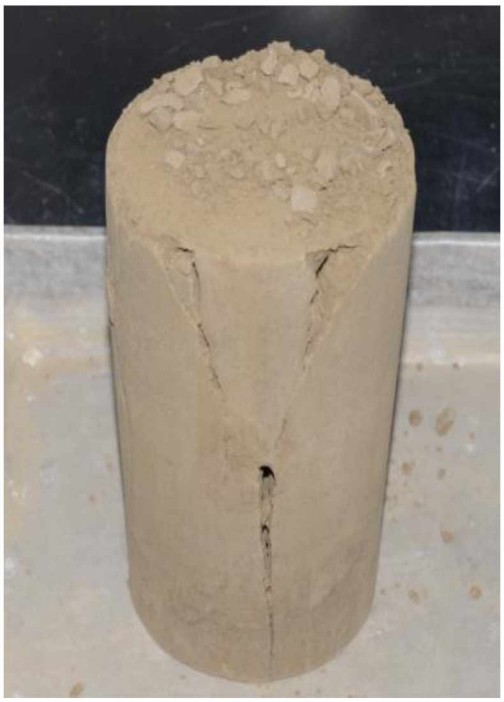

(c) Photo of soil 5 after failure

Figure 5.6 Deformation of soil 5 at different shearing stages.

5.6.3 Total Volume Change and Stress-Strain Behavior

To calculate the total volume of the soil specimen, an arbitrary point on the top circular edge was connected to all other points on the same circle to form the top surface. The bottom surface was formed the same way such that an enclosed 3D surface was created. The volume of the enclosed 3D surface was integrated and considered as the total soil volume from which the specific volume and degree of saturation of the soils was derived. Figure 5.7a presents the average matric suction changes in the two high-suction tensiometers during the triaxial shearing tests for all soils. Nearly all soil specimens experienced continuous decreases in matric suction during triaxial shearing. Unlike other soils, matric suction in soil 1 (water content of 6.0% and

confining pressure of 5 kPa) first decreased and then increased after the vertical strain was greater than 1.5%.

Figure 5.7b shows the changes in specific volumes for all soil specimens during triaxial shearing. All soils exhibited similar characteristics: volumes decrease in the early stage (within 1% of axial strain) of shearing and dilate afterwards. Figure 5.7c reports the stress-strain curves for eleven triaxial shearing tests. An unloading process was applied during shearing for some of the soil specimens. All stress-strain curves indicated hardening at the initial shearing stage, which was followed by subsequent softening. Due to the low confining pressures (5 or 40 kPa), all tested soil specimens failed at axial strains of less than 2%. Generally, soil specimens with lower initial moisture had higher stiffness and shear strength. Also, soil strengths were higher when the applied confining pressure was higher (40 kPa). These test results were considered reasonable. From the stress-strain curves, the soil stress states at failure, including matric suction, and net minor and major principal stresses were obtained (see Table 5.2).

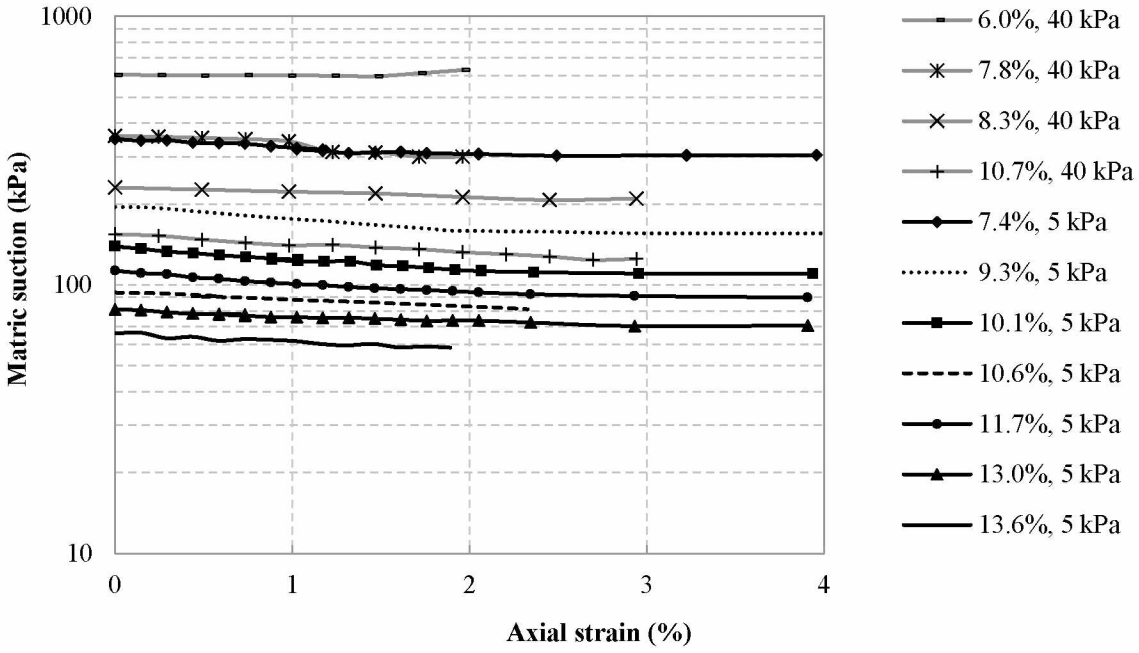

(a) Matric suction variation during tesing

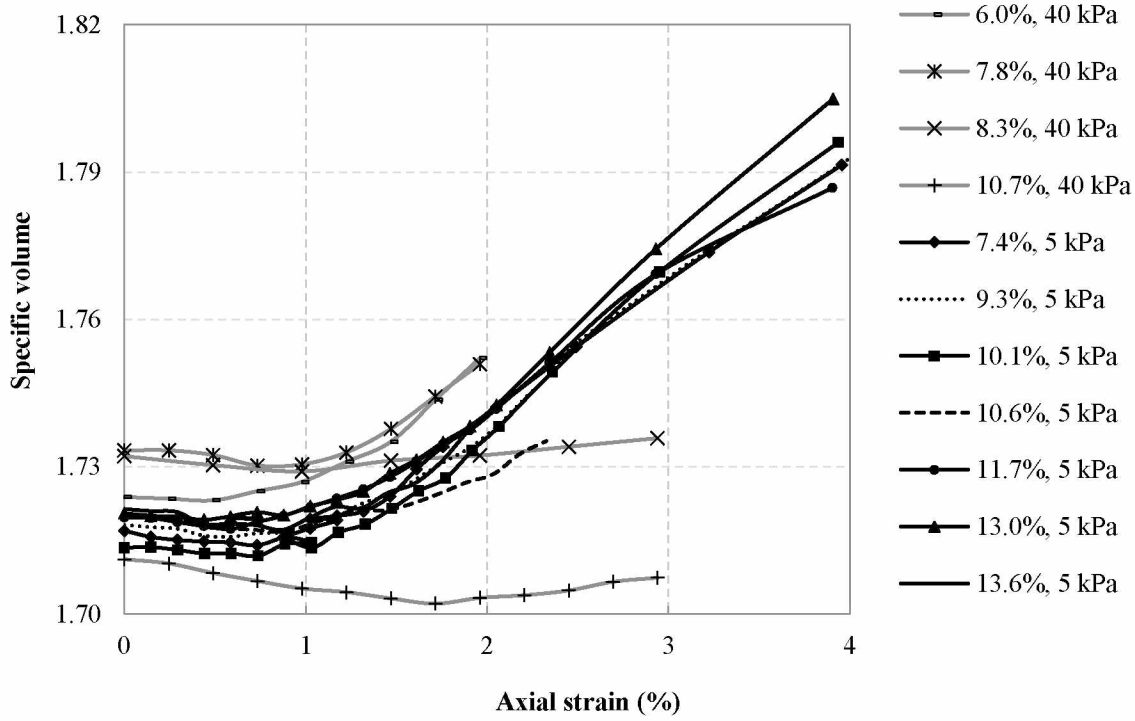

(b) Volume change during testing

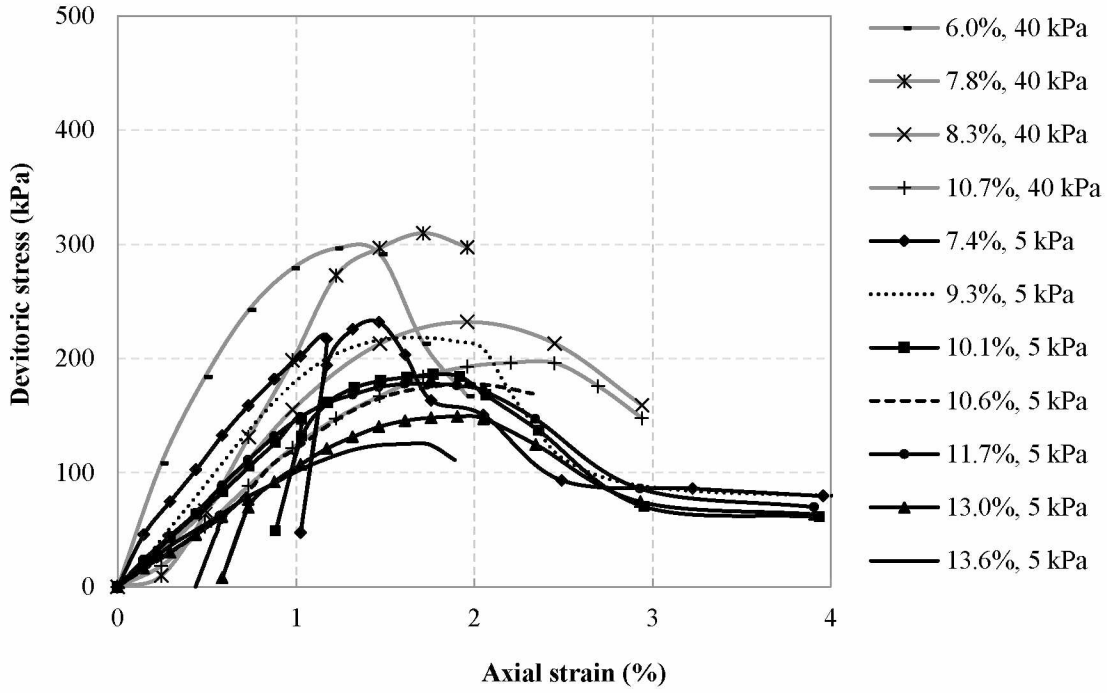

(c) Stress-strain curves

Figure 5.7 Compression test results for specimens under different confining pressures.

5.7 Calibration of Shear Strength Parameters

In the modified unconfined compression tests, the stress paths of the soil during triaxial compression tests were recorded. Figure 5.8 shows the Mohr circles at failure for all soil specimens. These test results can be used to calibrate the shear strength parameters of unsaturated soils.

In conventional soil mechanics, model parameters are calibrated based on experimental tests. The goal of model calibration is to find appropriate parameters that best predict soil response in relation to the available experimental tests. Usually, some kind of redundancy in data points occurs for model calibration that best represents soil behavior, especially when soil

behavior is highly nonlinear. As a result, calibration of a model will inevitably involve some statistical analysis (Mattsson et al. 2001 and Cekerevac et al. 2006).

Mathematically, calibration of a shear strength parameter for unsaturated soils is a process of minimizing error between measured soil strengths and the soil strengths predicted by Equation 5.1 by varying the parameters c', ϕ', and ϕ^b. Since c', ϕ', and ϕ^b have physical meanings, there are also some constraints as follows:

$c' > 0$, $0 < \phi' < \pi/2$, and $0 < \phi^b < \pi/2$ Equation 5.2

Calibration of the shear strength of unsaturated soils using the results from modified unconfined compression tests is simplified into a constrained optimization problem: find a combination of the model parameters of c', ϕ', and ϕ^b, which can minimize the overall difference between measured and predicted shear strength of

$$F\ X = \sum_{i=1}^{n} w_i \left[\tau_{fm\ i} - \tau_{fp\ i} \right]^2 \quad \text{Equation 5.3}$$

subject to constraints in Equation 5.2. In order to use Equation 5.1, the net normal stress at the failure plane $\sigma - u_{a\ f}$ must be known. However, $\sigma - u_{a\ f}$ is related to c', ϕ', and ϕ^b, which are unknown and need to be calibrated. An alternative version of Equation 5.1 is proposed to solve the problem. Equation 5.1 can be rewritten as follows:

$$\tau_f = c_a' + \left(\sigma - u_{a\ f} \right) \tan \phi' \quad \text{Equation 5.4}$$

where $c_a' = c' + \left(u_a - u_{w\ f} \right) \tan \phi^b$, apparent cohesion. Similar to shear strength for saturated soils, Equation 5.4 can be written in terms of major and minor principal stress at failure:

$$\sigma_{1f} - u_a = \left(\sigma_{3f} - u_a \right) \tan^2 \left[\frac{\pi}{4} + \frac{\phi'}{2} \right] + 2c_a \tan \left[\frac{\pi}{4} + \frac{\phi'}{2} \right] \quad \text{Equation 5.5}$$

or

$$(\sigma_{1f} - u_a) = (\sigma_{3f} - u_a)\tan^2\left[\frac{\pi}{4} + \frac{\phi'}{2}\right] + 2\left[c' + (u_a - u_w)_f \tan\phi^b\right]\tan\left[\frac{\pi}{4} + \frac{\phi'}{2}\right] \quad \text{Equation 5.5}$$

Mathematically, calibration of the shear strength of unsaturated soils using the results from modified unconfined compression tests is done to find an appropriate combination of c', ϕ', and ϕ^b, which can minimize the overall difference between measured net major principal stress at failure $(\sigma_{1f} - u_a)_m$ and the theoretical results, as predicted by Equation 5.4 for measured $(\sigma_{3f} - u_a)_m$ and $(u_a - u_w)_{fmi}$ under the constraints of Equation 5.2. The corresponding objective function can be expressed as follows using the Euclidean norm and the independent state variables of all experimental points at virgin states:

$$F(X) = \sum_{i=1}^{n} w_i \left[(\sigma_{1fm} - u_a)_i - (\sigma_{1fp} - u_a)_i \right]^2$$
$$= \sum_{i=1}^{n} w_i \left\{ (\sigma_{1fm} - u_a)_i - \left((\sigma_{3f} - u_a)_i \tan^2\left[\frac{\pi}{4} + \frac{\phi'}{2}\right] + 2\left[c' + (u_a - u_w)_{fmi} \tan\phi^b\right]\tan\left[\frac{\pi}{4} + \frac{\phi'}{2}\right]\right)\right\}^2$$

Equation 5.6

If all experimental results have the same weight w_i of 1, the above objective function is actually the least-squares method, in which the objective function is defined as the sum of the squares of the difference between the experimental $(\sigma_{1f} - u_a)_m$ value versus the theoretical values predicted by Equation 5.5 (that is, the sum of the squares of the residuals). The "best" fit is defined as a combination of model parameters that results in the least error between results from the performed tests compared with the predicted values using Equation 5.6. The least-squares method finds its optimum when the sum of squared residuals, F(X), is the minimum subject to constraints in Equation 5.2. Since all the Mohr circles for all soil specimens at failure are known, even if the soil specimens used in the modified unconfined compression tests are at different suction levels, the results can still be used to calibrate the shear strength parameters of the soil.

The modified unconfined compression test results for soil specimens sheared under different confining pressure levels (5 kPa and 40 kPa) were used to evaluate the unsaturated soil shear strength. The popular Broydon–Fletcher–Goldfarb–Shanno (BFGS) method (Rao 1996), which is a quasi-Newton method, was used to calibrate the model parameters. It was found that c', ϕ', and ϕ^b were 72.4 kPa, 19.5°, and 4.8°, respectively. A R^2 of 87.3% indicated a good correlation between test results and predictions. The obtained Mohr–Coulomb failure envelope and Mohr circles for soil specimens with different moisture contents at failure were also plotted in Figure 5.8.

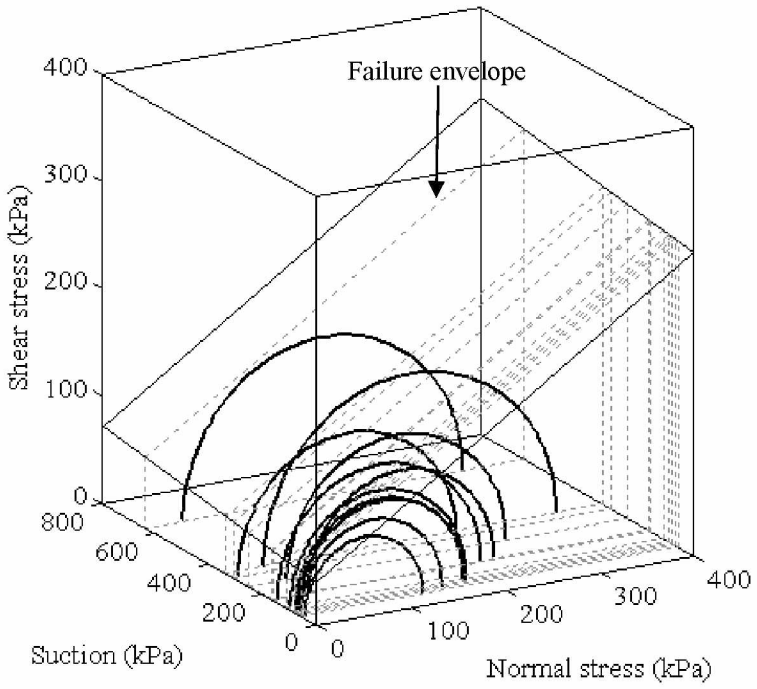

Figure 5.8 Mohr circles at failure and failure envelope for compacted Fairbanks silt.

5.8 Cost and Time

The modified unconfined compression testing system is simple and cost-effective to develop. The camera and lens used in this study cost $1,700. It took $2,500 to fabricate two high-suction tensiometers. All these components are readily available to universities, industrial

labs, and consulting companies. Depending upon the loading steps and suction levels in the soil, an undrained triaxial shearing test typically takes 5-10 hours to accomplish. As a result, this type of test can be justified for time-sensitive engineering projects.

5.9 Conclusions

This paper presents a modified unconfined compression testing system to investigate the stress-strain behavior of unsaturated soils at low confining stresses. Negative air pressure was used to provide the low confining pressure needed for the tests. High-suction tensiometers were used to monitor soil matric suction variation during testing. A noncontact photogrammetric method was used to accurately reconstruct the 3D model of unsaturated soil specimens from images taken by a low-cost digital camera. The constructed soil model can provide the full-field 3D soil deformation from which both total and localized volume changes are calculated. A simple and objective method was proposed to calibrate the unsaturated shear strength from undrained triaxial shearing tests conducted on the proposed testing system. A series of tests were performed to demonstrate the use of the modified unconfined compression testing system in evaluating the stress-strain behavior of unsaturated soil under different confining stresses. Results from this study indicate that the newly developed modified unconfined compression testing system is cost-effective for rapid and reliable evaluation of stress-strain behavior of unsaturated soils under low confining stresses.

5.10 References

Albert, J., H. G. Maas, A. Schade, and W. Schwarz, Pilot studies on photogrammetric bridge deformation measurement. *Proceedings of the 2nd IAG Commission IV Symposium on Geodesy for Geotechnical and Structural Engineering*, pp. 21-24 May, Berlin, Germany, 2002.

Alonso, E.E., A. Gens, and A. Josa. A constitutive model for partially saturated soils. *Géotechnique*, Vol. 40, No. 3, 1990, pp. 405-430.

ASTM. D2166-00. Standard Test Method for Unconfined Compressive Strength of Cohesive Soil. American Society for Testing and Materials, Philadelphia, PA, 2000.

Bao, C.G, B.W, Gong, and L.T. Zhan. Properties of unsaturated soils and slope stability for expansive soils. *Proceedings of the 2nd International Conference on Unsaturated Soils.* Beijing: International Academic Publishers, Vol. 2, 1998, pp. 71-98.

Bishop, A. W. and I. B. Donald, The experimental study of partly saturated soil in the triaxial apparatus. *Proceedings,* 5th *International Conference on Soil Mech*anics, 1, 1961, pp.13-21.

Caruso, A. and A. Tarantino. A shear box for testing unsaturated soils from medium to high degrees of saturation. *Géotechnique*, Vol. 54, No. 4, 2004, pp. 281-284.

Cekerevac, C., S. Girardin, G., Klubertanz, and L. Laloui, Calibration of an elasto-plastic constitutive model by a constrained optimization procedure. *Computers and Geotechnics,* Vol. 33, No. 8, 2006, pp.432-443.

Chae, J.G., B.S. Kim, S.W. Park, and S. Kato. Effect of suction on unconfined compressive strength in partly saturated soils. *KSCE Journal of Civil Engineering,* Vol. 14, No. 3, 2010, pp.281-290.

Chiu, C.F., Y.J. Cui, P. Delage, E. De Laure, and E. Haza. Lessons learnt from suction monitoring during centrifuge modelling. In: Tarantino, A., Romero, E., and Cui, Y.J. (Eds.), *Advanced Experimental Unsaturated Soil Mechanics*. Balkema, Leiden, 2005, pp. 3-8.

Colmenares, J.E., and A.M. Ridley. Stress-strain and strength relationships for a reconstituted clayey silt. *Proceedings of the 3rd International Conference on Unsaturated Soils*. UNSAT, 2002, Vol. 2, pp. 481-484.

Cui, Y.J., and P. Delage. Yielding and plastic behavior of an unsaturated compacted silt. *Géotechnique*, Vol. 46, No. 2, 1996, pp. 291-311.

Cui, Y.J., A.M. Tang, A. Mantho, and E. De Laure. Monitoring field soil suction using a miniature tensiometer. *Geotechnical Testing Journal,* Vol. 31, No. 1, 2008, pp. 95-100.

Delage, P. Experimental unsaturated soil mechanics. *Proceedings of the 3rd International Conference on Unsaturated Soils*. Recife, Brazil, UNSAT, 2002, Vol. 3, pp. 973-996, Juca, J.F.T., De Campos, T.M.P., Marino, F.A.M. (Eds.), Balkema.

FHWA. *Geotechnical Aspects of Pavements Reference Manual*. Available online at: http://www.fhwa.dot.gov/engineering/geotech/pubs/05037/05037.pdf, 2006.

Fredlund, D. G., and H. Rahardjo. *Soil Mechanics for Unsaturated Soils*. John Wiley & Sons, New York, 1993.

Fredlund, D.G., N.R. Morgenstern, and A. Widgerr. The shear strength of unsaturated soils. *Canadian Geotechnical Journal*, Vol. 15, No. 3, 1978, pp. 313-321.

GDS. An introduction to GDS Mid-Plane Pore Pressure Transducer. 2010. Available at http://www.youtube.com/watch?v=g9-fqSMbIBU

Godt, J.W., R.L. Baum, W.Z. Savage, D. Salciarini, W.H. Schulz, and E.L. Harp. Transient deterministic shallow landslide modeling: requirements for susceptibility and hazard assessments in a GIS framework, *Engineering Geology*, Vol. 102, 2008, pp. 214-226.

Guan,Y. and D.G. Fredlund, Use of tensile strength of water for the direct measurement of high soil suction. *Canadian Geotechnical Journal,* Vol. 36, 1997, pp. 604-614.

Hampel, U. and H.G. Maas. Application of digital photogrammetry for measuring deformation and cracks during load tests in civil engineering material testing. *Optical 3-D Measurement Techniques,* VI, Vol. II, 2003, pp. 80-88.

Hoyos, L.R. Experimental and computational modeling of unsaturated soil behavior under true triaxial stress states. *Ph.D. dissertation*, Georgia Institute of Technology, Atlanta, 1998.

Jotisankasa, A. Collapse behavior of a compacted silty clay. *Ph.D. thesis*, Imperial College, London, 2005.

Ladd, R.S. Preparing test specimens using undercompaction. *Geotechnical Testing Journal*, Vol. 1, No. 1, March 1978, pp. 16-23.

Le, T.T., Y.J. Cui, J.J. Munoz, P. Delage, A.M. Tang, and X.L. Li. Studying the hydric and mechanical coupling in Boom clay using an oedometer equipped with a high capacity tensiometer. *Frontiers of Architecture and Civil Engineering in China*, Vol. 5, No. 2, 2011, pp.160-170.

Li, L. and X. Zhang. Development of a New High-Suction Tensiometer. Soil behavior and Geomechanics: 2014, pp. 416-425. doi: 10.1061/9780784413388.043.

Lin, H., and D. Penumadu. Strain localization in combined axial-torsional testing on Kaolin clay. *Journal of Engineering Mechanics*, Vol. 132, No. 5, 2006, pp. 555-564.

Maas, H. G., U. Hampel, and M. Schulze. Application of digital photogrammetry and computer tomography for measuring deformations, cracks and structural changes during load tests of textile reinforced test objects. *Proceedings of the 2nd Colloquium on Textile Reinforced Structures,* 2003.

Mattsson, H., M. Klisinski, and K. Axelsson. Optimisation routine for identification of model parameters in soil plasticity. *International Journal for Numerical and Analytical Methods in Geomechanics*, Vol. 25, No. 5, 2001, pp. 435-472.

Mendes, J. Assessment of the impact of climate change on an instrumented embankment: An unsaturated soil mechanics approach. *Ph.D. thesis*, Durham University, 2011. Available online: http://etheses.dur.ac.uk/612/

Mendes, J., D. Gallipoli, D. Toll, C.E. Augarde, and F.D. Evans, A system for field measurement of suctions using removable suction probes. In: Toll, D.G., Augarde, C.E., Gallipoli, D., and Wheeler, S.J. (Eds.), Unsaturated Soils: Advances in Geo-Engineering, *Proceedings, 1st European Conference on Unsaturated Soils*, Durham, 2008, pp. 219-225.

Mikhail, E.M., J.S. Bethel, and J.C. McGlone, *Introduction to Modern Photogrammetry*. John Wiley & Sons, Inc. ISBN 0-471-30924-9, 2001.

Ng, C.W.W, L.T. Zhan, and C.G. Bao Performance of an unsaturated expansive soil slope subjected to artificial rainfall infiltration. *Géotechnique*, Vol. 53, No. 2, 2002, pp. 143-157.

Rao, S.S. *Engineering Optimization, Theory and Practice*. 3d ed. John Wiley & Sons, Inc., 1996.

Ridley, A.M., and J.B. Burland, A new instrument for the measurement of soil moisture suction. *Géotechnique*, Vol. 43, No. 2, 1993, pp. 321-324.

Sharma, R.S. Mechanical behavior of unsaturated highly expansive clays. *Ph.D. thesis*, University of Oxford, UK, 1998.

Sivakumar, V. A critical state framework for unsaturated soil. *Ph.D. thesis*, University of Oxford. 1993.

Tang, A.M., A.N. Ta, Y.J. Cui, and J. Thiriat. Development of a large-scale infiltration tank for determination of the hydraulic properties of expansive clays. *Geotechnical Testing Journal*, Vol. 32, No. 5, 2009, pp.385-396.

Tarantino, A., and S. Tombolato. Coupling of hydraulic and mechanical behaviour in unsaturated compacted clay. *Géotechnique*, Vol. 55, No. 4, 2005, pp. 307-317.

Teixeira, P.F., and F.A.M. Marinho. Determination of the soil water retention curve by means of high capacity tensiometers. *XIII Congresso Brasileiro de Mecânica dos Solos e Engenharia Geotécnica*, Curitiba: COBRASEG, 2006, 1, pp. 423-427.

Toll, D.G., S.D.N. Lourenço, J. Mendes, D. Gallipoli, F.D. Evans, C.E. Augarde, Y.J. Cui, A.M. Tang, J.C. Rojas, L. Pagano, C. Mancuso, C. Zingariello, and A. Tarantino. Soil suction monitoring for landslides and slopes. *Quarterly Journal of Engineering Geology & Hydrogeology,* Vol. 44, 2011, pp. 23-33.

Triggs, B., P.F. McLauchlan, R.I. Hartley, and A.W. Fitzgibbon. Buddle adjustment –A modern synthesis. In: Triggs, B., Zisserman, A., and Szeliski, R. (Eds.), *ICCV-WS, LNCS*, Vol. 1983, 2000, pp. 298-375.

Zhan, L. Soil-water interaction in unsaturated expansive soil slopes. *Frontiers of Architecture and Civil Engineering in China*, Vol. 1, No. 2, 2007, pp. 198-204.

Zhang, X., L. Li, G. Chen, and R.L. Lytton. 2015. A photogrammetry-based method to measure total and local volume changes of unsaturated soils during triaxial testing. *Acta Geotechnica*, 10(1): 55-82.

CHAPTER 6. CONCLUSIONS AND RECOMMENDATIONS

In this study, a new triaxial testing system was developed for the constant water content triaxial tests on unsaturated soils. To investigate unsatuated soil behavior using the proposed triaxial test system, a series of constant water content tests was conducted on unsaturated soils with different water contents. Some conclusions are summariezed in the following section. A modified unconfined compression testing system, which is a simplified version of the new triaxial testing system, was also developed to investiagte unsaturated soil behaviors under low stress (less than 100 kPa) conditions.

6.1 Conclusions

1. A new high-suction tensiometer, based on a miniature pressure transducer, was designed, fabricated, saturated, and calibrated. After saturation, the maximum attainable suction was determined to be approximately 1100 kPa through free evaporation tests. The newly developed high-suction tensiometers were sucessesfully used to monitor unsaturated soil suction changes during the constant water content triaxial tests.

2. A new photogrammetry-based method was developed to measure soil deformations during triaxial testing. The newly developed photogrammetry-based method is significantly different from existing image-based methods. For this photogrammetry-based method, the camera used was carefully calibrated. The principle of photogrammetry was adopted to accurately determine the orientation of the camera stations where the images were captured. For one single measurement target on the specimen surface, multiple measurements were performed which significantly reduced the measurement error. The acrylic cell was assumed to be barrel-shaped and deformable with a uniform thickness. Deformation of the cell wall under different

chamber pressures could be captured through the photogrammetric technique. The optical ray tracing technique was adopted for refraction correction at the interfaces of the air to acrylic cell and the acrylic cell to water. Based upon the recorded 3D coordinates of the measurement targets on the specimen surface, a full-field 3D strain distribution could be extracted. With this photogrammetry-based method, the conventional triaxial test apparatus designed for saturated soils can be used for triaxial testing on unsaturated soils with little modification. Most importantly, the accuracy of the photogrammetry-based method can be self-checked. Another advantage of the photogrammetry-based method is that it can be utilized for deformation measurements of both saturated and unsaturated soils during triaxial testing with the same system setup.

3. A new triaxial testing system was presented to investigate behavior of unsaturated soils during the constant water content testing. In this system, the saturated high-suction tensiometers were used to monitor soil matric suction variation during testing. The newly developed photogrammetry-based method was used to accurately reconstruct the 3D models of unsaturated soils for full-field 3D deformation measurements. Through a series of constant water content triaxial tests on unsaturated soils, the proposed triaxial testing system proved to be a cost-effective way for unsaturated soil characterization. Due to the low permeability of unsaturated soils, the conventional way to characterize the shear strength and constitutive behavior of unsaturated soils using the suction-controlled test was very time-consuming. The use of constant water content tests significantly reduced the time to characterize an unsaturated soil from years to several days required. As a result, to investigate an unsaturated soil behavior, the constant water content test is a time-effective alternative when compared with the conventional suction-controlled triaxial tests.

4. A modified unconfined compression testing system was developed to investigate the behavior of unsaturated soils at low confining stresses. With this system, the equipment required for characterizing unsaturated soils was further simplified. Negative air pressure was used to provide the low confining pressure required for the triaxial tests. In this system, the saturated high-suction tensiometers were used to monitor soil matric suction variation during testing. A noncontact photogrammetric method was used to accurately reconstruct the 3D models of unsaturated soils based upon the images captured by a low-cost digital camera. An example was also given to demostrate the use of constant water content test results for shear strength characterization of unsaturated soils.

6.2 Recommendations

1. Usually, during triaxial testing, a soil specimen is considered as a soil element. In other words, the soil deformation during triaxial testing is assumed to be uniformly distributed. However, in this study, with the photogrammetry-based method, the unsaturated soil deformations during triaxial testing were measured in detail through the targets on soil surface. Significant volumetric strain nonuniformity during shearing was detected which is not consistent with the assumption of uniform soil deformation. As a result, the results from triaxial tests based upon this assumption may be questionable and misleading. More research effort dedicated to analyzing soil stress-strain behavior nonuniformity is recommended.

2. Two high-suction tensiometers were attached to the unsaturated soil surface for matric suction measurement during triaxial testing. Since the volumetric strain during triaxial testing is not uniformly distributed, it is reasonable to assume that matric suction variation during testing might not be uniform either. Thus, in order to obtain more representative suction variation

results, more tensiometers are recommended to be attached to the unsaturated specimen surface during triaxial testing.

3. A new triaxial testing system was presented to investigate the behavior of unsaturated soils at different confining stresses. However, at present, the suction-controlled triaxial test is still widely used for unsaturated soil characterization. The proposed undrained triaxial test system can be easily modified for the suction-controlled triaxial test. To be able to control soil suction during testing, the porous stone in the triaxial cell pedestal is replaced by a high air entry ceramic disc. Also, an air pressure tube connected to the top loading cap is installed for the purpose of suction control using the axis-translation technique. Soil volume change measurement during the suction-controlled triaxial test is exactly the same as that for the new triaxial testing system. So, the new suction-controlled testing system is much simpler when compared with the conventional system due to the use of the photogrammetry-based method for volume change measurement.

APPENDIX A PHOTOGRAMMETRY-BASED METHOD TO MEASURE TOTAL AND LOCAL VOLUME CHANGES OF UNSATURATED SOILS DURING TRIAXIAL TESTING[1]

Abstract

Triaxial tests have been widely used to evaluate soil behaviors. In the past few decades, several methods have been developed to measure the volume changes of unsaturated soil specimens during triaxial tests. A literature review indicates that until now it remains a major challenge for researchers to measure the volume changes of unsaturated soil specimens during triaxial testing. This paper presents a non-contact method to measure the total and local volume changes of unsaturated soil specimens using a conventional triaxial test apparatus for saturated soils. The method is simple and cost-effective, requiring only a commercially available digital camera to take images of an unsaturated soil specimen during triaxial testing from which an accurate 3D model of the soil specimen is reconstructed. In this proposed method, the photogrammetric technique is utilized to determine the orientations of the camera where the images are taken and the shape and location of the acrylic cell, multiple optical ray tracings are employed to correct the refraction at the air-acrylic cell and acrylic cell-water interfaces, and a least-square optimization technique is applied to estimate the coordinates of any point on the specimen surface. The paper first discusses the theoretical aspects of the proposed method. An image analysis on a caliper was then used to evaluate the accuracy of photogrammetric analysis in the air. A series of isotropic compression tests on a stainless steel cylinder were used to demonstrate the procedure and evaluate the accuracy of the proposed method, while triaxial shearing tests on a saturated sand specimen were used to evaluate the capacity of the proposed method for measuring the total and localized volume changes during triaxial testing. Results

obtained from the validation tests indicate that the accuracy for the photogrammetry in the air is about 10 um. The average accuracy for single point measurements in the triaxial tests ranges from 0.056 to 0.076 mm with standard deviations varying from 0.033 to 0.061 mm. The accuracy for total volume measurements is better than 0.25 %.

Keywords: Least-square optimization; Optical ray tracing; Photogrammetry; Triaxial test; Unsaturated soil; Volume change

[1]Zhang, X., Li, L., Chen, G., and Lytton, R. L., (2015), "A Photogrammetry-Based Method to Measure Total and Local Volume Changes of Unsaturated Soils during Triaxial Testing," Acta Geotechnica, Vol. 10, No.1, pp. 55-82.

List of Symbols

$x_I^{'}, y_I^{'}$	coordinates of the image point I in the physical coordinate system of x'Ay' (mm),
F_x, F_y	format sizes of the camera image sensor in x and y directions (mm),
m_I, n_I	coordinates of the image point *I* the pixel coordinate system *mAn* (pixel),
M, N	total pixel numbers of the camera image sensor in *x'* and *y'* directions (pixel),
x_I, y_I, z_I	x, y, and z coordinates of point I in the local coordinate system (xyz) (mm), subscript "I" represents the coordinates are associated with point I,
f	perpendicular distance between the pinhole and the image plane (equivalent to focus length of the camera) (mm),
P_x, P_y	coordinates of principal point in the physical coordinate system of x'Ay' (mm),
κ, ω, φ	three rotation angles from one coordinate system to another,
R	rotation matrix defined by the three rotation angles,
X_s, Y_s, Z_s	coordinates of a perspective center in global coordinate system,
X_I, Y_I, Z_I	x, y, and z coordinates of point I in the global coordinate system,
A, B, C	regression coefficients to determine the shape of the acrylic cell wall,
X_R, Y_R, Z_R	coordinates of the center of the acrylic cell in the global coordinate system,
$\vec{i}$	incident ray,
$\alpha_a, \beta_a, \gamma_a$	direction cosine of an optical ray,
d_i	travel distance of an optical ray,
$\vec{n_i}$	unit vector of the normal,

$\vec{r}_i$ unit vector for a refractive ray,

a_i, b_i, c_i coefficients for determination of d_i,

X_D, Y_D, Z_D coordinates of an intercept point on the outer surface of acrylic cell wall in the global coordinate system,

X_C, Y_C, Z_C coordinates of an intercept point on the inner surface of acrylic cell wall in the global coordinate system.

Introduction

The total and local volume changes of a soil specimen are essential parameters in understanding deformation and strength characteristics of soils. Triaxial tests have been widely used to evaluate constitutive behavior for both saturated and unsaturated soils. A saturated soil is a two-phase system which includes water and soil solids. For triaxial tests on saturated soils, the volume change is usually monitored by pore-water volume exchange of the sample. Figure 1a shows a conventional triaxial test apparatus for saturated soils. An unsaturated soil is commonly referred to as a three-phase system which includes water, air, and soil solid. The total volume change of unsaturated specimen is no longer equal to the pore water volume change. As a result, the conventional method to measure the volume change for saturated soil specimens is no longer applicable for unsaturated soils. In the past few decades, many research efforts have been made to develop alternative volume measurement methods for unsaturated soil in triaxial tests. This paper reviews the methods specially developed for volume measurements for unsaturated soils and methods developed for other purposes but can be potentially used for volume measurements for unsaturated soils. It is found that the existing methods have limitations and it remains a major challenge for researchers to measure the volume change of an unsaturated soil specimen during triaxial testing. A noncontact optical method is therefore developed to measure the total and local volume change of unsaturated soil specimens during triaxial testing by integrating photogrammetry, optical ray tracing, and least-square optimization techniques. This method allows the use of traditional triaxial test apparatus for saturated soils to perform tests for unsaturated soils with minor modifications. Only a commercially available digital camera is needed to take images of an unsaturated soil specimen during triaxial testing from which accurate 3D model of the soil specimen is reconstructed. This paper first discusses the theoretical

aspects of the proposed method. Then, results from three validation tests are presented to demonstrate the simplicity and accuracy of the proposed method.

Literature Review

A comprehensive literature search is conducted to review existing methods for the measurements of the volume changes of unsaturated soil specimens. The literature review includes two parts: methods specially designed for measuring volume changes for unsaturated soil specimens; and those developed for strain localization measurements but may potentially be used to measure volume changes. Table 1 summarizes the pros and cons of these methods. Detailed discussions for these methods are presented below.

Table 1 Existing methods for total and local volume changes for unsaturated soils

Method	Reference	Equippment Modification ?	Volume Change	Advantages	Disadvantages	Accuracy	Cost
Double Cell System	Bishop and Donald (1961)	Yes	Total	Straightforward good for large strains widely used	Difficult to calibrate, water absorption of acrylic cell, sensitive to temperature and pressure possible air buble in channel, leakage	>0.25%	$50K-$150K
Differential Pressure Transducer	Ng et al. (2002)	Yes	Total	Stable, insensitive to temperature suitable for large strains	Require careful calibrations, need use de-aired water, difficulty in air bubble removal	>0.25%	$50K-$150K
Measurement of Air and Water Volume Changes	Geiser (1999)	Yes	Total	Direct measurement on volume change of air and water	Assume air phase continuous, sensitive to temperature and atmospheric pressure, undetectable leakage	>0.25%	$30K
LVDT	Blatz and Graham (2000)	No	Local	suitable for small strains	Clamping problems for soft soils, limited measurements	0.01mm	$1K/each
Laser Scanner	Romero et al. (1997)	Yes	Local	Non-contact	High cost setup, sophisticated installation procedures	>5% (V)	>$30K
Digital Image Analysis with Refracion Correction	Macari et al. (1997)	No	Local	Non-contact, low cost	Require accurate control of camera position, multiple unrealistical assumptions (see discussions in paper)	0.2-0.3mm	<$2K
Digital Image Correlation	White et al. (2003)	No	Local	Non-contact, low cost	Cannot consider influence of refraction	>5% (V)	<$2K
X-ray CT	Desrues et al. (1996)	Yes	Total & Local	Non-contact, can detect internal local densification	High cost setup, sophisticated installation procedures potential health concern	>0.02mm	$200K-$2M
Photogrammetry with Refraction Correction	This Study	No	Total & Local	Non-contact, low cost, consider refraction	Computationally intensive	<0.076mm <0.25%	<$2K

Methods Specifically Developed for Measuring Volume Changes for Unsaturated Soil Specimens

Laloui et al. (2006) summarized the existing methods for measuring volume change of unsaturated soil specimens, which can be broadly classified into three categories: (i) measurement of the cell fluid, (ii) direct measurement of the air and water volumes, and (iii) direct measurement of the soil specimen volume change.

Measurement of the cell fluid

The principle of this method is to deduce unsaturated soil volume changes from volume changes in the confining cell liquid. Although the principle is simple, several problems are often associated with this method, such as immediate expansion of cell wall caused by a pressure increase, Plexiglas creep under constant stress, and possible water leakage. Theoretically speaking, a conventional triaxial cell for saturated soils as shown in Figure 1a can be used if carefully calibrated. However, the accuracy of the method depends on the quality of the calibration procedure, the volume capacity and the precision of the measurements. Numerous calibrations are needed since corrections depend on time, stress path, and stress level (Bishop and Donald 1961).

(a) Saturated Soils

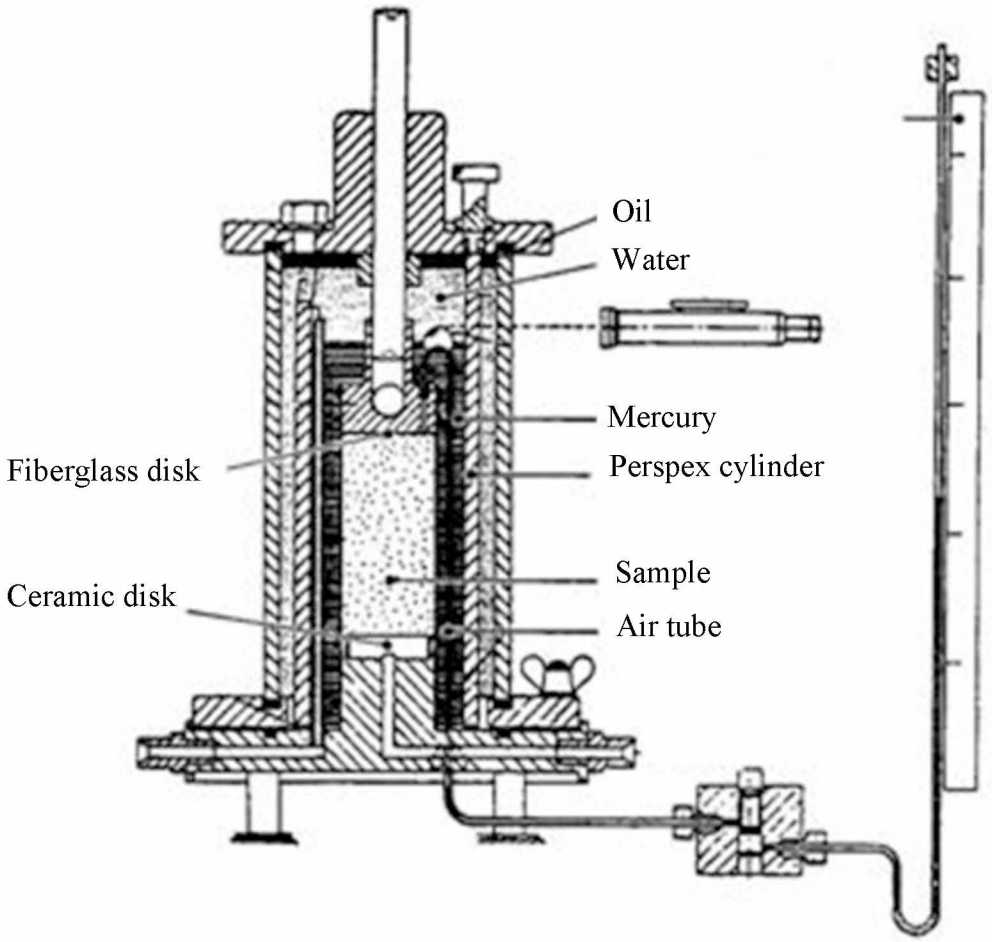

(b) Double-cell system for unsaturated soils (Bishop and Donald 1961)

Figure 1 Typical apparatuses for triaxial soil testing

Bishop and Donald (1961) added an inner cylinder sealed to the outer cell base to minimize the liquid volume (double-wall cell). Mercury was used as the cell fluid between the inner cylinder and the specimen to enhance accuracy. Water was used as the outer liquid while the mercury was enclosed in an internal jacket with the cell pressure applied to both sides of the jacket. The overall volume change of the soil specimen was then deduced by measuring the rise

or fall of the mercury vertical level in the inner cylinder. Josa et al. (1987) introduced the automatic monitoring of mercury level via a metal ring floating on its surface. Wheeler (1988) designed a double-wall cell to minimize the confining liquid in which an inner cylinder was sealed to both the top and the base of the cell. Equal cell pressures were applied to the inner and outer cells to avoid deformation of the inner cell. Soil volume change was then inferred from the volume leaving or entering the inner cell. Cui and Delage (1996) replaced mercury with water for safety reasons and measured water levels via high-precision cathetometer based readings. Further improvements to the inner cylinder technique have been introduced by Rampino et al. (1999). Ng et al. (2002) recorded the differential pressure between the water inside the open-ended inner cell and the water inside a reference tube using a high accuracy differential pressure transducer (Figure 1b). The double-wall cell method requires major equipment modifications and is therefore expensive. A double-wall cell testing system typically costs $150,000 and is complex to operate. It cannot eliminate errors from the deformations of the top and the base of the cell. In addition, air bubbles often exist in the inner cell and are difficult to remove. For the acrylic inner cell, water absorption is affected by pressure, temperature, and time, making the calibration of the system very difficult. For small specimens (38 mm in diameter), errors due to this absorption can be significant. Larger specimen however requires longer testing time which increases creep. Steel inner cell can be an alternative to solve the problem. However, for this non-transparent inner cell, it is difficult to examine the existence of air bubbles in the cell. The double-wall cell has been extensively used for unsaturated soil testing in the past five decades. A carefully calibrated double-wall cell can measure total volume change to an accuracy of 0.25% (GDS 2009).

Direct measurement of the air and water volumes

In this method, volume change of a soil specimen is obtained by measuring the air and water volume changes separately and adding them together (Geiser 1999; Laudahn et al. 2005). It requires adding an air-volume controller filled with air instead of water. To be successful, this method requires the air phase to be continuous. This method is sensitive to small temperature and atmospheric pressure changes. In addition, undetectable air leakage and diffusion through tubes, connections, and high-air-entry disk can also influence the accuracy of the measurements. The errors can be significant for consolidated drained tests, which often takes months to complete. Furthermore, excess pore air pressure can be generated during the test and lead to misleading volume changes. Various improvements were proposed to overcome these limitations. Geiser (1999) proposed a mixed air and water controller that allows reduction of air volume to the tubing only to minimize the errors from changes in atmospheric pressure and temperature. Laudahn et al. (2005) proposed a method for measuring pore-air volume changes in drained tests under atmospheric conditions. GDS Instruments adds a U-tube filled with ethanol to their volume controller for pore air to maintain the pore air always at atmospheric pressure (GDS 2009). Although these improvements are available, direct measurement of the air and water volumes is not extensively used by researchers at present.

Direct measurement of the soil specimen volume change

In this method, soil volume change is computed from the direct measurements of axial and radial specimen displacements. This category can be further divided into contact and non-contact methods.

Contact method: The contact method is a commonly used method in which local displacement sensors are directly attached onto the specimen to measure axial/radial deformations during the test (e.g., Clayton and Khatrush 1986). Generally, radial displacements are measured at one to three discrete points and assumptions are made as to the shape of the specimens to assess the volumetric strain. This method is generally applicable only for rigid specimens with small deformations. Measurements may become significantly inaccurate in measuring soil volume changes, such as in the case of a shear plane forming across the specimen (Laloui et al. 2006). It also requires the use of specially designed sensors such as miniature LVDTs (Costa-Filho 1982; Klotz and Coop 2002) and Hall Effect transducers (Clayton and Khatrush 1986). Errors could be raised due to seating, closing of gaps between components, and axial and radial alignment. Generally less than three measurements can be made due to the limited space inside the cell.

Non-contact method: Romero et al. (1997) reported the use of an electro-optical laser scanner to determine the lateral profiles of specimen for radial deformation. It also allowed detection of non-uniformities and localized deformations along the two diametrically opposite sides of the specimen. The technique requires costly modification and sophisticated installation procedures. A triaxial cell needs to be modified by opening a flat window for the laser ray to deal with the refraction from the cell wall and the confining fluid. Hird and Hajj (1995) proposed use of proximity transducers mounted on a rigid tube around the sample to provide an output voltage proportional to the distance of a lightweight conductive target placed on the specimen. Generally, this type of transducer is not waterproof and has to be sealed in housing. Another major drawback is that the target must be aligned with the sensor, which is difficult to satisfy.

Methods Specifically Developed for Measuring Strain Localizations

Even if a soil element is subject to a homogeneous stress at its boundary, localized strain concentration can occur and propagate into zones of localized shear deformation or shear band because of the inevitable non-uniformity of the mass and stiffness of the material. As a result, the values of stress and strain variables derived from boundary measurements of loads and displacements are only nominal. The only way to understand the localized deformation is to measure the full field of deformation in the specimen (Viggiani and Hall 2008). Several methods have been developed to track shear band including X-ray Computerized Tomography (CT), Digital Image Analysis (DIA) with refraction corrections, and Digital image correlation (DIC) (e.g. Desrues and Viggiani 2004; Desrues et al. 1996; Gachet et al. 2003; Lin and Penumadu 2007; Macari at al. 2001). These methods can potentially be used to measure the total and local volume changes for unsaturated soil specimen during triaxial testing. A brief literature review of these methods in geomaterial studies is presented as follows.

X-ray Computed Tomography (CT)

X-ray CT is a nondestructive imaging technique to detect the internal structure of an object using an X-ray source. When X-ray beam passes through an object, some photons are either scattered or completely absorbed, resulting in the attenuation of the intensity of beam. The amount of attenuation depends upon the photon energy, the chemical composition, and the density of the object. By interpreting the beam intensity data, information regarding the internal structure of an object can be obtained. The information is presented as two dimensional cross sections or stacked to develop 3D renderings of the object for which total and local volume change can be deduced. Roscoe (1970) used X-ray radiography to measure two dimensional (2D) strain fields in sand. From the early 1980s, X-ray tomography was used by Desrues and his

coworkers (Colliat-Dangus et al. 1988; Desrues 1984; Desrues et al. 1996) and later by Alshibli et al. (2000) to provide valuable 3D information on evolution of void ratio inside a shear band and its relation to critical state. In the past 20 years, using X-ray CT has changed from a pioneering high-tech exotic experimental approach to a still high-tech but well recognized powerful experimental method. The accuracy could be as high as several microns for small-size soil specimens. The major disadvantage of X-ray CT technique for triaxial soil testing is that it is too expensive. Since the steel and water attenuates the intensity of X-ray beam, conventional triaxial test apparatus cannot be used with X-ray CT for soil testing. A completely different new system such as the one at Washington State University (Razavi et al. 2007) is therefore needed for real-time soil characterizations during shearing with controlled confinement. At present very few such systems are available in the US. In addition, suction controlled triaxial tests for unsaturated soils are often time-consuming (weeks to months/test), which makes its use more expensive. Although possible and having many advantages, it is impractical to use the X-ray CT test to characterize real-time stress-strain behavior for unsaturated soils.

Digital Image Analysis with Refraction Correction

Digital Image Analysis (DIA) is an approach to make measurements using images captured by digital cameras (Gachet et al. 2003; Gachet et al. 2007; Macari et al. 1997; Sachan and Penumadu 2007). However, when a photo is taken for a 3D object using a digital camera, a 2D image is obtained and the depth of the object is lost. In order to make correct measurements, the orientation (including position and shooting direction) of the camera relative to the object are manually controlled in DIA in order to reconstruct its 3D dimensions. In addition, for soil triaxial testing as shown in Figure 1a, the presence of the confining acrylic chamber and the confining

water in the line of vision between the camera and the soil specimen creates an apparent distortion of the specimen which must be accounted for. Parker (1987) developed a two-dimensional model to use DIA with 2D refraction corrections to measure soil deformations in a conventional triaxial test cell. Macari et al. (1997) proposed a further improvement as shown in Figure 2. An idealized pinhole camera model is used which is installed "far away" from the soil specimen. To apply the DIA method by Macari et al. (1997), system calibrations must be performed first and several implicit requirements must be satisfied: (1) the soil specimen and the confining acrylic chamber are perfectly cylindrical and installed vertically; (2) the digital pinhole camera is placed perfectly at the horizontal direction and its shooting direction exactly passes through the center of the chamber; (3) the soil specimen is installed exactly at the center of the confining chamber and the relative positions of the camera, the chamber, and the soil specimen are accurately known; (4) deformation of acrylic cell wall under water pressure is negligible; and (5) when soil deforms, the deformations occur homogenously along the radial directions. With these assumptions, the Snell's law (Wolf 1995) is applied twice to determine the positions of the points on the surface of soil specimen. None of these conditions can be met in real conditions as demonstrated in this and the companion papers. The results of the image-based volume measurements depend greatly on how well the model conditions are satisfied throughout the test. Gachet et al. (2007) applied the DIA method to determine volume changes of an unsaturated soil from its lateral profiles. Lin and Penumadu (2006) used a method similar to Park (1987) to analyze a series of combined axial-torsional tests for kaolin clay under undrained conditions. For the measurement points on a specimen surface with spacing of 10 mm, the obtained accuracies of measurement are 0.2 mm and 0.3 mm in the vertical and circumferential direction, respectively.

In addition, the DIA method cannot provide measurements for the whole soil specimen since back view of the soil specimen is blocked by itself.

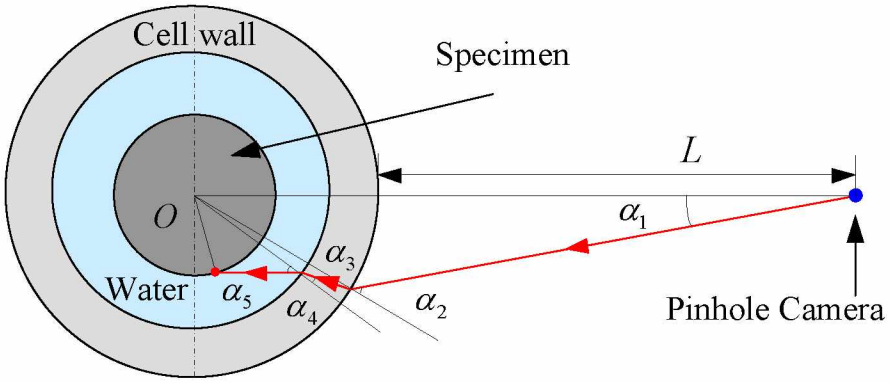

Figure 2. 2D Digital image analysis model with refraction correction (adopted from Macari et al. 1997)

Digital Image Correlation

Digital image correlation (DIC) measures displacements across an object surface based upon the assumption that all soils have their own unique textures in the form of different-colored grains and the light and shadow formed between adjacent grains when illuminated (Helm et al. 1996; Rechenmacher 2006; Rechenmacher and Medina-Cetina 2007; Sutton et al. 2000; White et al. 2003). These textures include numerous small clusters of uniquely colored pixels called subsets and their corresponding gray level variations represent unique mathematical entities that can be tracked during a deformation process. Figure 3 shows fractions of two images for a sand specimen before and after deformation (Rechenmacher and Medina-Cetina 2007). By best matching the pixel subsets through minimization of an error measure, such as normalized cross correlation (Sutton et al. 2000), subset straining and/or rotations can be captured and measured.

The pixel subset matching can be intensively performed so that nearly full-field displacement information can be obtained. Initially DIC displacements are analyzed incrementally from images taken at short time steps using a single digital camera at a fixed location. As a result, only 2D analysis can be performed. White et al. (2003) presented a DIC method for soil volume measurements which used digital images and particle image velocimetry analysis for measuring soil deformation. Rechenmacher and Medina-Cetina (2007) reported use of 3D-DIC to match pixel subset patterns reflected on surfaces of 3D objects in which the 3D object shape is discerned by utilizing two obliquely oriented digital cameras (Helm et al. 1996; Sutton et al. 2000). Based upon the 3D spatial information of the object, 3D displacements between consecutive sets of images are computed using the DIC concepts described above. Results indicated the vertical and horizontal displacements could be measured to an accuracy of ± 0.02 mm. The DIC method does not have a component to take the refraction into considerations and therefore cannot directly be used with the conventional triaxial test apparatus for saturated soils to measure the soil volume change. Rechenmacher (2006) and Rechenmacher and Medina-Cetina (2007) eliminated the refraction effect by carrying out triaxial tests under vacuum confinement without the use of a conventional confining cell. As a result, the confining pressure that can be applied is limited to one atmosphere. The DIC method was only used to measure local volume change (deformation) for a small area of soil specimen and cannot be used to measure displacements for the whole soil specimen.

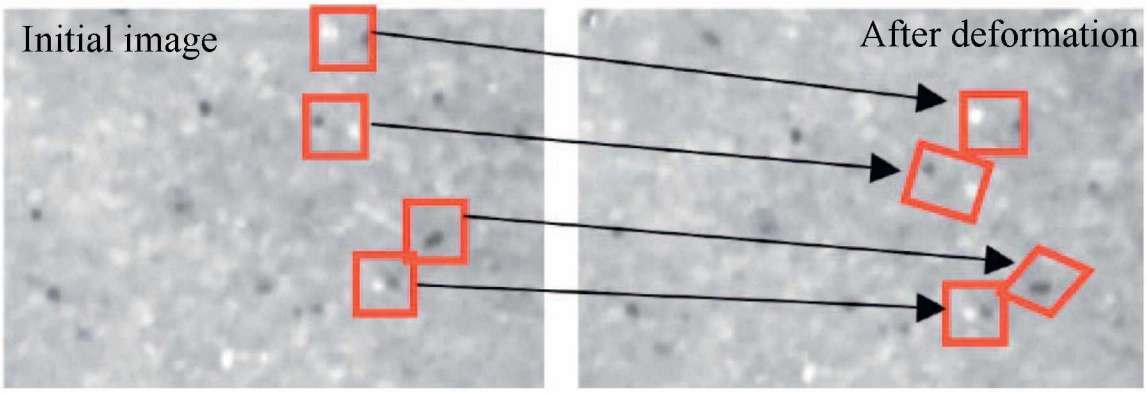

Figure 5. Digital image correlation pixel subset matching (Modified from Rechenmacher and Medina-Cetina 2007)

A Photogrammetry-Based New Method

As discussed above, at present, there is no simple and cost-effective method to accurately measure the total and local volume changes for unsaturated soil specimens during triaxial testing. Among all existing methods, image-based methods such as DIC and DIA have the least requirements on testing equipment and appear to be the most cost-effective. With the rapid developments of digital cameras and reduced cost, image based methods become more and more attractive. However, for measuring volume changes for unsaturated soils during triaxial testing, imaged-based methods suffer two limitations. First, the relative position of the camera to the object is essential to the reconstruction of 3D models from 2D images. In reality, it is difficult to accurately control the orientation of the camera. Second, effect of refraction as shown in Figure 1a is difficult to take into account. Snell's law is well-established theoretical equation (Wolf 1995). In order to apply the Snell's law, the shape and location of the acrylic cell relative to the camera position where an image is taken must be accurately determined. However, the acrylic cell as shown in Figure 1a is deforming during triaxial testing and its shape and location may

change at different cell pressures even if the camera is at a fixed position as proposed by Macari et al. (1997).

In order to overcome the aforementioned limitations in digital image measurements, a photogrammetry-based method was developed in this study to reconstruct 3D models of soil specimens. The reconstruction of 3D models utilizes images taken during triaxial testing with conventional triaxial test apparatus for saturated soils with minor modifications. The 3D reconstruction is achieved by integrating photogrammetry (Mikhail et al. 2001), optical-ray tracing, and least-square optimization. In this proposed method, the camera orientations and the relative shape and location of the acrylic cell are back-calculated from images taken during triaxial testing employing the photogrammetry technique to a high level of accuracy instead of manually controlled and measured.

The procedures of the proposed method are as follows: (1.) Attach measurement targets on the acrylic cell, the load frame, and the surface of the membrane (with soil specimen inside) as shown in Figure 4a. These targets are high contrast dots with special design which can be identified automatically by software. (2.) Take photographs using a calibrated camera around the acrylic cell with soil specimen inside. Figure 4b shows the top view of possible camera positions to reconstruct a full 3D model for a soil specimen during triaxial testing; (3.) Determine camera orientations and acrylic cell shape and location using the targets posted on the load frame and acrylic cell based upon photogrammetry; and (4.) Apply optical-ray tracing and least-square optimization techniques to determine 3D coordinates of any point on the soil specimen surface as discussed in the later sections.

Photographs can be taken at any orientation to obtain best quality and accuracy. Each photograph represents one measurement and as many photographs as possible can be used. The

major difference between the proposed method and the DIA is as follows: (1.) Camera is carefully calibrated; (2.) Multiple overlapping images are used instead of using one picture only; (3) An optimization process is performed to get the best accuracy of the result; (4.) In order to get the best effects for each point/zone the camera orientation is arbitrary instead of being manually controlled and positioned; (5.) The camera orientation for each photograph and actual shape and position of the confining acrylic chamber is calculated based upon the principle of photogrammetry; (6.) Full field 3D deformation instead of a profile or small area of the tested sample can be obtained using the proposed method when compared with the DIA method; and (7.) None of the assumptions used in Macari et al.(1997) method is needed.

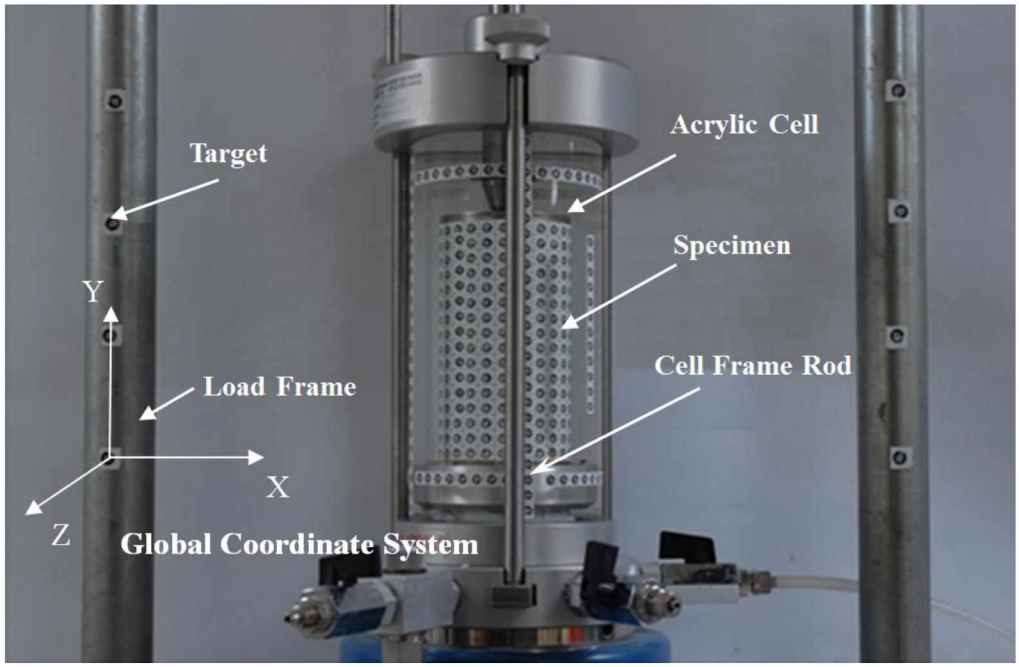

(a) System setup

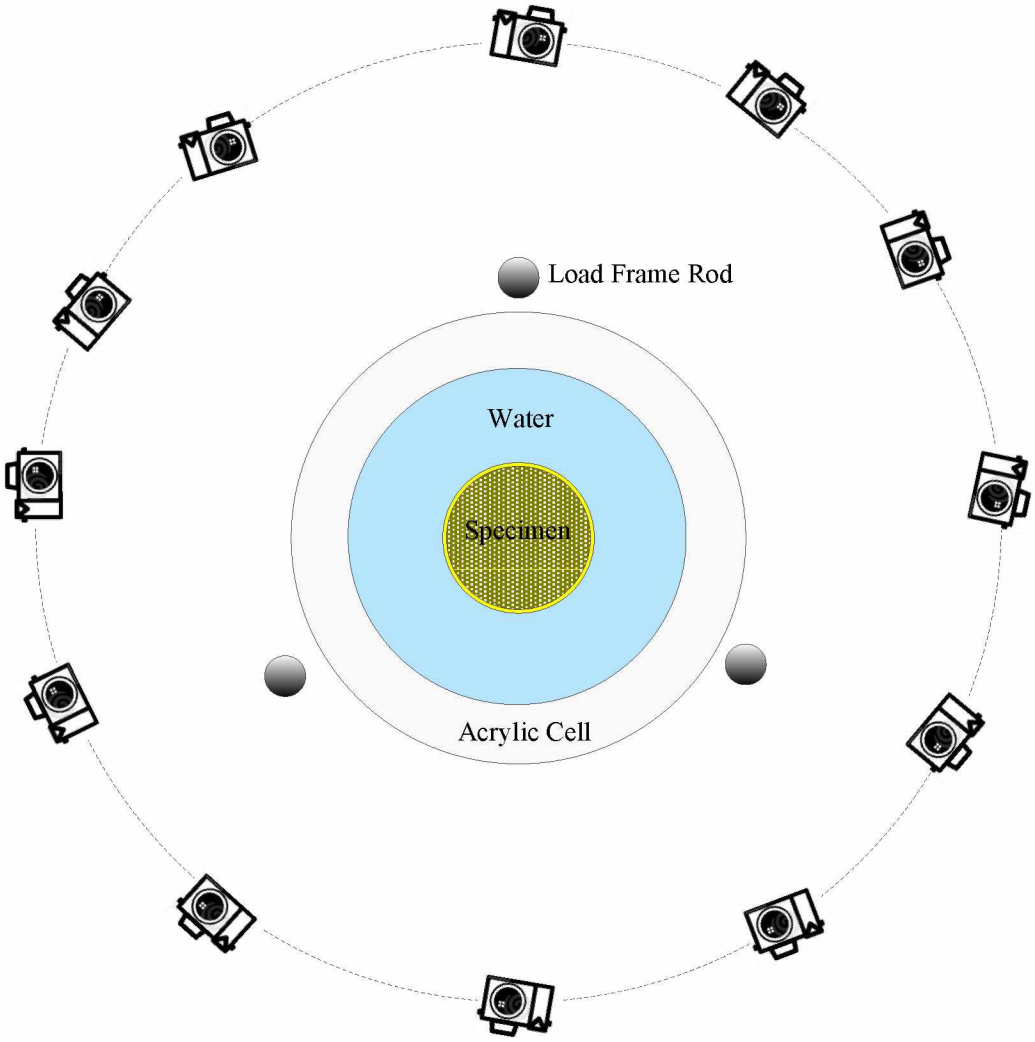

(b) Top view of camera positions during photographing

Figure 4 System setup and camera positions during photographing for the proposed method

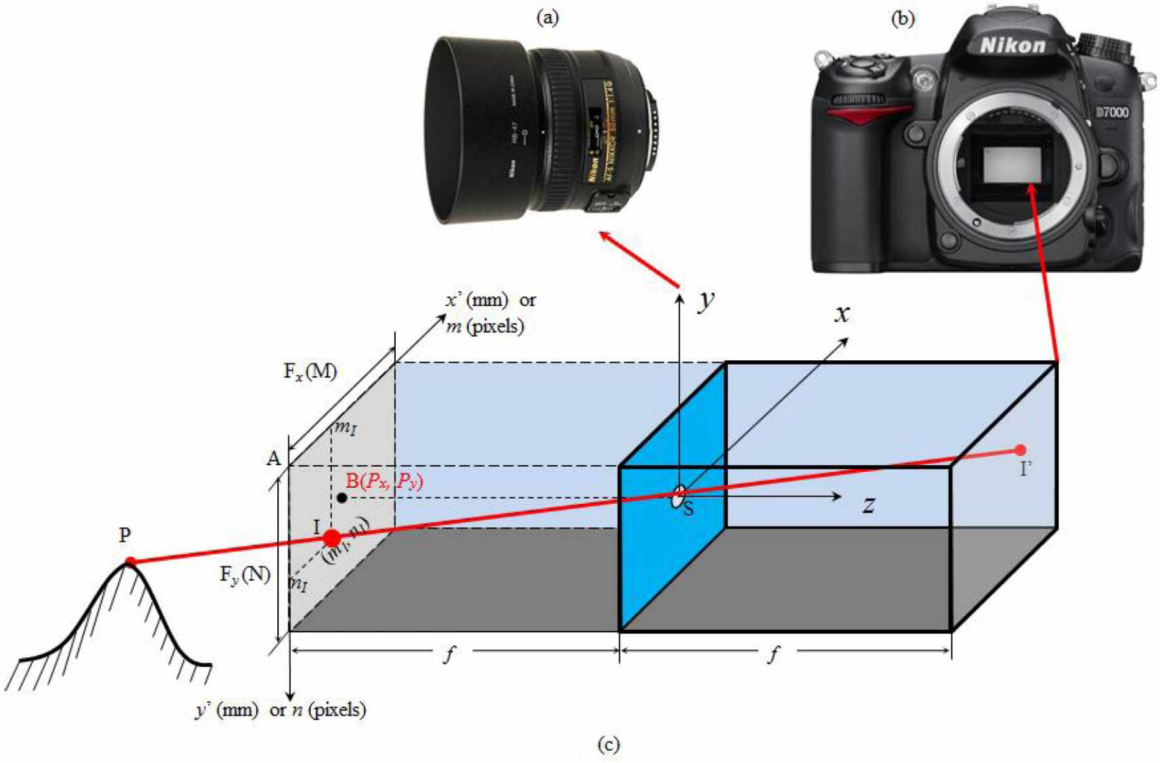

Figure 5 Pinhole camera model

Mathematical Description of the Proposed Method

The following sections introduce the founding principles of the proposed method, which can be described in four main steps:

Step 1: Use of Photogrammetry to Determine Camera Orientations

Photogrammetry is based upon a pinhole camera model (Mikhail et al. 2001) in which the small pinhole and the image plane correspond to perspective center of lens and image sensor of a commercial digital camera as shown in Figure 4. The light beam from an object point P passes through the pinhole S and forms an image point I' on the right image plane. In photogrammetry, the image plane in Figure 5 is depicted at the left to the pinhole, rather than at the right, as it would be the case with the image sensor of an actual camera. This allows one to work with

image geometry as found on a right-reading paper print or film dispositive rather than that found on a photographic negative. The new image point is then point I on the left image plane. The fundamental characteristic of the imaging process is that the pinhole S (perspective center of the camera), the image point I, and the object point P all lie on a line in space (called collinearity condition). In image analysis, the upper left corner of an image (point A as shown in Figure 5) is by default set as the origin of the coordinate system. Two coordinate systems are used, one is the pixel coordinate system in which the coordinates of an image point is defined by pixels (represent the smallest controllable element of a picture), and the other is the physical coordinate system in which the real sizes of the image sensor is used . For a camera image sensor with sizes of F_x and F_y, if it is divided into M columns and N rows of pixels in the x' and y' directions respectively, then the following relationship exists between the physical coordinate system and the pixel coordinate system for the same point I:

$$\begin{bmatrix} x_I' \\ y_I' \end{bmatrix} = \begin{bmatrix} F_x / M & 0 \\ 0 & F_y / N \end{bmatrix} \begin{bmatrix} m_I \\ n_I \end{bmatrix} \tag{1}$$

where,

x_I', y_I' = coordinates of the image point I in the physical coordinate system of $x'Ay'$ (mm),

F_x, F_y = format sizes of the camera image sensor in x and y directions (mm),

m_I, n_I = coordinates of the image point I the pixel coordinate system mAn (pixel), and

M, N = total pixel numbers of the camera image sensor in x' and y' directions (pixel).

In order to facilitate the following discussions, a local 3D coordinate system is often built with origin setting at the pinhole S (i.e. perspective center of the camera lens) as shown in Figure 5 and lowercase *x*, *y*, and *z* are used to represent the coordinates of any point in this system. The coordinates of the image point I in the local coordinate system can therefore be calculated from the following equations:

$$\begin{bmatrix} x_I \\ y_I \\ z_I \end{bmatrix} = \begin{bmatrix} x_I' - P_x \\ -y_I' + P_y \\ -f \end{bmatrix} \tag{2}$$

where,

x_I, y_I, and z_I = x, y, and z coordinates of point I in the local coordinate system (*xyz*) (mm), subscript "I" indicates the coordinates are associated with point I.

f = perpendicular distance between the pinhole and the image plane (equivalent to focus length of the camera) (mm), and

P_x, P_y = coordinates of point *B* in the physical coordinate system of *x'Ay'* (mm), where point B is the projection of point S on the image plane.

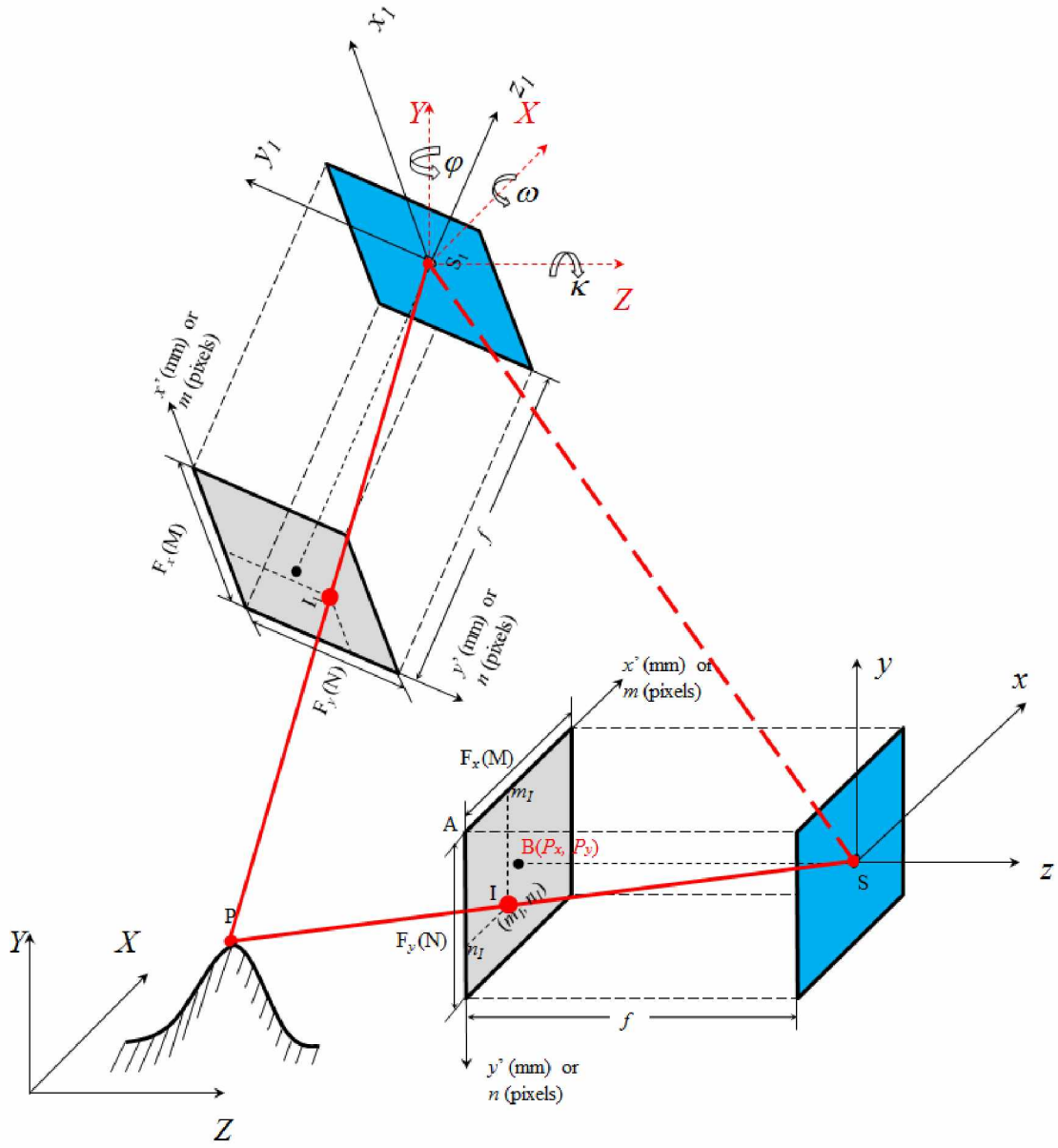

Figure 6. Principle of the Photogrammetry

The method proposed in this paper involves analyses of multiple images taken at different orientations as shown in Figure 4b. As a result, a global coordinate system is also needed so that all images are analyzed in the same coordinate system. For convenience, uppercase *X*, *Y*, and *Z* are used to represent the coordinates of any point in this system as shown

in Figure 6. When the image point I as shown in Figure 6 is taken, the orientation of the camera can be defined by six parameters: the coordinates of the perspective center of the camera S (X_s, Y_s, Z_s) and three rotational angles of κ, ω, ϕ of the *z'*- axis with the X-, Y-, and Z- axes in the global system (representing the shooting directions), then the coordinates of the image point I in the global coordinate system can be calculated as follows:

$$\begin{pmatrix} X_I \\ Y_I \\ Z_I \end{pmatrix} = R\ \omega,\varphi,\kappa \begin{pmatrix} x_I \\ y_I \\ z_I \end{pmatrix} + \begin{pmatrix} X_s \\ Y_s \\ Z_s \end{pmatrix} \tag{3}$$

where, R is a rotation matrix defined by the following equation:

$$R\ \omega,\varphi,\kappa = \begin{pmatrix} \cos\kappa\cos\varphi & -\sin\kappa\cos\varphi & \sin\varphi \\ \cos\kappa\sin\omega\sin\varphi+\sin\kappa\cos\omega & -\sin\kappa\sin\omega\sin\varphi+\cos\kappa\cos\omega & -\sin\omega\cos\varphi \\ -\cos\kappa\cos\omega\sin\varphi+\sin\kappa\sin\omega & \sin\kappa\sin\varphi\cos\omega+\cos\kappa\sin\omega & \cos\omega\cos\varphi \end{pmatrix} \tag{4}$$

X_s, Y_s, Z_s= coordinates of the pinhole S (perspective center of the camera) in the global system; and κ, ω, ϕ = rotational angles from local coordinate system to the global coordinate system (rotates about z, then y, then x axis).

If a second picture is taken using the same camera at position S_1 with a different shooting direction and the corresponding image point for the same object point P is I_1 in the second image, then lines SI, S_1I_1, and SS_1 have to be on the same plane since I and I_1 are conjugate image points of the same object point P and the following equation hold true:

$$\overrightarrow{SS_1} \bullet \overrightarrow{SI} \times \overrightarrow{S_1I_1} = 0 \tag{5}$$

Where

$$\overrightarrow{SS_1} = \begin{pmatrix} X_{S_1} \\ Y_{S_1} \\ Z_{S_1} \end{pmatrix} - \begin{pmatrix} X_S \\ Y_S \\ Z_S \end{pmatrix},\ \overrightarrow{SI} = \begin{pmatrix} X_S \\ Y_S \\ Z_S \end{pmatrix} - \begin{pmatrix} X_I \\ Y_I \\ Z_I \end{pmatrix} \text{ and } \overrightarrow{S_1I_1} = \begin{pmatrix} X_{S_1} \\ Y_{S_1} \\ Z_{S_1} \end{pmatrix} - \begin{pmatrix} X_{I_1} \\ Y_{I_1} \\ Z_{I_1} \end{pmatrix}$$

subscript "I_1" indicates the coordinates are associated with point I_1.

Equation 5 is the coplanarity condition of photogrammetry (Mikhail et al. 2001). In Equation 5, the camera positions (X_S, Y_S, Z_S) and shooting directions (κ, ω, ϕ) are unknowns while the rest are known parameters. Multiple equations can be established for multiple conjugate image points to solve the camera positions and orientations. Once the camera positions and orientations are known, the coordinates of the object point P can also be solved using the collinearity condition since the image points, perspective centers of the camera, and the object point all lie on a line in the space such as line PIS and P I_1S_1 in Figure 6. This is the principle of the photogrammetry. As a noncontact 3D measurement technique, photogrammetry has been used in different fields for more than 160 years and proven to be able to provide measurements with high accuracy (Mikhail et al. 2001). Figure 7 shows an example of camera orientations determined using the photogrammetry. Figures 7a and 7b shows two images 12 and 13 taken at different orientations. The measurement targets posted on the load frame and wall of the acrylic wall were used to determine the camera orientations for images 12 and 13 which were shown in Figure 7c. Note that camera stations 12 and 13 were not coplanar.

(a) Image 12 in the isotopic compression test with confining pressure of 600 kPa

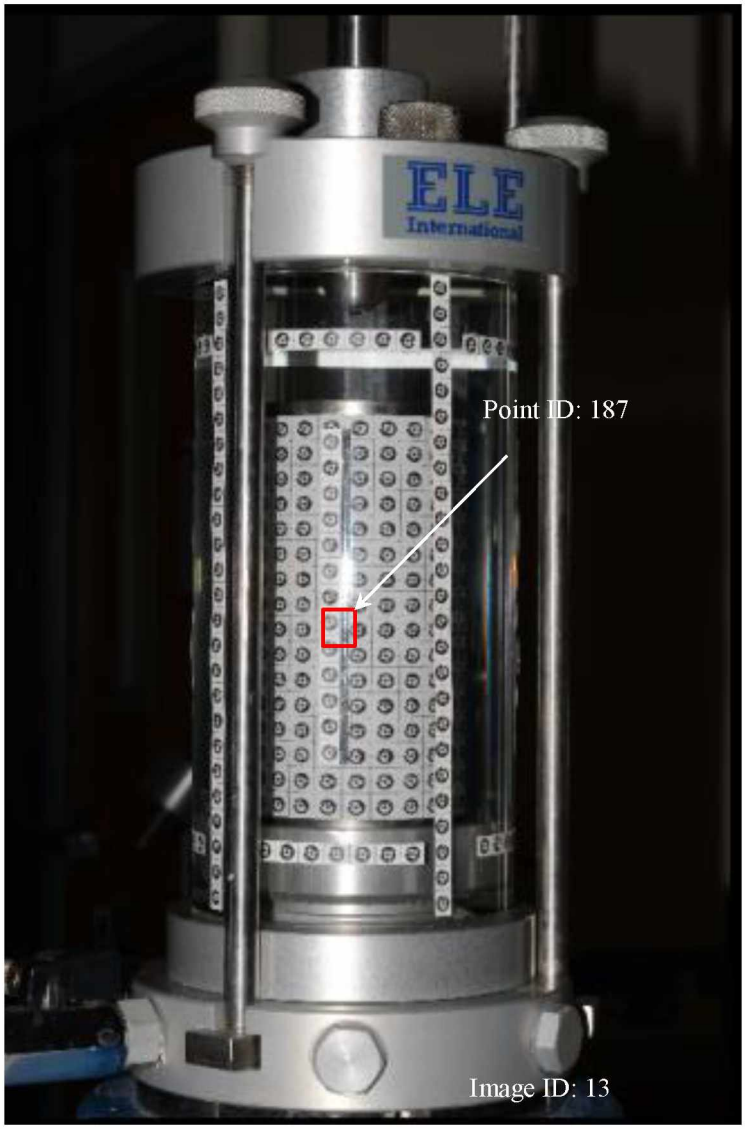

(b) Image 13 in the isotopic compression test with confining pressure of 600 kPa

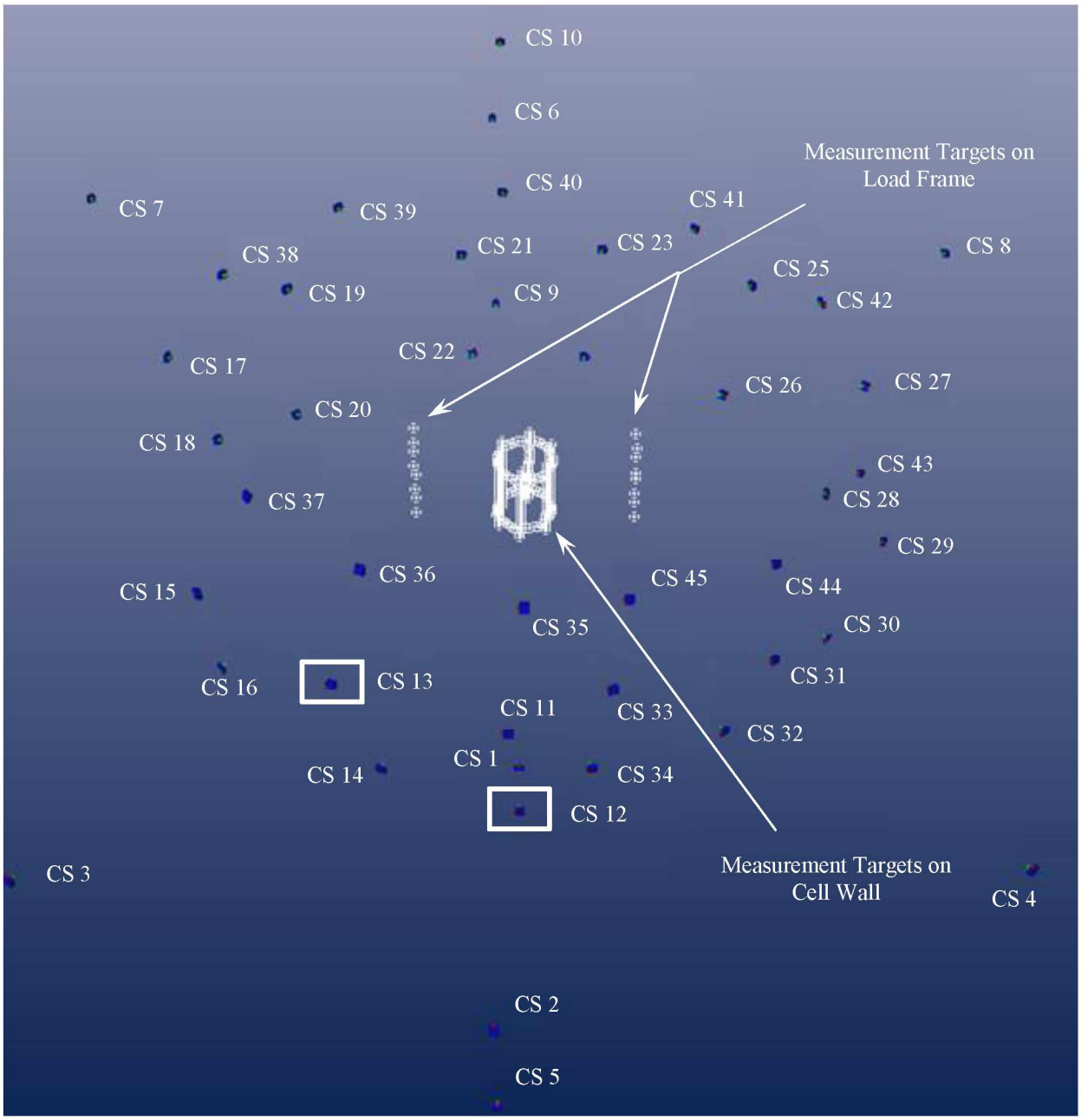

(c)

Figure 7 Photogrammetric analysis isotropic compression tests on a steel cylinder (a) Image at camera station 12; (b) Image at camera station 13; (c) Results from the photogrammetric analysis

Step 2: Determine the Shape and Location of Acrylic Cell

Figure 7c also shows the relative positions of the measurement targets posted on the surface of the acrylic wall which can be used to determine the shape and location of the acrylic wall in the global coordinate system. The acrylic cell generally has a cylindrical shape. If a local coordinate system is set at the center of the cylinder and the Y'-axis coincides with the center of the cylinder as shown in Figure 8, then the cylinder has the following mathematical expression:

$$X'^2 + Z'^2 = r^2 \tag{6}$$

where, r = radius of the cylinder.

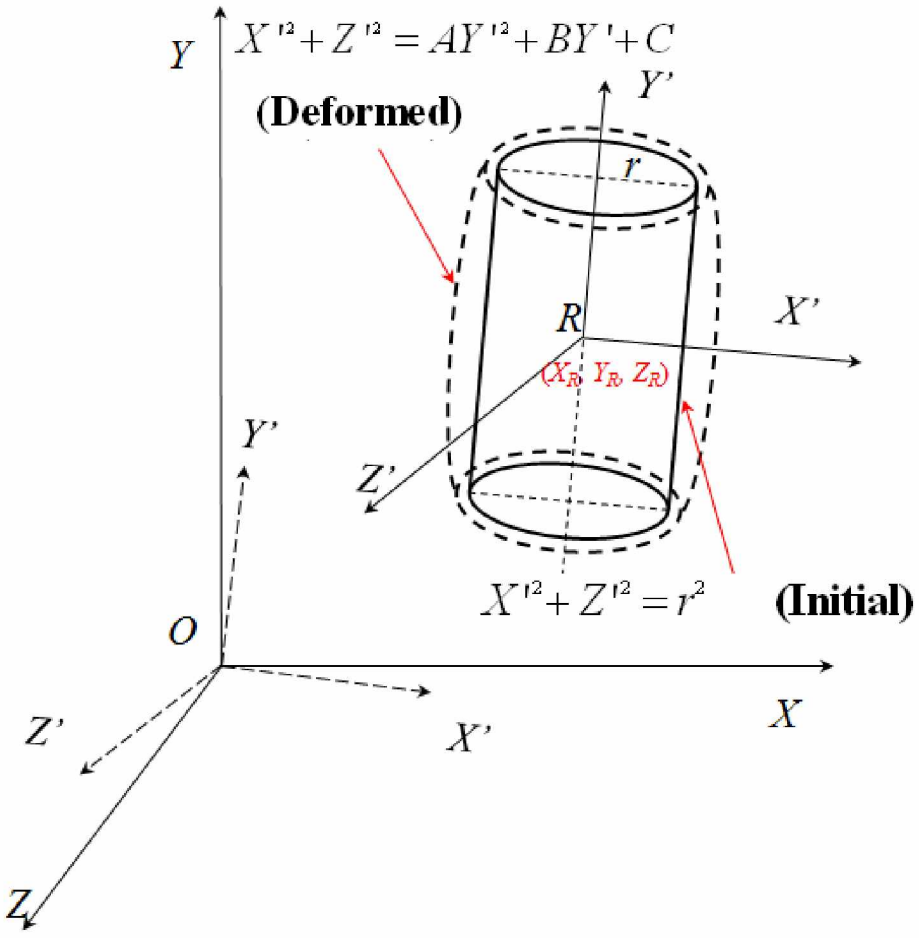

Figure 8. Initial and deformed shapes for the acrylic cell wall

In the triaxial testing, pressure applied to water inside the acrylic cell will cause expansions of the acrylic cell. This is the major reason why a double-cell system is needed for unsaturated soils. In this proposed method, it is suggested that the profile of the deformed acrylic cylinder be quadratic as follows:

$$X'^2 + Z'^2 = AY'^2 + BY' + C \tag{7}$$

or in a matrix form

$$\begin{bmatrix} X' & Y' & Z' \end{bmatrix} \begin{bmatrix} 1 & 0 & 0 \\ 0 & -A & 0 \\ 0 & 0 & 1 \end{bmatrix} \begin{bmatrix} X' \\ Y' \\ Z' \end{bmatrix} - \begin{bmatrix} X' & Y' & Z' \end{bmatrix} \begin{bmatrix} 0 \\ B \\ 0 \end{bmatrix} - C = 0 \tag{7a}$$

Where A, B, and C are parameters describing the expansion of the acrylic cell. When both A and B are zeros, Equation 7 becomes Equation 6 which represents a cylindrical shape. In reality, it could be difficult to set the global coordinate system at the center of the acrylic cell with the same coordinate as X'-, Y'- and Z'- axes since the acrylic cell keep deforming during the triaxial testing. The following equation is used to transform the acrylic cell from local coordinate system to the global coordinate system:

$$\begin{pmatrix} X' \\ Y' \\ Z' \end{pmatrix} = R_1 \left(\omega', \varphi', \kappa' \right) \left[\begin{pmatrix} X \\ Y \\ Z \end{pmatrix} - \begin{pmatrix} X_R \\ Y_R \\ Z_R \end{pmatrix} \right] \tag{8}$$

Where,

$$R_1 = \begin{pmatrix} \cos\varphi'\cos\kappa' & \cos\omega'\sin\kappa' + \sin\omega'\sin\varphi'\cos\kappa' & \sin\omega'\sin\kappa' - \cos\omega'\sin\varphi'\cos\kappa' \\ -\cos\varphi'\sin\kappa' & \cos\omega'\cos\kappa' - \sin\omega'\sin\varphi'\sin\kappa' & \sin\omega'\cos\kappa' + \cos\omega'\sin\varphi'\sin\kappa' \\ \sin\varphi' & -\sin\omega'\cos\varphi' & \cos\omega'\cos\varphi' \end{pmatrix} \tag{9}$$

X_R, Y_R, and Z_R are the coordinates of the center of the acrylic cell in the global coordinate system. κ', ω', ϕ' = rotational angles from global coordinate system to the local coordinate system (rotates about x, then y, then z axis).

By inserting Equation 8 into Equation 7a, the mathematical expression of the acrylic cell in the global coordinate system is obtained as follows:

$$F(X,Y,Z)=\begin{bmatrix} X-X_R \\ Y-Y_R \\ Z-Z_R \end{bmatrix}^T R_1^T \begin{bmatrix} 1 & 0 & 0 \\ 0 & \mathbf{-A} & 0 \\ 0 & 0 & 1 \end{bmatrix} R_1 \begin{bmatrix} X-X_R \\ Y-Y_R \\ Z-Z_R \end{bmatrix} - \begin{bmatrix} X-X_R \\ Y-Y_R \\ Z-Z_R \end{bmatrix}^T R_1^T \begin{bmatrix} 0 \\ B \\ 0 \end{bmatrix} - C = 0 \qquad (11)$$

Equation 11 indicates that in the global coordinate system, nine parameters are needed to describe the shape and location of a deformed acrylic cell: A, B, C, κ', ω', ϕ', X_R, Y_R, and Z_R. As shown in Figure 7c, 3D global coordinates of measurement targets on the surface of acrylic cell can be obtained using photogrammetry. These data (more than 9 points) can be used to best-fit the shape of the deformed acrylic cell to obtain the nine parameters for the determination of the shape and location of the acrylic cell in the global coordinate system. A least-square method was used for this purpose. The mathematical expression for this process is as follows:

To find a combination of

$$A\ B\ C\ X_R\ Y_R\ Z_R\ \omega'\ \varphi'\ \kappa' \qquad (12)$$

which can minimize

$$\sum_{i=1}^{n} F(X_i,Y_i,Z_i)^2 \qquad (13)$$

Where X_i, Y_i, Z_i are coordinates of the i^{th} measurement targets on the surface of the acrylic cell as shown in Figure 7c.

Step 3: Ray-Tracing Process

In the previous sections, photogrammetry is used to determine the 3D coordinates of points in the air as shown in Figure 7c. The objective of this paper is, however, to measure the total and local volume changes of soil specimens inside the acrylic chamber. As shown in Figures 1a, 2 and 9a, when a light ray passes through the water-acrylic and acrylic-air interfaces, it bends due to refractions. This disturbs the collinearity conditions and the photogrammetry cannot be used directly any more. A ray-tracing technique is used to overcome this limitation.

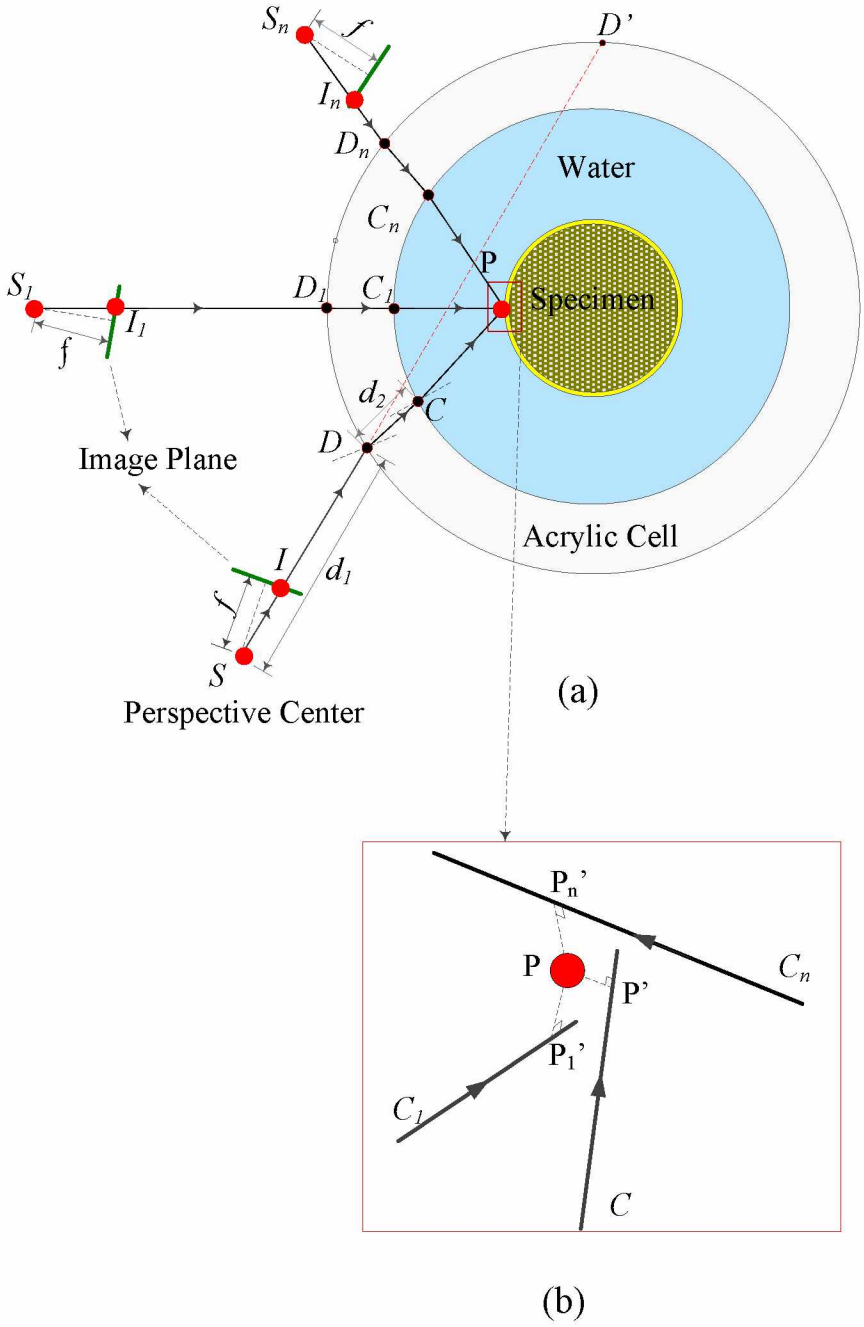

Figure 9. Schematic plot of ray-tracing process

It is well known that the path of a light ray is invariant under path reversal. For example, as shown in Figure 9a, a light ray PC is generated from a source point P on the surface of the soil

specimen, bends when traveling through the acrylic cell along line CD, and forms an image point I in the camera with a perspective center of S. Due to the reciprocity of the light ray, one can follow the light ray from the camera perspective center S through the image point I and points D and C back to the light source P. The information needed for the process includes the image itself, camera parameters, camera orientations, shape and location of the acrylic cell, cell wall thickness and refractive indices of the air, acrylic cell, and water. All these information are known and the mathematical expression of the ray-tracing process is as follows:

a) Find the line of incidence SI or SD

The light ray of incidence SI can be defined by a point S (X_s, Y_s, Z_s) and a unit direction vector passing points S and I:

$$\vec{i} = \begin{pmatrix} \alpha_a \\ \beta_a \\ \gamma_a \end{pmatrix} = \frac{\overrightarrow{SI}}{\left|\overrightarrow{SI}\right|} = \frac{1}{\sqrt{X_I - X_s\ ^2 + Y_I - Y_s\ ^2 + Z_I - Z_s\ ^2}} \begin{pmatrix} X_I - X_s \\ Y_I - Y_s \\ Z_I - Z_s \end{pmatrix} \tag{14}$$

The light ray SI intersects with the acrylic cell at point D with global coordinates of (X_D, Y_D, Z_D). Since point D is on the line SI, one has

$$\begin{pmatrix} X_D \\ Y_D \\ Z_D \end{pmatrix} = \begin{pmatrix} X_s \\ Y_s \\ Z_s \end{pmatrix} + d_1 \vec{i} \tag{15}$$

Where d_1 is the distance between points S and D. Point D is also on the outer surface of the acrylic cell. Therefore it satisfies Equation 11. By inserting Equation 15 into Equation 11, a quadratic Equation with d_1 as an unknown variable is obtained.

$$\left\{\begin{bmatrix} X_S - X_R \\ Y_S - Y_R \\ Z_S - Z_R \end{bmatrix} + d_1 \vec{i}\right\}^T R_1^T \begin{bmatrix} 1 & 0 & 0 \\ 0 & \mathbf{-A} & 0 \\ 0 & 0 & 1 \end{bmatrix} R_1 \left\{\begin{bmatrix} X_S - X_R \\ Y_S - Y_R \\ Z_S - Z_R \end{bmatrix} + d_1 \vec{i}\right\} - \left\{\begin{bmatrix} X_S - X_R \\ Y_S - Y_R \\ Z_S - Z_R \end{bmatrix} + d_1 \vec{i}\right\}^T R_1^T \begin{bmatrix} 0 \\ B \\ 0 \end{bmatrix} - C = 0 \quad (16)$$

or

$$ad_1^2 + bd_1 + c = 0 \quad (16a)$$

where,

$$a = \vec{i}^T R_1^T \begin{bmatrix} 1 & 0 & 0 \\ 0 & \mathbf{-A} & 0 \\ 0 & 0 & 1 \end{bmatrix} R_1 \vec{i}$$

$$b = \begin{bmatrix} X_S - X_R \\ Y_S - Y_R \\ Z_S - Z_R \end{bmatrix}^T R_1^T \begin{bmatrix} 1 & 0 & 0 \\ 0 & \mathbf{-A} & 0 \\ 0 & 0 & 1 \end{bmatrix} R_1 \vec{i} + \vec{i}^T R_1^T \begin{bmatrix} 1 & 0 & 0 \\ 0 & \mathbf{-A} & 0 \\ 0 & 0 & 1 \end{bmatrix} R_1 \begin{bmatrix} X_S - X_R \\ Y_S - Y_R \\ Z_S - Z_R \end{bmatrix} - \vec{i}^T R_1^T \begin{bmatrix} 0 \\ B \\ 0 \end{bmatrix}$$

$$c = \begin{bmatrix} X_S - X_R \\ Y_S - Y_R \\ Z_S - Z_R \end{bmatrix}^T R_1^T \begin{bmatrix} 1 & 0 & 0 \\ 0 & \mathbf{-A} & 0 \\ 0 & 0 & 1 \end{bmatrix} R_1 \begin{bmatrix} X_S - X_R \\ Y_S - Y_R \\ Z_S - Z_R \end{bmatrix} - \begin{bmatrix} X_S - X_R \\ Y_S - Y_R \\ Z_S - Z_R \end{bmatrix}^T R_1^T \begin{bmatrix} 0 \\ B \\ 0 \end{bmatrix} - C$$

Equation 16 or 16a has two roots, representing the distances from point S to the two intersection points with the outer surfaces of the acrylic wall D and D' as shown in Figure 9a, respectively. For point D,

$$d_1 = \frac{-b - \sqrt{b^2 - 4ac}}{2a} \quad (17)$$

The coordinates of point D can then be obtained by inserting Equation 17 into Equation 15.

b) Apply the Snell's law to find the angle of refraction at point D

The normal of the acrylic cell at point D can be calculated by differentiating Equation 11 at point D:

$$\overrightarrow{N_1} = \begin{pmatrix} \frac{\partial F}{\partial X} \\ \frac{\partial F}{\partial Y} \\ \frac{\partial F}{\partial Z} \end{pmatrix} = 2R_1^T \begin{bmatrix} 1 & 0 & 0 \\ 0 & \mathbf{-A} & 0 \\ 0 & 0 & 1 \end{bmatrix} R_1 \begin{bmatrix} X_D - X_R \\ Y_D - Y_R \\ Z_D - Z_R \end{bmatrix} - R_1^T \begin{bmatrix} 0 \\ B \\ 0 \end{bmatrix} \tag{18}$$

The unit vector of the normal is:

$$\overrightarrow{n_1} = \begin{pmatrix} \alpha_{n1} \\ \beta_{n1} \\ \gamma_{n1} \end{pmatrix} = \frac{\overrightarrow{N_1}}{\left|\overrightarrow{N_1}\right|} \tag{19}$$

where $\left|\overrightarrow{N_1}\right|$ is the magnitude of the normal vector $\overrightarrow{N_1}$.

In the three dimensional space, the Snell's law can also be expressed as follows (Please see the detailed derivation in the attachment):

$$\vec{r}_1 = \frac{n_a}{n_c}\vec{i} - \left(\frac{n_a}{n_c} \vec{i} \bullet \overrightarrow{n_1} + \sqrt{1 - \left(\frac{n_a}{n_c}\right)^2 \left(1 - \vec{i} \bullet \vec{n}_1\right)^2} \right) \vec{n}_1 \tag{20}$$

Where r_1 is the unit vector for the refractive ray DC, n_a and n_c are refractive indices for the air and acrylic cell, respectively.

c) Find the coordinate of point C at the acrylic cell-water interface

An assumption was made in this paper that the thickness of the acrylic wall is uniform and remains constant under pressure. As a result, the inner surface is expressed as follows:

$$\begin{bmatrix} X - X_R \\ Y - Y_R \\ Z - Z_R \end{bmatrix}^T R_1^T \begin{bmatrix} 1 & 0 & 0 \\ 0 & \mathbf{-A} & 0 \\ 0 & 0 & 1 \end{bmatrix} R_1 \begin{bmatrix} X - X_R \\ Y - Y_R \\ Z - Z_R \end{bmatrix} - \begin{bmatrix} X - X_R \\ Y - Y_R \\ Z - Z_R \end{bmatrix}^T R_1^T \begin{bmatrix} 0 \\ B \\ 0 \end{bmatrix} - \sqrt{C} - t^{\,2} = 0 \tag{21}$$

$$X'^2+Z'^2=AY'^2+BY'+\left(\sqrt{C}-t\right)^2 \tag{21a}$$

Where t is the thickness of the acrylic wall. Point C is the intersection point of the light ray with the inner surface. It is on the line DC and the following expression holds:

$$\begin{pmatrix} X_C \\ Y_C \\ Z_C \end{pmatrix} = \begin{pmatrix} X_D \\ Y_D \\ Z_D \end{pmatrix} + d_2 \vec{r_1} \tag{22}$$

Where d_2 is the distance between points C and D. Since point C is on the inner surface of the acrylic cell, it satisfies Equation 21. By inserting Equation 22 into Equation 21, a quadratic equation with d_2 as an unknown variable is obtained. The equation has two roots, representing the distances from point D to the two intersection points with the inner surfaces of the acrylic wall. For point C, d_2 can be calculated using Equation 23 with

$$d_2 = \frac{-b_1 - \sqrt{b_1^2 - 4a_1c_1}}{2a_1} \tag{23}$$

where,

$$a_1 = r_1^T R_1^T \begin{bmatrix} 1 & 0 & 0 \\ 0 & -\mathbf{A} & 0 \\ 0 & 0 & 1 \end{bmatrix} R_1$$

$$b_1 = \begin{bmatrix} X_D - X_R \\ Y_D - Y_R \\ Z_D - Z_R \end{bmatrix}^T R_1^T \begin{bmatrix} 1 & 0 & 0 \\ 0 & -\mathbf{A} & 0 \\ 0 & 0 & 1 \end{bmatrix} R_1 r_1 + r_1^T R_1^T \begin{bmatrix} 1 & 0 & 0 \\ 0 & -\mathbf{A} & 0 \\ 0 & 0 & 1 \end{bmatrix} R_1 \begin{bmatrix} X_D - X_R \\ Y_D - Y_R \\ Z_D - Z_R \end{bmatrix} - r_1^T R_1^T \begin{bmatrix} 0 \\ B \\ 0 \end{bmatrix}$$

$$c_1 = \begin{bmatrix} X_D - X_R \\ Y_D - Y_R \\ Z_D - Z_R \end{bmatrix}^T R_1^T \begin{bmatrix} 1 & 0 & 0 \\ 0 & -\mathbf{A} & 0 \\ 0 & 0 & 1 \end{bmatrix} R_1 \begin{bmatrix} X_D - X_R \\ Y_D - Y_R \\ Z_D - Z_R \end{bmatrix} - \begin{bmatrix} X_D - X_R \\ Y_D - Y_R \\ Z_D - Z_R \end{bmatrix}^T R_1^T \begin{bmatrix} 0 \\ B \\ 0 \end{bmatrix} - \left(\sqrt{C} - t\right)^2$$

Coordinates of point C can be calculated using Equation 22 with known d_2.

d) Apply the Snell's law a second time to find the angle of refraction at point C

The normal at point C of the inner surface of the acrylic cell can be calculated by differentiating Equation 21 at point C:

$$\overrightarrow{N_2} = \begin{pmatrix} \frac{\partial F}{\partial X} \\ \frac{\partial F}{\partial Y} \\ \frac{\partial F}{\partial Z} \end{pmatrix} = 2R_1^T \begin{bmatrix} 1 & 0 & 0 \\ 0 & \mathbf{-A} & 0 \\ 0 & 0 & 1 \end{bmatrix} R_1 \begin{bmatrix} X_C - X_R \\ Y_C - Y_R \\ Z_C - Z_R \end{bmatrix} - R_1^T \begin{bmatrix} 0 \\ B \\ 0 \end{bmatrix} \tag{24}$$

The unit vector of the normal is:

$$\overrightarrow{n_2} = \begin{pmatrix} \alpha_{n2} \\ \beta_{n2} \\ \gamma_{n2} \end{pmatrix} = \frac{\overrightarrow{N_2}}{\left|\overrightarrow{N_2}\right|} \tag{25}$$

Where $\left|\overrightarrow{N_2}\right|$ is the magnitude of the normal vector $\overrightarrow{N_2}$.

Apply the Snell's law again with the known incident unit vector u_r and the normal at point C n_2, the unit vector for line CP can be found as follows:

$$\overrightarrow{r_2} = \begin{pmatrix} \alpha_{r2} \\ \beta_{r2} \\ \gamma_{r2} \end{pmatrix} = \frac{n_c}{n_w}\overrightarrow{r_1} - \left(\frac{n_c}{n_w} \overrightarrow{r_1} \cdot \overrightarrow{n_2} + \sqrt{1 - \left(\frac{n_c}{n_w}\right)^2 \left(1 - \overrightarrow{r_1} \cdot \overrightarrow{n_2}\right)^2} \right) \overrightarrow{n_2} \tag{26}$$

Where r_2 is the unit vector for the refractive ray CP, n_w are refractive index for the water.

Step 4: Least-Square Optimization to Calculate Coordinates for Object Point

From Step 1 to Step 3, coordinates of point C and the direction of line CP can be found. The same process can be applied to image points I_1, I_2,….., and I_n in multiple images for the same object point P as shown in Figure 9a. If there is no error, all the re-tracing lines CP, C_1P,

and C_nP will converge to the same point P and only two re-tracing rays are sufficient to obtain the intersection point P. However, errors unavoidably exist in the measurement and computational processes and it is very likely for lines CP, C_1P_1, and C_nP_n not to intersect in the 3D space as shown in Figure 9b. A least-square optimization technique is used in this paper to overcome this limitation. It is considered that although the re-tracing ray CP, C_1P, and C_nP might not intersect with each other, each ray-tracing line represents an estimate of the light source of the object point P. As a result, the "true" location of point P should be close to those re-tracing rays and has the shortest distances to those re-tracing rays. It is therefore postulated that if the sum of square of a point's distances to all the re-tracing rays is the minimal, the point is the light source where all the rays are generated. Mathematically, the process to find the "true" location of the object point is to:

To find a combination of $X_P\ Y_P\ Z_P$ which can minimize (27)

$$\sum_{i=1}^{n} d_i^2 = \sum_{i=1}^{n} \begin{bmatrix} X_P - X_{C_i} \\ Y_P - Y_{C_i} \\ Z_P - Z_{C_i} \end{bmatrix}^T \begin{bmatrix} X_P - X_{C_i} \\ Y_P - Y_{C_i} \\ Z_P - Z_{C_i} \end{bmatrix} - \left\{ \begin{bmatrix} X_P - X_{C_i} \\ Y_P - Y_{C_i} \\ Z_P - Z_{C_i} \end{bmatrix}^T \begin{bmatrix} \alpha_{r2i} \\ \beta_{r2i} \\ \gamma_{r2i} \end{bmatrix} \right\}^2 \qquad (n \geq 3) \tag{28}$$

Where, X_{C_i}, Y_{C_i}, and Z_{C_i} represent the coordinate of the i^{th} point C_i intersecting with the inner surface of the acrylic cell, which are calculated from Equation 22. α_{r2i}, β_{r2i}, *and* γ_{r2i} represent the directional cosines of the refractive ray C_iP as expressed in Equation 26. At least three tracing rays are needed to use Equation 28 to estimate the coordinates for one point, which represents three measurements for the same point.

The previous sections discuss how the proposed method is used to calculate the 3D coordinates of one point on the surface of a soil specimen during triaxial testing. The same

approach applies to numerous points on the surface of the specimen and a 3D model of the specimen can then be constructed. With the 3D model of the soil specimen, the total volume changes and strain localizations for the whole soil specimen can be calculated, which will be discussed in the following sections.

Validation of the Proposed Method

Camera Calibration and Image Idealization

A commercially available digital single-lens reflex camera (Nikon D7000) with a 50 mm fixed focal length lens (AF-S Nikkor 50 mm f/1.4G) as shown in Figure 5a is used to take the photographs needed for the validation tests. The image sensor of the camera as shown in Figure 5b has a resolution of 16.2 million pixels (4928H: 3264V). As discussed in the previous sections, photogrammetry assumes the camera lens is a pinhole. A commercial camera often uses multiple lenses to focus light and its aperture is not a point. Instead of rendering straight lines for light rays, these lenses often slightly bend them either outwards or inwards. Consequently, an image taken for squares with a commercial camera (Figure 10a) subjects to either barrel (Figure 10b) or pincushion (Figure 10c) distortions. In addition, principal distance, principal point, and format size of the image sensor varies even for the same type of camera. The focal length of the lens is also likely to be different from the specifications in the user's manual. Thus, a camera must be calibrated before being used for extraction of precise and reliable 3D metric information from images.

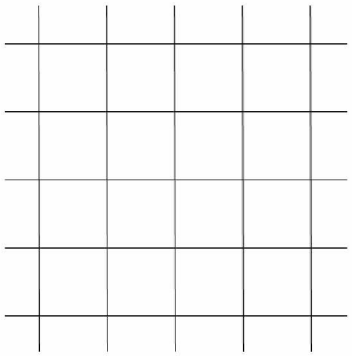

(a) No distortion

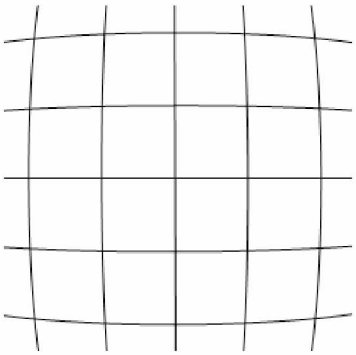

(b) Barrel distortion

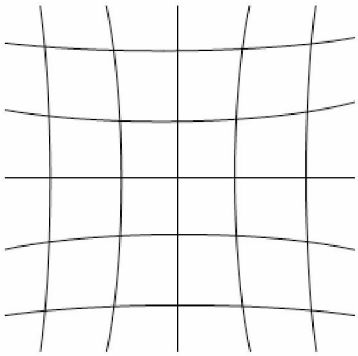

(c) Pincushion distortion

Figure 10. Effect of lens distortions

Numerous techniques have been developed for camera calibration since 1950s. The algorithms are generally based on ideal pinhole camera model, with the most popular approach

being the well-known self-calibrating bundle adjustment, which has made a high level of performance become commonplace (Triggs et al. 2000). Some commercial or free software have been developed for camera calibrations and are readily available (e.g. http://www.vision.caltech.edu/bouguetj/calib_doc/htmls/links.html). In this study, a software package called PhotoModeler Scanner from EOS systems Inc. (website: http://www.photomodeler.com/) is used to calibrate the camera used. The calibration is done by taking 12 images of a calibration sheet. The intrinsic (focal length, principal point, distortion parameters) and extrinsic (translation vector and rotation matrix) parameters are then calculated by analyzing the 12 images. Details regarding camera calibration are not elaborated here since it is a well-established technique. Table 2 shows the calibration results for the camera used in this study. As can be seen in Table 2, the 50 mm fixed focal length lens has an actual focal length 53.3864 mm when the camera is treated as an ideal pinhole camera model. The principal point is not exactly at the center of the image sensor before the camera calibration, either.

Table 2 Camera calibration results

Parameter	Before Idealization	After Idealization
f *(mm)*	53.3864	53.3864
M *(pixel)*	4928	4928
N *(pixel)*	3264	3264
F_x *(mm)*	23.9982	24.7439
F_y *(mm)*	15.8961	16.3871
P_x *(mm)*	12.0865	12.3720
P_y *(mm)*	8.1022	8.1936
K_1 *(10^{-5})*	5.443	0
K_2 *(10^{-9})*	-2.266	0
P_1 *(10^{-6})*	-3.094	0
P_2 *(10^{-6})*	2.023	0

The parameters in Table 2 were then used to correct the distorted images (taken by the camera from either barrel or pincushion distortion as shown in Figure 10b or 10c) to its "true" shape as shown in Figure 10a. This process is called "Image Idealization" in which the following equations were used:

$$\begin{aligned} x_c &= x + x\left[K_1(x^2+y^2) + K_2(x^2+y^2)^2\right] + P_1\left[(x^2+y^2) + 2x^2\right] + 2P_2xy \\ y_c &= y + y\left[K_1(x^2+y^2) + K_2(x^2+y^2)^2\right] + P_2\left[(x^2+y^2) + 2y^2\right] + 2P_1xy \end{aligned} \tag{29}$$

where,

x, y = point coordinates in x and y directions in the original images,

x_c, y_c = coordinates in x and y directions for the same point after image idealization,

K_1, K_2 = radial lens distortion parameters, and

P_1, P_2 = decentering lens distortion parameters.

After image idealizations, the images are ready to be used for the proposed photogrammetry-based method.

Accuracy of the Photogrammetric Analysis in the Air

The proposed method relies on photogrammetric analyses to accurately determine the camera orientations and locations and shapes of the acrylic cell to correct the effect of refractions. Before evaluating the accuracy of the proposed method, the accuracy of photogrammetric analyses is evaluated. Figure 11 shows the setup of a photogrammetric analysis performed on a Craftsman 150 mm caliper with resolution of 0.05 mm. The caliper is placed on an A4 paper with 432 measurement targets. Six images are taken from different orientations and processed to back-calculate the camera orientations and position of any point of interest on the

caliper. The scale for the photogrammetric analysis is established by setting the center-to-center distance between 0 and 150 mm graduates on the main scale to be 150 mm. The scale is then used to measure the distances between the major tick marks on the main scale with an interval of 10 mm. Table 3 lists the analysis results. It can be seen that the errors for the measurements varied from 3 microns to 30 microns and the average error and average absolute error are -1.4 micron and 10 microns, respectively. Among the ten measurements, seven of the measurement errors are less than 10 microns. These errors represent the accuracy of the photogrammetric analysis in the air for determination of camera orientations and locations and shapes of the acrylic cell.

Equipment, Testing Materials, and Experimental Design for Triaxial Validation Tests

The conventional ELE triaxial test apparatus for saturated soils as shown in Figure 4 is used to validate the proposed method on 3D reconstruction during triaxial testing. Two materials are used: a stainless steel cylinder and saturated sand as shown in Figures 4 or 7 and 12, respectively.

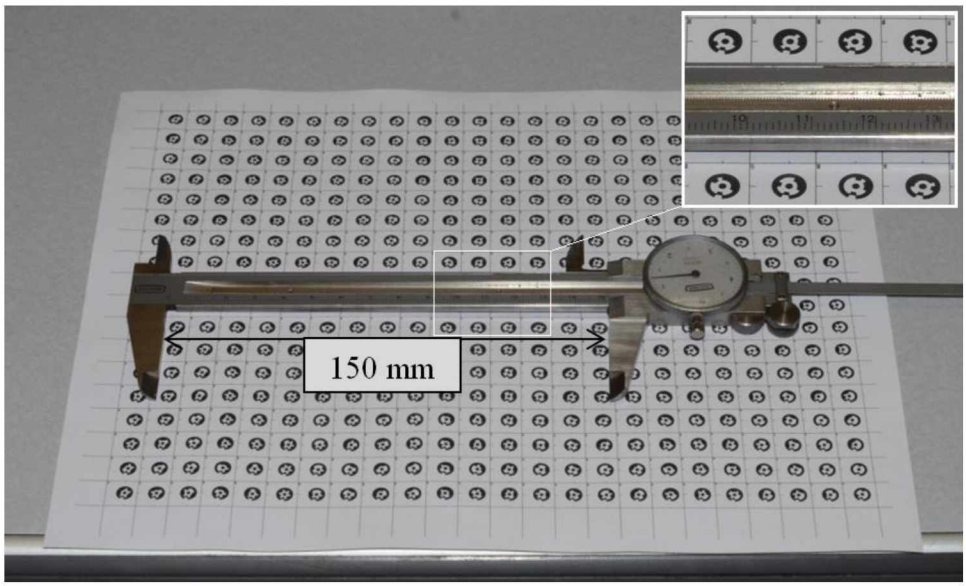

Figure 11 Photogrammetric analyses on a caliper

Experimental Design for Isotropic Compression Tests on the Stainless Steel Cylinder

For the validation tests on the stainless steel cylinder as shown in Figure 4a or Figures 7a and b, the confining acrylic chamber is 8″ in height, 4″ in outer diameter, and 0.24″ in thickness with a refractive index of 1.491. A total number of 16 measurement targets are posted on the load frame to set up the global coordinate system so that all the measurements can be compared in the same coordinate system as shown in Figure 4a. A total of 218 measurement targets are posted on the outside surface of the acrylic chamber, which include 2 circles (39 targets / circle) and 8 vertical stripes (12-25 targets/strip). A total of 336 measurement targets (21 targets/circle × 16 circles) are posted on the steel cylinder surface to facilitate the measurements and analysis.

The experimental program includes reconstruction of 3D models of the steel cylinder under following conditions using the proposed method: 1. exposed in air, 2. installed in the triaxial test apparatus with 0 kPa, 200 kPa, 400 kPa, and 600 kPa of confining pressures. The tests are performed in the following way: (1) firmly fix the stainless steel cylinder on the bottom

platen of the triaxial test apparatus without the confining chamber (acrylic cell); (2) take photographs from different orientations; (3) carefully install the confining chamber and slowly fill it with water; (4) take photographs from different orientations without applying any confining pressure; (5) increase the confining water pressure to 200 kPa and take photographs from different orientations; and (6) repeat the steps in (5) with the confining water pressures of 400 kPa and 600 kPa, respectively. Figure 4b shows a typical pattern how the photographs are taken. Better measurement accuracy is achieved by: (1) taking at least five photographs from different orientations for each area/point of interest, (2) ensuring sufficient overlap between adjacent pictures, and (3) capturing photographs from different view angles. For each test mentioned above, approximately 50 pictures were captured, which took 3-5 minutes. The images at different confining pressure are then analyzed to reconstruct the 3D model of the steel cylinder.

Modulus of elasticity of stainless steel ranges from 180 GPa to 200 GPa. With the applied maximum confining pressure of 600 kPa in this study, the volumetric strain is less than 1×10^{-5} and the steel cylinder can be considered as rigid. A rigid specimen provides a good reference for evaluating measurement accuracy for the proposed method. Since photogrammetry is a well-established technique with high level of measurement accuracy, the reconstructed 3D model for Case 1 is used as the "true" result to evaluate the accuracy of the proposed method.

Experimental Design for Drained Tests on Saturated Sand

Beside isotropic compression tests on the stainless steel cylinder, drained triaxial shearing tests are also performed on a saturated sand specimen to validate the ability of the proposed method for total and local volume change measurements. As shown in Figures 12a and 12b, the confining acrylic chamber used in this group of tests is 12″ in height, 6.5″ in outer diameter, and 0.38″ in thickness with a refractive index of 1.491. A total number of 174 measurement targets

are posted on the outside surface of the acrylic chamber, including 2 circles (55 targets/circle) and 4 vertical stripes (16 targets/strip).

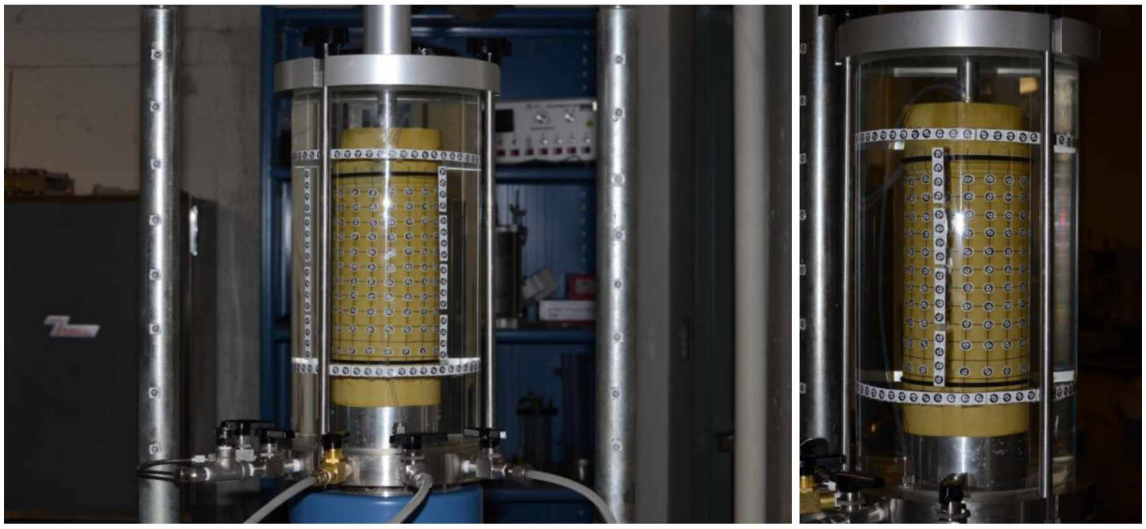

(a) **(b)**

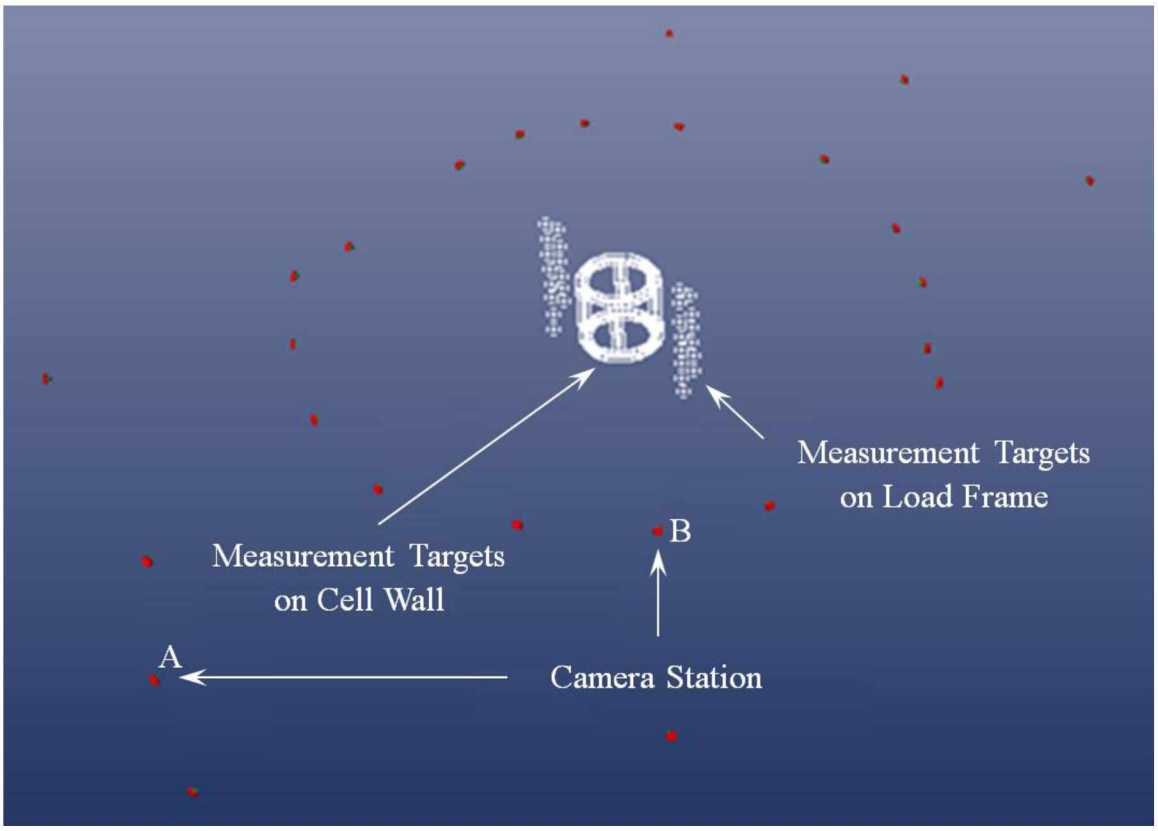

(c)

Figure 12 Photogrammetric analysis for triaxial shearing tests on a saturated sand specimen (a) Image at camera station A; (b) Image at camera station B; and (c) Results from the photogrammetric analysis

Oven dried standard Ottawa fine sand is used to fabricate a specimen with a diameter and height of 71 mm and 137 mm, respectively. After compaction, the specimen is carefully mounted on the pedestal of the triaxial cell. A suction of 50 kPa is applied to hold the sand specimen in place during sealing. Then, a total of 176 measurement targets (16 targets/circle × 11 circles) are posted on the pre-gridded membrane. To ensure that the volume change of the specimen can be well represented by the movement of those measurement targets, two circles of measurement targets are posted on the top cap and the pedestal. In this way, the entire specimen is covered by

the measurement targets. After this, cell chamber is installed and filled with tap water. To shorten the saturation process of the sand specimen, carbon dioxide (CO_2) is used to slowly seep upward from the bottom of the specimen to replace air in sand. Then, de-aired water is allowed to enter the sand specimen from the bottom to top. After this, a back pressure of 400 kPa is applied to dissolve the CO_2 in the sand specimen for several hours. Net confining pressure is maintained to be constant at 35 kPa during this saturation process. When a B-value of 0.98 is reached, saturation process is considered to be completed. Then, the chamber and back pressures are simultaneously decreased to 100 kPa and 0 kPa, respectively. Drained triaxial shearing test is performed after this.

For all triaxial shearing tests, a confining pressure of 100 kPa is applied. A vertical displacement rate of 1 mm/min is applied to generate some volume change of the saturated specimen. During loading, drainage valve is kept open to allow water to flow in or out of the specimen. The volume change of the specimen is recorded by monitoring the amount of water flowing in or out of the sand. At every 2 or 3 mm of vertical displacement, load is paused and drainage valve is shut off. Then, the images are captured for future analysis. In this way, there is no volume change on the specimen during image capturing. For each volume measurement by using the proposed method, approximately 25 images around the specimen are taken following the pattern as shown in Figure 12. The validation test is stopped when a total displacement of 15 mm is reached.

Presentation of Test Results

One limitation of the proposed method is that it is computation-intensive. A standalone computer program called PhotoSoilVolume has been developed to perform the required

calculations in the following sections. Figure 13 shows the flowchart for the implementation of the proposed method. For each test, the computations take about 5-10 minutes.

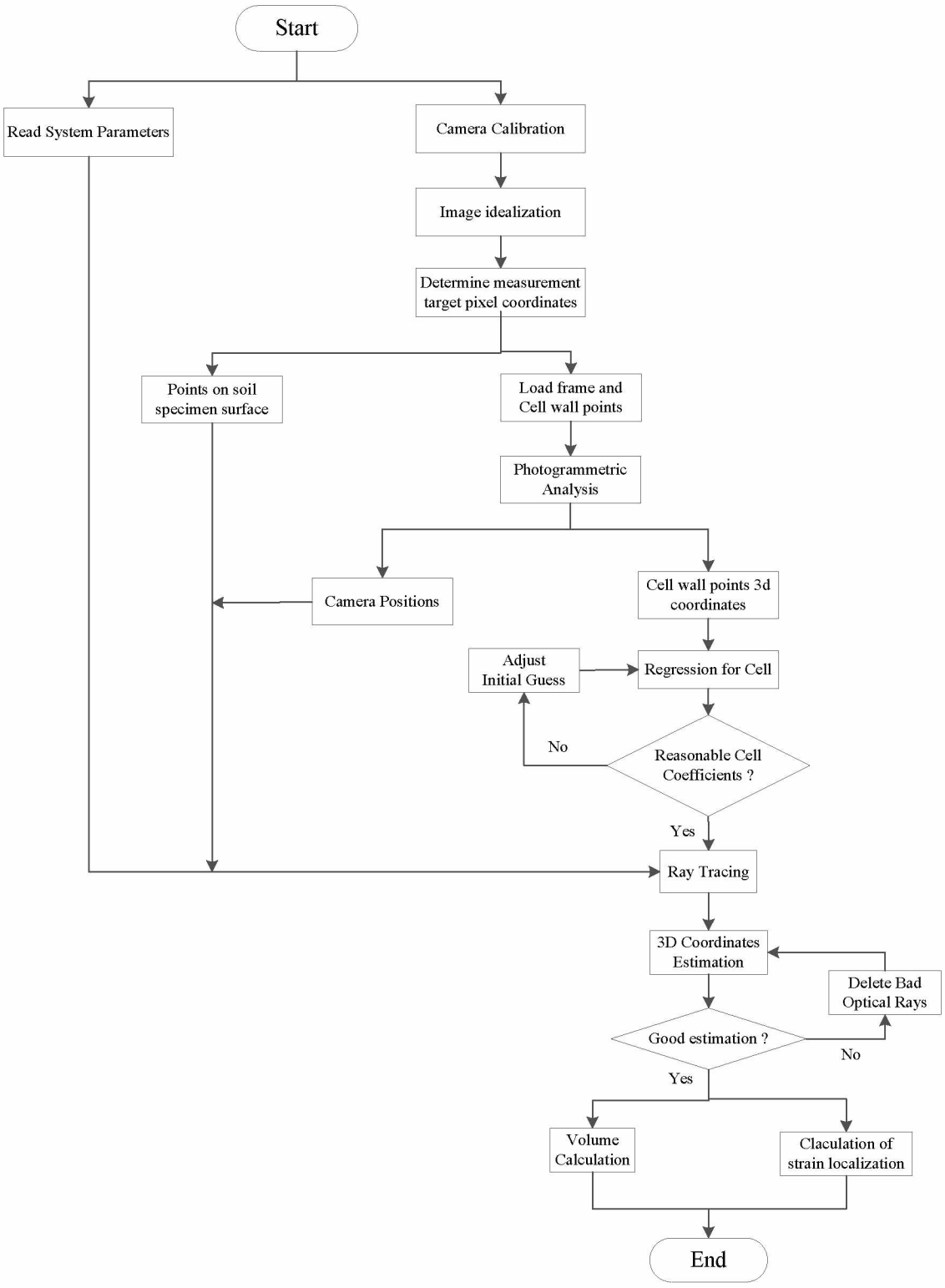

Figure 13 Flowchart for the method implementation

Test Results on the Stainless Steel Cylinder

1. 3D reconstruction of acrylic cell chamber

In the proposed method, measurement targets are posted on the surface of the acrylic cell and photogrammetry is used to determine the camera orientations and to measure the 3D coordinates of these points to define the shapes and positions of the acrylic cell. Figures 7a and 7b are two of 45 images taken during the isotropic compression test for the steel cylinder with a confining water pressure of 600 kPa. All the images are idealized using Equation 29 with calibrated camera parameters listed in Table 2. The measurement targets posted on the load frame and the surface of the acrylic cell are used to perform a photogrammetric analysis from which the camera orientations and the coordinates of the measurement points are calculated, while the measurement targets on the specimen surface are influenced by refraction and left for further analyses. Figure 7c shows the photogrammetric analysis results for confining water pressure of 600 kPa. In Figure 7c, CS represents camera station, while the white dots represent the locations of the measurement targets on the surface of the acrylic cell chamber.

The shape and position of the acrylic cell are described by equation (11) with nine parameters: A, B, C, X_R, Y_R, Z_R, κ, ω, and ϕ. Table 4 shows the parameter values obtained by best-fitting the surface measurement points under different cell pressures. In these parameters, κ, ω, and ϕ represent the rotational angles of the acrylic cell relative the established global system. Since the acrylic cell is axisymmetric, ϕ can always set to be zero and the result is not influenced. As can be seen in Table 4, the acrylic cell is not perfectly vertical compared with the established global system since κ and ω are not zero. They remain relatively constant, indicating the acrylic cell is fairly stable with no rotations during the tests.

A, B, and C are related to the radius profile of the acrylic cell in the vertical direction and the radii of the acrylic cell at different heights are calculated by the following equation:

$$r = \sqrt{AY^2 + BY + C} \tag{30}$$

where r is of the radius of the acrylic cell and Y is the coordinate in the vertical direction. Figure 14 shows the change of acrylic cell radii in the vertical direction under different cell pressures. It is found that even under zero confining pressure, the acrylic cell is not perfectly cylindrical, which might be plastic deformations caused by previous tests. Figure 14 also indicates the acrylic cell did deform into a barrel shape under applied cell pressures. The maximum change in radius is about 300 micron (from 50.2 to 50.5 mm), which is an order larger than the accuracy of the photogrammetry in air as demonstrated by the photogrammetric analysis on the caliper. The associated change of water volume in the acrylic cell at a confining pressure of 600 kPa is about 2.8% for a specimen with a diameter of 2 inch and height of 4 inch, which is much larger than the accuracy of 0.25% achieved by the double-cell triaxial test apparatus. In addition, the test durations in this study is very short (less than 2 hours). Most suction-controlled triaxial tests for unsaturated soils are very lengthy and commonly take several weeks or months. As a result, the deformation due to creep could be even bigger. X_R, Y_R, and Z_R represent the coordinates of the center of the barrel-shaped acrylic cell. As can be seen in Table 4, X_R and Z_R values do not change very much, while Y_R value changes slightly due to the expansion of the acrylic cell as shown in Figure 14. The acrylic cell expands to different shapes and positions at different cell pressures. It is worth noting that for isotropic compression tests at different water pressures, pictures are taken at arbitrary and therefore different positions. Consequently, tests performed on the rigid stainless steel cylinder are "different" tests at different confining pressures.

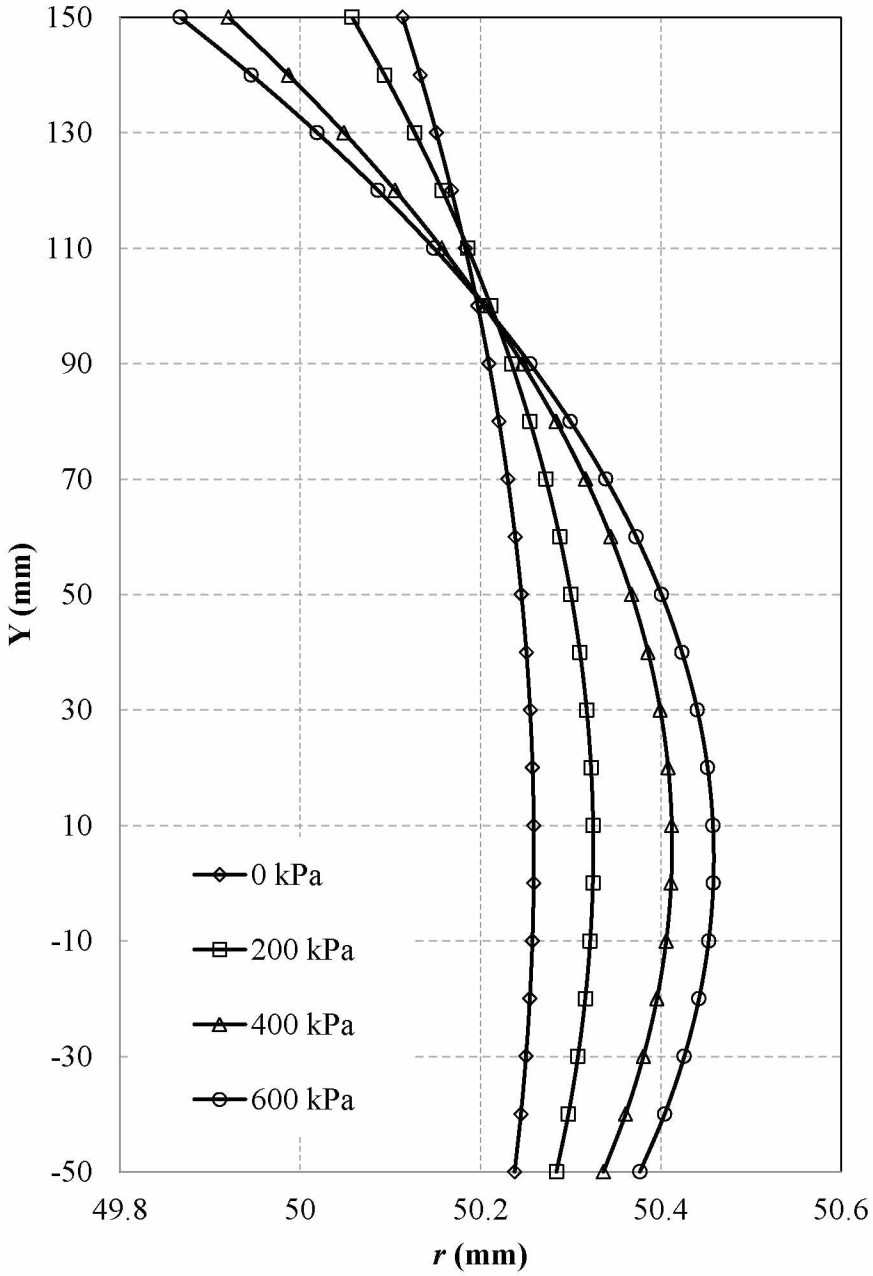

Figure 14 Cell radius changes at different confining pressures

2. Accuracy for point measurements

Once the camera orientations for each images and the shape and position of the acrylic cell in the global coordinate system are known (e.g. Figure 7c and Table 4, respectively), multiple ray-tracings are performed to obtain 3D coordinates of any point on the specimen surface using the proposed method. Figure 15a shows the multiple ray-tracing processes used to calculate the 3D coordinates of one point (point 187 as shown in Figures 7a and 7b) on the surface of the stainless steel cylinder during triaxial testing using PhotoSoilVolume. A total of seven photos with ID numbers of 12, 13, 14, 29, 30, 35, and 36 (also shown in Figure 7c), respectively are used for point 187. Figure 15b shows the enlargement of the seven tracing rays near point 187. They are lines in the 3D space without interception point. The least-square optimization is used to estimate the location of point 187. It is found that the "distances" between these tracing rays and the estimated point of 187 vary from 0.014 mm to 0.094 mm with an average of 0.049 mm, indicating that the proposed method has a high level of accuracy.

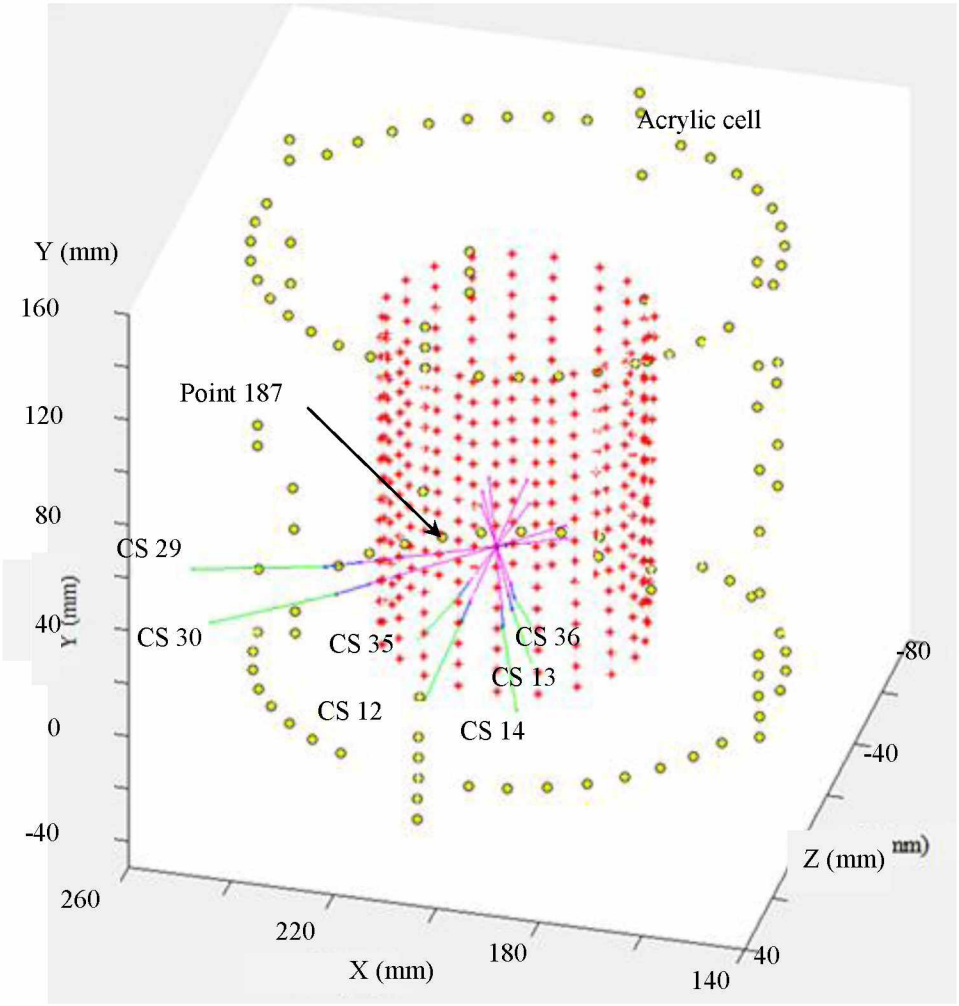

(a) Ray-tracing process for point 187 at confining pressure of 600 kPa (from PhotoSoilVolume)

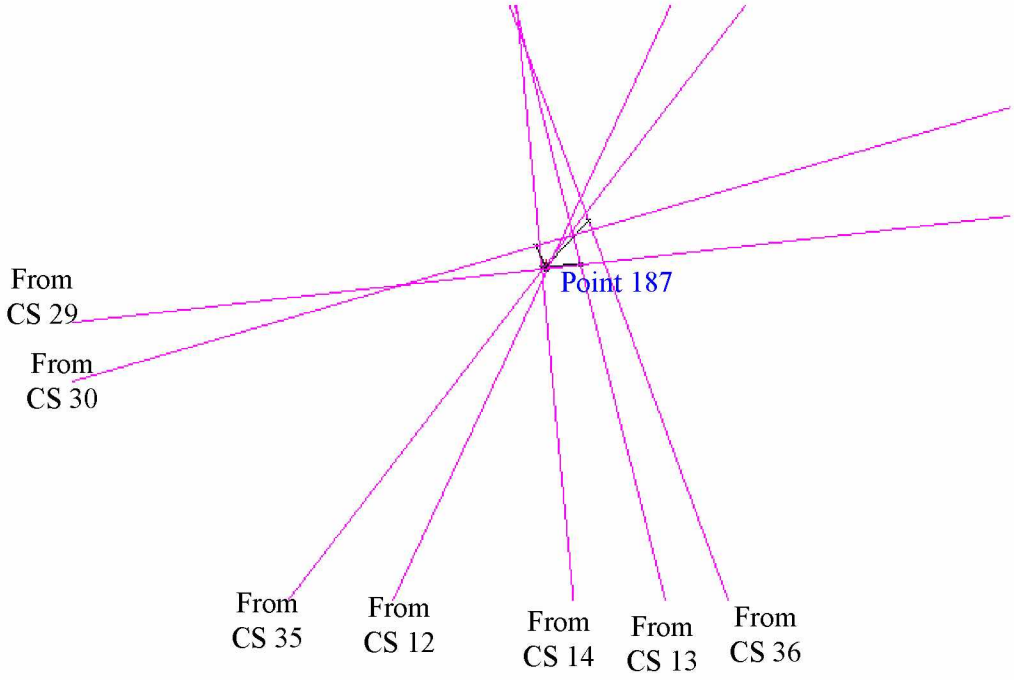

(b) Enlargement near point 187(from PhotoSoilVolume).

Figure 15 Ray-tracing process for point 187

The same approach is applied to all the other points and a 3D model of the specimen surface is constructed as shown in Figure 15a. The results are then compared under the same global coordinate system as shown in Figure 16a with the results calculated for the steel cylinder when exposed in the air (Test 1) by assuming results for Test 1 ("in air") are the "true" values. Figure 16a shows the 3D results for all the tests. Figures 16b and 16c show the comparison of test results for cross sections 1 and 16, respectively. Due to the limited space, the 2D image for cross sections 2 and 15 are not presented. No visible difference is found for all the test results. Using the global coordinate system as shown in Figure 4a, measurement errors are also estimated by calculating the displacement of each point "moving" from its position in Test 1 (exposed in the air) to those obtained from the proposed method in the other tests when the steel cylinder

subjected to different confining pressures. It is found that the average errors for 336 targets ranged from 0.056 mm to 0.076 mm with standard deviations varying from 0.033 to 0.061mm.

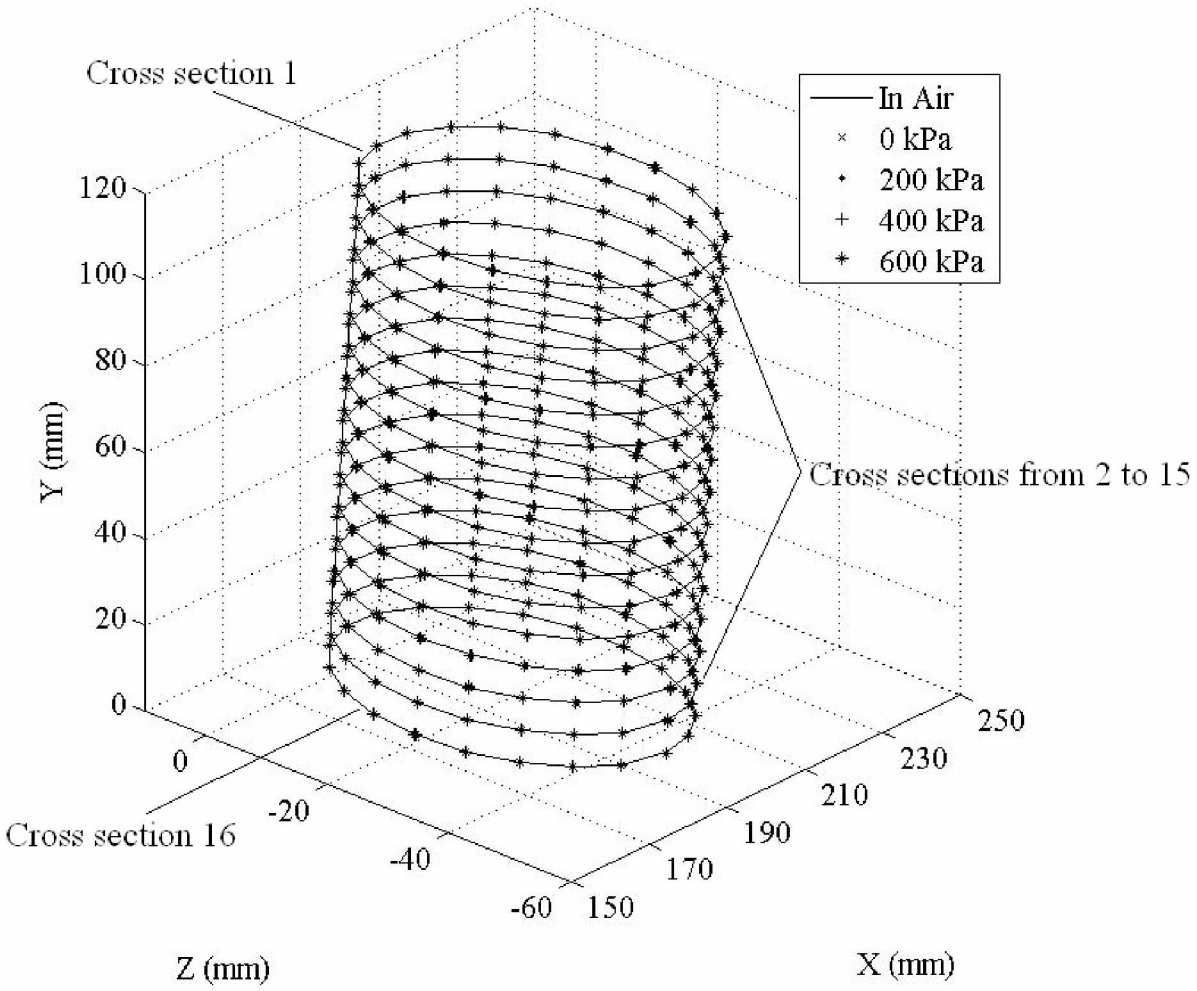

(a) 3D presentation of test results under different confining pressures

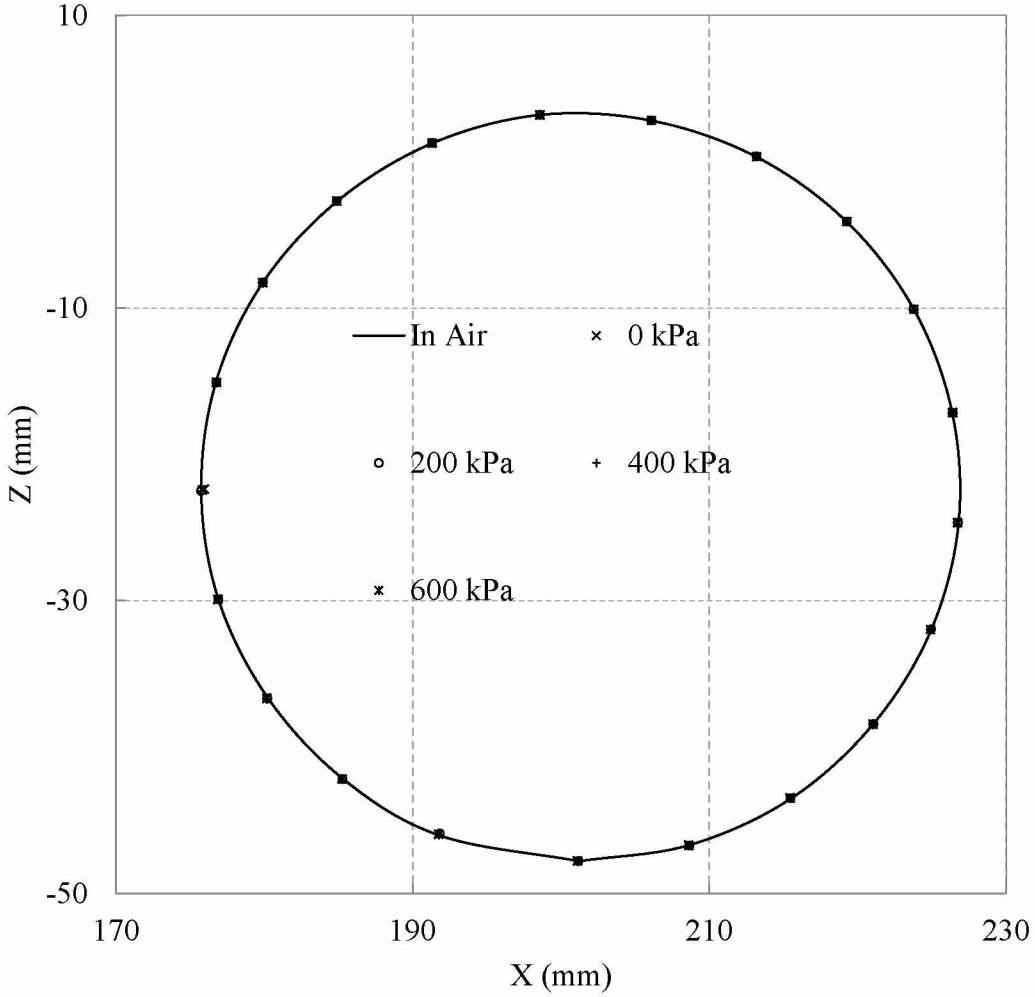

(b) Cross section 1

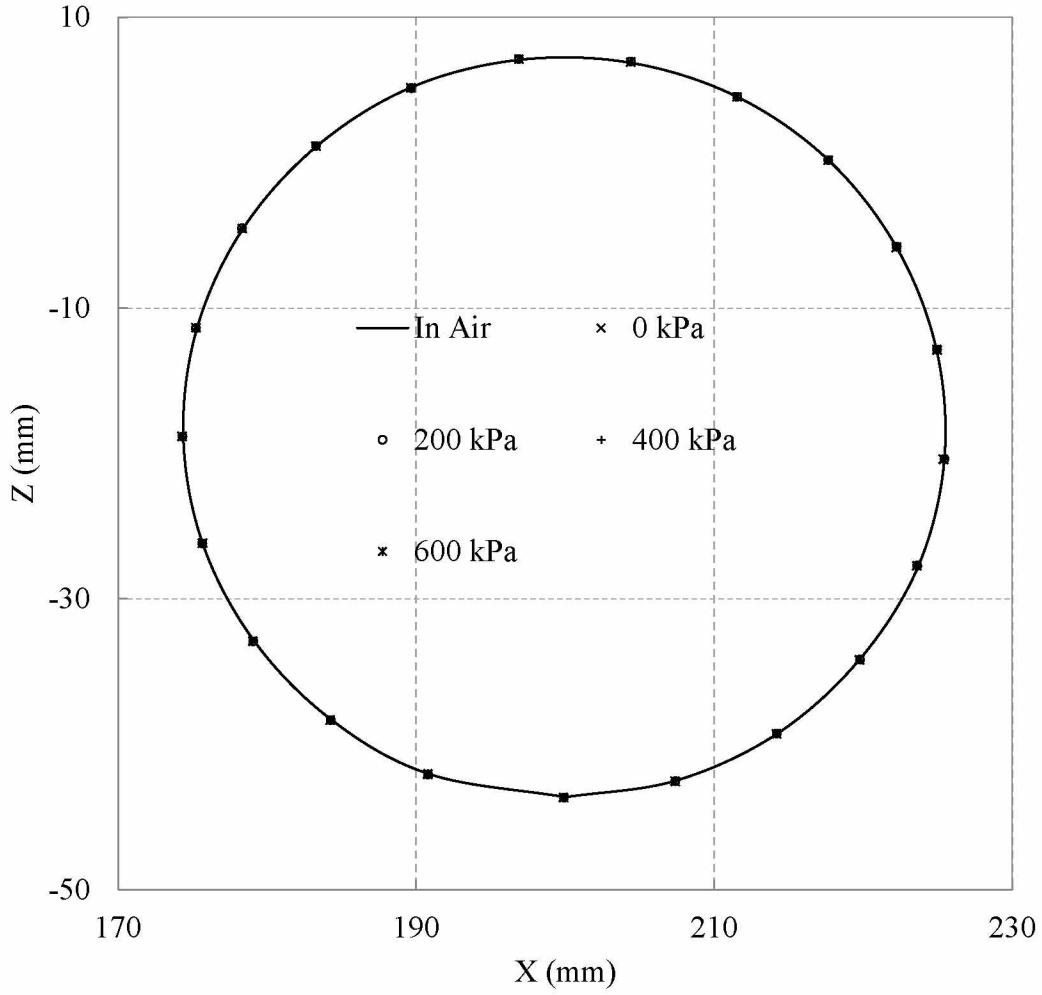

(c) Cross section 16

Figure 16 Comparison of test results under different confining pressures

3. Accuracy for the total volume measurements

Different from the DIA and DIC methods, the proposed method can be used to construct a full field 3D model for the whole specimen instead of a part of the specimen. Once the full field 3D model for the whole specimen is obtained, the total volume of the soils specimen can be calculated. After the 3D coordinates of points on the specimen surface are obtained as shown in

Figure 15a, a triangular surface mesh is first generated with a hollow cylindrical shape (similar to those in Figure 17). An arbitrary point on the top circular edge is then connected to all the other points on the same circle to form the top surface. The bottom surface is formed in the same way such that an enclosed 3D surface is formed from which the total volume of the specimen is calculated for all the tests. The total volumes of the cylinder vary from 221.525 cm^3 (600 kPa) to 221.813 cm^3 (200 kPa), while the corresponding "true" value is 222.039 cm^3 (measured in air). The errors range from 0.131% to 0.232%, indicating the accuracy of the proposed method was high. Analysis of the test results also indicate that many assumptions used in the Macari et al. (1997) cannot be satisfied. For example, without calibration, a commercial camera cannot be treated as ideal pinhole camera and it is very difficult to accurately control its position through manual installation. The confining chamber deforms under pressure and the soil specimen is almost impossible to be installed at the center of the chamber.

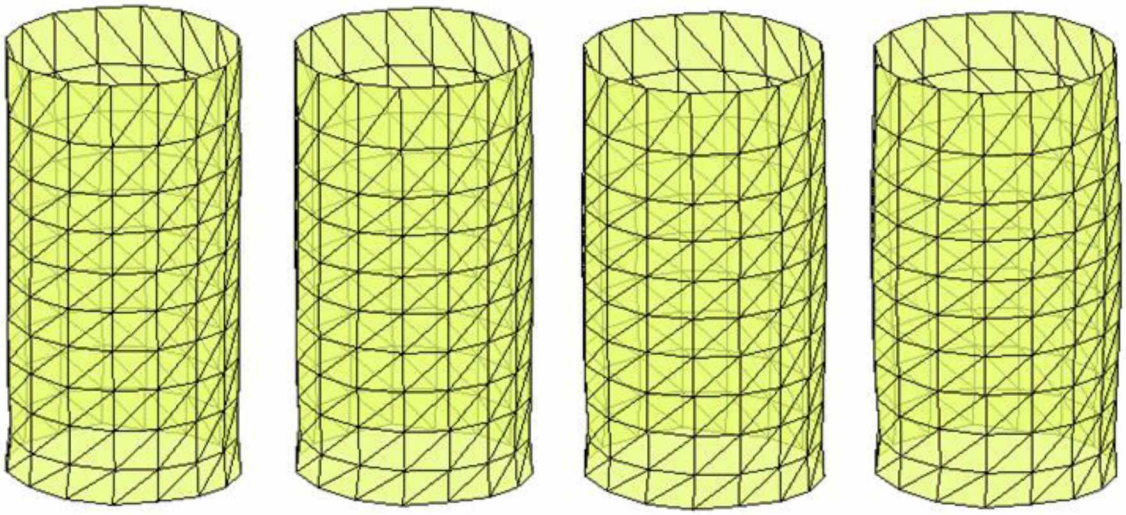

(a) 0 mm (b) 2 mm (c) 4 mm (d) 6 mm

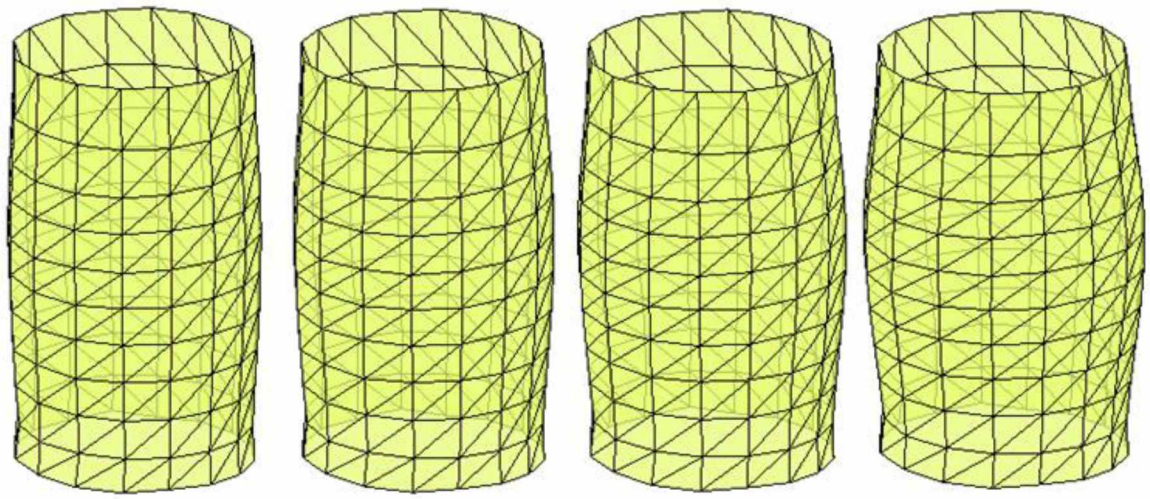

(e) 8 mm (f) 10 mm (g) 12 mm (h) 15 mm

Figure 17 Soil deformations under axial displacement levels

Test Results on the Saturated Sand

A series of drained triaxial shearing tests on a saturated sand specimen are used to demonstrate the ability of the proposed method to measure both total volume changes and strain localizations. Figure 17 shows the changes in soil shapes at axial displacements of 0, 2, 4, 6, 8, 10, 12, and 15 mm, respectively, obtained using the proposed method. The soil specimen has approximately a cylindrical shape at the initial stage. There is no obvious change in shape when the axial displacement is 2 mm. With increase in the axial displacement, the soil specimen gradually bulges at the center into a coke bottle shape. The diameter of the specimen at the center is the largest and first narrows towards the two ends and then increases again at the two ends. The shapes are reasonable since the friction between the soil and the loading platens restrains the soil specimen from deforming.

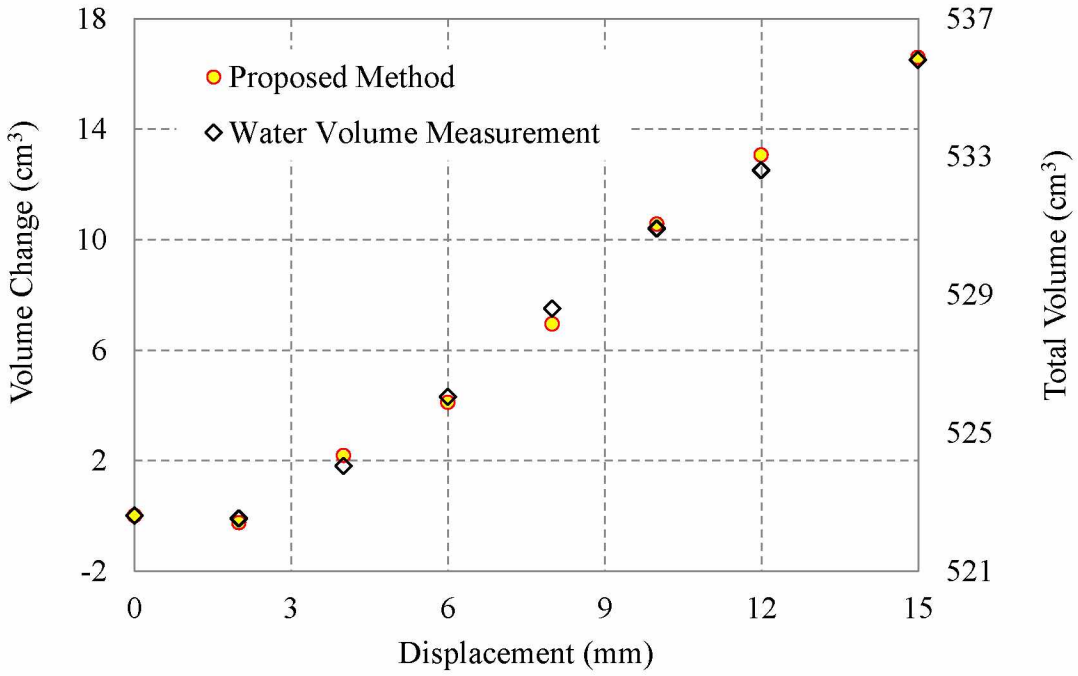

Figure 18 Comparison of volume changes from two different methods

The total volumes of the soil at different axial displacements are calculated using the method discussed previously. The volume changes of the soil specimen are also obtained by direct measurement of the volume of water coming in and out of the soil. It is worth noting that the proposed method measures the absolute volume and volume changes, while the conventional water volume measurements only provides the volume changes relative to the initial conditions. This is beneficial since in the proposed method each measurement is independent of each other. If there is an error in the initial volume measurement, it will not be transferred into later measurements. In order to make valid comparisons, the initial volumes of the soil specimen for the water volume change method are assumed to be the same as the soil volume obtained from the proposed method at confining pressure of 100 kPa with 0 mm of axial displacement, and only the volume changes are compared. Figure 18 shows the comparison of results obtained from the

two different methods. As can be seen, both results indicate that the specimen experiences contractions when the axial displacement changes from 0 to 2 mm and dilations for the displacement from 2 mm to 15 mm, respectively. The difference in volume changes obtained from the two methods is small during the whole process with the average and maximum differences being 0.051% and 0.108%, respectively. Considering that the accuracy of volume change measurements by directly monitoring water volume changes is about 0.25% (GDS 2009), it is concluded that the proposed method can produce results comparable to those obtained from the conventional direct measurement of water volume changes.

A numerical interpolation technique similar to that in Lin and Penumadu (2006) is used to generate a continuous deformation field from the obtained discrete points on the specimen surface. Figure 19 shows the vertical strains developed in the soil specimen at different vertical displacement levels. It can be seen from Figure 19 that the distribution of vertical displacement and strain is generally uniform until vertical displacement reaches 6mm. Note from Figure 17 that the shear band is not visible to the human eye and the specimen still looks relatively uniform. However, the contour plot in Figure 19 clearly shows that the strain localization is fully developed when the vertical displacement is 15 mm.

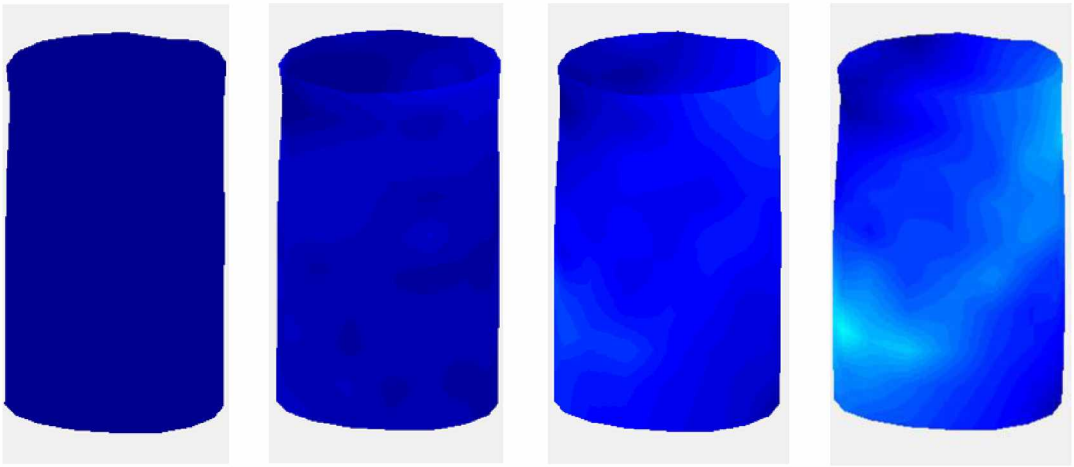

(b) 0 mm (b) 2 mm (c) 4 mm (d) 6 mm

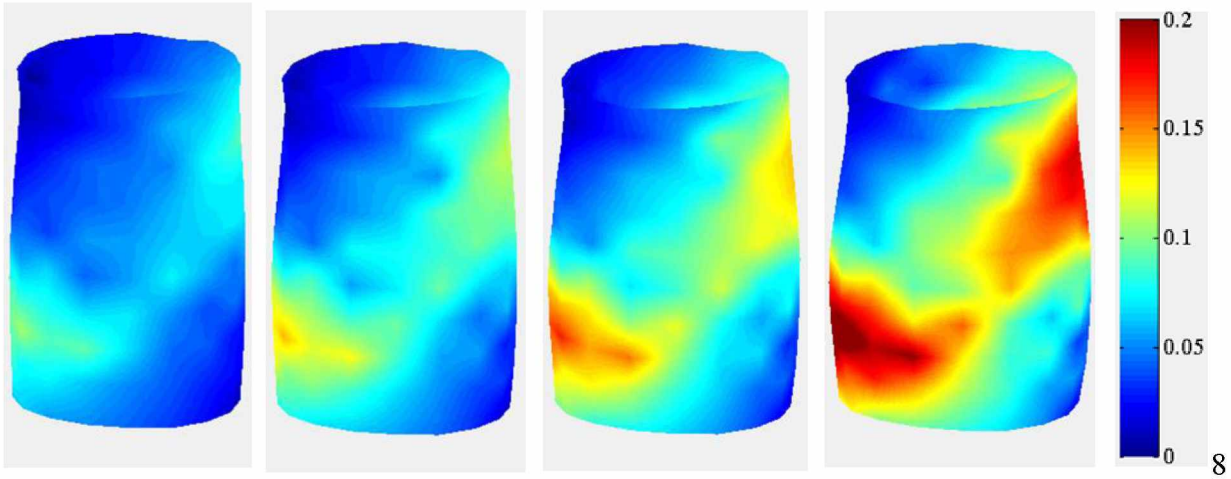

8 mm (f) 10 mm (g) 12 mm (h) 15 mm

Figure 19 Vertical strains under axial displacement levels

Advantages of the Proposed Method

There are several advantages in the proposed method over the existing image-based methods. Firstly, the camera is carefully calibrated to satisfy the requirements of the ideal pinhole camera model. Table 2 indicates that if the camera is not calibrated, the error caused by the difference in focal length alone is more than 6%, not counting the errors caused by

distortions. Secondly, the camera orientations for each photograph are calculated based upon the principle of photogrammetry to an accuracy of 10 microns. This eliminates the requirement of accurate control of camera orientations in other image-based method and allows images to be taken at any arbitrary positions. This is advantageous since images are taken at very short distances with the best shooting directions to improve the accuracy of the measurements. In the validation tests, all photos are taken at distance from 590 mm to 740 mm, while in the method proposed by Macari et al. (1997), the camera must be set "far away" from the specimen to make sure the camera is approximately an ideal pinhole camera with shooting direction passing the center of the soil specimen. In addition, it is well known that the magnitudes of distortions at the center of the images are less than that near the borders of the images (as shown in Figures 10b and 10c). This proposed method uses points near the center of an image only for the calculation. As a result, higher accuracy can be obtained. Snell's law is a theoretical equation for refraction correction as long as the incident ray and the normal at the incident point were correct. Thirdly, using photogrammetry technique, shape and location of the used confining chamber (acrylic cell) is accurately determined based on 3D coordinates of the measurement targets posted on cell wall surface. Under different confining pressure levels, movements of the measurement targets on the cell wall surface are well captured which eliminates the error from assuming a fixed chamber location and shape. The mathematical model used for cylindrical or barrel shaped objects well represents the shape and location of the test chamber. Fourthly, an optimization process is performed to get the best accuracy of the multiple images. In the proposed method, each image represents a measurement and each image includes many specimen surface points. At least three ray-tracing processes were used to determine the coordinate of any point on the specimen surface. Normally, much more than five images are used to calculate the coordinates for a point.

The redundancy can significantly improve the accuracy of the measurements and eliminate any assumptions regarding the specimen deformations.

Conclusions

In this paper, a photogrammetry-based method is developed to reconstruct 3D model of a soil specimen during triaxial tests using conventional triaxial test apparatus. It can be used for both saturated and unsaturated soils and both total and local volume changes can be calculated. The key features of the proposed method include: use of photogrammetry to determine camera orientations and location of the acrylic cell, application of ray-tracing technique to accommodate the light bending due to refraction, and implementation of the least-square optimization to estimate the 3D coordinates of points on the specimen surface. The method essentially extends the application of photogrammetry from one optical medium to multiple media. The method is cost-effective since only a commercially available digital camera is needed and minor modification is needed for the conventional triaxial test apparatus for saturated soils.

Results obtained from the validation tests indicate that the accuracy for the photogrammetry in the air is about 10 microns. For preliminary triaxial tests performed in this study, the average accuracy for single point measurements ranges from 0.056 mm to 0.076 mm with standard deviations varying from 0.033 to 0.061mm. The accuracy for total volume measurements is better than 0.25%. Such accuracy is higher than or at least comparable to those from existing methods, indicating the proposed method is sufficiently accurate for triaxial testing for both saturated and unsaturated soils. One limitation of the proposed method could be its intensive computation requirement. However, a computer program called PhotoSoilVolume has been developed to perform the required calculations in a few minutes.

References

Alshibli KA, Sture S, Costes NC, Lankton ML, Batiste SN, Swanson RA (2000) Assessment of localized deformations in sand using X-Ray computed tomography. Geotech Testing J 23(3):274-299.

Bishop AW, Donald IB (1961) The Experimental Study of Partly Saturated Soil in the Triaxial Apparatus. Proceedings of the 5th International Conference on Soils Mechanic, Paris, Vol. 1: 13–21.

Blatz JA, Graham J (2003) Elastic-plastic modeling of unsaturated soil using results from a new triaxial test with controlled suction. Géotechnique, 53(1):113–122.

Clayton CRI, Khatrush SA (1986) A New Device for Measuring Local Axial Strains on Triaxial Specimens. Géotechnique 36, No.4: 593–597.

Clayton CRI, Khatrush SA, Bica AVD, Siddique A (1989) The use of Hall effect semiconductors in geotechnical instrumentation. Geotech Testing J 12(1):69–76.

Colliat-Dangus JL, Desrues J, Foray P (1988) Triaxial Testing Of Granular Soil Under Elevated Cell Pressure. Advanced Triaxial Testing For Soil And Rocks - ASTM Stp 977, Ed R.T. Donaghe- R.C. Chaney And M.L. Silver, ASTM: 290-310.

Costa-Filho de LM (1982). Measurement of axial strains in triaxial tests on London Clay. Geotech Testing J 8(1):3–13.

Cui YJ, Delage P (1996) Yielding and plastic behavior of an unsaturated compacted silt. Géotechnique 46, No.2:291–311.

Desrues J (1984) La localisation de la déformation dans les matériaux granulaires . thèse de Doctorat es Sciences , PhD thesis, USMG and INPG, Grenoble, France.

Desrues J, Chambon R, Mokni M, Mazerolle F (1996) Void ratio evolution inside shear bands in triaxial sand specimens studied by computed tomography. Géotechnique 46, No. 35:29– 546.

Desrues, J. and Viggiani, G. (2004). "Strain localization in sand: an overview of the experimental results obtained in Grenoble using stereophotogrammetry", International Journal for Numerical and Analytical Methods in Geomechamcs, Vol. 28, No. 4, 279-321.

Gachet P, Geiser F, Laloui L, Vulliet L(2007) Automated Digital Image Processing for Volume Change Measurement in Triaxial Cells, Geotech Testing J 30(2): 98-103.

Gachet P, Klubertanz G, Vulliet L, Laloui L (2003). Interfacial behavior of unsaturated soil with small-scale models and use of image processing techniques. Geotech Testing J 26(1):12–21.

GDS (2009): http://www.epccn.com/gds/datasheets/UNSAT_Datasheet.pdf

Geiser F (1999) Comportément mécanique d'um limon non saturé: étude expérimentale et modélisation constitutive. Ph.D. thesis, Swiss Federal Institute of Technology, Lausanne, Switzerland.

Helm JD, McNeill SR, Sutton MA (1996) Improved 3D image correlation for surface displacement measurement. Opt. Eng. (Bellingham), 35(7):1911–1920.

Hird CC, Hajj AR (1995) A simulation of tube sampling effects on the stiffness of clays. Geotech Testing J 18(1):3–14.

Josa A, Alonso EE, Lloret A, Gens A (1987) Stress–strain behaviour of partially saturated soils. In: Proc. of the 9th European conference on soil mechanics and foundation engineering, Dublin, vol 2:561–564.

Klotz EU, Coop MR (2002) On the identification of critical state lines for sands, Geotech Testing J 25(3):288-301.

Ladd, R. S. (1978). "Preparing test specimens using undercompaction." ASTM Geotechnical Testing Journal, 1(1), 16-23.

Lade PV (1988) Automatic volume change and pressure measurement devices for triaxial testing of soils. Geotech Testing J 11(4):263–268.

Laloui L, Pe´ron H, Geiser F, Rifa'i A, Vulliet L (2006) Advances in volume measurement in unsaturated triaxial tests. Soils Found 46(3):341–349.

Laudahn A, Sosna K, Bohac J (2005) A simple method for air volume change measurement in triaxial tests. Geotech Testing J 28(3):313–318.

Lin H, Penumadu D (2006) Strain Localization in Combined Axial-Torsional Testing on Kaolin Clay. J. Eng. Mech., 132(5):555-564.

Macari EJ, Parker JK, Costes NC (1997). Measurement of volume changes in triaxial tests using digital imaging techniques. Geotech Testing J 20(1):103–109.

Mikhail EM, Bethel JS, McGlone JC (2001) Introduction to Modern Photogrammetry. John Wiley & Sons, Inc. ISBN 0-471-30924-9

Ng CWW, Zhan LT, Cui YJ (2002) A new simple system for measuring volume changes in unsaturated soils. Canadian Geotechnical Journal 39(3): 757–764.

Parker JK (1987). Image processing and analysis for the mechanics of granular materials experiment. ASME Proceedings of the 19th SE Symposium on System Theory, Nashville, TN, March 2, ASME, New York.

Rampino C, Mancuso C, Vinale F (1999) Laboratory testing on an unsaturated soil: equipment, procedures, and first experimental results. Can Geotech J 36(1):1–12.

Razavi MR, Muhunthan B, Al Hattamleh O (2007) Representative Elementary Volume Analysis of Sands using X-ray Computed Tomography. Geotech Testing J 30(3):212-219.

Rechenmacher AL (2006) Grain-scale processes governing shear band initiation and evolution in sands. J. Mech. Phys. Solids, 54:22–45.

Rechenmacher AL, Medina-Cetina Z (2007) Calibration of constitutive models with spatially varying parameters. Journal of Geotechnical and Geo-environmental Engineering, American Society of Civil Engineers, 133(12): 1567-1576.

Romero E, Facio JA, Lloret A, Gens A, Alonso EE (1997) A New Suction and Temperature Controlled Triaxial Apparatus. Proceedings of the 14th International Conference on Soil Mechanics and Foundation Engineering, Hamburg, Vol. 1: 185–188.

Roscoe KH (1970). The influence of strains in soil mechanics. Géotechnique 20(2):129–170.

Sachan A, Penumadu D (2007) Strain localization in solid cylindrical clay specimens using Digital Image Analysis (DIA) technique. Soils and Foundations, 47:67-78.

Sutton MA, McNeill SR, Helm JD, Chao YJ (2000) Advances in two-dimensional and three-dimensional computer vision. Top. Appl. Phys., 77:323-372.

Triggs B, McLauchlan PF, Hartley RI, Fitzgibbon AW (2000). Buddle Adjustment – A Modern Synthesis, In: Triggs, B., Zisserman, A., and Szeliski, R. (eds.) ICCV-WS 1999. LNCS, vol.1983: 298-375.

Viggiani G, Hall S (2008) Full-field measurements, a new tool for laboratory experimental geomechanics, Fourth Symposium on Deformation Characteristics of Geomaterials, IOS Press, Amsterdam, vol.1: 3-26.

Wheeler SJ (1988) The undrained shear strength of soils containing large gas bubbles. Géotechnique 38(3):399–413.

White D, Take W, Bolton M (2003) Measuring soil deformation in geotechnical models using digital images and PIV analysis. Proc., 10th Int. Conf. on Computer Methods and Advances in Geomechanics, Tuscon, Ariz., Balkema, Rotterdam, The Netherlands: 997–1002.

Wolf, K. B. (1995), "Geometry and dynamics in refracting systems", European Journal of Physics 16: 14–20.

Attachment: Derivation of the Snell's law in the 3D space

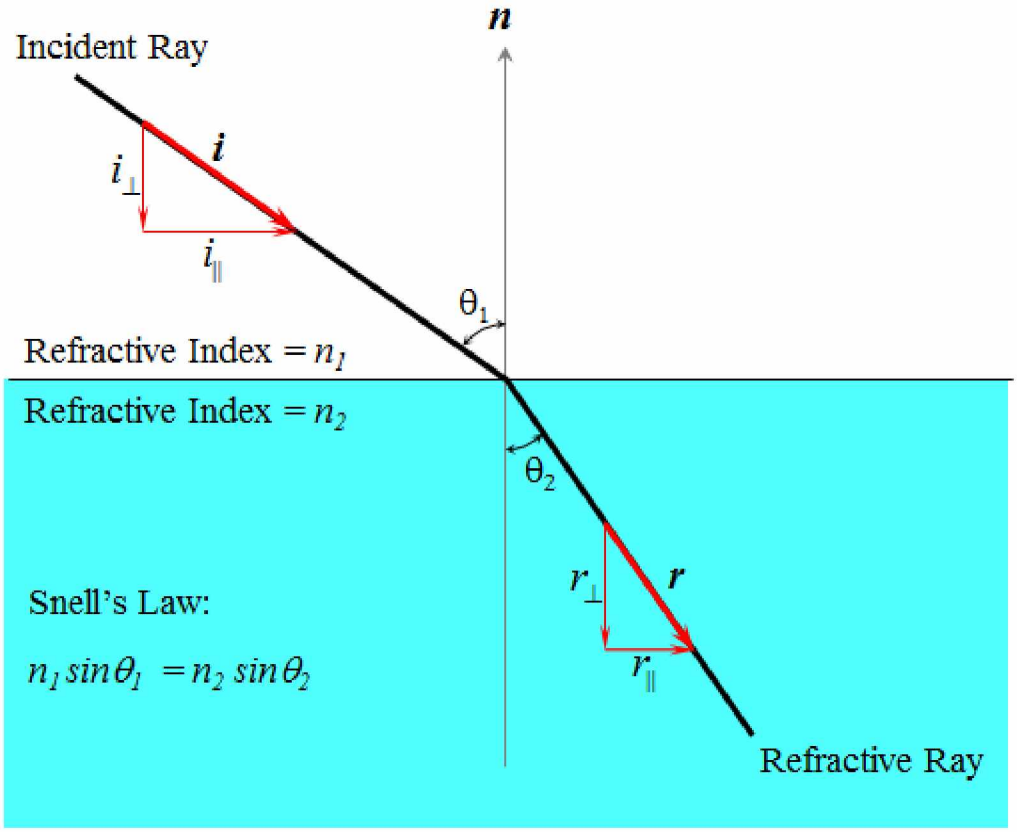

Figure A1. Snell's Law

The scalar form of the Snell's law is normally expressed as follows (Wolf 1995):

$$\frac{n_1}{n_2} = \frac{\sin\theta_2}{\sin\theta_1} \tag{A1}$$

where,

n_1 and n_2 = refraction indices for two media, and

θ_1 and θ_2 = incident and refraction angles with respect to the normal at the refractive boundary.

In the proposed method, incident and refractive rays are often expressed as vectors in 3D space. As a result, it is more convenient to use the vector form of Snell's law. Its derivations are as follows:

$\vec{i}$ and $\vec{r}$ are unit directional vectors in space for the incident and refractive rays as shown in the Figure A1, respectively. $\vec{n}$ is the surface normal to the refractive boundary at the intersection point and also a unit directional vector pointing to the side of the incident ray. To facilitate the discussion, both $\vec{i}$ and $\vec{r}$ are first resolved into two components: one is parallel to *n* and the other is perpendicular to *n*.

$$\vec{i} = \vec{i_{\perp}} + \vec{i_{||}} \tag{A2}$$

$$\vec{r} = \vec{r_{\perp}} + \vec{r_{||}} \tag{A3}$$

Where subscripts "$\perp$" and "||" represents direction parallel to and perpendicular to $\vec{n}$, respectively.

It is worth noting that θ_1 and θ_2 are scalars and have ranges from 0 to 90°. Consequently, the following relationships exist:

$$\vec{i} \bullet \vec{n} = -\cos\theta_1 \tag{A4}$$

$$\left|\vec{i_{||}}\right| = \sin\theta_1 \tag{A5}$$

$$\left|\vec{r_{||}}\right| = \sin\theta_2 \tag{A6}$$

Both $\vec{i_{\perp}}$ and $\vec{r_{\perp}}$ are parallel to $\vec{n}$ but with opposite direction, therefore, they can be expressed as follows:

$$\vec{i_{\perp}} = -\cos\theta_1 \vec{n} \tag{A7}$$

$$\vec{r_{\perp}} = -\cos\theta_2 \vec{n} \tag{A8}$$

Combining Equations A2 and A6, one has,

$$\vec{i_{\parallel}} = \vec{i} - \vec{i_{\perp}} = \vec{i} + \cos\theta_1 \vec{n} \tag{A9}$$

$\vec{i_{\parallel}}$ and $\vec{r_{\parallel}}$ are also parallel to each other. Therefore,

$$\vec{r_{\parallel}} = \left|\vec{r_{\parallel}}\right| \frac{\vec{i_{\parallel}}}{\left|\vec{i_{\parallel}}\right|} = \sin\theta_2 \frac{\vec{i_{\parallel}}}{\sin\theta_1} = \frac{\sin\theta_2}{\sin\theta_1} \vec{i} + \cos\theta_1 \vec{n} \tag{A10}$$

Plugging Equations A1 and A4 into Equation A10, one has,

$$\vec{r_{\parallel}} = \frac{n_1}{n_2}\left[\vec{i} - \left(\vec{i} \bullet \vec{n}\right) \vec{n}\right] \tag{A11}$$

Combining Equations A1, A4, and A8, one has,

$$\begin{aligned} \vec{r_{\perp}} &= -\cos\theta_2 \vec{n} = -\sqrt{1-\sin^2\theta_2}\,\vec{n} = -\sqrt{1-\left(\frac{n_1}{n_2}\sin\theta_1\right)^2}\,\vec{n} = -\sqrt{1-\left(\frac{n_1}{n_2}\right)^2 \left(1-\cos^2\theta_1\right)}\,\vec{n} \\ &= -\sqrt{1-\left(\frac{n_1}{n_2}\right)^2\left[1-\left(\vec{i}\bullet\vec{n}\right)^2\right]}\,\vec{n} \end{aligned} \tag{A12}$$

Substituting Equations A10 and A11 into Equation A3 yields:

$$\vec{r} = \frac{n_1}{n_2}\vec{i} - \left(\frac{n_1}{n_2}\left(\vec{i}\bullet\vec{n}\right) + \sqrt{1-\left(\frac{n_1}{n_2}\right)^2\left[1-\left(\vec{i}\bullet\vec{n}\right)^2\right]}\right)\vec{n} \tag{A13}$$

Equation A13 requires four inputs to calculate the unit vector for the refractive ray $\vec{r}$: $\vec{i}$, $\vec{n}$, n_1 and n_2.